Quasilinear and Nonlinear Wave-Particle Interactions in Magnetospheric Plasmas

Allanson, Oliver; Zhang, Xiao-Jia; Omura, Yoshiharu

DOI:
10.3389/978-2-8325-3710-7

frontiers | Research Topics

Quasilinear and nonlinear wave-particle interactions in magnetospheric plasmas

Edited by
Oliver Allanson, Xiao-Jia Zhang and Yoshiharu Omura

Published in
Frontiers in Astronomy and Space Sciences

ISSN 1664-8714
ISBN 978-2-8325-3710-7
DOI 10.3389/978-2-8325-3710-7

About Frontiers

Frontiers is more than just an open access publisher of scholarly articles: it is a pioneering approach to the world of academia, radically improving the way scholarly research is managed. The grand vision of Frontiers is a world where all people have an equal opportunity to seek, share and generate knowledge. Frontiers provides immediate and permanent online open access to all its publications, but this alone is not enough to realize our grand goals.

Frontiers journal series

The Frontiers journal series is a multi-tier and interdisciplinary set of open-access, online journals, promising a paradigm shift from the current review, selection and dissemination processes in academic publishing. All Frontiers journals are driven by researchers for researchers; therefore, they constitute a service to the scholarly community. At the same time, the *Frontiers journal series* operates on a revolutionary invention, the tiered publishing system, initially addressing specific communities of scholars, and gradually climbing up to broader public understanding, thus serving the interests of the lay society, too.

Dedication to quality

Each Frontiers article is a landmark of the highest quality, thanks to genuinely collaborative interactions between authors and review editors, who include some of the world's best academicians. Research must be certified by peers before entering a stream of knowledge that may eventually reach the public - and shape society; therefore, Frontiers only applies the most rigorous and unbiased reviews. Frontiers revolutionizes research publishing by freely delivering the most outstanding research, evaluated with no bias from both the academic and social point of view. By applying the most advanced information technologies, Frontiers is catapulting scholarly publishing into a new generation.

What are Frontiers Research Topics?

Frontiers Research Topics are very popular trademarks of the *Frontiers journals series*: they are collections of at least ten articles, all centered on a particular subject. With their unique mix of varied contributions from Original Research to Review Articles, Frontiers Research Topics unify the most influential researchers, the latest key findings and historical advances in a hot research area.

Find out more on how to host your own Frontiers Research Topic or contribute to one as an author by contacting the Frontiers editorial office: frontiersin.org/about/contact

Quasilinear and nonlinear wave-particle interactions in magnetospheric plasmas

Topic editors

Oliver Allanson — University of Exeter, United Kingdom
Xiao-Jia Zhang — The University of Texas at Dallas, United States
Yoshiharu Omura — Kyoto University, Japan

Citation

Allanson, O., Zhang, X.-J., Omura, Y., eds. (2023). *Quasilinear and nonlinear wave-particle interactions in magnetospheric plasmas*. Lausanne: Frontiers Media SA. doi: 10.3389/978-2-8325-3710-7

Table of contents

frontiers | Frontiers in Astronomy and Space Sciences

TYPE Original Research
PUBLISHED 11 August 2022
DOI 10.3389/fspas.2022.971358

OPEN ACCESS

EDITED BY
Xiao-Jia Zhang,
University of California, Los Angeles, United States

REVIEWED BY
Oliver Allanson,
University of Exeter, United Kingdom
Yikai Hsieh,
Kyoto University, Japan

*CORRESPONDENCE
Jay M. Albert,
jay.albert@us.af.mil

SPECIALTY SECTION
This article was submitted to Space Physics, a section of the journal Frontiers in Astronomy and Space Sciences

RECEIVED 17 June 2022
ACCEPTED 15 July 2022
PUBLISHED 11 August 2022

CITATION
Albert JM, Artemyev A, Li W, Gan L and Ma Q (2022), Analytical results for phase bunching in the pendulum model of wave-particle interactions.
Front. Astron. Space Sci. 9:971358.
doi: 10.3389/fspas.2022.971358

Analytical results for phase bunching in the pendulum model of wave-particle interactions

Jay M. Albert [1]*, Anton Artemyev [2], Wen Li [3], Longzhi Gan [3] and Qianli Ma [3,4]

[1]Air Force Research Laboratory, Kirtland AFB, Rio Rancho, NM, United States, [2]Department of Earth, Planetary, and Space Sciences, University of California, Los Angeles, Los Angeles, CA, United States, [3]Center for Space Physics, Boston University, Boston, MA, United States, [4]Department of Atmospheric and Oceanic Sciences, University of California, Los Angeles, Los Angeles, CA, United States

Radiation belt electrons are strongly affected by resonant interactions with cyclotron-resonant waves. In the case of a particle passing through resonance with a single, coherent wave, a Hamiltonian formulation is advantageous. With certain approximations, the Hamiltonian has the same form as that for a plane pendulum, leading to estimates of the change at resonance of the first adiabatic invariant I, energy, and pitch angle. In the case of large wave amplitude (relative to the spatial variation of the background magnetic field), the resonant change in I and its conjugate phase angle ξ are not diffusive but determined by nonlinear dynamics. A general analytical treatment of slow separatrix crossing has long been available and can be used to give the changes in I associated with "phase bunching," including the detailed dependence on ξ, in the nonlinear regime. Here we review this treatment, evaluate it numerically, and relate it to previous analytical results for nonlinear wave-particle interactions. "Positive phase bunching" can occur for some particles even in the pendulum Hamiltonian approximation, though the fraction of such particles may be exponentially small.

KEYWORDS

wave-particle interactions, radiation belts, nonlinear, hamiltonian, test particle simulation

1 Introduction

Cyclotron-resonant interactions with whistler mode waves are of major importance for the dynamics of radiation belt electrons (Bortnik and Thorne, 2007). Many numerical studies of test particles interacting with coherent, monochromatic waves in an inhomogeneous background magnetic field have demonstrated that cyclotron-resonant interactions lead to changes in particle energy and pitch angle, due to the breaking of an adiabatic invariant (Chang and Inan, 1983; Bortnik et al., 2008). For sufficiently small amplitude waves these changes are diffusive, associated with a random wave-particle phase (Albert, 2010), but larger waves induce systematic, asymmetric changes, whose detailed behavior can be described in terms of phase bunching and phase trapping (Albert, 1993). Estimates of the associated energy and pitch angle ranges of

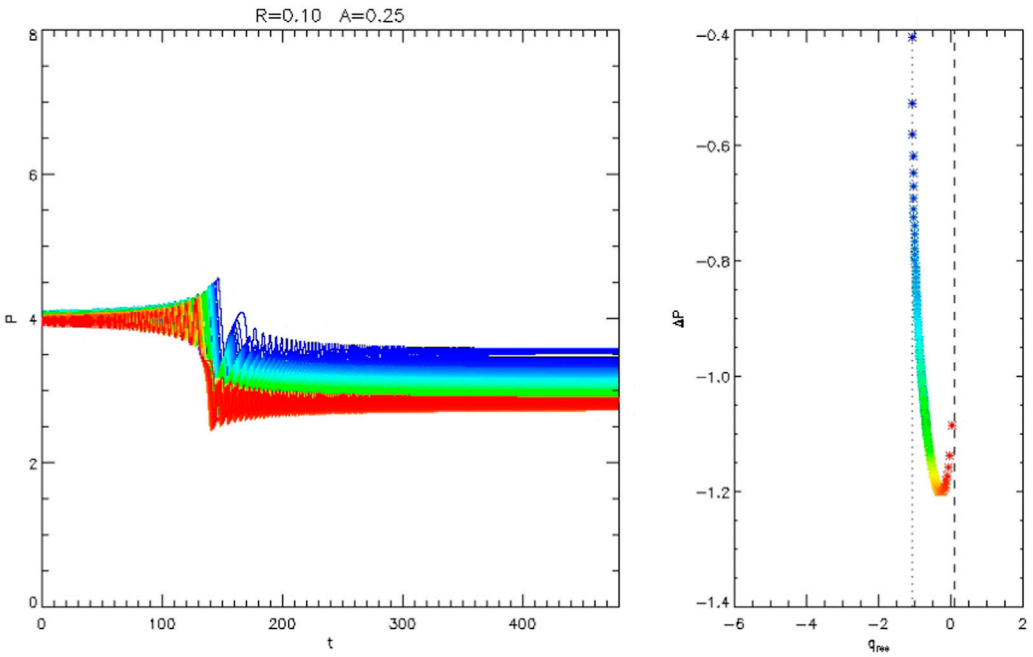

FIGURE 1
Trajectories of 120 particles from numerical integration of the equations of motion specified by the Hamiltonian of Eq. 11, with inhomogeneity parameter $R = 0.1$ and wave amplitude parameter $A = 0.25$. Left: P vs. t, showing systematic decrease associated with phase bunching at resonance. In this case, all values of ΔP are negative. Right: Change in P vs. the value of q at resonance. The dotted and dashed vertical lines show the calculated values q_{turn} and $q_x + 2\pi$, respectively, as discussed in the text.

such electrons have been given by, e.g., Albert (2002) and Albert et al. (2021). These processes are in turn deeply connected to nonlinear wave generation or growth (Omura et al., 2008).

For electrons interacting with parallel-propagating whistler mode waves, phase trapping causes a sustained increase in particle energy and pitch angle, while phase bunching (that is, without trapping) causes these quantities to decrease; the lost particle energy can feed wave growth. Theory and simulation indicate that for representative wave and particle parameters, phase bunching has much higher probability than phase trapping in each resonant interaction. Typical particle trajectories showing phase bunching, obtained with a Hamiltonian formulation to be discussed below, are shown in Figures 1, 2. The variables P and q, defined in Section 3, are related, respectively, to the first adiabatic invariant I and its conjugate phase ξ, which are reviewed in Section 2.

Albert (1993) obtained an analytical estimate of the change in the first adiabatic invariant (and therefore energy and pitch angle) caused by phase bunching in the highly nonlinear limit, though the dependence on resonant wave-particle phase seen in numerical simulations was not accounted for. A more detailed expression can be written formally as an explicit but infinite and intractable integral, which must still be evaluated numerically; however, averaging over the appropriate phase and interchanging integrals leads to a much more manageable expression (Neishtadt, 1999); this is presented in Section 4. Furthermore, the very general treatment of adiabatic invariant changes of Cary et al. (1986) can be applied to this problem, leading to a detailed and reliable approximation that retains the phase dependence in closed form. This treatment quantitiatively captures the numerical observation that phase bunching-induced changes exhibit a spread of values, including some that are in fact in the positive direction. This is discussed in Section 5. Depending on the parameters used, adiabatic invariant increase may be physically significant yet too infrequent to detect from direct numerical simulation with a small number of particles.

2 Hamiltonian formulation

Albert (1993) and Albert (2000) derived a Hamiltonian $\mathcal{K}(I, \xi, z)$ appropriate for motion near a resonance. Recapping the definitions and results of those papers, equations of motion for the normalized first adiabatic invariant $I \approx (p_\perp/mc)^2\,(\omega/2\Omega)$ and the canonically conjugate angle ξ (a combination of wave phase and particle gyrophase) issue from a Hamiltonian $\mathcal{K}$, given by

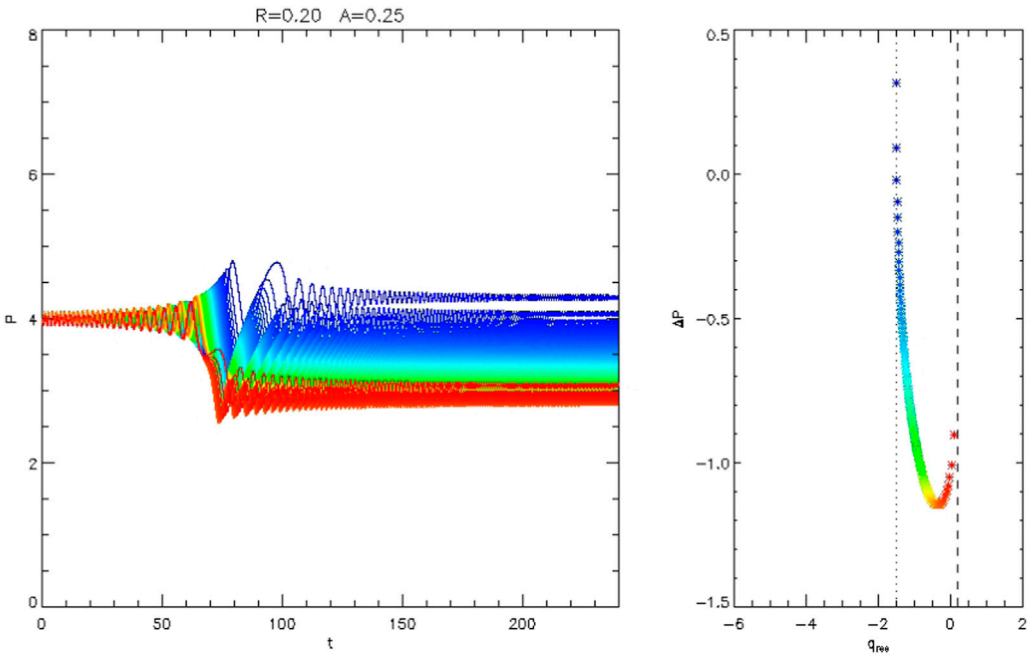

FIGURE 2
Trajectories of 120 particles from numerical integration of the equations of motion specified by the Hamiltonian of Eq. 11, with inhomogeneity parameter $R = 0.2$ and wave amplitude parameter $A = 0.25$. Left: P vs. t, showing systematic decrease associated with phase bunching at resonance. In this case, most but not all values of ΔP are negative. Right: Change in P vs. the value of q at resonance. The dotted and dashed vertical lines show the calculated values q_{turn} and $q_x + 2\pi$, respectively, as discussed in the text.

$$\begin{aligned} \mathcal{K} &= \mathcal{K}_0(I,z) + \mathcal{K}_1(I,z)\sin\xi, \\ \mathcal{K}_0 &= \eta_z(I - c_2) - \sigma_z s\ell P_0(I,z), \\ P_0 &= \sqrt{\left(\frac{I-c_2}{s\ell}\right)^2 - 1 - 2\frac{\Omega}{\omega}I}. \end{aligned} \tag{1}$$

The distance z along the field line plays the role of time, so that $d\xi/dz = \partial\mathcal{K}/\partial z$ and $dI/dz = -\partial\mathcal{K}/\partial\xi$. Here ω is the wave frequency, Ω is the (local, unsigned, nonrelativistic) electron gyrofrequency, s is the sign of the particle charge, ℓ is the resonant harmonic number, and η_z is the parallel wave refractive index, $k_\parallel c/\omega$. P_0 is the normalized magnitude of $p_\parallel$, where $p_\perp$ and $p_\parallel$ are components of the physical momentum relative to the background magnetic field. The sign of $p_\parallel$ is given by $\sigma_z = \pm 1$. The constant of motion c_2 relates I and the particle kinetic energy E through

$$c_2 = I - s\ell\gamma, \tag{2}$$

where γ is the relativistic factor $1 + E/mc^2$. $\mathcal{K}_1$ is proportional to the wave amplitude; it is given in detail by Eqs. A2, A4 of Albert (2000), and for the special case of a parallel-propagating wave by Eqs. 2, 3 of Albert et al. (2021). As given in Appendix C of Albert (2000), changes in energy E and equatorial pitch angle α_0 are related to small resonant changes in I by

$$\frac{\Delta E}{mc^2} = \frac{\Delta I}{s\ell}, \qquad \Delta\alpha_0 = \frac{\Omega_{eq}/\omega - (\gamma/s\ell)\sin^2\alpha_0}{(p/mc)^2\sin\alpha_0\cos\alpha_0}\Delta I, \tag{3}$$

where $\ell \neq 0$, and Ω_{eq} is the equatorial value of Ω.

At a given location z, the resonant value of I is determined to lowest order by $\partial\mathcal{K}_0/\partial I = 0$, which corresponds to the standard resonance condition

$$\omega - k_\parallel v_\parallel = s\ell\Omega/\gamma. \tag{4}$$

This yields

$$\begin{aligned} I_{res} &= c_2 + (s\ell)^2\frac{\Omega}{\omega} + \sigma_z s\ell\eta_z P_{0,res}, \\ P_{0,res} &= \frac{1}{\sqrt{\eta_z^2 - 1}}\sqrt{1 + 2\frac{\Omega}{\omega}c_2 + \left(\frac{s\ell\Omega}{\omega}\right)^2}, \end{aligned} \tag{5}$$

which generalize Eqs. 5, 6 of Albert et al. (2021) to arbitrary values of $s\ell$. The z dependence of I_{res} is characterized by $\partial I_{res}/\partial\Omega$, which can be written as

$$\frac{\partial I_{res}}{\partial\Omega} = s\ell\sigma_z\frac{\eta_z I_{res} - s\ell\sigma_z P_{0,res}}{\omega(\eta_z^2 - 1)P_{0,res}}. \tag{6}$$

For the prototype situation of an electron ($s = -1$) in primary resonance ($\ell = -1$) and heading toward the equator ($\sigma_z = -1$), as considered here, this quantity is always negative; both z and the gyrofrequency Ω decrease and I_{res} increases. The correspondence between Eq. 1 and the gyro-averaged Lorentz equations of motion was investigated by Albert et al. (2022).

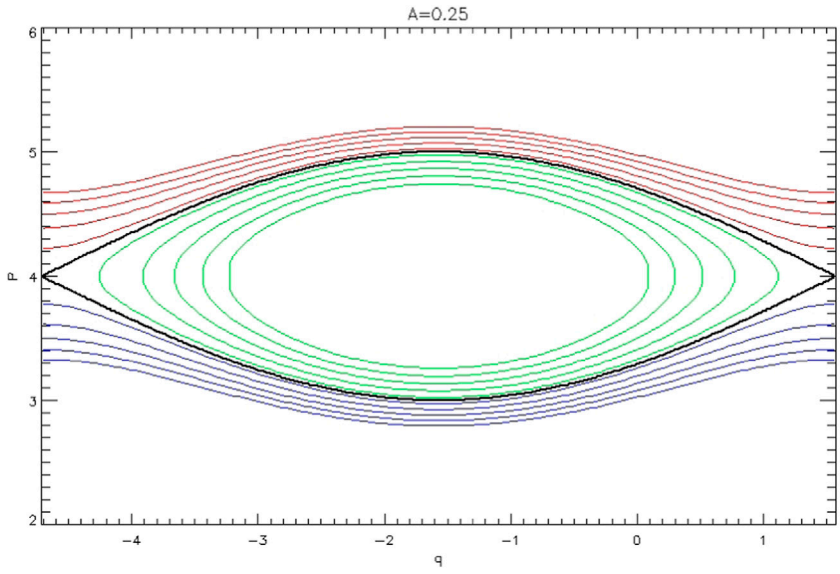

FIGURE 3
Contours of the pendulum Hamiltonian $H(P, q)$ given by Eq. 10, with $A = 0.25$. If the inhomogeneity parameter R is small but positive, the separatrix (shown in black) slowly rises. At resonance near the X-point, particles cross from red contours to blue (phase bunching) or green (phase trapping) contours.

3 Pendulum hamiltonian

A Taylor expansion of $\mathcal{K}_0$ in Eq. 1 gives the pendulum-like form

$$M(I, \xi, z) = \frac{G_r}{2}(I - I_{res})^2 + F_r \sin \xi \tag{7}$$

where $G_r = \partial^2 \mathcal{K}_0 / \partial I^2$ and $F_r = \mathcal{K}_1$, both evaluated at resonance. Albert (2000) obtained the estimate

$$G_r \approx \frac{\eta_z^2 - 1}{s\ell\sigma_z P_0}. \tag{8}$$

It is convenient to define σ_F and σ_G as the signs of F_r and G_r, respectively, so that $F = \sigma_F F_r$ and $G = \sigma_G G_r$ are positive. Then Eq. 7 can be brought into the same form as Equation 72 of Cary et al. (1986) by changing variables to

$$\tau = \sigma_G z, \quad P = GI, \quad q = \xi - \sigma_F \sigma_G \frac{\pi}{2}. \tag{9}$$

The equations of motion in these variables are then given by the Hamiltonian

$$H(P, q, \tau) = \frac{1}{2}(P - P_{res})^2 - 2A \sin^2(q/2), \tag{10}$$

with $P_{res} = GI_{res}$ and $A = FG$. Typical contours at fixed $P_{res}(\tau)$ are shown in Figure 3. For the prototype configuration (with $s = \ell = \sigma_z = -1$) G_r is negative, so $dP_{res}/d\tau = \sigma_G G(dI_{res}/dz)$ is positive. Albert et al. (2021) and Artemyev et al. (2021) considered a more general version of Eq. 7 which retains a factor of $\sqrt{I}$ in the wave term, which can distort the separatrix shape in order to maintain $I > 0$. This can lead to "positive phase bunching" for particles with small initial values of I (Kitahara and Katoh, 2019; Gan et al., 2020). However, as seen in Figure 2, this can occur even in the pendulum approximation.

Transforming from P to $p = P - P_{res}$ in Eq. 10 gives

$$K(p, q, \tau) = \frac{p^2}{2} - A(1 - \cos q - Rq), \tag{11}$$

where both A and the inhomogeneity parameter $R = (dP_{res}/d\tau)/A$ are positive and will be taken as constant. This idealization eliminates the possibility of phase trapping, which involves expansion of the Hamiltonian separatrix to engulf neighboring trajectories.

Trajectories of 120 particles from numerical integration of the equations of motion specified by the Hamiltonian of Eq. 11 are shown in Figure 1, with inhomogeneity parameter $R = 0.1$ and wave amplitude parameter $A = 0.25$. In this case, all values of ΔP are negative. In Figure 2 the wave amplitude parameter A is the same but the inhomogeneity parameter has been increased to $R = 0.2$, resulting in positive ΔP for some values of q at resonance.

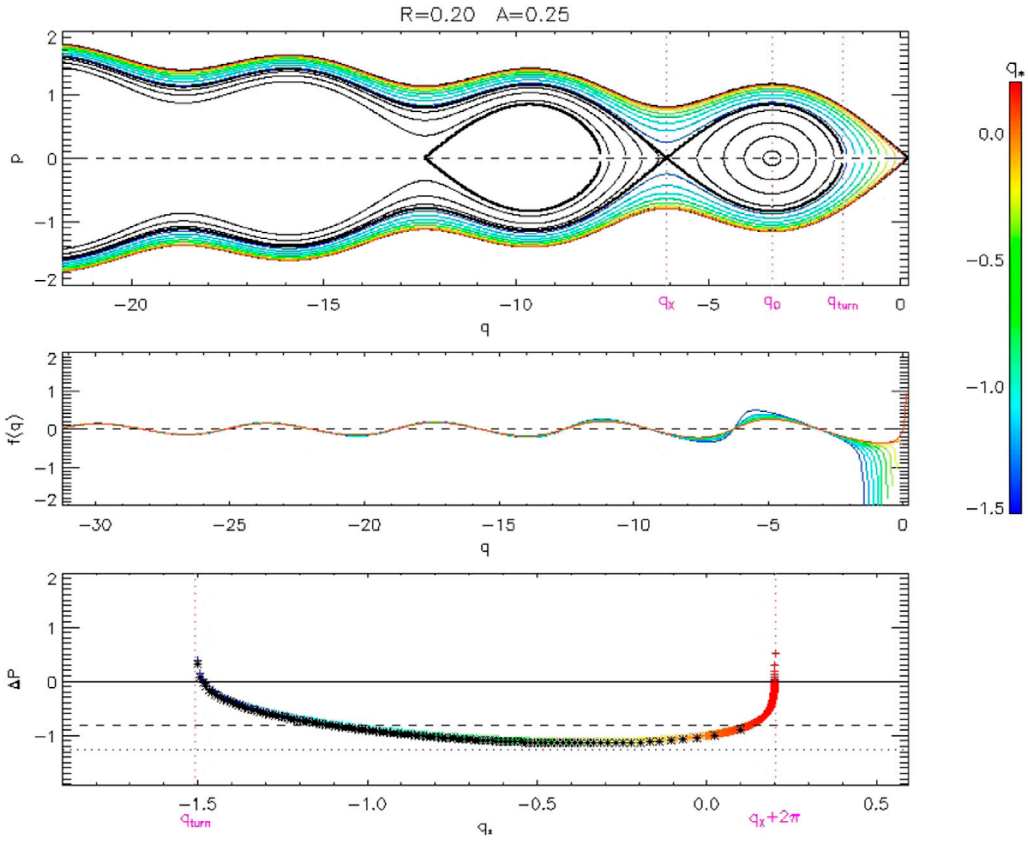

FIGURE 4
Top: Contours of $K(p, q)$ for parameters $R = 0.2$ and $A = 0.25$, color-coded by q_* (the value of q at $p = 0$). Middle: The function appearing in the integral of Eq. 13. Bottom: The colored symbols show ΔP vs. q_* from numerical evaluation of Eq. 13, which is negative for most but not all values of q_*. The horizontal dashed line shows the averaged value, and the horizontal dotted line shows the value $-(8/\pi)\sqrt{A}$ applicable to $R = 0$. The black symbols show the values from Figure 2.

4 Integral expression for changes in invariant

Contours of K, from Eq. 11, are shown in the top panel of Figure 4. The linearly unstable X-point obeys $\tan q_x = R/\sqrt{1-R^2}$ and the stable O-point obeys $\tan q_o = R/(-\sqrt{1-R^2})$, with the branch choices $-2\pi < q_x < -3\pi/2$ and $-3\pi/2 < q_o < -\pi$. The value q_{turn} is the second location where the curve through an X-point crosses $p = 0$, with $q_x < q_o < q_{turn} < q_x + 2\pi$. Finally, q_* refers to where a general trajectory crosses $p = 0$, with $q_{turn} < q_* < q_x + 2\pi$.

The change in P can be expressed as

$$\Delta P = \int dq \frac{dP/d\tau}{dq/d\tau} = \int dq \frac{-\partial H/\partial q}{\partial K/\partial p} = \int \frac{A \sin q \; dq}{\sqrt{2[K + A(1 - \cos q - Rq)]}}. \tag{12}$$

The integral over q is taken from $-\infty$ to the value q_* and then back to $q = -\infty$, where q_* is the value of q as the curve crosses $p = 0$. It is sufficient to integrate from $-\infty$ to q_* and double the result. It is convenient to define $h = (K + A)/AR$ and $a = 1/R$, so that

$$\Delta P = \sqrt{\frac{2A}{R}} \int_{-\infty}^{q_*} \frac{\sin q \; dq}{\sqrt{h - a\cos q - q}}. \tag{13}$$

Note that $h(p, q + 2\pi) = h(p, q) + 2\pi$.

This infinite, oscillatory integral is carried out along contours of $h(p, q)$. The middle panel shows values of the integrand, and indicates that a wide range of q values contribute to the total integral. The bottom panel shows numerical evaluations (in color), which are generally negative but can be positive near $q_* = q_{turn}$ or $q_* = q_x + 2\pi$. Also shown, as black symbols, are the values from the simulations of Figure 2. The excellent agreement is expected since Eq. 13 and the equations of motion from Eq. 11 should be exactly equivalent.

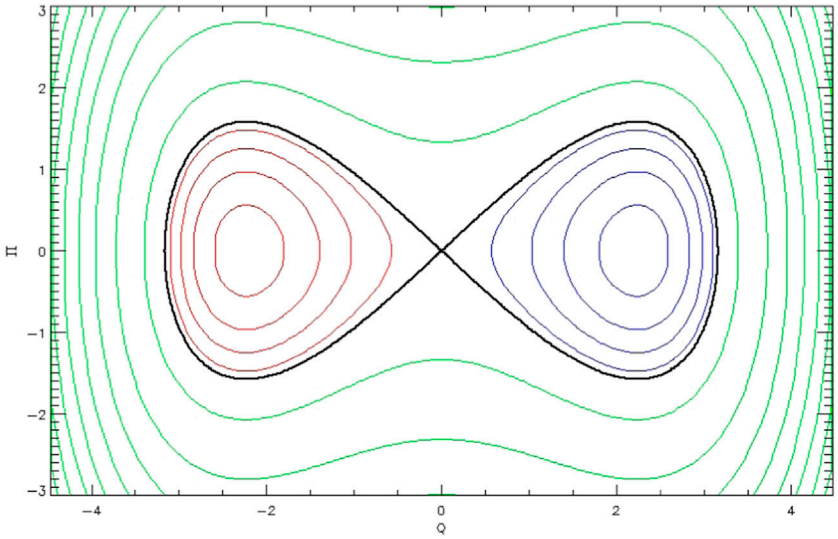

FIGURE 5
Contours of a two-lobe Hamiltonian of the form of Eq. 19. The contour colors correspond to those of Figure 3.

4.1 Average value of ΔP

The integral for ΔP cannot be carried out in closed form, but it can be averaged with respect to q_* analytically. Averaging with respect to q_* is equivalent to averaging with respect to h (Cary et al., 1986; Itin et al., 2000), with the range q_{turn} to $q_x + 2\pi$ corresponding to the range h_x to $h_x + 2\pi$ (since $h_{turn} = h_x$). Following Neishtadt (1999) and Artemyev et al. (2018), the curves are integrated separately over the ranges $q < q_x$ (region 1) and $q > q_x$ (region 2), with the latter combined with the (p, q) island (region 3). For region 1,

$$\begin{aligned} I_1 &= \int_{h_x}^{h_x+2\pi} dh \int_{-\infty}^{q_x} \frac{\sin q\, dq}{\sqrt{h - a\cos q - q}} \\ &= \int_{-\infty}^{q_x} 2dq \sin q \left[\sqrt{h_x + 2\pi - a\cos q - q} - \sqrt{h_x - a\cos q - q} \right] \\ &= -\int_{q_x-2\pi}^{q_x} 2dq \sin q \sqrt{h_x - a\cos q - q}. \end{aligned} \tag{14}$$

Next, noting that along the q axis $h \equiv h_0 = a\cos q + q$,

$$\begin{aligned} I_2 + I_3 &= \int_{q_x}^{q_x+2\pi} dq \int_{h_0}^{h_x+2\pi} dh \frac{\sin q}{\sqrt{h - a\cos q - q}} \\ &= \int_{q_x}^{q_x+2\pi} 2dq \sin q \sqrt{h_x + 2\pi - a\cos q - q}. \end{aligned} \tag{15}$$

Thus $I_1 + I_2 + I_3 = 0$. Finally, I_3 can be expressed as

$$\begin{aligned} I_3 &= \int_{q_x}^{q_{turn}} dq \int_{h_0}^{h_x} dh \frac{\sin q}{\sqrt{h - a\cos q - q}} \\ &= \int_{q_x}^{q_{turn}} 2dq \sin q \sqrt{h_x - a\cos q - q}. \end{aligned} \tag{16}$$

Writing $\sin q = (a \sin q - 1)/a + 1/a$ leads to $I_3 = S/a$, with

$$S = \int_{q_x}^{q_{turn}} 2dq \sqrt{h_x - a\cos q - q}, \tag{17}$$

which is the area of the (p, q) island. The average of ΔP over regions 1 and 2 is then

$$\langle \Delta P \rangle = -\frac{\sqrt{2AR}}{2\pi} S, \tag{18}$$

which becomes $-(8/\pi)\sqrt{A}$ as $R \to 0$, in agreement with the estimate obtained by Albert (1993).

5 Two-lobe hamiltonian

Cary et al. (1986) (hereafter CET) gives a comprehensive treatment of adiabatic invariant breaking due to crossing the separatrix of a Hamiltonian $\mathcal{H}(\Pi, Q)$ with the form

$$\mathcal{H}(\Pi, Q, t) = \omega \frac{\Pi^2 - Q^2}{2} + \delta H(\Pi, Q, \epsilon t), \tag{19}$$

where Π and Q are a pair of action-angle variables and the small quantity ϵ indicates that the crossing is slow. This form is chosen to facilitate analysis of motion near the X-point, but Appendix A of CET shows how an arbitrary Hamiltonian may be put into this form to arbitrary order in ϵ (the several typesetting errors in Eq. 10 notwithstanding). The phase portrait of this Hamiltonian has two lobes; typical contours of Eq. 19 are shown in Figure 5.

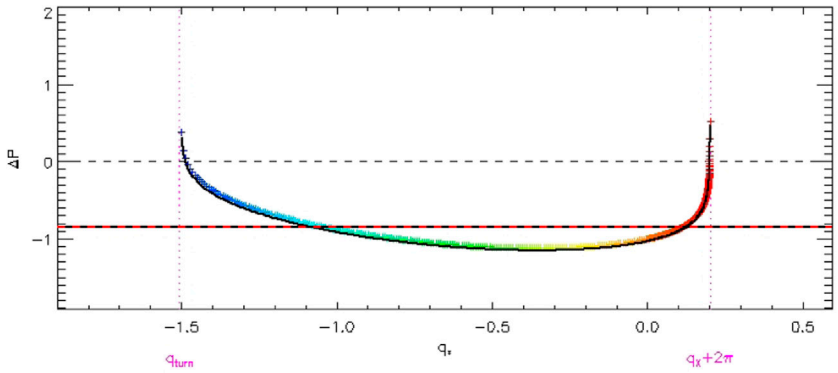

FIGURE 6
The colored symbols show ΔP vs. q_* from Eq. 20, which is negative for most but not all values of q_*. The solid horizontal line shows the averaged value, and the red dashed horizontal line shows the value from Eq. 18. The black symbols show the values from Figure 2. The dotted and dashed vertical lines show the calculated values q_{turn} and $q_x + 2\pi$, respectively, as discussed in the text.

Following a very complex sequence of calculations based on Eq. 19, two special cases are considered, described as symmetric and antisymmetric (which refer to the growth rates of the two lobes shown in 5, not their shapes). The symmetric case was applied to drift orbit bifurcation by Öztürk and Wolf (2007). The antisymmetric case applies to the pendulum Hamiltonian of Eq. 7 and its transformed version Eq. 11, which are of the same form as, respectively, Equation 72 and the subsequent one of CET. With a minor typesetting correction, Equation 84 of CET gives

$$\Delta P = -\frac{8}{\pi}A^{1/2} - \frac{h_0}{\pi A^{1/2}}\log\left|\frac{32A}{h_0}\right| - 2RA^{1/2}\left\{\left(\frac{1}{2}+\mu\right)\log|\mu| - \log\left|\frac{\Gamma(1+\mu)}{\sqrt{2\pi}}\right|\right\}, \tag{20}$$

where Equation 75 of CET has been used, and the notation

$$\mu = \frac{h_0}{2\pi RA} \tag{21}$$

has been introduced. Related expressions were presented by Neishtadt (1987). The leading term of Eq. 20 is the same as the estimate of Albert (1993).

To evaluate h_0 and μ in terms of $K(p, q, \tau)$ of Eq. 11, it is necessary to shift K by a constant:

$$h_0(q_*) = K(p=0, q_*, \tau) - K(p=0, q_x + 2\pi, \tau), \tag{22}$$

so that $h_0(q_x + 2\pi) = 0$ for consistency with the derivation. It can be shown that $K(q_*)$ is an increasing function of q_* between q_{turn} and $q_x + 2\pi$, so $h_0 \le 0$, and that μ correspondingly increases from -1 to 0. Eq. 9 of Tennyson et al. (1986), which was written in terms of $m_d = |\mu|$, is equivalent if $A = \omega = 1$.

Evaluation of Eq. 20 is shown in color in Figure 6. Also shown, as a black curve, are the values from Eq. 13. These two formulations are not exactly equivalent, but are in excellent agreement.

Equation 20 can be approximated near $\mu = 0$ as

$$\Delta P \approx -\frac{8}{\pi}A^{1/2} + RA^{1/2}\log\left|\frac{1}{2\pi\mu}\right|, \tag{23}$$

and near $\mu = -1$ as

$$\Delta P \approx -\frac{8}{\pi}A^{1/2} + 2RA^{1/2}\log\left|\frac{16}{R\sqrt{2\pi^3}}\left(\frac{1}{1+\mu} - \gamma_0\right)\right|, \tag{24}$$

where $\gamma_0 \approx 0.5772$ is the Euler constant. For small values of R, these estimates are positive only for very narrow ranges of μ, approximately

$$|\mu| < \frac{1}{2\pi}e^{-8/\pi R} \tag{25}$$

or

$$1 + \mu < \frac{2}{R}e^{-4\pi/R}, \tag{26}$$

respectively. For $R = 0.5$, these values are approximately 10^{-3} and 0.3, while for $R = 0.2$ they are 5×10^{-7} and 0.02, respectively. Thus $\Delta P > 0$ only for particles with μ near -1 or extremely near $\mu = 0$.

Equation 20 can be averaged over μ, giving

$$\langle \Delta P \rangle = -\frac{8}{\pi}A^{1/2}\left[1 - \frac{\pi R}{8}\left(1 + \log\frac{16}{\pi R}\right)\right]. \tag{27}$$

This value is shown as the thick black line in Figure 6, and agrees very well with Eq. (18), shown as the dashed red line.

Finally, comparing Eqs. 27, 18 gives the estimate

$$S = \frac{16}{\sqrt{2R}}\left[1 - \frac{\pi R}{8}\left(1 + \log\frac{16}{\pi R}\right)\right], \tag{28}$$

which should be useful in situations where R is slowly changing, and the probability of phase trapping is proportional to the rate of change of S (Artemyev et al., 2018).

6 Summary

Wave-particle interactions are frequently treated with a pendulum Hamiltonian equivalent to Eq. 11. With the wave amplitude parameter A and the inhomogeneity parameter R held constant, phase trapping does not occur, and changes in adiabatic invariant P due to phase bunching are formally expressible by the integral in Eq. 13. This result depends on the wave-particle phase q at resonance; positive values can occur but are uncommon. Averaging over that phase gives the more tractable expression 18, which is always negative.

Equation 20, which is a special case of a detailed analysis of the two-lobe Hamiltonian of Eq. 19, gives the change in P as an explicit function of q at resonance. Its average value, Eq. 27, agrees very well with Eq. 18, and it also accurately reproduces the numerically observed dependence on q, including positive values of ΔP (see Figure 6). Analytical estimates of the fraction of particles with these positive values were obtained, which are exponentially small for small values of R. Finally, combining the two treatments gives a good analytical approximation to the area bounded by the pendulum separatrix, whose rate of increase determines the probability of phase trapping.

Data availability statement

The original contributions presented in the study are included in the article/supplementary material, further inquiries can be directed to the corresponding author.

Author contributions

JMA conceived this work, and wrote and ran the simulations. AA helped analyze approaches to reducing the dimensionality of the system of equations. WL, QM, and LG consulted on the work and made several useful suggestions on the simulations and presentation.

Funding

JMA was supported by NASA grant 80NSSC19K0845 and the Space Vehicles Directorate of the Air Force Research Laboratory. WL, LG, and QM also acknowledge the NASA grants 80NSSC20K1506 and 80NSSC20K0698, NSF grant AGS-1847818, and the Alfred P. Sloan Research Fellowship FG-2018-10936.

Acknowledgments

The views expressed are those of the author and do not reflect the official guidance or position of the United States Government, the Department of Defense or of the United States Air Force. The appearance of external hyperlinks does not constitute endorsement by the United States Department of Defense (DoD) of the linked websites, or the information, products, or services contained therein. The DoD does not exercise any editorial, security, or other control over the information you may find at these locations.

Conflict of interest

The authors declare that the research was conducted in the absence of any commercial or financial relationships that could be construed as a potential conflict of interest.

The handling editor XJZ declared a shared affiliation with the authors AA, QM at the time of review.

Publisher's note

References

Albert, J. M., Artemyev, A. V., Li, W., Gan, L., and Ma, Q. (2021). Models of resonant wave-particle interactions. *JGR. Space Phys.* 126, e2021JA029216. doi:10.1029/2021JA029216

Albert, J. M., Artemyev, A., Li, W., Gan, L., and Ma, Q. (2022). Equations of motion near cyclotron resonance. *Front. Astron. Space Sci.* 9, 910224. doi:10.3389/fspas.2022.910224

Albert, J. M. (1993). Cyclotron resonance in an inhomogeneous magnetic field. *Phys. Fluids B Plasma Phys.* 5, 2744–2750. doi:10.1063/1.860715

Albert, J. M. (2000). Gyroresonant interactions of radiation belt particles with a monochromatic electromagnetic wave. *J. Geophys. Res.* 105, 21191–21209. doi:10.1029/2000JA000008

Albert, J. M. (2002). Nonlinear interaction of outer zone electrons with VLF waves. *Geophys. Res. Lett.* 29, 116-1–116-3. doi:10.1029/2001GL013941

Albert, J. M. (2010). Diffusion by one wave and by many waves. *J. Geophys. Res.* 115, A00F05. doi:10.1029/2009JA014732

Artemyev, A. V., Neishtadt, A. I., Vainchtein, D. L., Vasiliev, A. A., Vasko, I., and Zelenyi, L. (2018). Trapping (capture) into resonance and scattering on resonance: Summary of results for space plasma systems. *Commun. Nonlinear Sci. Numer. Simul.* 65, 111–160. doi:10.1016/j.cnsns.2018.05.004

Artemyev, A. V., Neishtadt, A. I., Albert, J. M., Gan, L., Li, W., and Ma, Q. (2021). Theoretical model of the nonlinear resonant interaction of whistler-mode waves and field-aligned electrons. *Phys. Plasmas* 28, 052902. doi:10.1063/5.0046635

Bortnik, J., and Thorne, R. M. (2007). The dual role of elf/vlf chorus waves in the acceleration and precipitation of radiation belt electrons. *J. Atmos. Sol. Terr. Phys.* 69, 378–386. doi:10.1016/j.jastp.2006.05.030

Bortnik, J., Thorne, R. M., and Inan, U. S. (2008). Nonlinear interaction of energetic electrons with large amplitude chorus. *Geophys. Res. Lett.* 35, L21102. doi:10.1029/2008GL035500

Cary, J. R., Escande, D. F., and Tennyson, J. L. (1986). Adiabatic-invariant change due to separatrix crossing. *Phys. Rev. A . Coll. Park.* 34, 4256–4275. doi:10.1103/PhysRevA.34.4256

Chang, H. C., and Inan, U. S. (1983). Quasi-relativistic electron precipitation due to interactions with coherent VLF waves in the magnetosphere. *J. Geophys. Res.* 88, 318. doi:10.1029/ja088ia01p00318

Gan, L., Li, W., Ma, Q., Albert, J. M., Artemyev, A. V., Bortnik, J., et al. (2020). Nonlinear interactions between radiation belt electrons and chorus waves: Dependence on wave amplitude modulation. *Geophys. Res. Lett.* 47, e2019GL085987. doi:10.1029/2019GL085987

Itin, A. P., Neishtadt, A. I., and Vasiliev, A. A. (2000). Captures into resonance and scattering on resonance in dynamics of a charged relativistic particle in magnetic field and electrostatic wave. *Phys. D. Nonlinear Phenom.* 141, 281–296. doi:10.1016/S0167-2789(00)00039-7

Kitahara, M., and Katoh, Y. (2019). Anomalous trapping of low pitch angle electrons by coherent whistler mode waves. *JGR. Space Phys.* 124, 5568–5583. doi:10.1029/2019JA026493

Neishtadt, A. I. (1987). On the change in the adiabatic invariant on crossing a separatrix in systems with two degrees of freedom. *J. Appl. Math. Mech.* 51, 586–592. doi:10.1016/0021-8928(87)90006-2

Neishtadt, A. (1999). "On adiabatic invariance in two-frequency systems," in *Hamiltonian systems with three or more degrees of freedom. NATO ASI series (series C: Mathematical and physical Sciences)*. Editor C. Simó (Dordrecht: Springer), 533, 193–213. doi:10.1007/978-94-011-4673-9_17

Omura, Y., Katoh, Y., and Summers, D. (2008). Theory and simulation of the generation of whistler-mode chorus. *J. Geophys. Res.* 113, A04223. doi:10.1029/2007JA012622

Öztürk, M. K., and Wolf, R. A. (2007). Bifurcation of drift shells near the dayside magnetopause. *J. Geophys. Res.* 112, A07207. doi:10.1029/2006ja012102

Tennyson, J. L., Cary, J. R., and Escande, D. F. (1986). Change of the adiabatic invariant due to separatrix crossing. *Phys. Rev. Lett.* 56, 2117–2120. doi:10.1103/PhysRevLett.56.2117

frontiers | Frontiers in Astronomy and Space Sciences

TYPE Original Research
PUBLISHED 15 August 2022
DOI 10.3389/fspas.2022.975123

OPEN ACCESS

EDITED BY
Xiao-Jia Zhang,
University of California, Los Angeles, United States

REVIEWED BY
Anton Artemyev,
Department of Earth, Planetary, and Space Sciences, College of Physical Sciences, University of California, Los Angeles, United States
Toshi Nishimura,
Boston University, United States

*CORRESPONDENCE
Mykhaylo Shumko,
msshumko@gmail.com

SPECIALTY SECTION
This article was submitted to Space Physics, a section of the journal Frontiers in Astronomy and Space Sciences

RECEIVED 21 June 2022
ACCEPTED 18 July 2022
PUBLISHED 15 August 2022

CITATION
Shumko M, Gallardo-Lacourt B, Halford AJ, Blum LW, Liang J, Miyoshi Y, Hosokawa K, Donovan E, Mann IR, Murphy K, Spanswick EL, Blake JB, Looper MD and Gillies DM (2022), Proton aurora and relativistic electron microbursts scattered by electromagnetic ion cyclotron waves. *Front. Astron. Space Sci.* 9:975123. doi: 10.3389/fspas.2022.975123

Proton aurora and relativistic electron microbursts scattered by electromagnetic ion cyclotron waves

Mykhaylo Shumko[1,2]*, Bea Gallardo-Lacourt[1,3], Alexa Jean Halford[1], Lauren W. Blum[4], Jun Liang[5], Yoshizumi Miyoshi[6], Keisuke Hosokawa[7], Eric Donovan[5], Ian R. Mann[8], Kyle Murphy, Emma L. Spanswick[5], J. Bernard Blake[9], Mark D. Looper[9] and D. Megan Gillies[5]

[1]NASA's Goddard Space Flight Center, Greenbelt, MD, United States, [2]Department of Astronomy, University of Maryland, College Park, MD, United States, [3]Department of Physics, The Catholic University of America, Washington, DC, United States, [4]University of Colorado in Boulder, Boulder, Colorado, United States, [5]University of Calgary in Calgary, Calgary, AB, Canada, [6]Institute for Space-Earth Environmental Research, Nagoya University, Nagoya, Japan, [7]University of Electro-Communications, Tokyo, Japan, [8]University of Alberta in Edmonton, Edmonton, AB, Canada, [9]The Aerospace Corporation, Los Angeles, CA, United States

Charged particle precipitation from Earth's magnetosphere results in stunning displays of the aurora and energy transfer into the atmosphere. Some of this precipitation is caused by wave-particle interactions. In this study, we present an example of a wave-particle interaction between Electromagnetic Ion Cyclotron waves, and magnetospheric protons and electrons. This interaction resulted in a co-located isolated proton aurora and relativistic electron microbursts. While isolated proton aurora is widely believed to be caused by Electromagnetic Ion Cyclotron waves, this unique observation suggests that these waves can also scatter relativistic electron microbursts. Theoretically, nonlinear interactions between Electromagnetic Ion Cyclotron waves and electrons are necessary to produce the intense sub-second microburst precipitation. Lastly, detailed analysis of the auroral emissions suggests that no chorus waves were present during the event. This is in contrast to the most commonly associated driver of microbursts, whistler mode chorus waves, and supports other less commonly considered driving mechanisms.

KEYWORDS

EMIC, SAMPEX, THEMIS, microburst, proton aurora, all-sky-imager

1 Introduction

Since the Van Allen radiation belts were discovered by Van Allen (1959) and Vernov and Chudakov (1960), the loss of radiation belt electrons due to wave-particle interactions has been modeled with quasilinear diffusion theory (e.g., Kennel and Petschek, 1966; Summers et al., 1998; Summers, 2005; Thorne et al., 2005). On long time scales, this model leads to accurate quantification of particle energization and loss (e.g., Lyons and Thorne, 1973; Claudepierre et al., 2020). On shorter time scales, however, quasilinear diffusion does not accurately predict precipitating fluxes on second or sub-second timescales (e.g., Bortnik et al., 2008; Albert and Bortnik, 2009; Saito et al., 2012; Miyoshi et al., 2015; Mozer et al., 2018; Shumko et al., 2018). The importance of nonlinear scattering in regard to particle loss is still unknown. Indeed, even the variety of mechanisms that nonlinearly scatter radiation belt electrons is still unknown (e.g. Grach and Demekhov, 2020; Bortnik et al., 2022). Scattering mechanisms that lead to electron microburst precipitation are of particular interest here; while there is a plethora of observational evidence linking whistler mode chorus waves to electron microbursts, only Douma et al. (2018) shows observational evidence of microbursts scattered by Electromagnetic Ion Cyclotron (EMIC) waves.

Microbursts are intense bursts of electron precipitation that typically last ≈ 100 ms (Shumko et al., 2021). Microburst energies span from tens of keV all the way up to > 1 MeV (Anderson and Milton, 1964; Parks, 1967; O'Brien et al., 2003; Blum et al., 2015; Douma et al., 2017; Shumko et al., 2020b; Kawamura et al., 2021; Shumko et al., 2021; Zhang et al., 2022). The microburst L-MLT distribution peaks in the outer radiation belt L-shells and in the 0–12 MLT region (Lorentzen et al., 2001; O'Brien et al., 2003).

Whistler mode chorus waves share many similarities with microbursts, including similar distribution in MLT and duration (of chorus rising tone elements) (Teng et al., 2017; Meredith et al., 2020; Shumko et al., 2021). These similarities led to a widely-accepted conclusion that microbursts are most often scattered by whistler mode chorus waves (e.g., Lorentzen et al., 2001). This is further supported by theory. Both Miyoshi et al. (2020) and Chen et al. (2020) show that rising tone whistler mode chorus waves can rapidly—and nonlinearly—scatter microburst electrons over the wide range of energies.

EMIC waves are an another type of plasma wave that can pitch angle scatter energetic protons and electrons into Earth's atmosphere (e.g., Cornwall, 1965; Summers et al., 1998; Spasojević et al., 2004; Jordanova, 2007; Halford et al., 2016; Yahnin et al., 2021). EMIC waves are typically generated near the magnetic equator by anisotropic ions and are often bounded in frequency by the ion gyrofrequencies into three primary bands: hydrogen, helium, and oxygen (e.g., Gary et al., 1995; Blum et al., 2012; Saikin et al., 2015). In the magnetosphere, EMIC waves are spatially confined in L-Shell and extended in MLT (Mann et al., 2014; Blum et al., 2017). When some of the EMIC wave power enters the ionosphere, it can duct and be observed over a large geographical area (Woodroffe and Lysak, 2012; Mann et al., 2014; Kim et al., 2018).

During their generation and subsequent propagation away from the magnetic equator, EMIC waves can precipitate 10 s keV protons (e.g., Miyoshi et al., 2008; Shoji and Omura, 2011). When the protons impact the atmosphere, they decelerate via charge-exchange: the bare proton strips an electron from an atmospheric molecule and becomes a neutral hydrogen atom in an excited state (Kivelson et al., 1995). This hydrogen atom, newly decoupled from the magnetic field, then emits hydrogen-specific auroral light, primarily in the Lyman-α (121.57 nm), Balmer-α (653.3 nm), and Balmer-β (486.1 nm) lines (e.g., Gallardo-Lacourt et al., 2021). Davidson (1965) and Fang et al. (2004) show that this charge exchange process will spatially smear a fine beam of precipitating protons into a ≈ 100 km radius proton aurora patch.

Similarly, EMIC waves can also scatter relativistic electrons (e.g., Summers et al., 1998; Khazanov et al., 2014; Kubota et al., 2015; Remya et al., 2015; Zhang X.-J. et al., 2016; Kubota and Omura, 2017; Zhu et al., 2020; Grach et al., 2021). The theoretical work by Omura and Zhao (2013) is most relevant here: they demonstrated that EMIC waves can scatter relativistic microbursts into the atmosphere. There, these precipitating electrons experience bremsstrahlung deceleration and emit X-ray photons which are absorbed before they reach the ground (Winckler et al., 1958; Woodger et al., 2015). Therefore, relativistic electron precipitation can only be observed directly in space and indirectly via the secondary X-rays in the upper atmosphere.

Some satellites in low Earth orbit (LEO) are well-equipped to observe this dual electron-proton precipitation that is often attributed to EMIC wave scattering (e.g., Miyoshi et al., 2008; Nishimura et al., 2014; Zhang J. et al., 2016; Qin et al., 2018; Capannolo et al., 2021). These studies often show EMIC precipitation structure that lasts a few to 10s of seconds. From the vantage point of a high-inclination satellite in LEO, these durations can correspond to either the spatial size or temporal duration (Shumko et al., 2020a,b). Nevertheless, EMIC-driven electron precipitation on faster time scales is seldom observed. In fact, Douma et al. (2018) is the only study to our knowledge which shows sub-second electron precipitation associated with an EMIC wave. These authors presented the results of a magnetic conjunction between the Solar Anomalous and Magnetospheric Particle Explorer (SAMPEX) satellite in the northern hemisphere and a ground-based magnetometer in Halley, Antarctica. During the conjunction, SAMPEX observed three > 1 MeV electron microbursts.

Due to the aforementioned EMIC wave ducting and a lack of auroral observations, it is difficult to co-locate the EMIC wave and microbursts in the Douma et al. (2018) conjunction. However, observing an EMIC wave on the ground, together

with co-located proton and electron precipitation, will provide more convincing evidence of EMIC-driven electron microbursts. We present such a study here.

Early on 20 January 2007, the Canadian Array for Real-time Investigations of Magnetic Activity (CARISMA) magnetometers spread throughout Canada observed an EMIC wave lasting almost 2 hours. This wave generated an isolated proton aurora (IPA) patch that was observed by a Time History of Events and Macroscale Interactions during Substorms (THEMIS) all-sky imager (ASI) and a meridional scanning photometer. Meanwhile, the SAMPEX satellite passed directly through the proton aurora and observed very rapid and intense >1 MeV electron microbursts.

2 Materials and methods

2.1 Instruments

2.1.1 Canadian array for real-time investigations of magnetic activity

We used the CARISMA (Mann et al., 2008) magnetometers to identify EMIC waves. The instruments consist of fluxgate and induction coil magnetometers deployed throughout Canada. Here we use the fluxgate magnetometer from Gillam (CARISMA-GILL) that is close to the ASI that observed the proton aurora. The magnetometer data is collected in two modes: 1- and 8-Hz sample rates. We use the 1-Hz data here.

2.1.2 Solar anomalous and magnetospheric particle explorer

We used the SAMPEX satellite to identify relativistic microbursts. It was launched in July 1992 into a 520, −, 760 km altitude, 82° inclination low Earth orbit (Baker et al., 1993; 2012). The Heavy Ion Large Telescope (HILT; Klecker et al., 1993) observed >1 MeV electrons. HILT was a large rectangular chamber with the aperture on one end, and 16 solid state detectors on the other. During this event HILT pointed to zenith and the electron counts were accumulated from all of the solid state detectors at a 20 ms cadence.

2.1.3 Time history of events and macroscale interactions during substorms all-sky imager

We use the THEMIS ASIs to study the auroral light. The THEMIS ASIs are an array of charged-coupled device (CCD) auroral cameras spread across Canada and Alaska (Harris et al., 2009; Mende et al., 2009). Each white light imager uses a fisheye lens to expand its field of view to 170°, corresponding to 9° latitudinal and 1 h magnetic local time (MLT) coverage (Donovan et al., 2006; Mende et al., 2009).

The 256 × 256 pixel images are taken at a 3-s cadence: a 1-s exposure is followed by 2-s processing. To analyze the white light images, we used the THEMIS ASI skymap calibration files that are provided by the University of Calgary. The calibration data contain, among other things, arrays that map each pixel to (latitude, longitude) coordinates at an assumed auroral emission altitude.

In this study, we use the THEMIS ASI camera stationed in The Pas (THEMIS-TPAS) to study the proton aurora. Furthermore, we briefly use the THEMIS ASI at Gillam (THEMIS-GILL) to identify the proton aurora, but the aurora was overwhelmed by light pollution in that part of THEMIS-GILL's sky.

2.1.4 Meridian scanning photometer

And lastly, we used the Northern Solar Terrestrial Array (NORSTAR) meridian scanning photometers (MSPs) to understand the multispectral properties of the aurora. MSPs are designed to measure the latitudinal location and brightness of aurora at the meridian. We use four channels from the MSP at Gillam (MSP-GILL): 470.9 nm blue-line, 486.0 nm H_β (i.e.. the Balmer-β emission line), 557.7 nm green-line, and 630 nm red-line (Jackel, 2005). See Unick et al. (2017) for a comprehensive description of the operation and calibration of MSPs.

2.2 Methods

Our analysis consists of two main steps: calculate the CARISMA wave spectrum, and map the THEMIS-TPAS images and SAMPEX footprints to 110 km altitude.

To calculate the CARISMA frequency-time spectrum, we used the Windowed Fast Fourier Transform algorithm implemented by Scipy's spectrogram ()function (Virtanen et al., 2020). We used the Tukey window (also known as the tapered cosine) that had a 256-s length. The windows overlapped by 128 s (50% of the window length).

Then, to accurately compare the two datasets, we mapped the THEMIS-TPAS ASI images and the SAMPEX location to the same altitude. For the images, we mapped the THEMIS-TPAS pixels along their line of sight to their (latitude, longitude) at a 110 km altitude. We used the aforementioned skymap files, together with Python's pymap3d (Hirsch, 2016), and aurora-asi-lib (Shumko, 2022) libraries to do this. For SAMPEX, we mapped its location to its magnetic field footprint at 110 km altitude. For this we used the IRBEM-Lib magnetic field library (Boscher et al., 2012) with the IGRF magnetic field model (Thébault et al., 2015).

3 Results

From approximately 00:00–01:40 UT on 20 January 2007, nine CARISMA magnetometers deployed around central Canada observed EMIC wave power between 0.25–0.4 Hz, classified as Pc

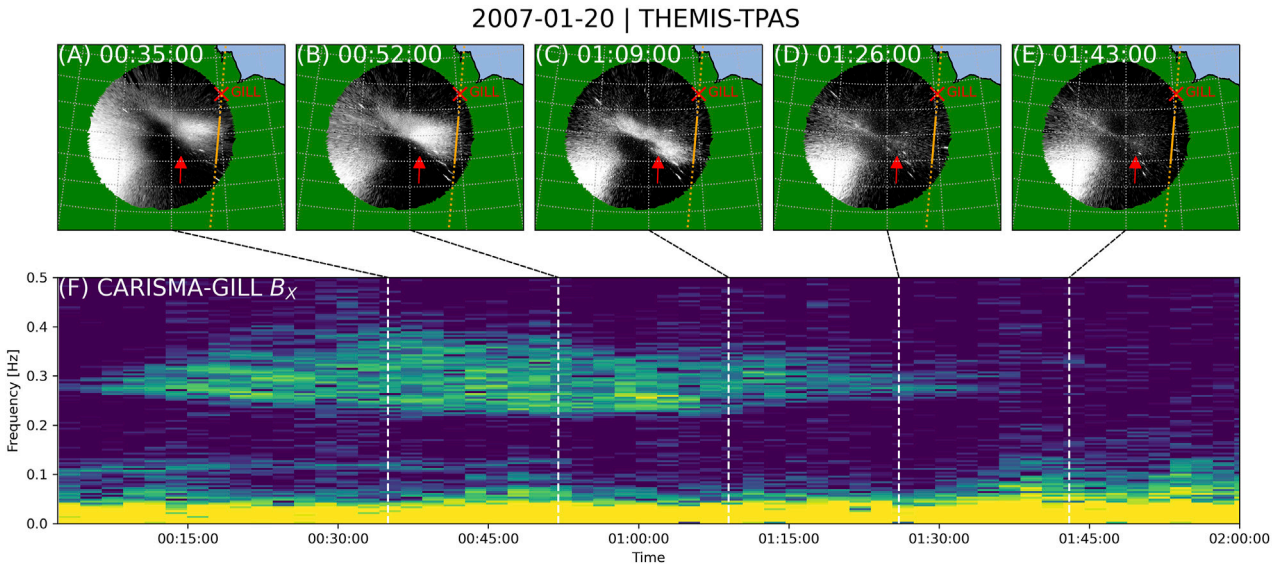

FIGURE 1
Select ASI images and magnetic field spectrum from the first 2 hours on 2007–01-20. **(A–E)** show select THEMIS ASI images from The Pas (TPAS). The intensity bounds are identical between the panels. Light pollution from twilight and other terrestrial sources is in the lower-left corner (south-west). The red arrows point to the proton aurora that the imager observed in **(A–C)**. The red X shows the location of the ASI and MSP at Gillam. The dotted orange line shows the GILL-MSP field of view, with the solid orange highlighting the 62° – 65° magnetic latitudes. **(F)** shows the B_X component of the magnetic field variations observed by a CARISMA magnetometer in Gillam. The proton aurora coincided with the EMIC wave in **(A–C)**, after which the magnetic wave power and proton aurora simultaneously faded in **(D,E)**.

1 (Jacobs et al., 1964). Figure 1F and Supplementary Video S1 show the EMIC wave observed at CARISMA-GILL. The primary band of the EMIC wave spanned 0.25–0.4 Hz. A second weaker band, centered around 0.1 Hz, ended earlier around 01:00 UT. Supplementary Figure S1 shows the spatial extent of the EMIC wave as observed on the ground: it shows a map of Canada with the CARISMA magnetometer locations that observed EMIC waves highlighted. The EMIC wave amplitude was largest at the Island Lake magnetometer (CARSIMA-ISLL), 275 km south of CARISMA-GILL. The wave appeared to be almost linearly polarized with the semi-major axis pointing north, suggesting that the EMIC wave entered the ionosphere near ISLL (Woodroffe and Lysak, 2012).

The 0.25–0.4 Hz EMIC wave band coincided with an auroral patch that was observed concurrently by two THEMIS ASIs located at Gillam (GILL) and The Pas (TPAS). The ASIs observed the aurora from just after the cameras turned on at sunset until 01:40 UT. THEMIS-TPAS is 500 km south-west of THEMIS-GILL and the auroral patch was observed in between the two imagers. While THEMIS-TPAS observed the patch in the region of the sky away from sunset, THEMIS-GILL observed the aurora light superposed with a strong background light consisting of twilight and terrestrial light. Thus, our analysis focused on THEMIS-TPAS. At TPAS the sunset was at 23:03 UT the previous day and twilight lasted until 01:09 UT on January 20th. The TPAS imager turned on at 00:22:06 UT and was initially saturated by twilight. The image in Figure 1A, taken at 00:35 UT, was the earliest time when the auroral patch was clearly visible. Panels (E) and (F) in Figure 1 show that both the auroral patch and EMIC waves vanished simultaneously around 01:45 UT, indicating that the auroral patch was driven by the EMIC wave.

Next, we investigate what particles created the auroral patch light. Figure 2 shows a multi-spectral keogram from MSP-GILL in panels (A)-(D) and a THEMIS-TPAS keogram along MSP-GILL's field of view in panel (E). We show MSP-GILL's field of view at 110 km altitude in Figures 1A–E with the dotted orange line. Figures 2A–D shows that the green and H_β MSP channels observed an intensity enhancement corresponding to magnetic latitudes $\lambda = 62°–65°$ that we highlighted in Figures 1A–E with the solid orange line. The H_β MSP channel is sensitive to precipitating 10 s keV protons, while the green MSP channel is sensitive to secondary electrons that were generated by the protons (Sakaguchi et al., 2008). While the aurora intensity was dim in the H_β channel, we confirmed that it was not observed in the MSP's 480 and 495 nm background channels.

Since we're using THEMIS-TPAS images, we need to compare its light to MSP-GILL to identify the proton emission. Figure 2E shows a keogram constructed along the MSP-GILL field of view using data extracted from the THEMIS-TPAS ASI images. The field of view grazed the auroral patch that THEMIS-TPAS observed—enough that the two can be

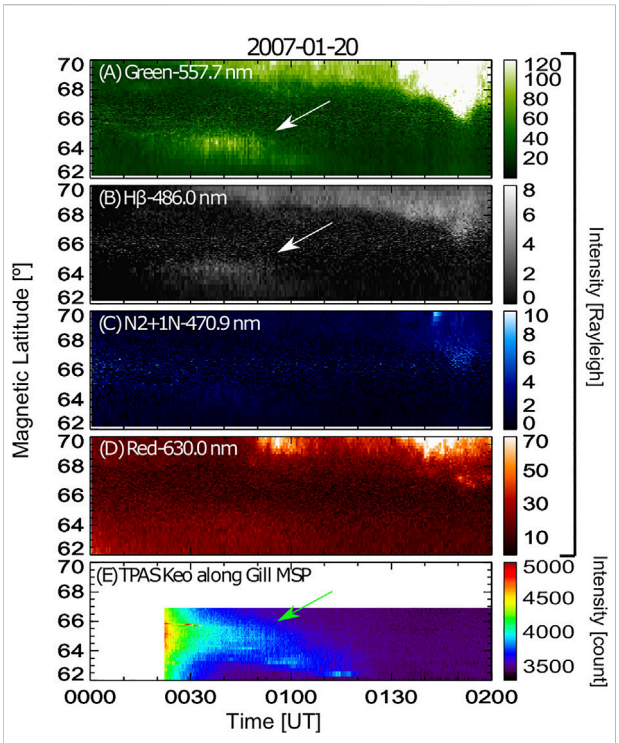

FIGURE 2
Keograms from Gillam and The Pas. **(A–D)** show the MSP intensity in the H_β, blue, and red channels. **(E)** shows a keogram constructed along the MSP-GILL field of view using data extracted from the THEMIS-TPAS ASI images. The matching aurora intensity in **(A,B,E)** confirm that the aurora observed by THEMIS-TPAS right after sunset was generated by protons.

compared. The auroral patch observed by THEMIS-TPAS was constrained to $\lambda = 62^\circ$–65° along the MSP's field of view. Thus, the auroral patch seen in the ASI images was caused by the precipitating 10 s keV protons, confirmed with the MSP-GILL, and is an IPA.

At 00:40 UT SAMPEX orbited above the IPA and directly observed precipitating relativistic electrons. Supplementary Video S1 and Figure 3 show the conjunction that was at approximately L = 5 and MLT = 17 h. Figures 3A–D shows the mapped THEMIS-TPAS image with the SAMPEX orbit footprint superposed as a dotted red line and the instantaneous footprint as a red circle. Figure 3E shows that HILT observed a handful of >1 MeV electron microbursts. We used the fitting method described in Shumko et al. (2021) to estimate microburst durations. Some of the microbursts lasted ≈ 100 ms, while three had a ≈ 300 ms duration.

Two more instruments onboard SAMPEX, the Proton/Electron Telescope (PET; Cook et al., 1993) and the Low-Energy Ion Composition Analyzer (LICA; Mason et al., 1993), observed precipitation at this time that we show in Supplementary Figure S2. PET is sensitive to >400 keV electrons and clearly observed many microbursts at a 100 ms cadence. Electron precipitation was also observed by LICA's stop microchannel plate that was sensitive to >25 keV electrons. However, LICA's time resolution was 1 s, so microbursts are difficult to identify. The clearest exception is the microburst observed at 00:40:30 UT shown in Supplementary Figure S2. The three SAMPEX instruments' integral response make it difficult to infer the energy of the precipitating electrons—we can only claim that some of the electrons had a >1 MeV energy. Furthermore, the SAMPEX instruments show signs of time-energy dispersion. However, we are unable to reliably verify dispersion because the time synchronization between instruments was of order 1 second—longer than the theoretical sub-second energy dispersion.

4 Discussion

This event shows strong evidence of EMIC-driven IPA concurrent with >1 MeV electron microbursts. The EMIC wave was observed throughout central Canada for almost 2 hours. The wave precipitated 10 s keV protons in a localized patch which then generated the IPA light—confirmed by the white-light observed by THEMIS-TPAS and the H_β light observed by MSP-GILL. The wave also precipitated intense and rapid >1 MeV electron microbursts that SAMPEX observed directly above the IPA.

While Miyoshi et al. (2008) and Jordanova et al. (2008), and others show that quasilinear diffusion can model the gradual EMIC-driven relativistic electron precipitation, it is unable to model the intense sub-second relativistic microbursts studied here. Nonlinear EMIC-electron scattering models are probably needed. Albert and Bortnik (2009) show that nonlinear interactions between electrons and monochromatic EMIC waves lead to rapid electron transport in pitch angle (and negligible transport in energy). The scattering efficiency of relativistic electrons is strongly dependent on the gyrophase difference between the wave and particle and on the inhomogeneity parameter. Albert and Bortnik (2009) describe the inhomogeneity parameter as quantifying the strength of the EMIC wave relative to the inhomogeneity of the magnetospheric plasma and magnetic field.

Omura and Zhao (2012) extended this work from a monochromatic wave to rising tones, generated by the EMIC triggered emission mechanism (e.g., Grison et al., 2013; Sakaguchi et al., 2013). The authors found that the most effective EMIC-MeV electron scattering occurs with EMIC rising tones and repeated encounters with the wave as the electrons bounce: the EMIC wave is relatively stationary compared to a bouncing MeV electron. Omura and Zhao (2013) applied this theory to model EMIC-driven MeV microbursts. Here, the authors found that EMIC rising tones are very efficient at trapping relativistic electrons and

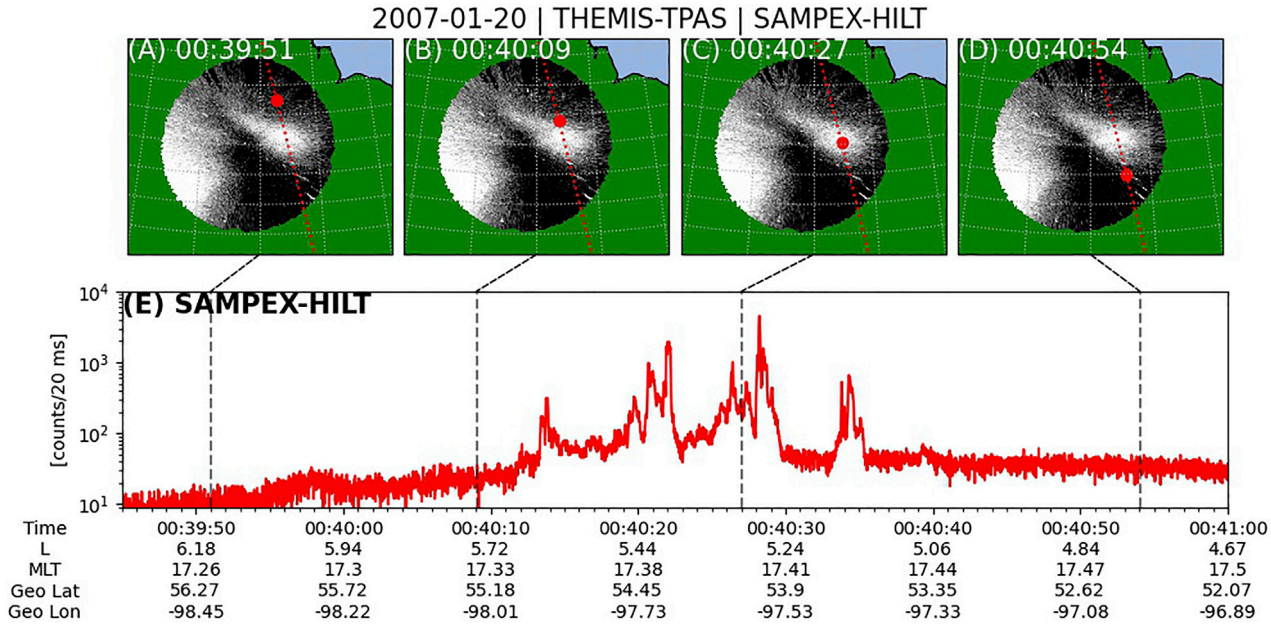

FIGURE 3
Select ASI images, and relativistic electron microbursts observed during the conjunction. **(A–D)** show select THEMIS ASI images from The Pas mapped to 110 km altitude. The SAMPEX footprint and its instantaneous position are shown by the dotted red line and the large red circle. The intensity bounds are identical between the images. **(E)** shows the SAMPEX-HILT time series with vertical guides at times that correspond to the ASI images in **(A–D)**. The minor ticks are at every second. The HILT instrument observed microbursts only when it passed above the proton aurora.

transporting them into the loss cone when the inhomogeneity parameter is less than one. The authors simulated an EMIC wave that propagated away from the magnetic equator to higher magnetic latitudes for 37 s. As the electrons bounced (with a sub-second bounce period), they repeatedly passed through and resonated with the wave for ≈ 20 ms. This led to efficient pitch angle transport of the resonant electrons into the loss cone. Figure 8b in Omura and Zhao (2013) shows an envelope of precipitating electrons with intense subsecond electron enhancements superposed; thus, the authors classified them as microbursts.

Thus, our observations are theoretically supported by Omura and Zhao (2013)'s results. Nonlinear wave-particle interactions between EMIC rising tones and electrons are necessary to generate these microbursts. Other studies including Nakamura et al. (2019), and Zhu et al. (2020) also presented evidence of nonlinear scattering of electron by EMIC rising tones that resulted in sub-minute flux variations observed by the Van Allen Probes (Mauk et al., 2012). That said, given that EMIC rising tones are necessary for nonlinear microburst scattering, our observations do not show clear EMIC rising tones. This is unsurprising, because ground-based observations of EMIC rising tones are rare—likely explained by the smoothing of the frequency dispersion during the propagation to the ground. In fact, Nomura et al. (2016) claims to be the first to have find EMIC rising tones on the ground.

We consider one final scenario: collocated EMIC and chorus waves. In this case, the EMIC waves were responsible for the IPA while the chorus waves were responsible for microbursts. While there were no direct equatorial wave measurements in this L-MLT region at this time, the MSP-GILL can infer the presence of 10 s keV electrons that are associated with lower-band chorus (Thorne et al., 2010). The green-to-blue MSP ratio is a good proxy for the precipitating electron energy spectrum: higher green-to-blue ratios correspond to lower energy electron precipitation (Rees and Luckey, 1974; Shepherd et al., 1996). The keograms in Figure 2 show an emission in the green but not the blue line. The large green-to-blue ratio indicates an absence of 10 s keV electron precipitation and thus suggest an absence of lower-band chorus waves that are capable of scattering MeV electrons.

The chorus-microburst model is admittedly very simple and widely accepted. But, our results suggest that there are multiple ways to scatter microbursts. Perhaps this is unsurprising, given that microbursts are broadly defined by their intensity and sub-second duration—so we would classify any wave-particle interaction capable of producing rapid precipitation as microbursts.

In conclusion, our observations show EMIC-driven precipitation of both 10 s keV protons that resulted in IPA light, and >1 MeV electron microbursts. Since relativistic electrons were not observed above the full extent of the

proton aurora, this means that the relativistic microburst electrons are episodic: a very specific triggering condition must have been met. Douma et al. (2018) showed an example of EMIC-driven microbursts, but the waves and MeV electrons were observed in opposite hemispheres, and no proton aurora was observed to localize the EMIC wave. Thus, our event is arguably the strongest evidence yet of nonlinear interactions between EMIC waves and electrons, leading to microburst precipitation. Our results are theoretically supported, despite the scant observational evidence in the published literature. Further, this study shows the indispensable utility of ground-based observations to gain a more comprehensive understanding of wave-particle interactions.

Data availability statement

Publicly available datasets were analyzed in this study. This data can be found here: CARISMA: https://www.carisma.ca/carisma-data-repository, THEMIS: https://data.phys.ucalgary.ca/sort_by_project/THEMIS/asi/MSP: https://data.phys.ucalgary.ca/sort_by_project/GO-Canada/GO-Storm/msp/IDLsav/SAMPEX: https://izw1.caltech.edu/sampex/DataCenter/.

Author contributions

MS, BG-L, KM, and AH first conceived the idea to look for SAMPEX-THEMIS ASI conjunctions. Both KH and YM first highlighted the uniqueness of this conjunction. AH wrote the draft introduction and MS wrote the rest of the manuscript. BG-L made Figure 2 and MS made the other plots. JL, ED, ES, and DG provided the THEMIS ASI and MSP data and expertise. JB and ML provided the SAMPEX data and analysis support. LB helped analyze the SAMPEX microburst observations. IM provided the CARISMA data. All authors contributed to manuscript revision, read, and approved the submitted version.

Funding

MS and BG-L acknowledge the support provided by the NASA Postdoctoral Program at the NASA's Goddard Space Flight Center, administered by Oak Ridge Associated Universities under contract with NASA. AH was supported in part by the Goddard Internal Funding Model which funds the Space Precipitation Impacts team with grant HISFM21. LB was supported by NASA H-SR award #80NSSC21K1682. YM was supported by JSPS 16H06286, 20H01959, and 21H04526.

Acknowledgments

This work was also in part inspired by preparation work for the LAMP rocket mission (NNH17ZDA001N-HTIDeS), and the ISSI Team "Dynamics of Electromagnetic Ion Cyclotron Wave Activity in the Earth's Magnetosphere". CARISMA is operated by the University of Alberta, funded by the Canadian Space Agency. The auroral data was in part analyzed using the aurora-asi-lib library which can be found at https://aurora-asi-lib.readthedocs.io/ and is archived at https://doi.org/10.5281/zenodo.4746446.

Conflict of interest

The authors declare that the research was conducted in the absence of any commercial or financial relationships that could be construed as a potential conflict of interest.

Publisher's note

Supplementary material

The Supplementary Material for this article can be found online at: https://www.frontiersin.org/articles/10.3389/fspas.2022.975123/full#supplementary-material

References

Albert, J., and Bortnik, J. (2009). Nonlinear interaction of radiation belt electrons with electromagnetic ion cyclotron waves. *Geophys. Res. Lett.* 36, L12110. doi:10.1029/2009gl038904

Anderson, K. A., and Milton, D. W. (1964). Balloon observations of x rays in the auroral zone: 3. High time resolution studies. *J. Geophys. Res. (1896-1977)* 69, 4457–4479. doi:10.1029/JZ069i021p04457

Baker, D., Mazur, J., and Mason, G. (2012). SAMPEX to reenter atmosphere: Twenty-year mission will end. *Space weather.* 10. doi:10.1029/2012sw000804

Baker, D. N., Mason, G. M., Figueroa, O., Colon, G., Watzin, J. G., and Aleman, R. M. (1993). An overview of the solar anomalous, and magnetospheric particle explorer (SAMPEX) mission. *IEEE Trans. Geosci. Remote Sens.* 31, 531–541. doi:10.1109/36.225519

Blum, L., Bonnell, J., Agapitov, O., Paulson, K., and Kletzing, C. (2017). Emic wave scale size in the inner magnetosphere: Observations from the dual van allen probes. *Geophys. Res. Lett.* 44, 1227–1233. doi:10.1002/2016gl072316

Blum, L., Li, X., and Denton, M. (2015). Rapid MeV electron precipitation as observed by SAMPEX/HILT during high-speed stream-driven storms. *J. Geophys. Res. Space Phys.* 120, 3783–3794. doi:10.1002/2014ja020633

Blum, L. W., MacDonald, E. A., Clausen, L. B. N., and Li, X. (2012). A comparison of magnetic field measurements and a plasma-based proxy to infer emic wave distributions at geosynchronous orbit. *J. Geophys. Res.* 117. doi:10.1029/2011JA017474

Bortnik, J., Albert, J. M., Artemyev, A., Li, W., Jun, C.-W., Grach, V. S., et al. (2022). Amplitude dependence of nonlinear precipitation blocking of relativistic electrons by large amplitude emic waves. *Geophys. Res. Lett.* 49, e2022GL098365. doi:10.1029/2022gl098365

Bortnik, J., Thorne, R., and Inan, U. S. (2008). Nonlinear interaction of energetic electrons with large amplitude chorus. *Geophys. Res. Lett.* 35, L21102. doi:10.1029/2008gl035500

[Dataset] Boscher, D., Bourdarie, S., O'Brien, P., Guild, T., and Shumko, M. (2012). *Irbem-lib library*.

Capannolo, L., Li, W., Spence, H., Johnson, A. T., Shumko, M., Sample, J., et al. (2021). Energetic electron precipitation observed by firebird-ii potentially driven by emic waves: Location, extent, and energy range from a multievent analysis. *Geophys. Res. Lett.* 48, e2020GL091564. doi:10.1029/2020GL091564

Chen, L., Breneman, A. W., Xia, Z., and Zhang, X.-j. (2020). Modeling of bouncing electron microbursts induced by ducted chorus waves. *Geophys. Res. Lett.* 47, e2020GL089400. doi:10.1029/2020gl089400

Claudepierre, S. G., Ma, Q., Bortnik, J., O'Brien, T. P., Fennell, J. F., and Blake, J. B. (2020). Empirically estimated electron lifetimes in the earth's radiation belts: Comparison with theory. *Geophys. Res. Lett.* 47, e2019GL086056. doi:10.1029/2019gl086056

Cook, W. R., Cummings, A. C., Cummings, J. R., Garrard, T. L., Kecman, B., Mewaldt, R. A., et al. (1993). Pet: A proton/electron telescope for studies of magnetospheric, solar, and galactic particles. *IEEE Trans. Geosci. Remote Sens.* 31, 565–571. doi:10.1109/36.225523

Cornwall, J. M. (1965). Cyclotron instabilities and electromagnetic emission in the ultra low frequency and very low frequency ranges. *J. Geophys. Res. (1896-1977)* 70, 61–69. doi:10.1029/JZ070i001p00061

Davidson, G. T. (1965). Expected spatial distribution of low-energy protons precipitated in the auroral zones. *J. Geophys. Res.* 70, 1061–1068. doi:10.1029/jz070i005p01061

Donovan, E., Mende, S., Jackel, B., Frey, H., Syrjäsuo, M., Voronkov, I., et al. (2006). The themis all-sky imaging array—System design and initial results from the prototype imager. *J. Atmos. Solar-Terrestrial Phys.* 68, 1472–1487. doi:10.1016/j.jastp.2005.03.027

Douma, E., Rodger, C. J., Blum, L. W., and Clilverd, M. A. (2017). Occurrence characteristics of relativistic electron microbursts from SAMPEX observations. *J. Geophys. Res. Space Phys.* 122, 8096–8107. doi:10.1002/2017JA024067

Douma, E., Rodger, C. J., Clilverd, M. A., Hendry, A. T., Engebretson, M. J., and Lessard, M. R. (2018). Comparison of relativistic microburst activity seen by SAMPEX with ground-based wave measurements at Halley, Antarctica. *J. Geophys. Res. Space Phys.* 123, 1279–1294. doi:10.1002/2017JA024754

Fang, X., Liemohn, M. W., Kozyra, J. U., and Solomon, S. C. (2004). Quantification of the spreading effect of auroral proton precipitation. *J. Geophys. Res.* 109, A04309. doi:10.1029/2003ja010119

Gallardo-Lacourt, B., Frey, H., and Martinis, C. (2021). Proton aurora and optical emissions in the subauroral region. *Space Sci. Rev.* 217, 10–36. doi:10.1007/s11214-020-00776-6

Gary, S. P., Thomsen, M. F., Yin, L., and Winske, D. (1995). Electromagnetic proton cyclotron instability: Interactions with magnetospheric protons. *J. Geophys. Res.* 100, 21961–21972. doi:10.1029/95JA01403

Grach, S., VeronikaDemekhov, G., and Andrei (2020). Precipitation of relativistic electrons under resonant interaction with electromagnetic ion cyclotron wave packets. *J. Geophys. Res. Space Phys.* 125, e2019JA027358. doi:10.1029/2019ja027358

Grach, V. S., Demekhov, A. G., and Larchenko, A. V. (2021). Resonant interaction of relativistic electrons with realistic electromagnetic ion–cyclotron wave packets. *Earth Planets Space* 73, 129–217. doi:10.1186/s40623-021-01453-w

Grison, B., Santolik, O., Cornilleau-Wehrlin, N., Masson, A., Engebretson, M., Pickett, J., et al. (2013). Emic triggered chorus emissions in cluster data. *J. Geophys. Res. Space Phys.* 118, 1159–1169. doi:10.1002/jgra.50178

Halford, A. J., Fraser, B. J., Morley, S. K., Elkington, S. R., and Chan, A. A. (2016). Dependence of emic wave parameters during quiet, geomagnetic storm, and geomagnetic storm phase times. *J. Geophys. Res. Space Phys.* 121, 6277–6291. doi:10.1002/2016JA022694

Harris, S., Mende, S., Angelopoulos, V., Rachelson, W., Donovan, E., Jackel, B., et al. (2009). Themis ground based observatory system design. *THEMIS Mission* 2009, 213–233. doi:10.1007/978-0-387-89820-9_10

Hirsch, M. (2016). pymap3d: Python 3d coordinate conversions for geospace. doi:10.5281/zenodo.213676

[Dataset] Jackel, B. (2005). Mpa: Meridian photometer array. Avalilable at: https://aurora.phys.ucalgary.ca/norstar/msp/inst.html (Accessed 06 15.2022).

Jacobs, J., Kato, Y., Matsushita, S., and Troitskaya, V. (1964). Classification of geomagnetic micropulsations. *J. Geophys. Res.* 69, 180–181. doi:10.1029/jz069i001p00180

Jordanova, V. K., Albert, J., and Miyoshi, Y. (2008). Relativistic electron precipitation by emic waves from self – consistent global simulations. *J. Geophys. Res.* 113. doi:10.1029/2008JA013239

Jordanova, V. K. (2007). Modeling geomagnetic storm dynamics: New results and challenges. *J. Atmos. Sol. – Terr. Phys.* 69, 56–66. doi:10.1016/j.jastp.2006.06.016

Kawamura, M., Sakanoi, T., Fukizawa, M., Miyoshi, Y., Hosokawa, K., Tsuchiya, F., et al. (2021). Simultaneous pulsating aurora and microburst observations with ground-based fast auroral imagers and cubesat firebird-ii. *Geophys. Res. Lett.* 48, e2021GL094494. doi:10.1029/2021gl094494

Kennel, C. F., and Petschek, H. (1966). Limit on stably trapped particle fluxes. *J. Geophys. Res.* 71, 1–28. doi:10.1029/jz071i001p00001

Khazanov, G., Sibeck, D., Tel'Nikhin, A., and Kronberg, T. (2014). Relativistic electron precipitation events driven by electromagnetic ion-cyclotron waves. *Phys. Plasmas* 21, 082901. doi:10.1063/1.4892185

Kim, H., Hwang, J., Park, J., Miyashita, Y., Shiokawa, K., Mann, I. R., et al. (2018). Large-scale ducting of pc1 pulsations observed by swarm satellites and multiple ground networks. *Geophys. Res. Lett.* 45 (12), 703712–12. doi:10.1029/2018GL080693

Kivelson, M. G., Kivelson, M. G., and Russell, C. T. (1995). *Introduction to space physics*. Cambridge: Cambridge University Press.

Klecker, B., Hovestadt, D., Scholer, M., Arbinger, H., Ertl, M., Kastele, H., et al. (1993). Hilt: A heavy ion large area proportional counter telescope for solar and anomalous cosmic rays. *IEEE Trans. Geosci. Remote Sens.* 31, 542–548. doi:10.1109/36.225520

Kubota, Y., and Omura, Y. (2017). Rapid precipitation of radiation belt electrons induced by emic rising tone emissions localized in longitude inside and outside the plasmapause. *J. Geophys. Res. Space Phys.* 122, 293–309. doi:10.1002/2016ja023267

Kubota, Y., Omura, Y., and Summers, D. (2015). Relativistic electron precipitation induced by emic-triggered emissions in a dipole magnetosphere. *J. Geophys. Res. Space Phys.* 120, 4384–4399. doi:10.1002/2015ja021017

Lorentzen, K., Blake, J., Inan, U., and Bortnik, J. (2001). Observations of relativistic electron microbursts in association with vlf chorus. *J. Geophys. Res.* 106, 6017–6027. doi:10.1029/2000ja003018

Lyons, L. R., and Thorne, R. M. (1973). Equilibrium structure of radiation belt electrons. *J. Geophys. Res.* 78, 2142–2149. doi:10.1029/ja078i013p02142

Mann, I., Milling, D., Rae, I., Ozeke, L., Kale, A., Kale, Z., et al. (2008). The upgraded carisma magnetometer array in the themis era. *Space Sci. Rev.* 141, 413–451. doi:10.1007/s11214-008-9457-6

Mann, I. R., Usanova, M. E., Murphy, K., Robertson, M. T., Milling, D. K., Kale, A., et al. (2014). Spatial localization and ducting of emic waves: Van allen probes and ground-based observations. *Geophys. Res. Lett.* 41, 785–792. doi:10.1002/2013GL058581

Mason, G. M., Hamilton, D. C., Walpole, P. H., Heuerman, K. F., James, T. L., Lennard, M. H., et al. (1993). Leica: A low energy ion composition analyzer for the study of solar and magnetospheric heavy ions. *IEEE Trans. Geosci. Remote Sens.* 31, 549–556. doi:10.1109/36.225521

Mauk, B., Fox, N. J., Kanekal, S., Kessel, R., Sibeck, D., and Ukhorskiy, a. A. (2012). "Science objectives and rationale for the radiation belt storm probes mission," in *The van allen Probes mission* (Berlin, Germany: Springer), 3–27.

Mende, S., Harris, S., Frey, H., Angelopoulos, V., Russell, C., Donovan, E., et al. (2009). The themis array of ground-based observatories for the study of auroral substorms. *THEMIS Mission* 2009, 357–387. doi:10.1007/978-0-387-89820-9_16

Meredith, N. P., Horne, R. B., Shen, X.-C., Li, W., and Bortnik, J. (2020). Global model of whistler mode chorus in the near-equatorial region (– λ m– ¡ 18). *Geophys. Res. Lett.* 47, e2020GL087311. doi:10.1029/2020gl087311

Miyoshi, Y., Saito, S., Kurita, S., Asamura, K., Hosokawa, K., Sakanoi, T., et al. (2020). Relativistic electron microbursts as high-energy tail of pulsating aurora electrons. *Geophys. Res. Lett.* 47, e2020GL090360. doi:10.1029/2020GL090360

Miyoshi, Y., Saito, S., Seki, K., Nishiyama, T., Kataoka, R., Asamura, K., et al. (2015). Relation between fine structure of energy spectra for pulsating aurora

electrons and frequency spectra of whistler mode chorus waves. *J. Geophys. Res. Space Phys.* 120, 7728–7736. doi:10.1002/2015ja021562

Miyoshi, Y., Sakaguchi, K., Shiokawa, K., Evans, D., Albert, J., Connors, M., et al. (2008). Precipitation of radiation belt electrons by emic waves, observed from ground and space. *Geophys. Res. Lett.* 35, L23101. doi:10.1029/2008gl035727

Mozer, F., Agapitov, O., Blake, J., and Vasko, I. (2018). Simultaneous observations of lower band chorus emissions at the equator and microburst precipitating electrons in the ionosphere. *Geophys. Res. Lett.* 45, 511–516. doi:10.1002/2017gl076120

Nakamura, S., Omura, Y., Kletzing, C., and Baker, D. N. (2019). Rapid precipitation of relativistic electron by EMIC rising-tone emissions observed by the Van Allen Probes. *J. Geophys. Res. Space Phys.* 124, 6701–6714. doi:10.1029/2019JA026772

Nishimura, Y., Bortnik, J., Li, W., Lyons, L., Donovan, E., Angelopoulos, V., et al. (2014). Evolution of nightside subauroral proton aurora caused by transient plasma sheet flows. *J. Geophys. Res. Space Phys.* 119, 5295–5304. doi:10.1002/2014ja020029

Nomura, R., Shiokawa, K., Omura, Y., Ebihara, Y., Miyoshi, Y., Sakaguchi, K., et al. (2016). Pulsating proton aurora caused by rising tone pc1 waves. *J. Geophys. Res. Space Phys.* 121, 1608–1618. doi:10.1002/2015JA021681

O'Brien, T., Lorentzen, K., Mann, I., Meredith, N., Blake, J., Fennell, J., et al. (2003). Energization of relativistic electrons in the presence of ulf power and mev microbursts: Evidence for dual ulf and vlf acceleration. *J. Geophys. Res.* 108, 1329. doi:10.1029/2002ja009784

Omura, Y., and Zhao, Q. (2012). Nonlinear pitch angle scattering of relativistic electrons by emic waves in the inner magnetosphere. *J. Geophys. Res.* 117. doi:10.1029/2012ja017943

Omura, Y., and Zhao, Q. (2013). Relativistic electron microbursts due to nonlinear pitch angle scattering by emic triggered emissions. *J. Geophys. Res. Space Phys.* 118, 5008–5020. doi:10.1002/jgra.50477

Parks, G. K. (1967). Spatial characteristics of auroral-zone x-ray microbursts. *J. Geophys. Res. (19641896-1977)* 72, 215–226. doi:10.1029/JZ072i001p00215

Qin, M., Hudson, M., Millan, R., Woodger, L., and Shekhar, S. (2018). Statistical investigation of the efficiency of emic waves in precipitating relativistic electrons. *J. Geophys. Res. Space Phys.* 123, 6223–6230. doi:10.1029/2018ja025419

Rees, M., and Luckey, D. (1974). Auroral electron energy derived from ratio of spectroscopic emissions 1. model computations. *J. Geophys. Res.* 79, 5181–5186. doi:10.1029/ja079i034p05181

Remya, B., Tsurutani, B., Reddy, R., Lakhina, G., and Hajra, R. (2015). Electromagnetic cyclotron waves in the dayside subsolar outer magnetosphere generated by enhanced solar wind pressure: Emic wave coherency. *J. Geophys. Res. Space Phys.* 120, 7536–7551. doi:10.1002/2015ja021327

Saikin, A., Zhang, J.-C., Allen, R., Smith, C., Kistler, L., Spence, H., et al. (2015). The occurrence and wave properties of h+-he+-and o+-band emic waves observed by the van allen probes. *J. Geophys. Res. Space Phys.* 120, 7477–7492. doi:10.1002/2015ja021358

Saito, S., Miyoshi, Y., and Seki, K. (2012). Relativistic electron microbursts associated with whistler chorus rising tone elements: Gemsis-rbw simulations. *J. Geophys. Res.* 117. doi:10.1029/2012ja018020

Sakaguchi, K., Kasahara, Y., Shoji, M., Omura, Y., Miyoshi, Y., Nagatsuma, T., et al. (2013). Akebono observations of emic waves in the slot region of the radiation belts. *Geophys. Res. Lett.* 40, 5587–5591. doi:10.1002/2013gl058258

Sakaguchi, K., Shiokawa, K., Miyoshi, Y., Otsuka, Y., Ogawa, T., Asamura, K., et al. (2008). Simultaneous appearance of isolated auroral arcs and pc 1 geomagnetic pulsations at subauroral latitudes. *J. Geophys. Res.* 113. doi:10.1029/2007ja012888

Shepherd, M. G., Gattinger, R. L., and Jones, A. V. (1996). Observation and analysis of ni 520.0 nm auroral emissions. *J. Atmos. Terr. Phys.* 58, 579–599. doi:10.1016/0021-9169(95)00059-3

Shoji, M., and Omura, Y. (2011). Simulation of electromagnetic ion cyclotron triggered emissions in the earth's inner magnetosphere. *J. Geophys. Res.* 116. doi:10.1029/2010ja016351

Shumko, M. (2022). aurora-asi-lib: easily download, plot, animate, and analyze aurora all sky imager (ASI) data. doi:10.5281/zenodo.4746446

Shumko, M., Blum, L. W., and Crew, A. B. (2021). Duration of individual relativistic electron microbursts: A probe into their scattering mechanism. *Geophys. Res. Lett.* 48, e2021GL093879. doi:10.1029/2021gl093879

Shumko, M., Johnson, A., O'Brien, T. P., Turner, D. L., Greeley, A. D., Sample, J. G., et al. (2020a). Electron microburst size distribution derived with AeroCube-6. *J. Geophys. Res. Space Phys.* 125, e2019JA027651. doi:10.1029/2019JA027651

Shumko, M., Johnson, A. T., Sample, J. G., Griffith, B. A., Turner, D. L., O'Brien, T. P., et al. (2020b). Electron microburst size distribution derived with AeroCube-6. *J. Geophys. Res. Space Phys.* 125, e2019JA027651. doi:10.1029/2019ja027651

Shumko, M., Turner, D. L., O'Brien, T. P., Claudepierre, S. G., Sample, J., Hartley, D. P., et al. (2018). Evidence of microbursts observed near the equatorial plane in the outer van allen radiation belt. *Geophys. Res. Lett.* 45, 8044–8053. doi:10.1029/2018GL078451

Spasojević, M., Frey, H. U., Thomsen, M. F., Fuselier, S. A., Gary, S. P., Sandel, B. R., et al. (2004). The link between a detached subauroral proton arc and a plasmaspheric plume. *Geophys. Res. Lett.* 31, L04803. doi:10.1029/2003GL018389

Summers, D. (2005). Quasi-linear diffusion coefficients for field-aligned electromagnetic waves with applications to the magnetosphere. *J. Geophys. Res.* 110. doi:10.1029/2005ja011159

Summers, D., Thorne, R. M., and Xiao, F. (1998). Relativistic theory of wave-particle resonant diffusion with application to electron acceleration in the magnetosphere. *J. Geophys. Res.* 103, 20487–20500. doi:10.1029/98ja01740

Teng, S., Tao, X., Xie, Y., Zonca, F., Chen, L., Fang, W., et al. (2017). Analysis of the duration of rising tone chorus elements. *Geophys. Res. Lett.* 44, 12–074. doi:10.1002/2017gl075824

Thébault, E., Finlay, C. C., Beggan, C. D., Alken, P., Aubert, J., Barrois, O., et al. (2015). International geomagnetic reference field: The 12th generation. *Earth Planets Space* 67, 158. doi:10.1186/s40623-015-0313-0

Thorne, R. M., Ni, B., Tao, X., Horne, R. B., and Meredith, N. P. (2010). Scattering by chorus waves as the dominant cause of diffuse auroral precipitation. *Nature* 467, 943–946. doi:10.1038/nature09467

Thorne, R. M., O'Brien, T., Shprits, Y., Summers, D., and Horne, R. B. (2005). Timescale for mev electron microburst loss during geomagnetic storms. *J. Geophys. Res.* 110. doi:10.1029/2004ja010882

Unick, C. W., Donovan, E., Connors, M., and Jackel, B. (2017). A dedicated H-beta meridian scanning photometer for proton aurora measurement. *J. Geophys. Res. Space Phys.* 122, 753–764. doi:10.1002/2016ja022630

Van Allen, J. A. (1959). The geomagnetically trapped corpuscular radiation. *J. Geophys. Res. (1896-1977)* 64, 1683–1689. doi:10.1029/JZ064i011p01683

Vernov, S., and Chudakov, A. (1960). Investigation of radiation in outer space. *Sov. Phys. Usp.* 3, 230–250. doi:10.1070/pu1960v003n02abeh003269

Virtanen, P., Gommers, R., Oliphant, T. E., Haberland, M., Reddy, T., Cournapeau, D., et al. (2020). SciPy 1.0: Fundamental algorithms for scientific computing in Python. *Nat. Methods* 17, 261–272. doi:10.1038/s41592-019-0686-2

Winckler, J. R., Peterson, L., Arnoldy, R., and Hoffman, R. (1958). X-rays from visible aurorae at minneapolis. *Phys. Rev.* 110, 1221–1231. doi:10.1103/PhysRev.110.1221

Woodger, L., Halford, A., Millan, R., McCarthy, M., Smith, D., Bowers, G., et al. (2015). A summary of the barrel campaigns: Technique for studying electron precipitation. *J. Geophys. Res. Space Phys.* 120, 4922–4935. doi:10.1002/2014ja020874

Woodroffe, J. R., and Lysak, R. L. (2012). Ultra-low frequency wave coupling in the ionospheric alfvén resonator: Characteristics and implications for the interpretation of ground magnetic fields. *J. Geophys. Res.* 117. doi:10.1029/2011JA017057

Yahnin, A. G., Popova, T. A., Demekhov, A. G., Lubchich, A. A., Matsuoka, A., Asamura, K., et al. (2021). Evening side emic waves and related proton precipitation induced by a substorm. *J. Geophys. Res. Space Phys.* 126, e2020JA029091. doi:10.1029/2020JA029091

Zhang, J., Halford, A. J., Saikin, A. A., Huang, C.-L., Spence, H. E., Larsen, B. A., et al. (2016a). Emic waves and associated relativistic electron precipitation on 25–26 january 2013. *J. Geophys. Res. Space Phys.* 121, 11, 086086100. doi:10.1002/2016JA022918

Zhang, X.-J., Angelopoulos, V., Mourenas, D., Artemyev, A., Tsai, E., and Wilkins, C. (2022). Characteristics of electron microburst precipitation based on high-resolution elfin measurements. *JGR. Space Phys.* 127, e2022JA030509. doi:10.1029/2022ja030509

Zhang, X.-J., Li, W., Ma, Q., Thorne, R., Angelopoulos, V., Bortnik, J., et al. (2016b). Direct evidence for emic wave scattering of relativistic electrons in space. *J. Geophys. Res. Space Phys.* 121, 6620–6631. doi:10.1002/2016ja022521

Zhu, H., Chen, L., Claudepierre, S. G., and Zheng, L. (2020). Direct evidence of the pitch angle scattering of relativistic electrons induced by emic waves. *Geophys. Res. Lett.* 47, e2019GL085637. doi:10.1029/2019gl085637

frontiers | Frontiers in Astronomy and Space Sciences

TYPE Original Research
PUBLISHED 30 August 2022
DOI 10.3389/fspas.2022.986061

OPEN ACCESS

EDITED BY
Oliver Allanson,
University of Exeter, United Kingdom

REVIEWED BY
Ashley Greeley,
The Catholic University of America, United States
Murong Qin,
Boston University, United States

*CORRESPONDENCE
S. Chakraborty,
suman.chakrabarty37@gmail.com

SPECIALTY SECTION
This article was submitted to Space Physics,
a section of the journal
Frontiers in Astronomy and Space Sciences

RECEIVED 04 July 2022
ACCEPTED 08 August 2022
PUBLISHED 30 August 2022

CITATION
Chakraborty S, Chakrabarty D, Reeves GD, Baker DN and Rae IJ (2022), Statistical investigation on equatorial pitch angle distribution of energetic electrons in Earth's outer radiation belt during CME- and CIR-driven storms. *Front. Astron. Space Sci.* 9:986061. doi: 10.3389/fspas.2022.986061

Statistical investigation on equatorial pitch angle distribution of energetic electrons in Earth's outer radiation belt during CME- and CIR-driven storms

S. Chakraborty[1,2]*, D. Chakrabarty[2], G. D. Reeves[3], D. N. Baker[4] and I. J. Rae[1]

[1]Department of Mathematics, Physics and Electrical Engineering, Northumbria University, Newcastle-upon-Tyne, United Kingdom, [2]Space and Atmospheric Sciences Division, Physical Research Laboratory, Ahmedabad, India, [3]Space Science and Applications Group, Los Alamos National Laboratory, Los Alamos, NM, United States, [4]Laboratory for Atmospheric and Space Physics, University of Colorado Boulder, Boulder, CO, United States

We present a statistical investigation (September 2012 - September 2017) of pitch angle distribution (PAD) of energetic electrons (~30 keV - 1 MeV) in the outer radiation belt (L ≥ 3) during CME- and CIR-driven geomagnetic storms using Van Allen Probe measurements. We selected geomagnetic storms based on minimum of SYM-H being less than -50 nT and classified the storms according to their drivers. Thus, we obtained 23 CME- and 24 CIR-driven storms. During the storm intervals, pitch angle resolved electron flux measurements are obtained from the MagEIS instrument on-board Van Allen Probe-A spacecraft. We assume symmetric pitch angle distributions around 90° pitch angle and fit the observed PADs with Legendre polynomials after propagating them to the magnetic equator. Legendre coefficients c_2 and c_4, and the ratio R = $|c_2/c_4|$ are used to categorize the different PAD types. To resolve the spatio-temporal distribution of PADs, these coefficients are binned in 5 L-shell bins, 12 MLT bins for seven energy channels and four storm phases. We found that several hundreds of keV electrons exhibit clear dependence on local time, storm phases and storm drivers, with increased anisotropy for CME-driven storms during main and early recovery phases. On the contrary, we found that tens of keV electrons do not exhibit significant dependence on these parameters. We have discussed the different physical mechanisms responsible for the observed MLT dependent PADs and found drift-shell splitting to be the major contributor.

KEYWORDS

pitch angle distribution, outer radiation belt, energetic electrons, van allen probes, geomagnetic storms, CME, CIR

Introduction

The earth's radiation belt electron dynamics is highly complex, resulting from a delicate competition between different acceleration, transport and loss mechanisms (e.g., Friedel et al. (2005)). The acceleration mechanism is mostly driven by inward radial diffusion of radiation belt electrons from higher to lower radial distances, or local wave-particle interactions with various magnetospheric waves, or a combination of the two (e.g., Schulz and Lanzerotti (1974); Southwood and Kivelson (1981); Elkington et al. (2003); Horne et al. (2003); Baker and Kanekal (2008); Ukhorskiy et al. (2009); Zong et al. (2009); Thorne (2010); Claudepierre et al. (2013); Reeves et al. (2013); Ma et al. (2015); Boyd et al. (2016); Zong et al. (2017)). Interplanetary (IP) shocks generating strong electric field impulse can also cause rapid energization of radiation belt electrons within a time scale of few minutes (e.g., Foster et al. (2015); Kanekal et al. (2016)). The loss mechanism is driven by pitch-angle scattering of electrons and subsequent atmospheric precipitation led by wave-particle interactions (e.g., Thorne (1977); Rodger et al. (2007); Reidy et al. (2021)), or magnetopause shadowing caused by sudden magnetospheric compression (e.g., Yu et al. (2013); Staples et al. (2020); Cohen et al. (2021)), or a combination of both (e.g., Summers and Thorne (2003); Bortnik et al. (2006); Shprits et al. (2006); Ukhorskiy et al. (2006); Turner et al. (2012); Blum et al. (2015); Shprits et al. (2017)). The relativistic electron dynamics also show strong dependence on several factors, such as, geomagnetic activity, solar wind driving conditions, spatial location, local time, and background magnetospheric conditions (e.g., Li et al. (1997); Reeves et al. (1998, 2003); Meredith et al. (2003); Lee et al. (2013); Ni et al. (2013); Thorne et al. (2013b,a); Baker et al. (2013, 2014b,a)). To comprehensively understand the underlying physical processes responsible for the complex radiation belt electron dynamics, an useful approach is to investigate the evolution of electron pitch angle distribution (PAD). This is because electrons of different energies at different pitch angles respond differently to the external influences (e.g., Chakraborty et al. (2021)) and therefore, PADs can provide important information on the source and loss processes in a specific region.

There are several types of PADs for electrons in the outer radiation belt. The simplest of them is the isotropic distribution, which is usually observed in the midnight MLT sector at geosynchronous (GEO) orbit for substorm-injected electrons having energy in the range of few tens to hundreds of keV (Asnes et al., 2005). Some other commonly observed outer radiation belt electron PADs are the pancake distribution, butterfly distribution and flat top distribution. The pancake distribution is the most prevalent type of PAD for outer radiation belt electrons. This type of PAD is mostly found on the dayside and is identified by electron flux maximum at 90° pitch angle (e.g., West et al. (1973); Gannon et al. (2007)). The mechanisms that have been attributed to the formation of this type of PAD are pitch angle diffusion caused by wave-particle interaction and inward radial diffusion (Schulz and Lanzerotti (1974); Summers et al. (1998); Horne et al. (2003); Xiao et al. (2009b,a, 2012, 2014); Thorne et al. (2013c)). The butterfly PAD is generally observed at nightside at larger L-shells and is characterized by lower electron fluxes at 90° pitch angle compared to field-aligned directions. This type of distribution, at larger L-shells, is mostly attributed to drift-shell splitting of electrons in an asymmetric magnetic field (e.g., Sibeck et al. (1987); Selesnick and Blake (2002)), while at lower L-shells, past studies have shown that wave-particle interactions with chorus and/or magnetosonic waves can generate this type of PAD (e.g., Horne et al. (2005); Li et al. (2016)). The flat top PAD is generally observed at dawn and dusk local times at larger L-shells and has almost similar electron fluxes spread over a wide pitch angle range around 90° pitch angle. Wave-particle interaction is believed to generate this type of PAD and it is considered to be an intermediate distribution between the pancake and butterfly PADs (e.g., Horne et al. (2003); Zhao et al. (2017)).

Past studies have shown that radiation belt electron equatorial pitch angle distributions exhibit an energy dependence. Most of the equatorial PADs of 1–10s of keV electrons in the outer radiation belt are pancake shaped (e.g., Zhao et al. (2020)). On the contrary, for hundreds of keV to few MeV electrons, pancake PADs are prevalent on the dayside of both the outer and inner magnetosphere, while butterfly PADs are prevalent on the nightside magnetosphere over extended radial distances (e.g., West et al. (1973); Gannon et al. (2007); Ni et al. (2015); Pandya et al. (2020)). The electron PADs have also been found to depend on geomagnetic activity, L-shell and magnetic local time (MLT) (e.g., Shi et al. (2016)). During geomagnetic disturbed periods, the anisotropy of electron PADs have been found to increase: pancake PADs become more 90°-peaked. This has mostly been attributed to chorus acceleration for regions outside the plasmasphere and electromagnetic ion cyclotron (EMIC) wave scattering for regions inside the plasmasphere (e.g., Ni et al. (2015)). However, butterfly PADs do not exhibit strong correlation with solar wind parameters, specifically, solar wind dynamic pressure (Ni et al., 2016).

In recent years, several studies have examined the statistical relationship between energetic particle equatorial pitch angle distributions, different phases of geomagnetic storms, and solar wind drivers using Van Allen Probe observations. Ni et al. (2015) used 15 months of electron flux measurements from the Relativistic Electron Proton Telescope (REPT) instrument onboard the Van Allen Probes to study the storm time evolution of PADs of ultra-relativistic (> 2 MeV) electrons. They used sinusoidal functions of the form $\sin^n(\alpha)$ to fit the observed pitch angle distribution, and used the sine power n to indicate pitch angle anisotropy. The results from Ni et al. (2015) showed that n increases with geomagnetic activity, suggesting

increased pitch angle anisotropy during storm main phase. Pandya et al. (2020) used 5 years of Van Allen Probe REPT measurements to study the variation of pitch angle distribution of relativistic electrons (1.8–6.3 MeV) during different phases of 55 geomagnetic storms driven by different solar wind drivers, namely, coronal mass ejections (CMEs) and corotating interacting regions (CIRs). Using the same sinusoidal fitting method, Pandya et al. (2020) found the PADs to exhibit strong dependence on MLT at higher L-shell (L ≈ 5), while at lower L-shells (L ≈ 3), the electron PADs are found to be less affected by geomagnetic activity and storm phase. Although, they couldn't find any significant dependence of the relativistic electron PADs on the storm drivers (27 CMEs and 28 CIRs). Greeley et al. (2021) studied the energization and isotropization of the same outer radiation belt relativistic and ultra-relativistic electron population (1.8–7.7 MeV) using REPT measurements and sinusoidal fitting methods during storms driven by CMEs and CIRs. They found that electron PADs are, in general, more anisotropic for CME-driven storms compared to CIR-driven storms. Also, the PADs of higher energy electrons are more anisotropic than lower energy electrons, and the anisotropy peaks within a day of DST_{min}. The isotropization of electron PADs were also found to have faster rates for CME-driven storms than CIR-driven storms. Smirnov et al. (2022) used Van Allen Probe Magnetic Electron Ion Spectrometer (MagEIS) instrument measurements to examine equatorial PADs of electrons in the energy range 30 keV - 1.6 MeV during 129 geomagnetic storms in the entire Van Allen Probe era (2012–2019). They used sinusoidal functions to fit the observed PADs for day and night MLT sectors. Smirnov et al. (2022) found that on the dayside, the distributions are mainly pancake which become more 90° peaked during the storm main phase, and this anisotropy increases with electron energy. They also found butterfly PADs to be more prevalent on the nightside at higher L-shells during geomagnetic quiet conditions, that spread to lower L-shells during enhanced geomagnetic activity.

The previous studies discussed above, although, provide a comprehensive picture of the storm-time evolution of electron PADs in the outer radiation belt, the effect of storm drivers (CMEs/CIRs) on the electron population having energies in the range of few tens to several hundreds of keV has not yet been investigated. Therefore, in this study, using 5 years (September 2012 to September 2017) of energetic electron flux (~30 keV to ~1 MeV) measurements from the MagEIS instrument on board the Van Allen Probe-A spacecraft, we have extensively examined the evolution of equatorial PADs in the outer radiation belt (L ≥ 3) as a function of L-shell, MLT and electron kinetic energy during different phases of 23 CME- and 24 CIR-driven geomagnetic storms. The measured electron PADs have been propagated to the magnetic equator and 5-min averages have been calculated. To fit the equatorial PADs, a Legendre polynomial form has been adopted following the method used by Chen et al. (2014); Zhao et al. (2018, 2020), and the coefficients of Legendre polynomials are binned in radial distance (L), local time (MLT) and electron kinetic energy. The coefficients give us information about the electron PAD type and hence, the binned coefficients are plotted on L-MLT polar maps to study the characteristics of equatorial PADs during different phases of geomagnetic storms. The underlying physical mechanisms responsible for the observed PAD types have also been examined.

This paper is organized as follows: in *Data and event selection*, data used in this study and the event selection criteria are provided; in *Methodology*, the data analysis methodology is discussed; in *Results*, the statistical results are presented; in *Discussion and conclusion*, the possible physical mechanisms are discussed; and finally, in *Summary*, we provide our concluding remarks.

Data and event selection

The Magnetic Electron Ion Spectrometer (MagEIS) instrument of Energetic Particle, Composition, and Thermal Plasma Suite (ECT; Spence et al. (2013)) on board the Van Allen Probes flying near the equatorial plane (Mauk et al., 2013) provides high resolution electron flux measurements over an energy range of ~ 30 keV to 4 MeV (Blake et al., 2013; Spence et al., 2013). In this study, we have used the pitch angle resolved Level 3 MagEIS data from Probe A measurements during the period September 2012 to September 2017 at seven specific energy channels (33 keV, 80 keV, 143 keV, 226 keV, 346 keV, 597 keV, and 909 keV) binned to 11 pitch angles (8.19°, 24.55°, 40.91°, 57.27°, 73.64°, 90°, 106.36°, 122.73°, 139.09°, 155.45°, and 171.82°). Measurements from Electric and Magnetic Field Instrument Suite and Integrated Science (EMFISIS; Kletzing et al. (2013)) on board the Van Allen Probe - A spacecraft are also used to investigate the chorus and ULF (ultra-low frequency) wave activity during this period. The EMFISIS wave instruments collect survey measurements of the wave electric and magnetic fields during half-second collection periods every 6 s over 65 logarithmically spaced frequency intervals between ~1 Hz to ~12 kHz. EMFISIS is also equipped with a fluxgate magnetometer (FGM) that measures the magnetic field with a sampling rate of 64 vectors/sec. In this study, we have used the FGM data that provides magnetic field with 1 s resolution. The key solar wind parameters and geomagnetic indices are procured from the OMNIWEB data service with 1 min resolution.

To study the effects of storm drivers on the evolution of radiation belt electron PADs, we created a 5 year period database of geomagnetic storms from September 2012 to September 2017. To create the database, we selected storms such that the minimum SYM-H index was less than -50 nT and classified them according to their drivers, namely coronal mass ejections (CMEs) and corotating interacting regions (CIRs), the details of which are listed in Table 1. The list of storms in Table 1 consists of storms presented in Pandya et al. (2019) and other new storms

TABLE 1 List of CME- and CIR-driven geomagnetic storms.

Event	CME-associated storm	SYM-H_{min} (nT)	CIR-associated storm	SYM-H_{min} (nT)
1	2012-10-01	−138	2013-01-26	−62
2	2012-11-14	−118	2013-03-01	−76
3	2013-03-17	−132	2013-08-27	−64
4	2013-06-01	−137	2013-10-30	−57
5	2013-06-29	−111	2013-12-08	−72
6	2013-07-06	−80	2014-06-08	−72
7	2013-10-02	−90	2015-02-17	−70
8	2014-02-27	−101	2015-02-24	−76
9	2014-04-30	−76	2015-05-13	−98
10	2014-09-12	−97	2015-06-08	−105
11	2014-12-22	−65	2015-07-05	−87
12	2015-01-07	−135	2015-07-13	−71
13	2015-03-17	−234	2016-01-20	−95
14	2015-06-23	−208	2016-02-03	−60
15	2015-07-23	−83	2016-05-08	−105
16	2015-11-07	−106	2016-07-25	−51
17	2015-12-20	−170	2016-08-03	−63
18	2015-12-31	−117	2016-08-23	−83
19	2016-03-06	−110	2017-03-01	−74
20	2016-10-13	−114	2017-03-27	−86
21	2016-11-09	−55	2017-04-04	−50
22	2017-05-27	−142	2017-05-29	−142
23	2017-07-16	−67	2017-08-29	−64
24			2017-09-26	−74

to complete the 5 year period database. In addition, as our aim is to study the evolution of PADs during different phases of geomagnetic storms driven by different solar wind drivers, we also ensured that the selected storms are isolated events. The new ICME events identified in this work are supported by the event list published by Cane and Richardson (http://www.srl.caltech.edu/ACE/ASC/DATA/level3/icmetable2.htm), and the new CIR events are consistent with the list of SIR/HSS events during 1995–2017 published by M. Grandin, A. T. Aikio, and A. Kozlovsky (Grandin et al., 2019). After the storms are selected and classified, they are divided into different storm phases, defined as: main phase - the duration starting from the time when SYM-H index begins to monotonically decrease to when SYM-H reaches its minimum value; pre-storm phase - a period of 10 h prior to the main phase; early recovery phase - a period of 10 h after the main phase; and late recovery phase - a period of 10 h after the early recovery phase.

Methodology

To study the distribution of energetic electron PADs, the PADs need to be quantified. In the past, different models have been used to quantify PADs. Out of them, the most commonly used are PAD models of the form $\sin^n(\alpha)$, where n is the anisotropy index and α is the pitch angle (e.g., Garcia (1996); Vampola (1997)); and empirical models using the method of Legendre polynomial fitting (e.g., Chen et al. (2014); Zhao et al. (2018, 2020)). The problem with fitting models having the form of $\sin^n(\alpha)$ is that they can not represent butterfly PADs, whereas a complete set of Legendre polynomials can represent any form of PADs (Chen et al., 2014; Zhao et al., 2018, 2020). This makes Legendre polynomial fitting models better candidates to study electron PADs in the radiation belt. Chen et al. (2014), taking measurements from CRRES, Polar and LANL-GEO satellites and using the method of Legendre polynomial fitting developed an empirical model of relativistic electrons (~ 150 keV to 1.5 MeV) in the outer radiation belt. Later, Zhao et al. (2018) developed an empirical model of electron PADs in the slot region and inner radiation belt as a function of L-shell, MLT, electron energy and geomagnetic activity using 4 years of Van Allen Probe measurements and Legendre polynomials. Most recently, Zhao et al. (2020) using 7 years of data from Van Allen Probes HOPE instrument and Legendre polynomial fitting of observed PADs examined the equatorial PADs of 1–50 keV electrons in the inner magnetosphere. In this study, we have adapted the same method

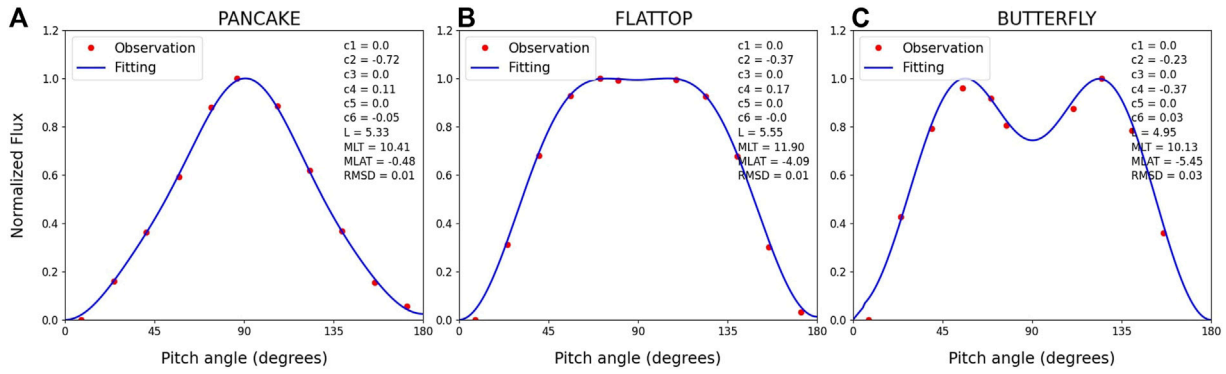

FIGURE 1
Examples of **(A)** pancake, **(B)** flattop and **(C)** butterfly pitch angle distributions. The red filled circles are normalized electron flux of 143 keV electrons measured by MagEIS instrument on-board the Van Allen Probe-A spacecraft (propagated to the magnetic equator and averaged in 5 min assuming symmetric distribution around 90° pitch angle), and blue curves show the Legendre polynomial fitting results. The first six Legendre coefficients (c_1– c_6), RMSD and magnetic ephemeris information (L, MLT, MLAT) are provided in each panel.

of Legendre polynomial fitting as described in Chen et al. (2014) and Zhao et al. (2018, 2020) to investigate the effect of storm drivers on the statistical properties of equatorial electron PADs in the outer radiation belt. Although the methodology adapted in this study is the same as mentioned in the previous works, the main focus of this study is to explore any characteristic differences in the PADs of outer radiation belt electrons spanning an energy range from tens of keV to MeV during storms driven by different storm drivers.

Towards that goal, the steps followed in this study can be described as: (1) We selected the electron flux data when Van Allen Probe-A was close to the magnetic equator with the absolute value of magnetic latitude (MLAT) less than 10°. This ensured that we have equatorial PADs with a wide pitch angle coverage. (2) The measured electron PADs are propagated to the magnetic equator using T89D (Tsyganenko, 1989) magnetic field model. The selection of electron flux data when the Van Allen Probe-A was within ±10° MLAT also assured that there is no large data gap near 90° pitch angle after propagating the observed local electron flux data to the magnetic equator. (3) 5-min averages of equatorial PADs are calculated from the ~ 10.8 s resolution data, assuming symmetric PADs around 90° pitch angle. (4) The measured 5-minute-averaged equatorial PADs are then fitted by Legendre polynomials and represented by a set of normalized Legendre coefficients (c_n). For a more comprehensive description of the Legendre polynomials and coefficients, the readers are encouraged to read the methodology sections of Chen et al. (2014); Zhao et al. (2018, 2020). In this study, we have included only those PADs that are well fitted by Legendre polynomials with a root-mean-square-deviation (RMSD) < 0.1.

Figure 1 shows examples of Legendre polynomial fitting results of the three most prevalent PAD types in the outer radiation belt: (a) pancake, (b) flat top and (c) butterfly. The fitting results are shown by blue curves and the measured equatorial PADs are shown by red filled circles. The sets of first six normalized Legendre coefficients $c_1 - c_6$ representing the different PAD types are shown at the top of each panel. Although a complete set of Legendre polynomials should be used to represent a PAD, in statistical studies, it is reasonable to retain only a handful of coefficients (Zhao et al., 2018). Chen et al. (2014) demonstrated that electron PADs in the outer radiation belt can be well categorized by Legendre polynomials up to the sixth order and therefore, in this study, we have used normalized Legendre coefficients up to c_6 to represent the measured PADs. Further, as we are considering symmetric PADs around 90° pitch angle, we have taken the odd order Legendre coefficients, i.e., c_1, c_3, and c_5 as zero. Therefore, c_2, c_4 and c_6 become the only three fitting parameters for representing the equatorial PADs. Chen et al. (2014) also showed that as n increases, the value of c_n becomes significantly small and therefore, different pairs of the first two even order Legendre coefficients (c_2, c_4) can be directly read for categorizing PAD types. In this study, our discussions will thus include only c_2 and c_4. Pancake PADs have negative and larger c_2 values and smaller values of $|c_4|$ (Figure 1A), flat top PADs have usually comparable values of c_2 and c_4 (Figure 1B), and butterfly PADs have negative and larger c_4 values and smaller/comparable values of c_2 (Figure 1C). Therefore, if we take ratio of the two coefficients, say $R = |\frac{c_2}{c_4}|$, then for pancake PADs, R will be greater than one; for flattop PADs, R will be comparable to one; and for butterfly PADs, R will be less than 1. Thus, the values of R can be used to directly identify the PAD types. To resolve the spatial and temporal distribution of PADs, the coefficients c_2 and c_4, and the parameter R are binned in L with bin width 0.8 L (5 bins from L = 3 to L = 7), MLT with bin width 2 h

(12 bins), electron energy E (7 energy channels) and storm phases (4 storm phases). Then, medians of the coefficients (c_2, c_4) and R in each (L, MLT, E, and storm phase) bin are derived, based on which the characteristics of ~30 keV to 1 MeV electron equatorial PADs in the outer radiation belt are presented. Further, to ensure that we have enough number of data points in each L-MLT bin for statistical evaluation, we considered only those bins that have at least 40 data points. This is because bins with few number of data points may falsely appear as MLT variation. Supplementary Figure S2 in the supporting document shows the distribution of data points in each L-MLT bin. Supplementary Figure S3 shows the distribution of the parameter R without excluding any bin to highlight the randomness of such distribution if we include bins with few number of data points.

To investigate the possible role of wave-particle interactions in driving the different PAD shapes, we examined the statistical properties of whistler mode chorus and Pc5 mode ULF waves during the period of our study. To identify the chorus waves having typical frequencies in the range 0.05–0.8 f_{ce}, where f_{ce} is the equatorial electron gyrofrequency, we used the criteria as described in Bingham et al. (2019), such as the Van Allen Probe-A is outside the plasmasphere, and the waves have planarity > 0.6 and ellipticity > 0.7. After identifying the chorus waves, the wave amplitudes are binned in (L, MLT, and storm phase) as defined earlier. To visualize the excitation of the waves, we defined an excitation factor (F) as the ratio of the chorus wave power in each individual (L, MLT, and storm phase) bin to the background chorus wave power. For background chorus wave power, we considered the minimum chorus wave power during the pre-storm phase. Finally, superposed epoch analyses (SEA) is performed to derive the median of the parameter F, based on which the role of chorus waves in outer radiation belt electron dynamics is discussed.

To study the statistical distribution of Pc5 mode ULF waves in the outer radiation belt, 1 s resolution magnetic field data from the fluxgate magnetometer of EMFISIS on board the Van Allen Probe-A spacecraft for the region L ≥ 3 are first projected on a mean-field aligned coordinate system to separate ULF field variations along directions both perpendicular and parallel to the magnetic field Takahashi et al. (1990). In this coordinate system, the mean field is defined as the 400 s running average of the magnetic field vector $\langle \mathbf{B} \rangle$. The individual components are defined as: (1) parallel component $\hat{e_z} = \langle \mathbf{B} \rangle / |\langle \mathbf{B} \rangle|$; (2) azimuthal component $\hat{e_y} = \langle \mathbf{B} \rangle \times \mathbf{r}$, where $\mathbf{r}$ is the position vector of the spacecraft with respect to the earth's center; and (3) radial component $\hat{e_x} = \hat{e_y} \times \hat{e_z}$. The magnetic field components are defined as: radial (poloidal) component $B_x = \mathbf{B} \cdot \hat{e_x}$ which is pointing radially outward; azimuthal (toroidal) component $B_y = \mathbf{B} \cdot \hat{e_y}$ which is positive eastward; and parallel (compressional) component $B_z = |\mathbf{B}| - |\langle \mathbf{B} \rangle|$, which is pointing along the magnetic field. Once the observed magnetic field has been resolved into its three directional components, a low-pass Butterworth filter with cut-off frequency of 10 mHz is applied to obtain wavelet power spectra covering the Pc5 frequency range (typically 2–7 mHz) Balasis et al. (2013). For wavelet analysis, we used Morlet mother wavelet function with $\omega_0 = 6$, as Morlet wavelet in the range $\omega_0 = 5$–10 provides high time resolution that is ideal for the study of ULF waves in the Pc4-5 range Balasis et al. (2013). This provided us with ULF wave power in the Pc5 frequency range for the three magnetic field components. We then manually identified and eliminated false wave events for each individual storm. Finally, SEA is performed to derive median Pc5 ULF wave power, based on which, the role of ULF waves in the outer radiation belt PAD is investigated.

Results

Using the methodology as described in *Methodology*, here we present the statistical results of radiation belt electron PADs as a function of L-shell, MLT and electron energy E during different phases of CME- and CIR-driven geomagnetic storms.

Figure 2 shows the L-MLT distribution of the medians of c_2 (left panel) and c_4 (right panel) at seven specific energy channels (from top to bottom: 33 keV, 80 keV, 143 keV, 226 keV, 346 keV, 597 and 909 keV) during pre-storm, main, early recovery and late recovery phase of CME-driven geomagnetic storms. For each plot, the Earth is at the centre and the Sun is to the left. MLT = 12 is indicated in the leftmost column, and the concentric circles denote L values from L = 1 to 7 with L-width of 2 R_E. The colorbar denotes the c_2 and c_4 values spanning a range from -1 to 1. From Figure 2, we can see that the coefficients c_2 and c_4 exhibit dependence on electron energy, storm phase, L-shell and MLT. We can also see that these coefficients exhibit opposite variations, the combined (c_2, c_4) values being consistent with those defined in *Methodology*. To understand these features explicitly, first, if we increase the electron energy during a particular storm phase, we can find that the distributions of c_2 and c_4 are different in different energy channels. As an example, during the pre-storm phase, we can see that in the low energy channels, c_2 values are, in general, negative at all L-shell and MLT, while in the higher energy channels, a clear day-night asymmetry can be seen: c_2 values are mostly negative on the dayside and positive on the nightside outside L = 4. The parameter c_4, on the other hand, at lower energy channels, is mostly positive inside L = 4 and near zero to slightly negative outside L = 4. At higher energies, at lower L-shells, c_4 is mostly near-zero, while at higher L-shell and nightside, it exhibits negative values. Second, keeping the energy fixed, if we compare the distribution of c_2 and c_4 during different storm phases, we can find the coefficients to show clear storm phase dependence, particularly in the medium and high energy channels. For example, during the pre-storm phase, c_2 (c_4) values of 597 keV electrons are mostly negative (near-zero) on the dayside and slightly positive (slightly negative) on the nightside outside L = 4. During the main phase, c_2 (c_4) values become mostly negative (positive) on the dayside and

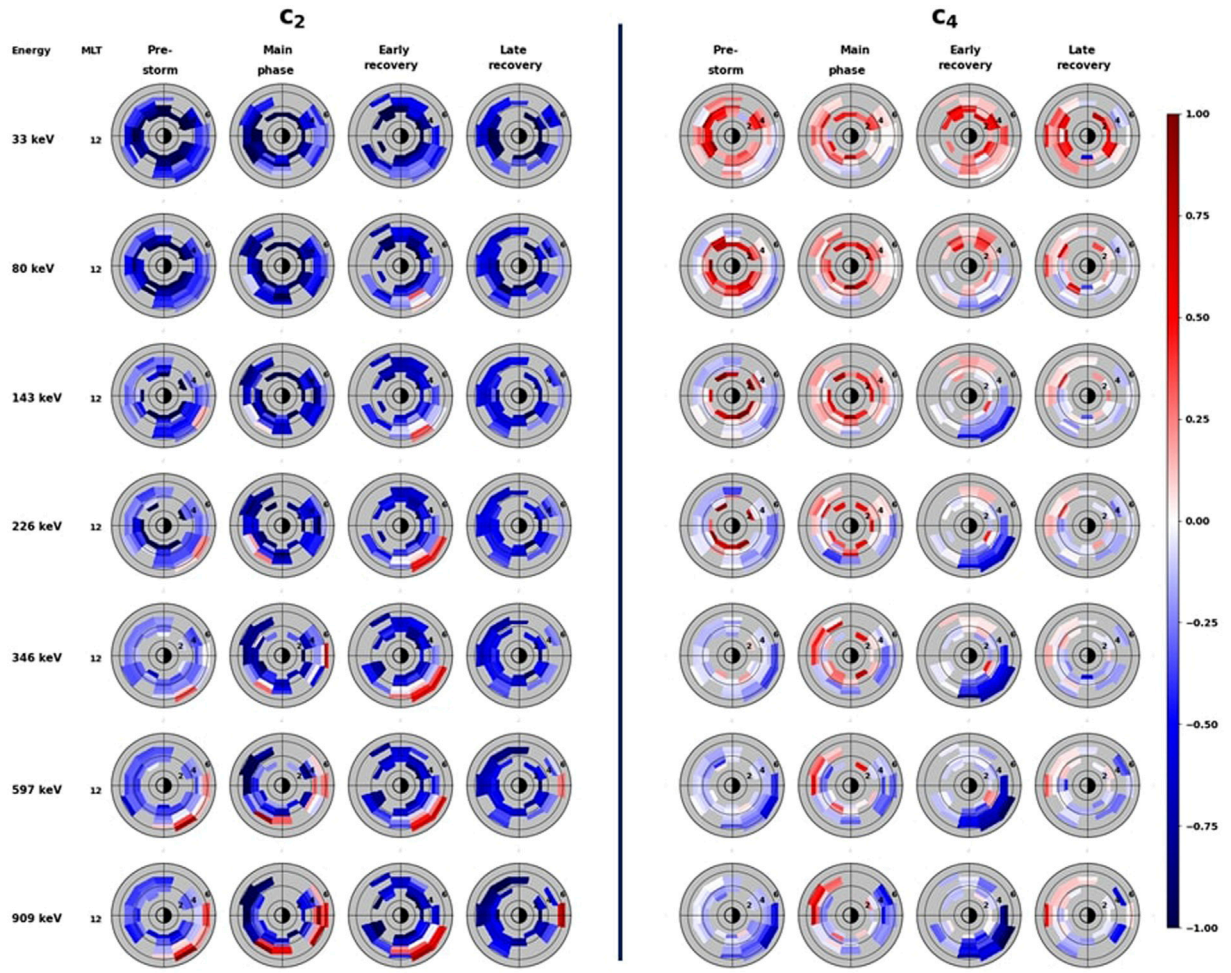

FIGURE 2
The distribution of coefficients c_2 (left panel) and c_4 (right panel) in a respective L-MLT bin during coronal mass ejection (CME) driven geomagnetic storms at seven specific energy channels, from top to bottom: 33 keV, 80 keV, 143 keV, 226 keV, 346 keV, 597 keV, and 909 keV. The columns correspond to different storm phases. MLT = 12 is indicated in the leftmost column and the concentric circles denote L values from L = 1 to 7 with L-width of 2 R_E. For each panel, the Earth is at the centre and the Sun is to the left. The colorbar represents the corresponding c_2 and c_4 values.

positive (negative) on the nightside. During the early recovery phase, the day-night asymmetry further increases. In the late recovery phase, the day-night asymmetry still persists, but the values become less intense, indicating reduced anisotropy. These examples also highlight the L-shell and MLT dependence that itself varies with electron energy and storm phase.

Figure 3 shows L-MLT distribution of the medians of c_2 and c_4 values for CIR-driven geomagnetic storms in the same manner as in Figure 2. Similar to CME-driven storms, the coefficients c_2 and c_4 exhibit energy dependence, L-shell dependence, day-night asymmetry and storm phase variations. The overall features of the variations in c_2 and c_4 are found to be common for both the storm drivers (CMEs/CIRs), the only difference being in the values of the coefficients, particularly in the higher energy channels. For CME-driven storms, the c_4 values in the energy range 597–909 keV are close to ~ -1 for L > 3 and MLT ≈18–4 during early recovery phase, whereas for CIR-driven storms, c_4 values are in the range -0.25 to -0.75 for L > 4 and MLT ≈16–2. This indicates slightly higher anisotropy in c_4 values for CME-driven storms compared to CIR-driven storms. One can also see that for CIR-driven storms, in the energy range 597–909 keV, c_2 values are close to ~ 1 for L > 5 and MLT ≈16–4 during the main phase, whereas for CME-driven storms, c_2 values are comparably smaller (~ 0.75).

Figure 4 shows L-MLT distribution of the medians of the ratio $R = |c_2/c_4|$ for CME-driven (left panel) and CIR-driven (right panel) geomagnetic storms. As defined in *Methodology*, pancake PADs have R > 1, flattop PADs have R ≈ 1 and butterfly PADs have R < 1. From the colorbar on the right, we can see that R > 1 values are denoted by red to deep red, R ≈ 1 values are denoted by slight red to

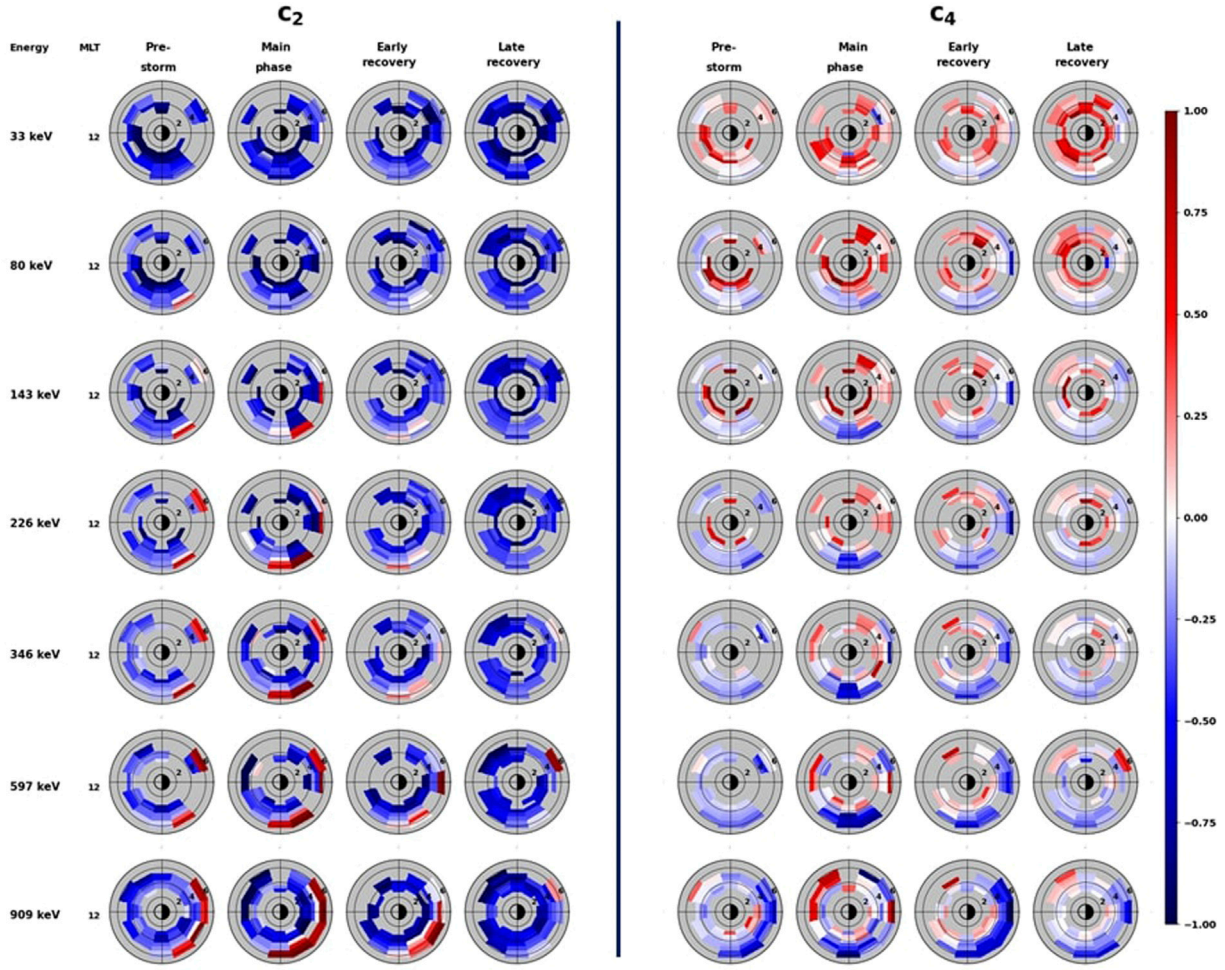

FIGURE 3
Same as in Figure 2 but during corotating interacting region (CIR) driven geomagnetic storms.

slight blue, and R < 1 values are denoted by blue to deep blue. These R values are used to identify the different PAD shapes. While identifying the different PAD shapes, we have excluded the single bins that exhibit random values as they might be manifestations of statistical bias and falsely indicate MLT variations. We mostly concentrate on the overall distribution and several intriguing features are revealed from Figure 4:

1. In the low energy channels (33–80 keV), the fitting results suggest that majority of PAD fits have values of R > 1 during all the four storm phases and both the storm drivers (CMEs/CIRs). This indicates that majority of tens of keV electrons in the outer radiation belt exhibit pancake PADs. This is in agreement with the results of Zhao et al. (2020): using observations from the HOPE instrument on board the Van Allen Probes and the same Legendre polynomial fitting technique, they showed that most of the tens of keV electron equatorial PADs in the inner magnetosphere during geomagnetically quiet (Kp ≤ 1+), moderate (1+ < Kp ≤ 3+), and active times (Kp > 3+) are pancake PADs.
2. In the medium energy channels (143–226 keV), for CME-driven storms, during the pre-storm and main phase, R values are > 1; during the early recovery phase, a day-night asymmetry in R values can be seen: R > 1 at the dayside and R ~ 1 or slightly < 1 at the nightside; and during the late recovery phase, R values again become mostly greater than 1. This indicates that during the pre-storm and main phase, majority of few 100s of keV electrons exhibit pancake PADs; during the early recovery phase, they exhibit pancake PADs at the dayside and flattop PADs at the nightside; and during the late recovery phase, the PADs again become mostly pancake shaped. Just as the combination of c_2 and c_4, and hence R provides information about the PAD shapes, changes in their values give an estimation of the pitch angle anisotropy. Higher

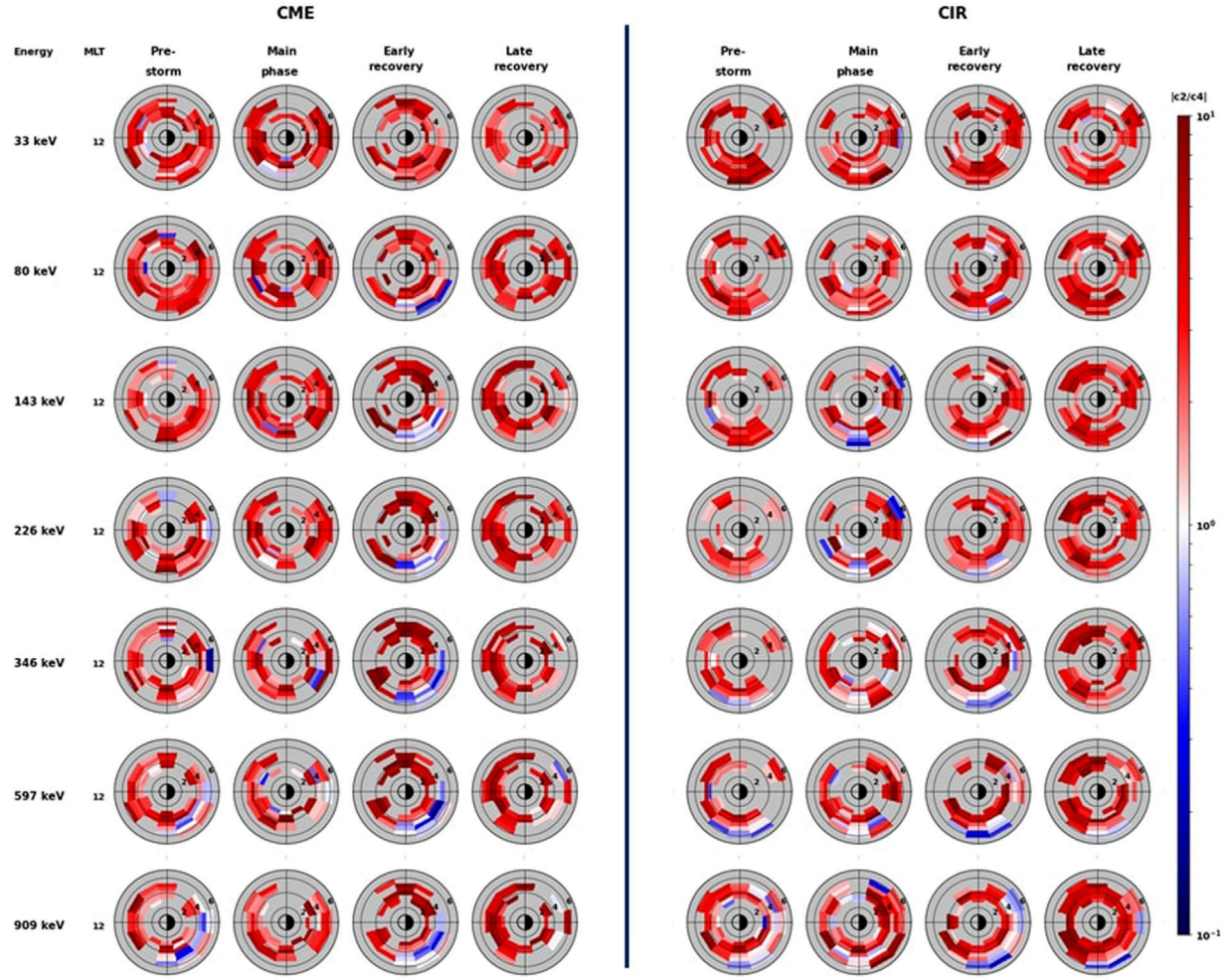

FIGURE 4
Comparison of the ratio R = $|c_2/c_4|$ between CME-driven (left panel) and CIR-driven (right panel) geomagnetic storms. R is plotted in the same manner as in Figure 2, 3.

values of R suggest higher anisotropy. From Figure 4, it can be seen that during the early and late recovery phases, R values are significantly larger which suggest greater pitch angle anisotropy during these storm phases. For CIR-driven storms, the fitting results suggest that during the pre-storm phase, R values are > 1; during the main phase, R values ~ 1 or slightly < 1 can be seen at ~ 18 MLT and ~ 2 to 5 MLT; and during the early and late recovery phases, R values again become > 1. This indicates that during the pre-storm and recovery phases, the PADs are mostly pancake, while during the main phase, flattop PADs can be seen at around the dusk and dawn MLT sectors. R values are also higher during the early and late recovery phases, suggesting enhanced anisotropy.

3. In the high energy channels (346–909 keV), for CME-driven storms, during the pre-storm phase, fitting results show that most of the dayside PAD fits have values of $R > 1$ while the nightside PAD fits have values of $R \sim 1$ or slightly < 1; during the main phase, R values are mostly greater than 1; during the early recovery phase, R values are largely > 1 at the dayside and < 1 at the nightside; and during the late recovery phase, R values at the dayside are still greater than 1, while a few patches of R values ~ 1 can be seen at the nightside for regions outside $L \approx 4$. This indicates that during the pre-storm phase, several 100s of keV electrons exhibit pancake PADs at the dayside and flattop/butterfly PADs at the nightside; during the main phase, the electron PAD shapes are mostly pancake; during the early recovery phase, the PADs at the dayside are pancake shaped while those at the nightside are butterfly shaped; and in the late recovery phase, electrons at the dayside exhibit pancake PADs while those at the nightside exhibit flattop PADs outside $L \approx 4$ and pancake PADs inside $L \approx 4$.

The ratio R also exhibits larger values during early and late recovery phases indicating increased anisotropy. For CIR-driven storms, the distribution of PADs during the different storm phases follows, in general, the same trend as for CME-driven storms, although the day-night asymmetry is less prominent: during the early recovery phase, R values are > 1 at the dayside and mostly ~ 1 with few bins of R values slightly less than 1 at the nightside. However, the anisotropy is high during the late recovery phase as evident from larger values of R. Also, during the late recovery phase, R values ~ 1 or < 1 are confined to regions $L > 6$ on the nightside, indicating that flattop/butterfly PADs are found outside $L = 6$ while pancake PADs are found inside $L = 6$.

Discussion and conclusion

The statistical results presented above suggest that there is a dependence of equatorial PADs on electron energy, geomagnetic activity, and spatial location, both radial (L-shell dependence) and azimuthal (MLT dependence). The equatorial PADs of few tens of keV electrons are pancake shaped during all the four phases of geomagnetic storms, although the distributions have higher anisotropy (higher R values) during the main and early recovery phases. For electrons having energy in the range of few to several hundreds of keV, the dayside PADs are mostly pancake shaped while butterfly PADs can be seen at night at higher L-shells. The anisotropy of PADs is also found to increase with geomagnetic activity. All of these results are in good agreement with the previous studies (see e.g., Ni et al. (2015, 2016); Pandya et al. (2020); Zhao et al. (2018, 2020); Greeley et al. (2021); Smirnov et al. (2022)). However, in addition, our results also show prominent influence of storm drivers (CMEs/CIRs) on the PADs of outer radiation belt electrons, especially in the medium (143–226 keV) and high (346–909 keV) energy channels. In general, the pitch angle distributions are found to be more anisotropic for CME-driven storms compared to CIR-driven storms during the storm main and/or early recovery phase.

The dependence of equatorial electron PADs on electron energy and geomagnetic activity has been extensively studied in the past and discussed in details in several papers (e.g., Sibeck et al. (1987); Selesnick and Blake (2002); Korth et al. (1999); Califf et al. (2014, 2017); Zhao et al. (2017, 2018, 2020)). The energy dependence of electron PADs has been attributed to the difference in radial flux gradients of electrons having different energies (see e.g., Zhao et al. (2020) and references therein). The dependence on geomagnetic activity has been explained to happen mostly due to the deformed magnetic field configurations, enhanced wave-particle interactions or/and changes in the electron radial flux gradients during geomagnetic disturbed times (see e.g., Zhao et al. (2018) and references therein). In the discussions that will follow, we will mainly focus on finding a possible explanation for the observed MLT dependence of electron pitch angle distributions.

The MLT dependence of electron PADS are especially found at higher energies and during the storm main phase and/or the early recovery phase. As an example, for CME-driven storms, for 909 keV electrons in the early recovery phase, butterfly PADs can be seen between $L \approx 5$ to 6 and MLT ≈18 to 3, while pancake PADs can be seen at all other MLTs and L-shells (Figure 4). One of the possible mechanism for such MLT dependence is enhanced drift-shell splitting caused by stretched geomagnetic fields during active times. Different processes can cause drift shell splitting, the y-component of the interplanetary magnetic field being one of the potential candidates. The IMF By-component exerts a torque on the magnetosphere, and in response, oppositely directed azimuthal flows occur in the dayside cusp. These azimuthal flows imply that open flux tubes are added asymmetrically to the tail lobes. For IMF $By > 0$, flux tubes are preferentially added to the dawn side and for IMF $By < 0$, flux tubes are preferentially added to the dusk side (Cowley, 1981). This results in an asymmetrical stretching of the geomagnetic field lines and can result in a day-night asymmetry in the pitch angle distribution of higher energy electrons. For the lower energy electrons, drift shell splitting can not generate butterfly PADs as they have positive radial flux gradients at larger L-shells (Zhao et al., 2018, 2020). This is the reason why tens of keV electrons exhibit pancake PADs at all L-shells and MLTs for different storm phases and both the storm drivers (Figure 4).

Other processes that can contribute to geomagnetic field line stretching and drift-shell splitting are magnetic depressions near the equator driven by injection of hot ions during magnetic disturbances due to the diamagnetic effect (e.g., Lyons (1977); Ebihara et al. (2008)); and changes in magnetic field B_z component near the equator (termed as magnetic dip or bz dip) during substorms (e.g., He et al. (2017); Xiong et al. (2017, 2019)). Past studies have reported that magnetic depressions by 50% or more during the storm main phase can produce nightside butterfly PADs, while 20% decrease in magnetic field B_z component can also contribute to these PADs (He et al. (2017); Xia et al. (2017); Xiong et al. (2017)). Xiong et al. (2019) statistically investigated the global distribution of magnetic dip related butterfly PADs of 466 keV and 2.1 MeV electrons using 6 years of Van Allen Probe measurements from 2012 to 2018. They found that the magnetic dip related butterfly PADs are confined mostly in the duskside to midnight sector within $4.5 < L < 6$. In our case, we also found butterfly PADs in the high energy channels (346–909 keV) confined in the nightside MLT sector for regions outside $L = 4.5$. This is consistent with the findings of Xiong et al. (2019), and thus, suggests that the nightside butterfly PADs may have been formed by substorm induced magnetic dips.

Apart from field line stretching and drift shell splitting, some past studies have reported contribution of local wave-particle interactions in the generation of different pitch angle distributions in different MLT sectors. Interaction with chorus and/or magnetosonic waves are known to generate butterfly PADs (e.g., Xiao et al. (2014); Yue et al. (2016)), while drift-resonance of ULF waves with 90° pitch angle electrons can lead to the formation of characteristic pancake PADs (e.g., Xiao et al.

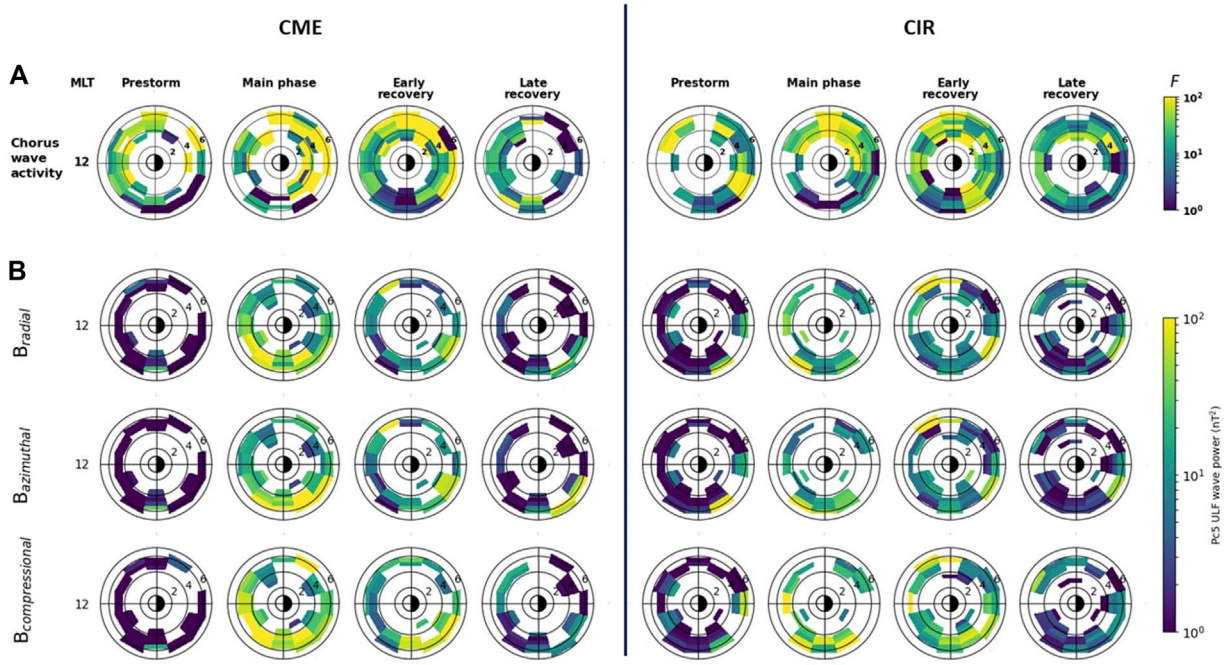

FIGURE 5
(A) L-MLT distribution of average integrated chorus wave excitation factor F during the four storm phases for coronal mass ejection (CME; left panels) and corotating interacting region (CIR; right panels) driven geomagnetic storms in the same manner as in Figures 2–4. The colorbar shows the excitation factor F in logarithmic scale **(B)** L-MLT distribution of ULF waves covering the Pc5 frequency range (2–7 mHz) for the three magnetic field components (radial, azimuthal and compressional) during the four phases of geomagnetic storms driven by CMEs (left panel) and CIRs (right panel). The colorbar at the right represents Pc5 ULF wave power.

(2009b,a, 2012, 2014); Thorne et al. (2013b)). Therefore, in this study, we statistically investigated any possible role of chorus and ULF waves in the observed MLT-dependence of PADs. In Figure 5A, we have shown the chorus wave excitation factor F (as defined in *Methodology*) during all the four storm phases and both the storm drivers. We find that during the early recovery phase of CME-driven storms, chorus wave power increases by almost two orders of magnitude above the background level between MLT = 20 and 10. For CIR-driven storms, during the early recovery phase, the increase in chorus wave power is relatively less intense. This region of enhanced chorus wave power coincides with the region of observed butterfly PADs, and therefore, it suggests that enhanced chorus wave activity might have contributed to the formation of butterfly PADs. In Figure 5B, we have shown the ULF wave power in Pc5 frequency range (2–7 mHz) for three magnetic field components, and during the four storm phases for both the storm drivers. We can see that during the main and early recovery phase of geomagnetic storms driven by both the storm drivers, the ULF wave power increases by almost two orders of magnitude above the pre-storm level, with slightly higher intensity for CME-driven storms than CIR-driven storms. We can also see that the enhancement in ULF wave power is mostly in the post-noon to pre-midnight sector. These observations suggest that Pc5 mode ULF waves might have played a role in the formation of pancake PADs. The results also highlight the difference in PADs between the two storm drivers: both chorus and ULF waves are comparably more intense during CME-driven storms, which might have resulted in the higher anisotropy of both pancake and butterfly PADs (higher R values, Figure 4) during CMEs than CIRs.

From the statistical results of both the electron pitch angle and magnetospheric wave distribution discussed above, although the regions of wave power enhancements during geomagnetic disturbed periods seem to coincide well with the corresponding PAD types, wave-particle interactions resulting the observed MLT dependent PADs does not seem to be a viable explanation. This is because, the MLT dependence is mostly observed at higher energies. An electron with energy 1 MeV at L = 5 will have a drift period of approximately 15 min. Therefore, to create such MLT-dependence, the local processes have to act faster than this drift period. Also, even if such local wave-particle interactions create a particular PAD type, the same distribution will be observed at all other MLTs. Another possibility is that the local processes have to act simultaneously on the electrons to create different PADs at different MLT sectors. As an example, if

the dayside processes make pancake PADs, then the dusk processes will have to change them to butterfly before the electrons drift to the night. Thus, based on these arguments, it seems that the magnetic field line stretching during geomagnetic disturbed times and drift-shell splitting resulted in the observed MLT dependent equatorial electron PADs.

Summary

The major findings from this study can be summarized as follows:

1. Tens of keV (33–80 keV) electrons exhibit mostly pancake PADs at all local times, and do not exhibit significant dependence on storm phases and storm drivers (CMEs/CIRs).
2. Few hundreds of keV (143–226 keV) electrons exhibit clear storm phase and storm driver dependence. For CME-driven storms during the prestorm and main phase, electrons have mostly pancake PADs; during the early recovery phase, the dayside PADs are pancake while nightside PADs are flattop; and during the late recovery phase, PADs again become mostly pancake shaped. For CIR-driven storms, the PADs during pre-storm and recovery phases are mostly pancake, while during the main phase, flattop PADs can be seen at around dusk and dawn, with enhanced anisotropy during the early and late recovery phases.
3. Several hundreds of keV (346–909 keV) electrons exhibit mostly pancake PADs on the dayside and butterfly PADs on the nightside, and show clear dependence on storm phases and storm drivers: for CME-driven storms during the pre-storm phase, these electrons exhibit pancake PADs on the dayside and flattop/butterfly PADs on the nightside; during the main phase, most of the PADs are pancake shaped; during the early recovery phase, they exhibit pancake PADs at the dayside and butterfly PADs at the nightside; and during the late recovery phase, they exhibit pancake PADs at the dayside and flattop PADs at the nightside at higher L-shells. For CIR-driven storms, which are overall less intensive than CME-driven storms, although the overall distribution remains almost similar to those during CME-driven storms, the PADs are less anisotropic (lower R values) compared to CME-driven storms during the main and recovery phases.
4. Magnetic field line stretching and drift-shell splitting during disturbed times resulted in the MLT dependent PAD of 346–909 keV electrons.

Data availability statement

Publicly available datasets were analyzed in this study. This data can be found here: https://cdaweb.gsfc.nasa.gov/cgi-bin/eval2.cgi, http://emfisis.physics.uiowa.edu/Flight/, http://www.rbsp-ect.lanl.gov/data_pub/, http://www.space.umn.edu/rbspefw-data/.

Author contributions

SC did all the analyses and wrote the paper under the supervision of DC. IJR helped in understanding the role of ULF waves in driving pitch angle anisotropy in the radiation belts. GDR helped in the interpretation and presentation of the results. DNB provided valuable comments on the paper.

Funding

SC is supported in part by STFC Grant ST/V006320/1 and NERC Grants NE/V002554/2 and NE/P017185/2, and in part by the Department of Space, Government of India. DC is supported by the Department of Space, Government of India. IJR is supported in part by STFC Grant ST/V006320/1 and NERC Grants NE/V002554/2 and NE/P017185/2.

Acknowledgments

The interplanetary parameters and geomagnetic indices are obtained from the website (https://cdaweb.gsfc.nasa.gov/cgi-bin/eval2.cgi). The Van Allen Probe data used in this study are available at the websites (http://emfisis.physics.uiowa.edu/Flight/ for EMFISIS, http://www.rbsp-ect.lanl.gov/data-pub/for ECT, and http://www.space.umn.edu/rbspefw-data/for EFW). The authors thank all of the MagEIS and EMFISIS teams of the Van Allen Probe for the data.

Conflict of interest

The authors declare that the research was conducted in the absence of any commercial or financial relationships that could be construed as a potential conflict of interest.

Publisher's note

Supplementary material

The Supplementary Material for this article can be found online at: https://www.frontiersin.org/articles/10.3389/fspas.2022.986061/full#supplementary-material

References

Asnes, A., Friedel, R. W., Stadsnes, J., Thomsen, M., Østgaard, N., and Cayton, T. (2005). Statistical pitch angle properties of substorm-injected electron clouds and their relation to dawnside energetic electron precipitation. *J. Geophys. Res.* 110, A05207. doi:10.1029/2004JA010838

Baker, D., and Kanekal, S. (2008). Solar cycle changes, geomagnetic variations, and energetic particle properties in the inner magnetosphere. *J. Atmos. Solar-Terrestrial Phys.* 70, 195–206. doi:10.1016/j.jastp.2007.08.031

Baker, D. N., Jaynes, A. N., Hoxie, V. C., Thorne, R. M., Foster, J. C., Li, X., et al. (2014a). An impenetrable barrier to ultrarelativistic electrons in the Van Allen radiation belts. *Nature* 515, 531–534. doi:10.1038/nature13956

Baker, D. N., Jaynes, A. N., Li, X., Henderson, M. G., Kanekal, S. G., Reeves, G. D., et al. (2014b). Gradual diffusion and punctuated phase space density enhancements of highly relativistic electrons: Van Allen Probes observations. *Geophys. Res. Lett.* 41, 1351–1358. doi:10.1002/2013GL058942

Baker, D. N., Kanekal, S. G., Hoxie, V. C., Henderson, M. G., Li, X., Spence, H. E., et al. (2013). A long-lived relativistic electron storage ring embedded in Earth's outer van allen belt. *Science* 340, 186–190. doi:10.1126/science.1233518

Balasis, G., Daglis, I. A., Georgiou, M., Papadimitriou, C., and Haagmans, R. (2013). Magnetospheric ULF wave studies in the frame of swarm mission: A time-frequency analysis tool for automated detection of pulsations in magnetic and electric field observations. *Earth Planets Space* 65, 1385–1398. doi:10.5047/eps.2013.10.003

Bingham, S. T., Mouikis, C. G., Kistler, L. M., Paulson, K. W., Farrugia, C. J., Huang, C. L., et al. (2019). The storm time development of source electrons and chorus wave activity during CME- and CIR-driven storms. *JGR. Space Phys.* 124, 6438–6452. doi:10.1029/2019JA026689

Blake, J. B., Carranza, P. A., Claudepierre, S. G., Clemmons, J. H., Crain, W. R., Jr., Dotan, Y., et al. (2013). The magnetic electron ion spectrometer (MagEIS) instruments aboard the radiation belt storm probes (RBSP) spacecraft. *Space Sci. Rev.* 179, 383–421. doi:10.1007/s11214-013-9991-8

Blum, L. W., Halford, A., Millan, R., Bonnell, J. W., Goldstein, J., Usanova, M., et al. (2015). Observations of coincident EMIC wave activity and duskside energetic electron precipitation on 18–19 January 2013. *Geophys. Res. Lett.* 42, 5727–5735. doi:10.1002/2015GL065245

Bortnik, J., Thorne, R. M., O'Brien, T. P., Green, J. C., Strangeway, R. J., Shprits, Y. Y., et al. (2006). Observation of two distinct, rapid loss mechanisms during the 20 November 2003 radiation belt dropout event. *J. Geophys. Res.* 111, A12216. doi:10.1029/2006JA011802

Boyd, A. J., Spence, H. E., Huang, C.-L., Reeves, G. D., Baker, D. N., Turner, D. L., et al. (2016). Statistical properties of the radiation belt seed population. *J. Geophys. Res. Space Phys.* 121, 7636–7646. doi:10.1002/2016JA022652

Califf, S., Li, X., Blum, L., Jaynes, A., Schiller, Q., Zhao, H., et al. (2014). THEMIS measurements of quasi-static electric fields in the inner magnetosphere. *JGR. Space Phys.* 119, 9939–9951. doi:10.1002/2014JA020360

Califf, S., Li, X., Zhao, H., Kellerman, A., Sarris, T. E., Jaynes, A., et al. (2017). The role of the convection electric field in filling the slot region between the inner and outer radiation belts. *JGR. Space Phys.* 122, 2051–2068. doi:10.1002/2016JA023657

Chakraborty, S., Chakrabarty, D., Reeves, G. D., Baker, D. N., Claudepierre, S. G., Breneman, A. W., et al. (2021). Van allen probe observations of disappearance, recovery and patchiness of plasmaspheric hiss following two consecutive interplanetary shocks: First results. *JGR. Space Phys.* 126. doi:10.1029/2020JA028873

Chen, Y., Friedel, R. H. W., Henderson, M. G., Claudepierre, S. G., Morley, S. K., and Spence, H. E. (2014). Repad: An empirical model of pitch angle distributions for energetic electrons in the Earth's outer radiation belt. *J. Geophys. Res. Space Phys.* 119, 1693–1708. doi:10.1002/2013JA019431

Claudepierre, S. G., Mann, I. R., Takahashi, K., Fennell, J. F., Hudson, M. K., Blake, J. B., et al. (2013). Van Allen Probes observation of localized drift resonance between poloidal mode ultra-low frequency waves and 60 keV electrons. *Geophys. Res. Lett.* 40, 4491–4497. doi:10.1002/grl.50901

Cohen, I. J., Turner, D. L., Michael, A. T., Sorathia, K. A., and Ukhorskiy, A. Y. (2021). Investigating the link between outer radiation belt losses and energetic electron escape at the magnetopause: A case study using multi-mission observations and simulations. *JGR. Space Phys.* 126. doi:10.1029/2021JA029261

Cowley, S. (1981). Magnetospheric asymmetries associated with the y-component of the IMF. *Planet. Space Sci.* 29, 79–96. doi:10.1016/0032-0633(81)90141-0

Ebihara, Y., Fok, M.-C., Blake, J. B., and Fennell, J. F. (2008). Magnetic coupling of the ring current and the radiation belt. *J. Geophys. Res.* 113. doi:10.1029/2008JA013267

Elkington, S. R., Hudson, M. K., and Chan, A. A. (2003). Resonant acceleration and diffusion of outer zone electrons in an asymmetric geomagnetic field. *J. Geophys. Res.* 108, 1116. doi:10.1029/2001JA009202

Foster, J. C., Wygant, J. R., Hudson, M. K., Boyd, A. J., Baker, D. N., Erickson, P. J., et al. (2015). Shock-induced prompt relativistic electron acceleration in the inner magnetosphere. *J. Geophys. Res. Space Phys.* 120, 1661–1674. doi:10.1002/2014JA020642

Friedel, R. H. W., Bourdarie, S., and Cayton, T. E. (2005). Intercalibration of magnetospheric energetic electron data. *Space weather.* 3. doi:10.1029/2005SW000153

Gannon, J. L., Li, X., and Heynderickx, D. (2007). Pitch angle distribution analysis of radiation belt electrons based on Combined Release and Radiation Effects Satellite Medium Electrons A data. *J. Geophys. Res.* 112. doi:10.1029/2005JA011565

Garcia, H. (1996). Energetic electron pitch angle distribution parameters at 6.6Re, as deduced from GOES X-ray observations. *Planet. Space Sci.* 44, 473–484. doi:10.1016/0032-0633(95)00144-1

Grandin, M., Aikio, A. T., and Kozlovsky, A. (2019). Properties and geoeffectiveness of solar wind high-speed streams and stream interaction regions during solar cycles 23 and 24. *J. Geophys. Res. Space Phys.* 124, 3871–3892. doi:10.1029/2018JA026396

Greeley, A. D., Kanekal, S. G., Sibeck, D. G., Schiller, Q., and Baker, D. N. (2021). Evolution of pitch angle distributions of relativistic electrons during geomagnetic storms: Van allen probes observations. *J. Geophys. Res. Space Phys.* 126. doi:10.1029/2020JA028335

He, Z., Chen, L., Zhu, H., Xia, Z., Reeves, G. D., Xiong, Y., et al. (2017). Multiple-satellite observation of magnetic dip event during the substorm on 10 october 2013. *Geophys. Res. Lett.* 44, 9167–9175. doi:10.1002/2017GL074869

Horne, R. B., Meredith, N. P., Thorne, R. M., Heynderickx, D., Iles, R. H. A., and Anderson, R. R. (2003). Evolution of energetic electron pitch angle distributions during storm time electron acceleration to megaelectronvolt energies. *J. Geophys. Res.* 108, 1016. doi:10.1029/2001JA009165

Horne, R. B., Thorne, R. M., Glauert, S. A., Albert, J. M., Meredith, N. P., and Anderson, R. R. (2005). Timescale for radiation belt electron acceleration by whistler mode chorus waves. *J. Geophys. Res.* 110, A03225. doi:10.1029/2004JA010811

Kanekal, S. G., Baker, D. N., Fennell, J. F., Jones, A., Schiller, Q., Richardson, I. G., et al. (2016). Prompt acceleration of magnetospheric electrons to ultrarelativistic energies by the 17 March 2015 interplanetary shock. *J. Geophys. Res. Space Phys.* 121, 7622–7635. doi:10.1002/2016JA022596

Kletzing, C. A., Kurth, W. S., Acuna, M., MacDowall, R. J., Torbert, R. B., Averkamp, T., et al. (2013). The electric and magnetic field instrument suite and integrated science (EMFISIS) on RBSP. *Space Sci. Rev.* 179, 127–181. doi:10.1007/s11214-013-9993-6

Korth, H., Thomsen, M. F., Borovsky, J. E., and McComas, D. J. (1999). Plasma sheet access to geosynchronous orbit. *J. Geophys. Res.* 104, 25047–25061. doi:10.1029/1999JA900292

Lee, D.-Y., Shin, D.-K., Kim, J.-H., Cho, J.-H., Kim, K.-C., Hwang, J. A., et al. (2013). Long-term loss and re-formation of the outer radiation belt. *JGR. Space Phys.* 118, 3297–3313. doi:10.1002/jgra.50357

Li, J., Bortnik, J., Thorne, R. M., Li, W., Ma, Q., Baker, D. N., et al. (2016). Ultrarelativistic electron butterfly distributions created by parallel acceleration due to magnetosonic waves. *JGR. Space Phys.* 121, 3212–3222. doi:10.1002/2016JA022370

Li, X., Baker, D. N., Temerin, M., Cayton, T. E., Reeves, E. G. D., Christensen, R. A., et al. (1997). Multisatellite observations of the outer zone electron variation during the November 3–4, 1993, magnetic storm. *J. Geophys. Res.* 102, 14123–14140. doi:10.1029/97JA01101

Lyons, L. R. (1977). Adiabatic evolution of trapped particle pitch angle distributions during a storm main phase. *J. Geophys. Res.* 82, 2428–2432. doi:10.1029/JA082i016p02428

Ma, Q., Li, W., Thorne, R. M., Ni, B., Kletzing, C. A., Kurth, W. S., et al. (2015). Modeling inward diffusion and slow decay of energetic electrons in the Earth's outer radiation belt. *Geophys. Res. Lett.* 42, 987–995. doi:10.1002/2014GL062977

Mauk, B. H., Fox, N. J., Kanekal, S. G., Kessel, R. L., Sibeck, D. G., and Ukhorskiy, A. (2013). Science objectives and rationale for the radiation belt storm probes mission. *Space Sci. Rev.* 179, 3–27. doi:10.1007/s11214-012-9908-y

Meredith, N. P., Thorne, R. M., Horne, R. B., Summers, D., Fraser, B. J., and Anderson, R. R. (2003). Statistical analysis of relativistic electron energies for cyclotron resonance with EMIC waves observed on CRRES. *J. Geophys. Res.* 108, 1250. doi:10.1029/2002JA009700

Ni, B., Bortnik, J., Thorne, R. M., Ma, Q., and Chen, L. (2013). Resonant scattering and resultant pitch angle evolution of relativistic electrons by plasmaspheric hiss. *JGR. Space Phys.* 118, 7740–7751. doi:10.1002/2013JA019260

Ni, B., Zou, Z., Gu, X., Zhou, C., Thorne, R. M., Bortnik, J., et al. (2015). Variability of the pitch angle distribution of radiation belt ultrarelativistic electrons during and following intense geomagnetic storms: Van Allen Probes observations. *JGR. Space Phys.* 120, 4863–4876. doi:10.1002/2015JA021065

Ni, B., Zou, Z., Li, X., Bortnik, J., Xie, L., and Gu, X. (2016). Occurrence characteristics of outer zone relativistic electron butterfly distribution: A survey of van allen probes REPT measurements. *Geophys. Res. Lett.* 43, 5644–5652. doi:10.1002/2016GL069350

Pandya, M., Bhaskara, V., Ebihara, Y., Kanekal, S. G., and Baker, D. N. (2020). Evolution of pitch angle-distributed megaelectron volt electrons during each phase of the geomagnetic storm. *JGR. Space Phys.* 125. doi:10.1029/2019JA027086

Reeves, G. D., Baker, D. N., Belian, R. D., Blake, J. B., Cayton, T. E., Fennell, J. F., et al. (1998). The global response of relativistic radiation belt electrons to the January 1997 magnetic cloud. *Geophys. Res. Lett.* 25, 3265–3268. doi:10.1029/98GL02509

Reeves, G. D., McAdams, K. L., Friedel, R. H. W., and O'Brien, T. P. (2003). Acceleration and loss of relativistic electrons during geomagnetic storms. *Geophys. Res. Lett.* 30. doi:10.1029/2002GL016513

Reeves, G. D., Spence, H. E., Henderson, M. G., Morley, S. K., Friedel, R. H. W., Funsten, H. O., et al. (2013). Electron acceleration in the heart of the van allen radiation belts. *Science* 341, 991–994. doi:10.1126/science.1237743

Reidy, J. A., Horne, R. B., Glauert, S. A., Clilverd, M. A., Meredith, N. P., Woodfield, E. E., et al. (2021). Comparing electron precipitation fluxes calculated from pitch angle diffusion coefficients to LEO satellite observations. *JGR. Space Phys.* 126. doi:10.1029/2020JA028410

Rodger, C. J., Clilverd, M. A., Thomson, N. R., Gamble, R. J., Seppälä, A., Turunen, E., et al. (2007). Radiation belt electron precipitation into the atmosphere: Recovery from a geomagnetic storm. *J. Geophys. Res.* 112. doi:10.1029/2007JA012383

Schulz, M., and Lanzerotti, L. (1974). *Particle diffusion in the radiation belts*. New York: Springer. doi:10.1007/978-3-642-65675-0

Selesnick, R. S., and Blake, J. B. (2002). Relativistic electron drift shell splitting. *J. Geophys. Res.* 107, 1265. doi:10.1029/2001JA009179

Shi, R., Summers, D., Ni, B., Fennell, J. F., Blake, J. B., Spence, H. E., et al. (2016). Survey of radiation belt energetic electron pitch angle distributions based on the Van Allen Probes MagEIS measurements. *J. Geophys. Res. Space Phys.* 121, 1078–1090. doi:10.1002/2015JA021724

Shprits, Y. Y., Kellerman, A., Aseev, N., Drozdov, A. Y., and Michaelis, I. (2017). Multi-MeV electron loss in the heart of the radiation belts. *Geophys. Res. Lett.* 44, 1204–1209. doi:10.1002/2016GL072258

Shprits, Y. Y., Thorne, R. M., Friedel, R., Reeves, G. D., Fennell, J., Baker, D. N., et al. (2006). Outward radial diffusion driven by losses at magnetopause. *J. Geophys. Res.* 111, A11214. doi:10.1029/2006JA011657

Sibeck, D. G., McEntire, R. W., Lui, A. T. Y., Lopez, R. E., and Krimigis, S. M. (1987). Magnetic field drift shell splitting: Cause of unusual dayside particle pitch angle distributions during storms and substorms. *J. Geophys. Res.* 92, 13485–13497. doi:10.1029/JA092iA12p13485

Smirnov, A., Shprits, Y., Allison, H., Aseev, N., Drozdov, A., Kollmann, P., et al. (2022). Storm-time evolution of the equatorial electron pitch angle distributions in Earth's outer radiation belt. *Front. Astron. Space Sci.* 9. doi:10.3389/fspas.2022.836811

Southwood, D. J., and Kivelson, M. G. (1981). Charged particle behavior in low-frequency geomagnetic pulsations 1. transverse waves. *J. Geophys. Res.* 86, 5643–5655. doi:10.1029/JA086iA07p05643

Spence, H. E., Reeves, G. D., Baker, D. N., Blake, J. B., Bolton, M., Bourdarie, S., et al. (2013). Science goals and overview of the radiation belt storm probes (RBSP) energetic particle, composition, and thermal Plasma (ECT) suite on NASA's van allen probes mission. *Space Sci. Rev.* 179, 311–336. doi:10.1007/s11214-013-0007-5

Staples, F. A., Rae, I. J., Forsyth, C., Smith, A. R. A., Murphy, K. R., Raymer, K. M., et al. (2020). Do statistical models capture the dynamics of the magnetopause during sudden magnetospheric compressions? *J. Geophys. Res. Space Phys.* 125. doi:10.1029/2019JA027289

Summers, D., and Thorne, R. M. (2003). Relativistic electron pitch-angle scattering by electromagnetic ion cyclotron waves during geomagnetic storms. *J. Geophys. Res.* 108, 1143. doi:10.1029/2002JA009489

Summers, D., Thorne, R. M., and Xiao, F. (1998). Relativistic theory of wave-particle resonant diffusion with application to electron acceleration in the magnetosphere. *J. Geophys. Res.* 103, 20487–20500. doi:10.1029/98JA01740

Takahashi, K., Mcentire, R. W., Lui, A. T. Y., and Potemra, T. A. (1990). Ion flux oscillations associated with a radially polarized transverse Pc 5 magnetic pulsation. *J. Geophys. Res.* 95, 3717–3731. doi:10.1029/JA095iA04p03717

Thorne, R. M. (1977). Energetic radiation belt electron precipitation: A natural depletion mechanism for stratospheric ozone. *Science* 195, 287–289. doi:10.1126/science.195.4275.287

Thorne, R. M., Li, W., Ni, B., Ma, Q., Bortnik, J., Baker, D. N., et al. (2013a). Evolution and slow decay of an unusual narrow ring of relativistic electrons near L ~ 3.2 following the September 2012 magnetic storm. *Geophys. Res. Lett.* 40, 3507–3511. doi:10.1002/grl.50627

Thorne, R. M., Li, W., Ni, B., Ma, Q., Bortnik, J., Chen, L., et al. (2013b). Rapid local acceleration of relativistic radiation-belt electrons by magnetospheric chorus. *Nature* 504, 411–414. doi:10.1038/nature12889

Thorne, R. M., Li, W., Ni, B., Ma, Q., Bortnik, J., Chen, L., et al. (2013c). Rapid local acceleration of relativistic radiation-belt electrons by magnetospheric chorus. *Nature* 504, 411–414. doi:10.1038/nature12889

Thorne, R. M. (2010). Radiation belt dynamics: The importance of wave-particle interactions. *Geophys. Res. Lett.* 37. doi:10.1029/2010GL044990

Tsyganenko, N. (1989). A magnetospheric magnetic field model with a warped tail current sheet. *Planet. Space Sci.* 37, 5–20. doi:10.1016/0032-0633(89)90066-4

Turner, D. L., Sphrits, Y., Hartinger, M., and Angelopoulos, V. (2012). Explaining sudden losses of outer radiation belt electrons during geomagnetic storms. *Nat. Phys.* 8, 208–212. doi:10.1038/nphys2185

Ukhorskiy, A. Y., Anderson, B. J., Brandt, P. C., and Tsyganenko, N. A. (2006). Storm time evolution of the outer radiation belt: Transport and losses. *J. Geophys. Res.* 111, A11S03. doi:10.1029/2006JA011690

Ukhorskiy, A. Y., Sitnov, M. I., Takahashi, K., and Anderson, B. J. (2009). Radial transport of radiation belt electrons due to stormtime Pc5 waves. *Ann. Geophys.* 27, 2173–2181. doi:10.5194/angeo-27-2173-2009

Vampola, A. (1997). "Outer zone energetic electron environment update," in Conference on the High Energy Radiation Background in Space. Workshop Record, 128–136. doi:10.1109/CHERBS.1997.660263

West, H. I., Jr., Buck, R. M., and Walton, J. R. (1973). Electron pitch angle distributions throughout the magnetosphere as observed on Ogo 5. *J. Geophys. Res.* 78, 1064–1081. doi:10.1029/JA078i007p01064

Xia, Z., Chen, L., Zheng, L., and Chan, A. A. (2017). Eigenmode analysis of compressional poloidal modes in a self-consistent magnetic field. *JGR. Space Phys.* 122 (10369–10), 381. doi:10.1002/2017JA024376

Xiao, F., Su, Z., Zheng, H., and Wang, S. (2009a). Modeling of outer radiation belt electrons by multidimensional diffusion process. *J. Geophys. Res.* 114. doi:10.1029/2008JA013580

Xiao, F., Yang, C., He, Z., Su, Z., Zhou, Q., He, Y., et al. (2014). Chorus acceleration of radiation belt relativistic electrons during March 2013 geomagnetic storm. *J. Geophys. Res. Space Phys.* 119, 3325–3332. doi:10.1002/2014JA019822

Xiao, F., Zhang, S., Su, Z., He, Z., and Tang, L. (2012). Rapid acceleration of radiation belt energetic electrons by Z-mode waves. *Geophys. Res. Lett.* 39. doi:10.1029/2011GL050625

Xiao, F., Zong, Q.-G., and Chen, L. (2009b). Pitch-angle distribution evolution of energetic electrons in the inner radiation belt and slot region during the 2003 Halloween storm. *J. Geophys. Res.* 114. doi:10.1029/2008JA013068

Xiong, Y., Chen, L., Xie, L., Fu, S., Xia, Z., and Pu, Z. (2017). Relativistic electron's butterfly pitch angle distribution modulated by localized background magnetic field perturbation driven by hot ring current ions. *Geophys. Res. Lett.* 44, 4393–4400. doi:10.1002/2017GL072558

Xiong, Y., Xie, L., Fu, S., and Pu, Z. (2019). Statistical study of energetic electron butterfly pitch angle distributions during magnetic dip events. *Geophys. Res. Lett.* 46, 13621–13629. doi:10.1029/2019GL085091

Yu, Y., Koller, J., and Morley, S. K. (2013). Quantifying the effect of magnetopause shadowing on electron radiation belt dropouts. *Ann. Geophys.* 31, 1929–1939. doi:10.5194/angeo-31-1929-2013

Yue, C., An, X., Bortnik, J., Ma, Q., Li, W., Thorne, R. M., et al. (2016). The relationship between the macroscopic state of electrons and the properties of chorus

waves observed by the Van Allen Probes. *Geophys. Res. Lett.* 43, 7804–7812. doi:10.1002/2016GL070084

Zhao, H., Baker, D. N., Califf, S., Li, X., Jaynes, A. N., Leonard, T., et al. (2017). Van allen probes measurements of energetic particle deep penetration into the low L region (L < 4) during the storm on 8 april 2016. *JGR. Space Phys.* 122 (12), 140–152. doi:10.1002/2017JA024558

Zhao, H., Friedel, R. H. W., Chen, Y., Baker, D. N., Li, X., Malaspina, D. M., et al. (2020). Equatorial pitch angle distributions of 1–50 keV electrons in Earth's inner magnetosphere: An empirical model based on the van allen probes observations. *JGR. Space Phys.* 126. doi:10.1029/2020JA028322

Zhao, H., Friedel, R. H. W., Chen, Y., Reeves, G. D., Baker, D. N., Li, X., et al. (2018). An empirical model of radiation belt electron pitch angle distributions based on van allen probes measurements. *JGR. Space Phys.* 123, 3493–3511. doi:10.1029/2018JA025277

Zong, Q.-G., Rankin, R., and Zhou, X. (2017). The interaction of ultra-low-frequency pc3-5 waves with charged particles in Earth's magnetosphere. *Rev. Mod. Plasma Phys.* 1, 10. doi:10.1007/s41614-017-0011-4

Zong, Q.-G., Zhou, X.-Z., Wang, Y. F., Li, X., Song, P., Baker, D. N., et al. (2009). Energetic electron response to ULF waves induced by interplanetary shocks in the outer radiation belt. *J. Geophys. Res.* 114. doi:10.1029/2009JA014393

frontiers | Frontiers in Astronomy and Space Sciences

TYPE Original Research
PUBLISHED 07 September 2022
DOI 10.3389/fspas.2022.981949

OPEN ACCESS

EDITED BY
Yoshiharu Omura,
Kyoto University, Japan

REVIEWED BY
Xueyi Wang,
Auburn University, United States
Shinji Saito,
National Institute of Information and Communications Technology, Japan

*CORRESPONDENCE
Vijay Harid,
vijay.harid@ucdenver.edu

SPECIALTY SECTION
This article was submitted to Space Physics,
a section of the journal
Frontiers in Astronomy and Space Sciences

RECEIVED 29 June 2022
ACCEPTED 09 August 2022
PUBLISHED 07 September 2022

CITATION
Harid V, Gołkowski M, Hosseini P and Kim H (2022), Backward-propagating source as a component of rising tone whistler-mode chorus generation. *Front. Astron. Space Sci.* 9:981949. doi: 10.3389/fspas.2022.981949

Backward-propagating source as a component of rising tone whistler-mode chorus generation

Vijay Harid[1]*, Mark Gołkowski[1], Poorya Hosseini[2] and Hoyoung Kim[3]

[1]Department of Electrical Engineering, University of Colorado Denver, Denver, CO, United States, [2]Space Exploration Sector, The Johns Hopkins University Applied Physics Laboratory, Laurel, MD, United States, [3]Space Sciences Laboratory, University of California, Berkeley, Berkeley, CA, United States

Whistler-mode chorus waves in the magnetosphere play a crucial role in space weather *via* wave–particle interactions. The past two decades have observed tremendous advances in theory and simulations of chorus generation; however, several details of the generation mechanism are still actively contended. To simulate chorus generation, a new envelope particle-in-cell code is introduced. The model produces a rising tone chorus element in a parabolic geomagnetic field. The initial chorus element "embryo" frequency is shown to initialize near the equator at the frequency of maximum linear growth. A backward resonant current is then observed to propagate upstream of the equator. The trajectory of the backward current follows that of a freely falling electron that has been de-trapped at the equator superimposed with forward motion at the group velocity. The backward current iteratively radiates a rising tone element where the highest frequency components are generated furthest upstream. The work provides new advancements in modeling chorus and corroborates other recent work that has also demonstrated a backward-moving source during the generation of coherent whistler-mode waves.

KEYWORDS

magnetospheric chorus, particle–in-cell (PIC) simulation, wave generation, gyro-resonant interactions, electron de-trapping

Introduction

Whistler-mode waves in the near-Earth space environment play an essential role in space weather dynamics (Ripoll et al., 2020). Of particular interest are magnetospheric whistler-mode chorus waves in the extremely low and very low frequency radio bands (< 30 kHz). Chorus typically consists of discrete rising (and sometimes falling) frequency tones and is most often observed in the dawn sector with the highest intensities (Meredith et al., 2012). Chorus is believed to be responsible for many important physical phenomena such as relativistic microbursts (Mozer et al., 2018), acceleration of "killer" electrons (Horne, 2007), and as a source of plasmaspheric hiss (Bortnik et al., 2008). As such, an

accurate understanding of the physical mechanisms that drive the generation of chorus waves is critical for space weather modeling.

The generation of chorus waves is well-known to be a consequence of the Doppler-shifted cyclotron instability, also known as the gyro-resonant instability (Helliwell, 1967; Nunn, 1974; Inan et al., 1978; Bell, 1984; Omura et al., 1991). Physically, counter-streaming geomagnetically trapped electrons can resonate with the circularly polarized whistler-mode waves when their intrinsic spiral motion (due to the background magnetic field) moves in unison with the polarization vector of the waves. This allows for considerable energy and momentum exchange since the resonant particles effectively observe a static wave field in their frame of reference. Specifically, the first-order resonance velocity of electrons is given by

$$v_r = \frac{\omega_c - \omega}{k}. \quad (1)$$

The quantities ω_c, ω, and k correspond to the gyrofrequency, the wave frequency, and the whistler-mode wavenumber, respectively. It should be noted that in this convention the resonance velocity is assumed to be positive (unlike the work by Omura et al. (2008)) in the presence of parallel propagating whistler-mode waves (same as Gołkowski and Gibby, 2017; Harid et al., 2014a; Harid et al., 2014b; Hosseini et al., 2019). The gyro-resonant mechanism is the starting point for analyzing and modeling the production of chorus waves.

The most common method of quantifying instabilities in plasmas is *via* the linear growth theory (Stix, 1992). In the case of whistler-mode waves, it can be shown that temperature anisotropy is the underlying mechanism by which waves can be generated (Kennel and Petschek, 1966). If the electron temperature perpendicular to the magnetic field is sufficiently higher than the parallel temperature, this anisotropy acts as a source of free energy and can amplify any random noise in the system. However, the linear approach only describes the initial stages of wave growth and not necessarily the evolution of the wave fields once the amplitudes are high enough to initiate nonlinear phenomena.

As far back as the 1970s, the generation mechanism of discrete VLF emissions was understood by theoreticians to be nonlinear in origin (Dysthe, 1971; Nunn, 1974; Roux and Pellat, 1978; Matsumoto, 1979). Given the high coherence of chorus waves, the wave–particle interaction process can be simplified by considering a quasi-monochromatic whistler-mode wave. It can be shown that particles with velocities that are close enough to the resonance velocity can be phase-trapped in the effective potential associated with the wave magnetic field (Inan et al., 1978; Bell, 1984; Omura et al., 1991; Albert, 2002). The phase-trapped particles are forced to stay in resonance with the wave over large spatial scales, and this effect is generally believed to be responsible for the generation of chorus. Even so, the detailed dynamics of phase-trapped particles during the wave generation process is still actively researched despite several decades of analysis (Trakhtengerts, 1999; Tao et al., 2017; Omura, 2021; Zonca et al., 2022). A key outstanding question is at what stage in the trapping process are the amplifying currents formed.

Prior to discussing the contemporary models of chorus generation, it is fruitful to provide some historical context behind their development. The earliest model describing the generation of chorus (and triggered emissions) was put forth by Helliwell (1967). In this framework, each wave frequency component is generated by electrons that are in adiabatic motion under the assumption that these particles are simultaneously in resonance. This phenomenological model is often referred to as the "consistent-wave" condition in the literature. Although the model describes many of the frequency-time features of VLF emissions, the original work was criticized as not rigorous in terms of failing to consider more realistic non-beam-like distributions and the effect of the geomagnetic inhomogeneity (Nunn et al., 1997). Moreover, 11 years after the work by Helliwell, Roux and Pellat (1978) described a model in which the frequency sweeps of VLF emissions are triggered by de-trapped particles at the back end of a whistler-mode wavepacket. The results bridged the lack of rigor from Helliwell's original theory with fundamental plasma physics; however, the model relied on the existence of a triggering wave, and it is not immediately clear if it can be applied to naturally generated chorus waves. A few years later, Vomvoridis et al. (1982) put forth a model that showed frequency change as proportional to wave amplitude *via* self-consistently maintaining an inhomogeneity ratio that maximizes wave growth *via* phase-trapping. However, just as in the work by Roux and Pellat, the theory of Vomvordis et al. also relied on the existence of a triggering wave. Furthermore, although the model assumed that frequency change could occur, an explanation for why the emissions occur was somewhat lacking. Since then, several prominent researchers have spent considerable effort expanding the theories and developing complex simulations of chorus based on fundamental physical equations (Trakhtengerts, 1999; Omura et al., 2008; Nunn et al., 2009; Summers et al., 2012; Crabtree et al., 2017).

By the mid-2000s, much of the work on nonlinear wave generation focused on a single theory based on an optimum wave amplitude and sweep rate (summarized in Omura, 2021). This theory relies on the creation of a phase-space "electron–hole" by trapped electrons with a shape that enforces resonant currents that maximize wave growth. In particular, the theory assumes that the rising tone chorus emission is generated exactly at the equator, which allows for a simple expression for the frequency sweep rate in terms of optimal wave amplitude (similar to Vomvoridis et al., 1982). Simultaneously, it is assumed that the wave amplitude is naturally optimized to not only grow at the fastest rate but also to sustain a sweep rate that permits the fastest growth *via* the resonant current component aligned with the wave magnetic field (Katoh and Omura, 2011). With all these

simplifications, the final theory results in the so-called "chorus equations" (Summers et al., 2012) directly simulated these equations and showed the formation of rising tones, similar to the morphology of chorus. Unlike the work by Helliwell (1967) and Roux and Pellat (1978), this model does not require the de-trapping of resonant particles nor does it require a triggered wave. A concern with this model, however, is that several simulations show that parts of the rising frequency chorus elements (and rising tone-triggered emissions) seem to occur upstream of the equator which violates the assumption of the theory (Hikishima et al., 2009; Tao et al., 2017; Nogi and Omura, 2022). Nevertheless, it provides a strong foundation for building future theoretical developments.

Recently, Tao et al. (2021) proposed the "trap-release-amplify" (TaRA) model of chorus generation. Specifically, they propose that a chorus wavepacket initiates at the equator and traps resonant particles. These resonant particles are released from the back end of the wave and then selectively generate a narrowband emission in accordance with the frequency that corresponds to maximum power transfer. The process continues in succession upstream and produces the entire chorus element. This element then propagates downstream and is sustained and distorted by nonlinear amplification, leading to a subpacket structure. An interesting aspect of their model is that it combines the consistent-wave theory of Helliwell (1967), the de-trapping of Roux and Pellat, (1978), and the optimum wave feature of Vomvoridis et al. (1982) and Katoh and Omura, (2011). Their work is an important step toward updating and unifying the theory of whistler-mode chorus generation.

Most recently, Nogi and Omura, (2022) demonstrated that triggered whistler-mode waves are generated *via* a backward-moving source. Specifically, the authors used a full-scale PIC code to model the triggering of whistler-mode waves due to an enforced coherent current source at the equator. They showed that the initial seed waves trapped resonant electrons upstream which are then released upstream. The released electrons then become phase-organized and radiate a new wavepacket at a higher frequency. The velocity of the backward-moving source wave is determined to be the difference in magnitude between the resonance velocity and group velocity (assuming that the wave and electrons are counter-streaming). This process continues in succession to generate the triggered emission. The emission itself is then sustained during propagation by the formation of a stable phase-space hole, which has also been identified by other researchers over the past decade (Omura et al., 2008; Nunn and Omura, 2012; Harid et al., 2014b; Gołkowski et al., 2019; Tao et al., 2021). Although the results are catered toward triggered VLF emissions, much of the analysis readily transfers over to the generation of whistler-mode chorus as well.

The work presented here reinforces a backward-moving source as an important mechanism of rising tone chorus element generation, which is a blend of the results by Tao et al. (2021) and Nogi and Omura, (2022). Specifically, we utilize a new type of particle simulation code that is catered to the production of coherent elements. As will be shown, the simulated chorus element is successively generated by a backward-traveling resonant current that is a superposition of backward adiabatic motion of a de-trapped electron and forward motion at the group velocity. The following sections cover important features of the code as well as the analysis of the simulation results.

Envelope particle-in-cell code

The high degree of nonlinearity associated with chorus generation is difficult to analytically approach. Computer simulations are thus the best alternative for understanding the details of the wave–particle interaction process. Over the past several decades, several different approaches have been utilized to reproduce salient features of the chorus.

The most common simulation technique for modeling wave generation is the particle-in-cell (PIC) method. PIC relies on using a large number of finite-sized "super-particles" which are pushed within the wave fields *via* the Lorentz force. Each super-particle is treated as an element of charge and current density, such that the net current and charge densities everywhere can be determined *via* straightforward superposition. Subsequently, the wave fields can be updated using a time-domain update scheme applied to Maxwell's equations (usually the well-known FDTD method). This methodology has been employed by numerous researchers to accurately model the generation of whistler-mode waves with both full PIC and hybrid PIC approaches (Omura et al., 2008; Hikishima et al., 2009; Xiao et al., 2017; Lu et al., 2019; Wu et al., 2020; Tao et al., 2021; Nogi and Omura, 2022). Although the standard PIC formalism is a powerful tool, it is often computationally intensive since millions (or even billions) of super-particles are needed to reduce noise, and they are continuously tracked for several thousands of time steps.

An alternative approach is direct solutions to the Vlasov equation (abbreviated as VCON methods, see review and discussion by Gołkowski et al. (2019)). A full VCON method is typically even more computationally stringent than PIC; however, simplifying assumptions permit feasible and low-noise simulations. The most famous VCON method is the VHS code originally demonstrated by Nunn (1990). The code was able to produce rising, falling, and hook-shaped triggered emissions and was also used to model chorus rising tones (Nunn et al., 2009). It relies on using envelope equations that greatly reduce the number of grid points needed to track the wave fields. Furthermore, the range of particle velocities is limited by only considering resonance velocities that translate to a fixed bandwidth of the wave (up to 3 kHz in the most recent version by Nunn (2021)). A drawback of the code was that, because of the manner in which the Lorentz force was

formulated, a single wave frequency and wavenumber had to be determined at every time step. This unavoidably requires artificial filtering of the wave fields which may also be filtering out important physical features.

We have developed a new 1D3V code that combines properties of PIC and the VHS code, known as E-PIC (envelope-PIC). Specifically, the wave fields are modeled using the envelope equation given by

$$\frac{\partial \tilde{B}_w}{\partial t} - v_g \frac{\partial \tilde{B}_w}{\partial z} = -\frac{\mu_0 v_g}{2} \tilde{J}_h. \tag{2}$$

Here, the quantity $\tilde{B}_w$ is the complex wave field, while $\tilde{J}_h$ is the complex hot current density. The quantities v_g and μ_0 represent the whistler-mode group velocity and free space permeability, respectively. The group velocity is selected according to an initial wave frequency (reference frequency of the envelope), which is assumed to be the frequency of maximum linear growth. As such, the envelope equations ignore group velocity dispersion effects. Similar equations have been derived by several other authors in the past (Nunn, 1974; Trakhtengerts, 1995; Omura et al., 2008; Gołkowski and Gibby, 2017) and have been utilized in several simulation and theoretical studies. The complex amplitude can be further expressed in terms of wave amplitude and phase, $\tilde{B}_w = |\tilde{B}_w| e^{j\phi_w}$; however, the complex notation allows for a more stable numerical scheme.

Concurrently, the equations of motion for electrons are given by

$$\frac{dv_\parallel}{dt} = \frac{q_e}{m} v_\perp \left|\tilde{B}_w\right| sin\left(\phi_w + \phi_r\right) - \frac{v_\perp^2}{2\omega_c} \frac{\partial \omega_c}{\partial z}, \tag{3}$$

$$\frac{dv_\perp}{dt} = \frac{q_e}{m} v_\perp \left|\tilde{B}_w\right| \left(v_\parallel + v_p\right) sin\left(\phi_w + \phi_r\right) + \frac{v_\perp v_\parallel}{2\omega_c} \frac{\partial \omega_c}{\partial z}, \tag{4}$$

$$\frac{d\phi_r}{dt} = -\left(\omega_c - \omega_0 - k_0 v_\parallel\right) - \frac{q_e}{m} \left|\tilde{B}_w\right| \frac{\left(v_\parallel + v_p\right)}{v_\perp} cos\left(\phi_w + \phi_r\right), \tag{5}$$

$$\frac{dz}{dt} = v_\parallel. \tag{6}$$

Eqs. 3–6 have been derived by several authors, and the equations govern the non-relativistic motion of electrons immersed in a whistler-mode wave in an inhomogeneous background magnetic field. In Eqs. 3–6, the quantities $v_\parallel, v_\perp$, and ϕ_r represent the electron parallel velocity, perpendicular velocity, and relative gyrophase, respectively. In particular, the gyrophase (ϕ_r) is defined to be relative to a wave with the pre-defined reference frequency (and wavenumber) of the wave (ω_0 and k_0) and not the instantaneous frequency. The reference wavenumber is given by the cold plasma dispersion relation, $k_0^2 = \frac{1}{c^2}\left(\omega_0^2 - \frac{\omega_p^2}{1-\frac{\omega_c}{\omega_0}}\right)$. It should be noted that the reference wavenumber is dependent on space since the gyrofrequency (ω_c) is inhomogeneous. Accordingly, the reference group velocity (v_g) and phase velocity (v_p) are also implicit functions of position.

The wave's instantaneous frequency, $\omega = \omega_0 + \frac{\partial \phi_w}{\partial t}$, will deviate from the original reference frequency during the generation of a rising tone element, and this variation will be captured by a more rapidly varying wave phase, ϕ_w. The same will be true of the instantaneous wavenumber, $k = k_0 + \frac{\partial \phi_w}{\partial z}$. As long as the spatial grid size and time step are chosen to be small enough, the rapid change in the wave fields corresponding to an increasing frequency will be captured. To demonstrate that this is the case, consider the "true" gyrophase, ϕ, which is given by $\phi = \phi_w + \phi_r$. This is typically the quantity that is tracked in theoretical analysis of whistler-mode wave–particle interactions (Nunn, 1974; Gołkowski et al., 2019; Omura, 2021). The time variation of ϕ is then defined by

$$\frac{d\phi}{dt} = \frac{d\phi_w}{dt} + \frac{d\phi_r}{dt}. \tag{7}$$

The second term, $\frac{d\phi_r}{dt}$, is the same as Eq. 5 and is thus already defined. The first term, $\frac{d\phi_w}{dt}$, can be expanded with the chain rule to give

$$\frac{d\phi_w}{dt} = \frac{\partial \phi_w}{\partial t} + v_\parallel \frac{\partial \phi_w}{\partial z}. \tag{8}$$

Here, it is assumed that $\frac{dz}{dt} = v_\parallel$ as defined by Eq. 6. Substituting Eq. 5 and Eq. 8 into Eq. 7 and using the definition of instantaneous frequency wavenumber then gives

$$\frac{d\phi}{dt} = -\left(\omega_c - \omega - k v_\parallel\right) - \frac{q_e}{m} \left|\tilde{B}_w\right| \frac{\left(v_\parallel + v_p\right)}{v_\perp} cos\left(\phi\right). \tag{9}$$

The result in **(9)** is the usual equation of motion for gyrophase where the first term corresponds to the instantaneous resonance condition while the second term represents centrifugal force (Inan et al., 1978). Thus, it has been shown that the equation for the relative gyrophase, ϕ_r, contains the same physics as the traditional gyrophase, ϕ, but without needing to calculate the instantaneous frequency and wavenumber at each time step. Thus, the instantaneous frequency of the wave does not need to be explicitly known during the simulation, and consequently, no artificial filtering is required. The relaxation of the filtering requirement is a highly desirable feature of this formalism. It should be noted that the reference frequency can be chosen arbitrarily; however, it allows for a more efficient simulation (i.e., fewer particles and fewer grid points) if it is chosen to be close to the frequency of maximum linear growth. These are unique features of the (E-PIC) formalism that sets it apart from the prior modeling work.

It is also worth noting that the equations of motion ignore any relativistic effects. However, for the physics of wave generation, the primary impact of including relativity will be to change the resonance velocity (Summers, 2005), alter the trajectories of adiabatic motion, and slightly modify the nonlinear threshold for trapping (Omura et al., 2008). Uniquely relativistic phenomena, such as turning acceleration (Furuya et al., 2008), only occur at ultra-relativistic energies and

are not relevant to the current analysis. As such, ignoring relativity is justified to provide insight into the physics of wave growth.

Unlike the VHS code and other VCON methods (Gibby, 2008; Harid et al., 2014b), the hot current density in E-PIC is determined using the super-particle approach, similar to PIC. That is, the total complex hot current density everywhere is synthesized by using

$$\tilde{J}_h = -q_e j \sum_n e^{-j\phi_r^{(n)}} v_\perp^{(n)} w^{(n)} S\left(z - z^{(n)}\right). \tag{10}$$

Here, the quantity $w^{(n)}$ represents the weight (equivalent to total charge) of the nth particle, while $S(z)$ is the normalized triangle shape-function of each particle that is used to interpolate onto the wave's ($\tilde{B}_w$) grid (Birdsall and Langdon, 2017).

The initial particle distribution is assumed to be specified at the equator as a function of $v_\perp$ and $v_\parallel$ (chosen as bi-Maxwellian in this study). The initial distribution of particles in gyrophase (ϕ_r) is uniformly distributed between 0 and 2π. However, due to the in-homogenous background field, a constant anisotropy bi-Maxwellian is not a valid equilibrium distribution (Summers et al., 2012). As such, Liouville's theorem is then used to conserve the value of the distribution function along adiabatic trajectories at locations away from the equator (Harid et al., 2014a). The super-particle weights and velocities are then assigned by sampling the distribution function on a uniform grid in phase-space, which is sometimes referred to as the "cold-start" condition. From this distribution, the initial hot current density is then determined using Eq. 10 and is used to step Eq. 2 forward in time.

The E-PIC code thus has the reduced computational requirements and uni-directionality of the envelope formalism (like VHS) and reduced phase-space bandwidth (like VHS), while retaining the ease of hot current calculation from PIC. The following section shows the results of a chorus element generation simulation using the E-PIC code.

Rising tone element simulation

In order to compare with the previous work, we use very similar simulation parameters as Tao et al. (2021). The initial distribution function is an anisotropic loss cone bi-Maxwellian (see Hikishima et al., 2009 for the closed form expression), which results in an equatorial linear growth rate that maximizes at approximately 3 kHz, which is thus chosen as the reference carrier frequency. It is worth noting that the initial temperature anisotropy takes the value of 81 in order to increase the numerical signal-to-noise ratio (SNR) and reduce the number of computational particles. As such, the growth rates are much higher than those expected for real chorus elements with the benefit of decreased computational time. This type of numerical trick has been employed by other published works as well in order to keep the number of super-particles in the 10s of millions instead of billions (Hikishima et al., 2009). Increasing the number of particles will require a large degree of parallelization (on a supercomputing platform) for which the code has not been designed yet. This is an area of active development, and future simulations will utilize more realistic parameters and a larger number of particles on a larger HPC platform. Nevertheless, the simulation described here is still useful for understanding the general mechanisms of generation and growth. The background gyrofrequency is assumed to be parabolic and is given by the expression, $\omega_C(z) = \omega_{c0}(1 + \delta z^2)$. The values of all the remaining relevant parameters used in the simulation are shown in Table 1.

TABLE 1 Background, wave, and grid parameters used in the simulation.

Physical quantity	Value
Reference carrier frequency, f_0	3 kHz
Electron gyrofrequency, f_{c0}	15 kHz
Plasma frequency, f_p	75 kHz
Coefficient of the parabolic magnetic field, δ	2.6512×10^{-9} m^{-2}
Number of simulation particles	25×10^6
Equatorial hot plasma density	0.68 $\frac{el}{cm^3}$
Ratio of hot to cold plasma density, N_h/N_c	0.01
Bi-Maxwellian thermal velocities: $v_{\perp TH}$, $v_{\parallel Th}$	0.45c, 0.05c
Bi-Maxwellian loss cone parameter, β	0.3
Number of spatial grid points, N_z	500
Number of time steps, N_t	7,293
Time step, Δt	8.73 μs
Grid spacing, Δz	1.202 km
Boundary of the simulation domain: $\frac{z_{max}\omega_{c0}}{c}$	94.28

Similar to the VHS formalism, the range of parallel velocities is limited such that they can resonate with waves between 2 and 4 kHz. The boundary condition for the particles follows "instantaneous mirroring" such that only the electron position is negated ($z \rightarrow -z$) if the parallel velocity exceeds the maximum limit or is below the minimum limit (corresponding to 4 and 2 kHz resonant waves, respectively), while all velocity components are conserved. The same condition is applied when electrons arrive at the left or right spatial boundaries of the simulation space. The wave boundary condition on the right hand side of the simulation enforces continuity of the derivative of the wave magnetic field (no injected wave), while the left hand side enforces simple outflow. The initial conditions on the wave magnitude are set identically to zero to ensure any generated waves are purely spontaneous. Furthermore, the envelope equations are updated with a backward semi-Lagrangian method, which, hence, circumvents the typical CFL stability condition. With all these simplifications, the E-PIC code runs

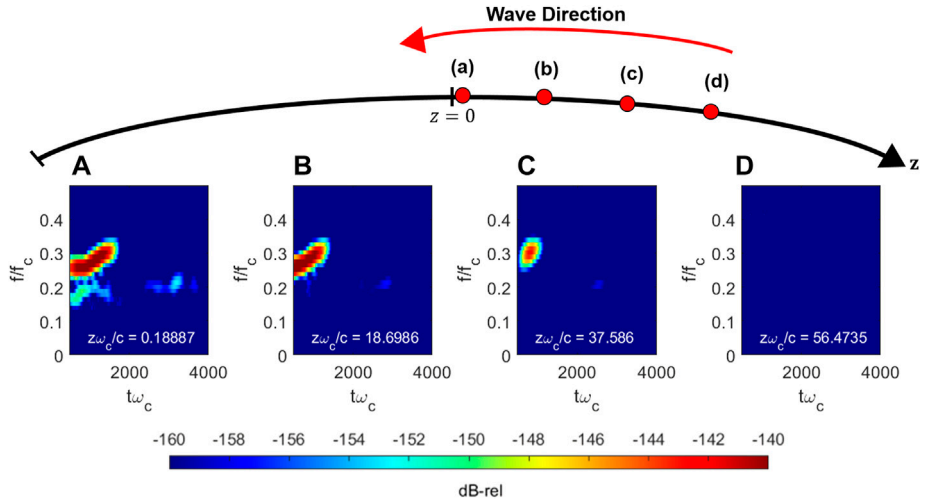

FIGURE 1
Spectrograms of the wave magnetic field starting at the **(A)** simulation equator and progressively more upstream **(B,C,D)**.

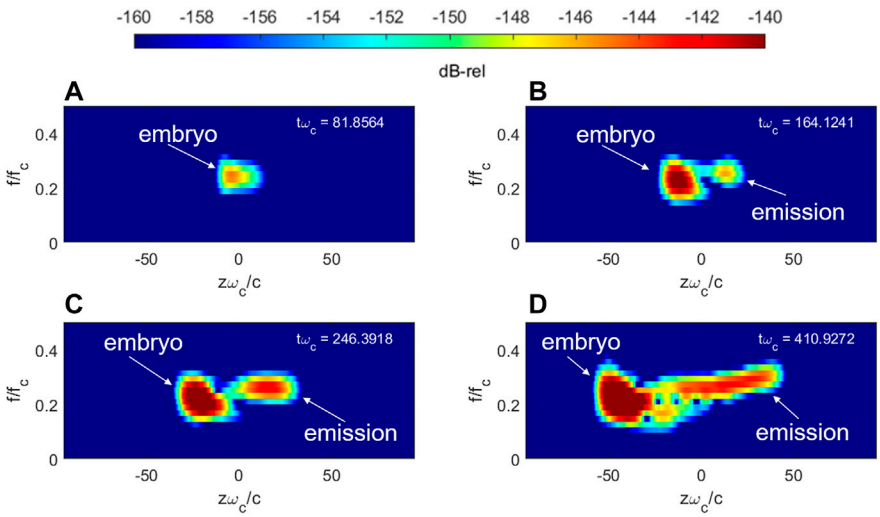

FIGURE 2
Spatial distribution of the wave frequency content during rising tone generation at progressively increasing snapshots in time. Earliest time **(A)** to latest time **(D)**.

approximately 5–10x faster than full PIC or hybrid PIC codes for this particular simulation setup.

The simulation generates a rising tone chorus element that is shown to be generated upstream of the equator. Figure 1 shows spectrograms of the wave fields at four locations along the field line that are upstream of the equator (opposite the direction of wave propagation). It is worth noting that the simulation results are shown in the same normalized space–time coordinates as employed by Hikishima et al. (2009). Specifically, Figure 1D shows a spectrogram of the wave furthest upstream ($\frac{z\omega_c}{c} = 56.47$), and it is apparent that no frequency components are present. Figure 1C shows a spectrogram closer to the equator ($\frac{z\omega_c}{c} = 37.58$), and it is apparent that a single frequency component is present at this point. Moving even closer to the equator ($\frac{z\omega_c}{c} = 18.69$), additional lower frequency components are shown to appear at early points in time, and the rising tone structure is shown to emerge. Finally, at the equator (or numerically close at $\frac{z\omega_c}{c} = 0.19$), the entire rising tone is present and represents a chorus element that will propagate and amplify downstream. Thus, as shown in Figure 1, the rising

tone chorus element is mostly created upstream of the equator in the direction opposite to the wave's propagation direction.

The generation of the rising tone element occurs upstream of the equator; however, the initial "embryo" frequency emerges at the equator approximately at the maximum linear growth frequency (as suggested by Omura (2021)). Figure 2 shows four subplots where the *y*-axis corresponds to frequency, while the *x*-axis corresponds to position, and each subplot corresponds to a progressively increased point in time. Figure 2A shows the spatial distribution of frequency at $t\omega_C = 81.85$.

As shown, an initial embryo frequency emerges at the equator and propagates downstream at the frequency of maximum linear growth. It is also noticeable that the wavepacket "stretches" upstream to some extent, which serves as the initial point for the remainder of the rising tone. Figure 2B shows the frequency components a short time later at $t\omega_C = 164.124$. It can be seen that a new higher frequency component emerges further upstream of the initial embryo. As time increases, as shown in Figures 2C,D, the remainder of the rising tone is generated while simultaneously propagating downstream, that is, the rising tone is sequentially generated upstream of the equator with the highest frequency components arising furthest downstream. It is worth noting that the emission eventually terminates at some point upstream (at approximately $\frac{z\omega_c}{c} = 50$) and turns the emission into an "element". However, it is currently unclear as to what underlying mechanism determines this termination point. It is potentially related to the "critical distance" described in Omura (2021); however, a detailed analysis of this is outside the current scope of this work.

It is worth noting that the embryo frequency component increases considerably in intensity (as shown by the dark red in Figures 2B–D) which is mostly a function of the artificially high anisotropy utilized in the simulation. This can be tuned in future works to determine the impact of the growth rate (and other parameters) on chorus generation.

Backward-propagating resonant current driving rising tone generation

The results shown in Figures 1, 2 clearly demonstrate that an embryonic component is generated at the equator, and the rising tone is subsequently generated upstream. However, it is still not immediately evident as to the mechanism by which the rising tone emerges. To assess a backward-moving source as a viable mechanism, a simple approach is *via* tracking the adiabatic trajectory of an initially de-trapped electron. Assuming that the embryo spontaneously emerges at the equator due to linear growth of thermal noise, the electrons that first encounter the embryonic wave from downstream will be phase-trapped and then rapidly ejected from the back end of the wavepacket. At this point, these de-trapped electrons now observe zero wave fields since they have been ejected into a region upstream where no waves exist. If the electrons have been phase-organized to any extent, as expected for phase-bunched electrons, for instance (where phase-bunching is based on the definition of Albert (2002)), a net current will be formed and a new wavepacket will be generated in its wake. Since the electrons are free falling out the back end of the wave, any "new" electrons that get trapped downstream by the freshly generated upstream wavepackets will already satisfy the local resonance condition and simply follow the trajectory of the electrons that were originally released by the embryo wave. At the same time, the waves are forced to be propagating in the forward (downstream direction) direction and will be supported by the resonant currents in the process. Thus, the constant flow of de-trapped electrons should result in a backward-going (i.e., upstream propagating) current that follows the adiabatic trajectory of the initially de-trapped electron stream superimposed with forward motion at the group velocity (as suggested by Nogi and Omura, (2022)). In order to confirm this hypothesis, the combined trajectory of adiabatic motion and group velocity motion can be calculated and compared to the hot current profile.

Assuming that the embryo wave generates at the frequency of maximum linear growth at the equator, the initially trapped electrons will have a parallel velocity equal to the local equatorial resonance velocity evaluated at the maximum linear growth rate frequency. From the equator, it can be assumed that electrons become quickly de-trapped and travel upstream adiabatically. The equation of motion governing the position of an electron, z_a, undergoing adiabatic motion after being released from resonance at the equator is given by

$$\frac{dz_a}{dt} = \frac{v_r(0)}{cos(\alpha_{eq})}\left(1 - \frac{\omega_c}{\omega_c(0)}sin(\alpha_{eq})^2\right)^{\frac{1}{2}}. \tag{11}$$

Here, the quantity α_{eq} is the pitch angle of the electron exactly at the equator. At the same time, the motion of the backward-propagating source must have the forward motion at the group velocity superimposed. Thus, the equation for the position of the backward-propagating source, z_s, is given by

$$\frac{dz_s}{dt} = \frac{dz_a}{dt} - v_g(z_s). \tag{12}$$

Although the group velocity should also vary with time if the frequency of the wave changes, the E-PIC formalism currently does not include this effect (as mentioned in the previous section), and it is thus ignored in this post-processing calculation. For simplicity, we consider a fixed pitch angle within the range used in the simulation, that is, $\alpha_{eq} \approx 65°$. This value also falls within the pitch angle range expected to contribute to nonlinear growth (Nunn, 1990). The equation of motion shown in Eq. 12 can be numerically integrated to get the expected trajectory of the backward-moving source.

Figure 3 shows the space–time profile of the hot current magnitude (a), the wave magnetic field magnitude (b), and the

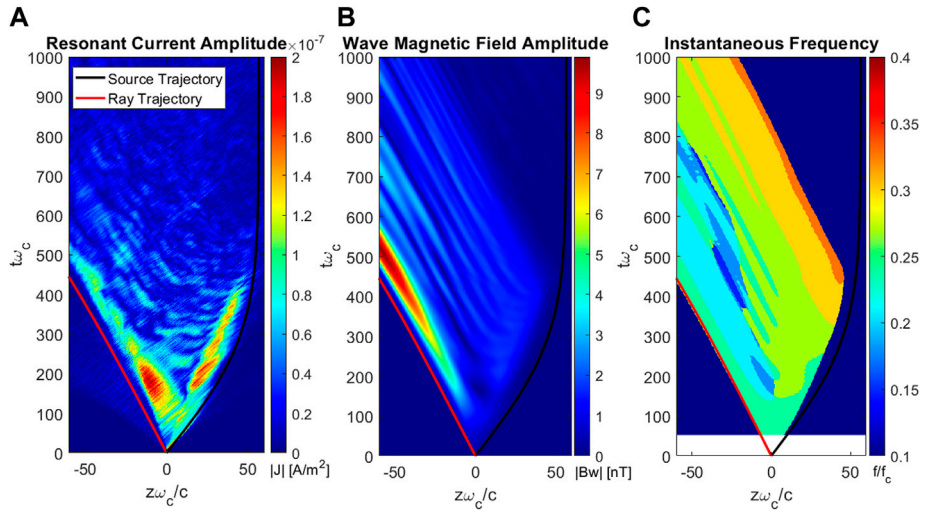

FIGURE 3
Space–time profiles of the **(A)** hot current density magnitude, **(B)** wave magnetic field magnitude, and **(C)** wave magnetic field instantaneous frequency. The source trajectory (Eq. 8) and the ray trajectory of a wave-front are superimposed as the black and red curves, respectively.

wave's instantaneous frequency (c), respectively. The instantaneous frequency is determined *via* the local maximum frequency on the spectrogram (using a 512-point FFT) and is only calculated for field amplitudes from 40 dB below the maximum amplitude up to the maximum amplitude (non-calculated points are shown in dark blue). As shown in Figure 3A, the hot current has a "V"-like structure that indicates both forward- and backward-going components. It should be noted that "backward" in this formalism corresponds to the component moving in the $+z$ direction. On top of the space-time profile of the current, the source trajectory from integrating Eq. 12 is shown by the black curve. It is evident that the trajectory of an initially resonant electron with the group velocity subtracted out very closely aligns with the enhancement in the backward current. This strongly suggests that the backward stream of hot current is due to the repeated trapping and de-trapping process that, on average, follows the adiabatic trajectory of the initially de-trapped particle with the group velocity motion superimposed (with an opposite sign). The same trajectory is superimposed on the wave's space–time profile in Figure 3B. It is evident that the expected trajectory of the source closely coincides with a backward-moving source that continuously radiates forward-going waves. Thus, the generation of the wave due to a backward-moving source that has also recently been shown by Nogi and Omura, (2022) in the context of VLF-triggered emissions that seem to also apply to the generation of whistler-mode chorus waves. It is also worth emphasizing that the source trajectory (Figure 3) is primarily utilized to visualize the average trajectory of the backward-going resonant current. The physically accurate picture is several successive bunches of particles that are constantly trapped and then de-trapped. This phenomenon is visible as the substructure in the resonant current profile in Figure 3A coincides with the source trajectory.

The envelope equation formalism of the E-PIC code only allows waves to propagate in the $-z$ direction in the absence of any currents. Thus, the forward-going waves are expected to approximately follow the trajectory of a ray moving at the group velocity, which is superimposed as the red curve on all the panels of Figure 3. It is clear that the propagation of the wave does indeed follow the expected ray trajectory. The forward-going component of the current is more complex since it must transit from the backward component that radiates the wave to the forward component that sustains the wave after it has been generated. Finally, Figure 3C shows that higher frequency components are generated upstream of the equator and then propagate downstream to form the chorus element and undergo some nonlinear distortion. Furthermore, the initial generation of new frequency components is also shown to closely coincide with the theoretical source trajectory from Eq. 12.

The simulation results thus confirm that the rising tone whistler-mode chorus element is generated upstream of the equator due to a free falling electron stream that is de-trapped by a spontaneously generated equatorial embryonic wave.

Conclusion

Despite several decades of observational and theoretical investigation of magnetospheric chorus, there remains considerable debate on the precise mechanism of cyclotron resonance that governs the frequency chirp of chorus

elements. A new E-PIC code has been developed to model chorus element generation in a parabolic magnetic field. We have shown that the chorus element initiates at the frequency of maximum linear growth at the equator. This embryo wave immediately phase-traps resonant electrons and releases them upstream. The de-trapped particles revert to adiabatic motion upstream of the equator, resulting in a backward-moving source. The motion of the backward-propagating source is consistent with the superposition of the adiabatic trajectory of an initially resonant electron and forward motion at the group velocity. Our results show that a blend of the conclusions by Tao et al. (2021) and Nogi and Omura (2022) seem to explain the origin of rising tone chorus elements. The results of this work thus provide valuable theoretical insight into the origin of the rising tone magnetospheric chorus.

Data availability statement

The original contributions presented in the study are publicly available. These data can be found at: Zenodo, https://doi.org/10.5281/zenodo.6565107, doi: 10.5281/zenodo.6565107.

Author contributions

All authors listed have made a substantial, direct, and intellectual contribution to the work and approved it for publication.

Conflict of interest

The authors declare that the research was conducted in the absence of any commercial or financial relationships that could be construed as a potential conflict of interest.

Publisher's note

All claims expressed in this article are solely those of the authors and do not necessarily represent those of their affiliated organizations, or those of the publisher, the editors, and the reviewers. Any product that may be evaluated in this article, or claim that may be made by its manufacturer, is not guaranteed or endorsed by the publisher.

References

Albert, J. M. (2002). Nonlinear interaction of outer zone electrons with VLF waves. *Geophys. Res. Lett.* 29, 116-1–116-3. doi:10.1029/2001GL013941

Bell, T. F. (1984). The nonlinear gyroresonance interaction between energetic electrons and coherent VLF waves propagating at an arbitrary angle with respect to the Earth's magnetic field. *J. Geophys. Res.* 89, 905–918. doi:10.1029/JA089iA02p00905

Birdsall, C. K., and Langdon, A. B. (2017). *Plasma physics via computer simulation*. Boca Raton: CRC Press. doi:10.1201/9781315275048

Bortnik, J., Thorne, R. M., and Meredith, N. P. (2008). The unexpected origin of plasmaspheric hiss from discrete chorus emissions. *Nature* 452, 62–66. doi:10.1038/nature06741

Crabtree, C., Ganguli, G., and Tejero, E. (2017). Analysis of self-consistent nonlinear wave-particle interactions of whistler waves in laboratory and space plasmas. *Phys. Plasmas* 24, 056501. doi:10.1063/1.4977539

Dysthe, K. B. (1971). Some studies of triggered whistler emissions. *J. Geophys. Res.* 76, 6915–6931. doi:10.1029/JA076i028p06915

Furuya, N., Omura, Y., and Summers, D. (2008). Relativistic turning acceleration of radiation belt electrons by whistler mode chorus. *J. Geophys. Res.* 113. doi:10.1029/2007JA012478

Gibby, A. R. (2008). *Saturation effects in VLF triggered emissions (ph.D.). ProQuest dissertations and theses*. United States – California: Stanford University.

Gołkowski, M., and Gibby, A. R. (2017). On the conditions for nonlinear growth in magnetospheric chorus and triggered emissions. *Phys. Plasmas* 24, 092904. doi:10.1063/1.4986225

Gołkowski, M., Harid, V., and Hosseini, P. (2019). Review of controlled excitation of non-linear wave-particle interactions in the magnetosphere. *Front. Astron. Space Sci.* 6. doi:10.3389/fspas.2019.00002

Harid, V., Gołkowski, M., Bell, T., and Inan, U. S. (2014a). Theoretical and numerical analysis of radiation belt electron precipitation by coherent whistler mode waves. *J. Geophys. Res. Space Phys.* 119, 4370–4388. doi:10.1002/2014JA019809

Harid, V., Gołkowski, M., Bell, T., Li, J. D., and Inan, U. S. (2014b). Finite difference modeling of coherent wave amplification in the Earth's radiation belts. *Geophys. Res. Lett.* 41, 8193–8200. doi:10.1002/2014GL061787

Helliwell, R. A. (1967). A theory of discrete VLF emissions from the magnetosphere. *J. Geophys. Res.* 72, 4773–4790. doi:10.1029/JZ072i019p04773

Hikishima, M., Yagitani, S., Omura, Y., and Nagano, I. (2009). Full particle simulation of whistler-mode rising chorus emissions in the magnetosphere. *J. Geophys. Res.* 114. doi:10.1029/2008JA013625

Horne, R. B. (2007). Acceleration of killer electrons. *Nat. Phys.* 3, 590–591. doi:10.1038/nphys703

Hosseini, P., Gołkowski, M., and Harid, V. (2019). Remote sensing of radiation belt energetic electrons using lightning triggered upper band chorus. *Geophys. Res. Lett.* 46, 37–47. doi:10.1029/2018GL081391

Inan, U. S., Bell, T. F., and Helliwell, R. A. (1978). Nonlinear pitch angle scattering of energetic electrons by coherent VLF waves in the magnetosphere. *J. Geophys. Res.* 83, 3235–3253. doi:10.1029/JA083iA07p03235

Katoh, Y., and Omura, Y. (2011). Amplitude dependence of frequency sweep rates of whistler mode chorus emissions. *J. Geophys. Res.* 116. doi:10.1029/2011JA016496

Kennel, C. F., and Petschek, H. E. (1966). Limit on stably trapped particle fluxes. *J. Geophys. Res.* 71, 1–28. doi:10.1029/JZ071i001p00001

Lu, Q., Ke, Y., Wang, X., Liu, K., Gao, X., Chen, L., et al. (2019). Two-dimensional gcPIC simulation of rising-tone chorus waves in a dipole magnetic field. *J. Geophys. Res. Space Phys.* 124, 4157–4167. doi:10.1029/2019JA026586

Matsumoto, H. (1979). "Nonlinear whistler-mode interaction and triggered emissions in the magnetosphere: A review," in *Wave instabilities in space plasmas, astrophysics and space science library*. Editors P. J. Palmadesso and K. Papadopoulos (Dordrecht: Springer Netherlands), 163–190. doi:10.1007/978-94-009-9500-0_13

Meredith, N. P., Horne, R. B., Sicard-Piet, A., Boscher, D., Yearby, K. H., Li, W., et al. (2012). Global model of lower band and upper band chorus from multiple satellite observations: Global model of whistler mode chorus. *J. Geophys. Res.* 117, n/a. doi:10.1029/2012ja017978

Mozer, F. S., Agapitov, O. V., Blake, J. B., and Vasko, I. Y. (2018). Simultaneous observations of lower band chorus emissions at the equator and microburst precipitating electrons in the ionosphere. *Geophys. Res. Lett.* 45, 511–516. doi:10.1002/2017GL076120

Nogi, T., and Omura, Y. (2022). Nonlinear signatures of VLF-triggered emissions: A simulation study. *JGR. Space Phys.* 127, e2021JA029826. doi:10.1029/2021JA029826

Nunn, D. (1974). A self-consistent theory of triggered VLF emissions. *Planet. Space Sci.* 22, 349–378. doi:10.1016/0032-0633(74)90070-1

Nunn, D., and Omura, Y. (2012). A computational and theoretical analysis of falling frequency VLF emissions. *J. Geophys. Res.* 117. doi:10.1029/2012JA017557

Nunn, D., Omura, Y., Matsumoto, H., Nagano, I., and Yagitani, S. (1997). The numerical simulation of VLF chorus and discrete emissions observed on the Geotail satellite using a Vlasov code. *J. Geophys. Res.* 102, 27083–27097. doi:10.1029/97JA02518

Nunn, D., Santolik, O., Rycroft, M., and Trakhtengerts, V. (2009). On the numerical modelling of VLF chorus dynamical spectra. *Ann. Geophys.* 27, 2341–2359. doi:10.5194/angeo-27-2341-2009

Nunn, D. (2021). The numerical simulation of the generation of lower-band VLF chorus using a quasi-broadband Vlasov Hybrid Simulation code. *Earth Planets Space* 73, 222. doi:10.1186/s40623-021-01549-3

Nunn, D. (1990). The numerical simulation of VLF nonlinear wave-particle interactions in collision-free plasmas using the Vlasov hybrid simulation technique. *Comput. Phys. Commun.* 60, 1–25. doi:10.1016/0010-4655(90)90074-B

Omura, Y., Katoh, Y., and Summers, D. (2008). Theory and simulation of the generation of whistler-mode chorus. *J. Geophys. Res.* 113. doi:10.1029/2007JA012622

Omura, Y. (2021). Nonlinear wave growth theory of whistler-mode chorus and hiss emissions in the magnetosphere. *Earth Planets Space* 73, 95. doi:10.1186/s40623-021-01380-w

Omura, Y., Nunn, D., Matsumoto, H., and Rycroft, M. J. (1991). A review of observational, theoretical and numerical studies of VLF triggered emissions. *J. Atmos. Terr. Phys.* 53, 351–368. doi:10.1016/0021-9169(91)90031-2

Ripoll, J. -F., Claudepierre, S. G., Ukhorskiy, A. Y., Colpitts, C., Li, X., Fennell, J. F., et al. (2020). Particle dynamics in the earth's radiation belts: Review of current research and open questions. *J. Geophys. Res. Space Phys.* 125. doi:10.1029/2019JA026735

Roux, A., and Pellat, R. (1978). A theory of triggered emissions. *J. Geophys. Res.* 83, 1433–1441. doi:10.1029/JA083iA04p01433

Stix, T. H. (1992). *Waves in plasmas*. Springer Science & Business Media.

Summers, D., Omura, Y., Miyashita, Y., and Lee, D.-H. (2012). Nonlinear spatiotemporal evolution of whistler mode chorus waves in Earth's inner magnetosphere. *J. Geophys. Res.* 117. doi:10.1029/2012JA017842

Summers, D. (2005). Quasi-linear diffusion coefficients for field-aligned electromagnetic waves with applications to the magnetosphere. *J. Geophys. Res.* 110. doi:10.1029/2005JA011159

Tao, X., Zonca, F., and Chen, L. (2021). A "trap-release-amplify" model of chorus waves. *JGR. Space Phys.* 126, e2021JA029585. doi:10.1029/2021JA029585

Tao, X., Zonca, F., and Chen, L. (2017). Identify the nonlinear wave-particle interaction regime in rising tone chorus generation. *Geophys. Res. Lett.* 44, 3441–3446. doi:10.1002/2017GL072624

Trakhtengerts, V. Y. (1999). A generation mechanism for chorus emission. *Ann. Geophys.* 17, 95–100. doi:10.1007/s00585-999-0095-4

Trakhtengerts, V. Y. (1995). Magnetosphere cyclotron maser: Backward wave oscillator generation regime. *J. Geophys. Res.* 100, 17205–17210. doi:10.1029/95JA00843

Vomvoridis, J. L., Crystal, T. L., and Denavit, J. (1982). Theory and computer simulations of magnetospheric very low frequency emissions. *J. Geophys. Res.* 87, 1473–1489. doi:10.1029/JA087iA03p01473

Wu, Y., Tao, X., Zonca, F., Chen, L., and Wang, S. (2020). Controlling the chirping of chorus waves via magnetic field inhomogeneity. *Geophys. Res. Lett.* 47, e2020GL087791. doi:10.1029/2020GL087791

Xiao, F., Liu, S., Tao, X., Su, Z., Zhou, Q., Yang, C., et al. (2017). Generation of extremely low frequency chorus in Van Allen radiation belts. *J. Geophys. Res. Space Phys.* 122, 3201–3211. doi:10.1002/2016JA023561

Zonca, F., Tao, X., and Chen, L. (2022). A theoretical framework of chorus wave excitation. *JGR. Space Phys.* 127, e2021JA029760. doi:10.1029/2021JA029760

frontiers | Frontiers in Astronomy and Space Sciences

TYPE Original Research
PUBLISHED 29 September 2022
DOI 10.3389/fspas.2022.986814

OPEN ACCESS

EDITED BY
Xiao-Jia Zhang,
University of California, United States

REVIEWED BY
Andrei Demekhov,
Polar Geophysical Institute (RAS), Russia
Qianli Ma,
Boston University, United States

*CORRESPONDENCE
John C. Foster,
jcfoster@mit.edu

SPECIALTY SECTION
This article was submitted to Space Physics,
a section of the journal
Frontiers in Astronomy and Space Sciences

RECEIVED 05 July 2022
ACCEPTED 12 September 2022
PUBLISHED 29 September 2022

CITATION
Foster JC and Erickson PJ (2022), Off-equatorial effects of the nonlinear interaction of VLF chorus waves with radiation belt electrons.
Front. Astron. Space Sci. 9:986814.
doi: 10.3389/fspas.2022.986814

Off-equatorial effects of the nonlinear interaction of VLF chorus waves with radiation belt electrons

John C. Foster* and Philip J. Erickson

Massachusetts Institute of Technology Haystack Observatory, Westford, MA, United States

Nonlinear processes are involved in both the growth of VLF chorus waves and the energization of radiation belt electrons trapped in the wave potential. Nonlinear theory has led to analytic formulae describing both these processes. To investigate these processes, observations from the Van Allen Probes twin spacecraft provide simultaneous *in situ* information on VLF chorus waves, radiation belt and injected electrons, and local plasma parameters. We combine the theoretical treatment summarized by Omura (2021) with these *in situ* observations to investigate the characteristics and effects of nonlinear radiation belt processes at the off-equatorial location of the spacecraft observations. We show the smooth phase transition between initial subpackets of chorus wave elements, conducive to extended trapping and enhancement of resonant electrons. The structure of the chorus wave element changes as it propagates away from the equator. Frequency dispersion due to the variation of parallel wave group velocity with frequency contributes to the chorus waveform frequency sweep rate observed at an off-equatorial location. Nonlinear damping at the local value of ½ f_{ce} progressively erodes wave amplitude at frequencies above ½ f_{ceEQ}. We examine the important dependencies of the nonlinear inhomogeneity factor on the time rate of change of the wave frequency and the field-aligned gradient of the magnetic field and discuss their implication for the energization of trapped non-relativistic and MeV electrons. The 0.5–2% energy gain we find for 3–6 MeV seed electrons indicates that prompt local acceleration of highly relativistic and ultra-relativistic radiation belt electrons can take place directly through their nonlinear interaction with an individual VLF chorus wave element.

KEYWORDS

nonlinear processes. wave-particle interactions, VLF chorus, electron acceleration, nonlinear inhomogeneity factor, radiation belt electrons

1 Introduction

Baker et al., 2014 show that both slow diffusive and rapid energization are important physical mechanisms for radiation belt recovery following large geomagnetic storms, as exemplified by dynamic conditions during March 2013. In particular, the time scale of energization for relativistic particles can be greatly shortened by nonlinear processes. The energization of radiation belt electrons is a multi-step process involving VLF chorus waves and a population of seed particles (Jaynes et al., 2015). Using *in situ* Van Allen Probes observations, Foster et al., 2014 focused on conditions surrounding a prompt relativistic electron recovery following the major geomagnetic storm on 17 March 2013. They concluded that nonlinear processes must be involved to account for the 30–60 min 10x increase in multi-MeV fluxes observed at L ~ 4.

The growth of rising-frequency chorus elements involves nonlinear cyclotron resonance (n = 1) with 10–100 s keV electrons that are injected into the inner magnetosphere during substorm dipolarization events (e.g. Foster et al., 1976). The chorus waves in turn can energize 100 s keV seed electrons to MeV energies through further nonlinear processes (Kubota and Omura, 2018). The electrons giving energy to the wave are untrapped resonant electrons that form a hole in velocity phase space and are decelerated by the wave electric field, transferring energy to the wave. By contrast, those electrons accelerated by the wave are trapped by the wave potential with a number density much less than that of the untrapped resonant electrons. Demekhov et al., 2006's theoretical investigation shows that generating resonant particles are untrapped, but relativistic/higher energy electrons satisfy the trapping condition. Important in both these nonlinear processes is the inhomogeneity factor, S (Omura et al., 2008; 2019). S is a function of local parameters, the time rate of change of the wave frequency, df/dt, and the gradient of the Earth's magnetic field along the direction of wave propagation, dB/dx (x is distance along the wave propagation direction away from the wave generation region). The generation of a wave subpacket with fixed frequencies occurs in a critical region near the equator where the df/dt term in the S-factor equations dominates the dB/dx gradient term. For the Van Allen Probes data we present, the gradient term is dominant and our point of observation is off-equatorial in the sense that it is outside the critical region of wave development where the df/dt terms are dominant. Omura (2021) has provided an extensive review of the nonlinear theory of the generation of chorus wave elements and their effect in the nonlinear acceleration of radiation belt electrons, and notes that the acceleration of electrons >100 keV and the wave generation by electrons <100 keV can be treated independently.

Combining nonlinear theory with Van Allen Probes observations, Foster et al., 2017 quantitatively investigated the energization potential of observed chorus waves, finding good overall agreement with characteristics of local acceleration of 1–3 MeV radiation belt electron population seen during the 17 March 2013 event. Later, Hsieh and Omura (2018) and Omura et al. (2019) further extended the theoretical analysis of the nonlinear energization potential of VLF chorus rising tones to the case of obliquely propagating waves [e.g. Santolik et al. (2009)], including both cyclotron (n = 1) and Landau (n = 0) interactions. They found that nonlinear trapping of relativistic electrons by the Lorentz force of the perpendicular wave magnetic field resulted in effective electron acceleration (Omura et al., 2019). The analysis of Demekhov et al., 2006 concluded that energy gain is independent of wave amplitude for trapped particles. Artemyev et al. (2012) found that Landau-resonant acceleration, including low-latitude effects from magnetic field inhomogeneity driving phase velocity variation, is most effective for 10–100 keV particles.

In the following sections, we illustrate further aspects of nonlinear acceleration processes, using a merger of *in situ* observations with nonlinear theoretical analyses that focus on the specific off-equatorial location of the Van Allen Probes observations. We show the smooth phase transition between initial subpackets of chorus wave elements, conducive to extended trapping and enhancement of resonant electrons. Foster et al., 2021 pointed out the steepening of the observed chorus waveform frequency sweep rate, df/dt, near the local value of 1/4 f_{ce} for several cases and noted that it was generally seen in their observations of strong chorus elements. Here we address the effects of frequency dispersion on df/dt with a simple model based on the off-equatorial observations of df/dt and the frequency dependences of the wave group velocity, V_g, and wave normal angle, WNA. Invoking the theory/simulation studies of Hsieh and Omura (2018) of chorus wave damping around 1/2 f_{ce}, half the local electron cyclotron frequency, we use the observed characteristics of lower-band chorus emissions to determine both the magnetic field strength (f_{ce}) and starting frequency for the chorus emission in the equatorial wave generation region.

We employ the theoretical treatment developed in Omura et al., 2019 to investigate the dependency of the nonlinear inhomogeneity factors S0 and S1, for Landau and cyclotron resonant interactions, on df/dt and dB/dx using directly observed wave and plasma parameters. We examine the separate contributions of df/dt and dB/dx terms to the nonlinear energization of sub-relativistic through ultra-relativistic seed electrons. We find that prompt local acceleration of highly relativistic and ultra-relativistic (>3 MeV) radiation belt electrons can take place directly through their nonlinear interaction with an individual VLF chorus wave element.

2 17 March 2013 event

During the 17 March 2013 storm, the Van Allen Probes A and B spacecraft (Mauk et al., 2012) crossed the inner portions of the outer electron radiation belt at the time of a substorm injection with ~1 h time separation along the same spatial orbital trajectory. They were well situated to observe the characteristics and effects of local acceleration through quantification of conditions before and after energization took place. As RBSP-A traveled inbound from L ~ 5.5 to L ~ 3, its

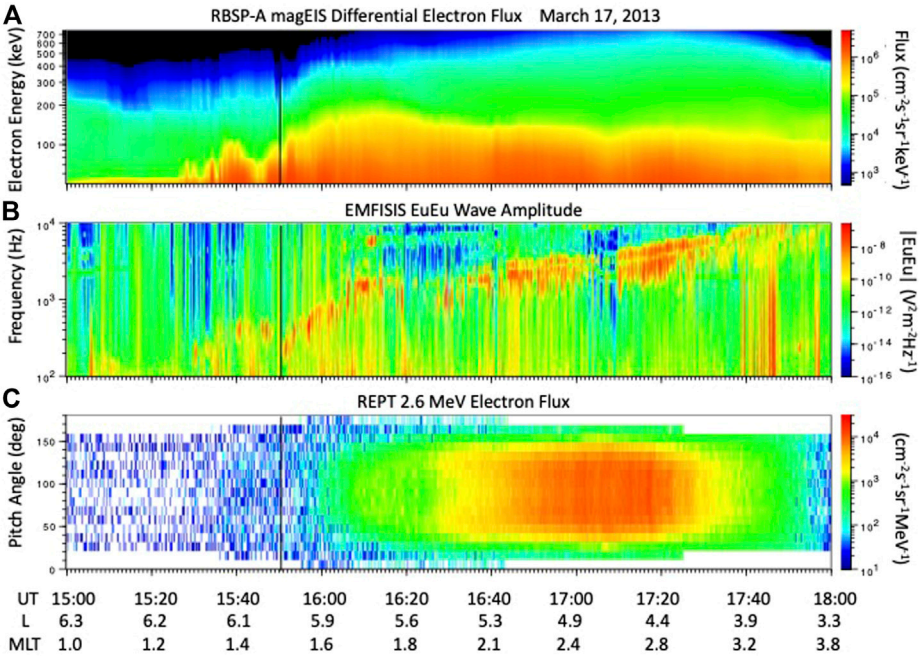

FIGURE 1
RBSP-A *in situ* observations of the rapid recovery of MeV radiation belt electron fluxes on 17 March 2013. The black line marks the spacecraft location (L ~ 6; 1.5 MLT) at 15:50 UT.**(A)** MagEIS spectogram of lower energy electron fluxes associated with chorus wave growth.**(B)** EMFISIS WFR electric field spectorgram showing the onset of strong VLF chorus waves. **(C)** Pitch angle dependence of REPT 2.6 MeV electron flux.

observations form a time history of the lower energy (50–several 100 keV) electron population [MagEIS (Blake et al., 2013)], resultant VLF chorus intensification [EMFISIS (Kletzing et al., 2012)], and MeV electron recovery [REPT (Baker et al., 2012)]. RBSP-A data for this period are presented in Figure 1, showing intensification of 2.6 MeV electron flux reaching > 10^4 cm^{-2} s^{-1} sr^{-1} MeV^{-1} following the onset of intense rising tone chorus and the earthward injection of 50–100 s keV electrons. RBSP-B preceded RBSP-A across the same region of the outer radiation belt by ~1 h and those data are presented in Figure 2. Temporal change is seen by comparing RBSP-A observations (disturbance) with those of RBSP-B (background) over the same spatial region. Both RBSP-A at L ~ 6.0 and RBSP-B at L ~ 4.9 observed a sharp increase of 50–200 keV electron flux at ~15:50 UT, indicative of the earthward injection of low energy electrons accompanied by VLF chorus intensification. RBSP-A 2.6 MeV electron flux began increasing immediately after 15:50, exceeding the background RBSP-B observations by 10x over the range of L from ~5.7 to 4.9. During the event 100 keV electron injection was accompanied by chorus wave growth at 1–3 kHz frequencies and an order of magnitude increase in MeV electron flux in ~1 h.

Figure 3 presents the variation of REPT relativistic phase space density (PSD) observed as RBSP-B preceded RBSP-A along successive outbound (curves 1 and 2, before the injection/recovery event) and inbound (curves 3 and 4, during recovery) orbits. PSD is labeled by the three phase space momentum coordinates: the first adiabatic invariant M, the second adiabatic invariant K, and the drift shell L* associated with the third adiabatic invariant (Chen et al., 2006). In Figure 3 PSD for M = 2,500 MeV/G, K = 0.25 is plotted vs. L*. At the ~15:50 UT time of the 100 s keV injection, both RBSP-A at L* = 4.45 and RBSP-B at L* = 3.95 began to see increasing 2,500 MeV/G PSD as the multi-MeV electron flux began to increase. For the subsequent 1-h interval, RBSP-A observed a post-injection PSD that amounted to a 10x increase at L* = 4 with respect to the RBSP-B observations at that position 1 hour earlier. Figure 3 gives clear evidence of the rapid local acceleration (Reeves et al., 2013) of MeV radiation belt electrons that occurred during this recovery event.

3 Chorus wave observations

Three-axis burst mode EMFISIS (Kletzing et al., 2012) observations of wave electric and magnetic fields (28.6 μs time resolution; ~12 kHz maximum observable frequency) are used to investigate electron interactions with individual chorus rising tones on a sub-millisecond time scale. We analyze individual chorus wave elements following the method described by Foster et al., 2017,

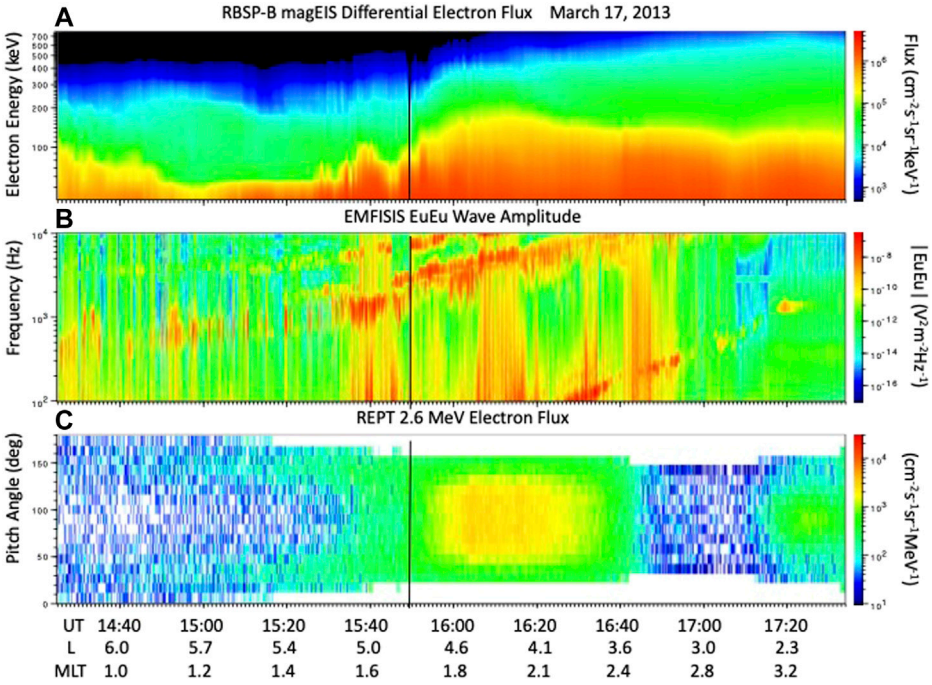

FIGURE 2
RBSP-B *in situ* observations following the format of Figure 1. The black line marks the spacecraft location (L ~ 4.8; 1.7 MLT) at 15:50 UT. RBSP-B observed pre-recovery background conditions across L 6 to 4.8 as it preceded RBSP-A by ~ 1 h. **(A)** MagEIS spectogram of lower energy electron flux. **(B)** EMFISIS WFR electric field spectorgram. **(C)** Pitch angle dependence of REPT 2.6 MeV electron flux.

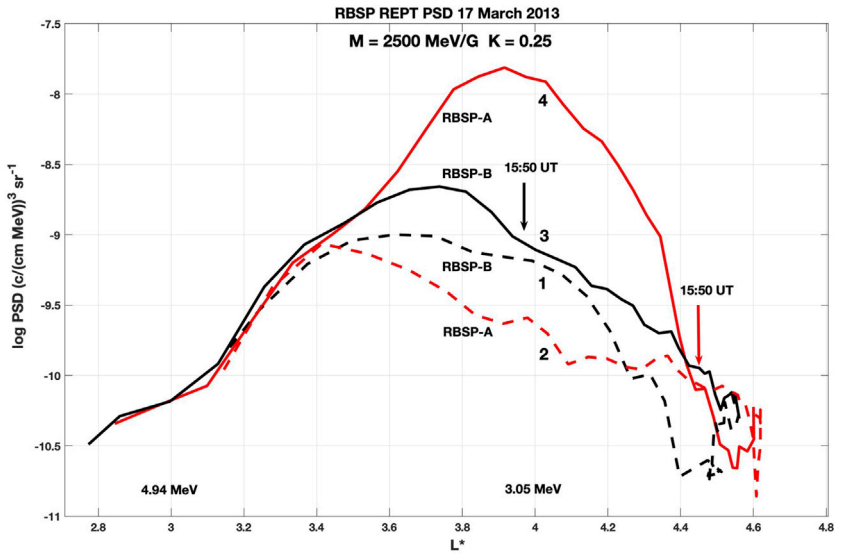

FIGURE 3
Van Allen Probes A and B power spectral density (PSD) vs. L plots showing the onset of the rapid recovery at 15:50 UT seen in Figure 1A. Curve numbers indicate the order in which the spacecraft crossed L* = 4 as RBSP-B preceded RBSP-A by ~ 1 h along successive outbound (dashed curves 1 and 2) and inbound (solid curves 3 and 4) orbits. A 10x increase in 2,500 MeV/G PSD observed by RBSP-A was associated with the injections and development of strong VLF risers.

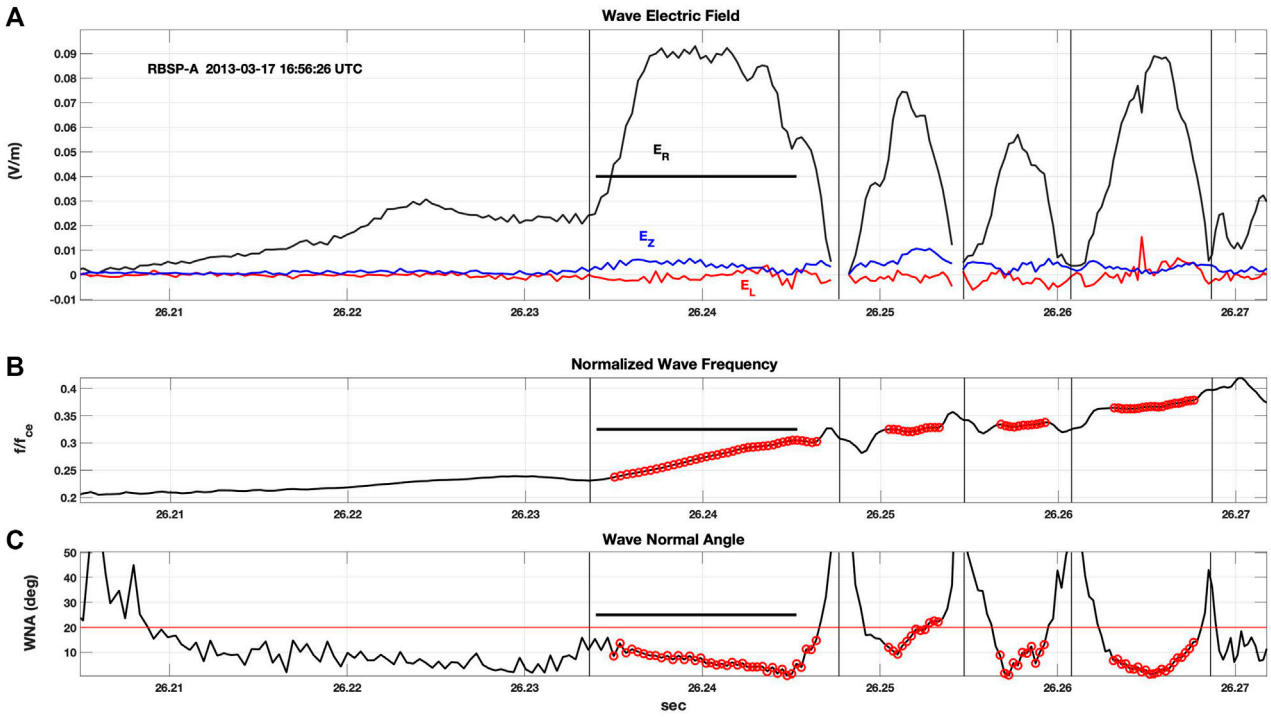

FIGURE 4
Five well-defined subpackets are seen during a strong chorus element at 16:56:26 UT. A black horizontal line in each panel highlights the 11 ms interval further analyzed and described in Figures 5, 6, 9–11. **(A)** Magnetic field aligned (E_Z) and right (E_R) and left (E_L) circularly polarized components of the wave electric field reveal an initial slowly growing subpacket followed by a second strong subpacket with E_R reaching 80 mV/m. **(B)** Normalized wave frequency (f/f_{ce} local) rises steeply during the strong second subpacket. Time intervals with $E_R > 40$ mV/v are highlighted in red in all panels.**(C)** Subpacket development is characterized by wave normal angle (WNA) < 20 deg (red line). During the second subpacket WNA decreases steadily from 16 deg to 2 deg.

determining wave magnetic and electric field components, wave frequency, wave vector, and wave normal angle on a wave cycle by cycle basis. An example of this analysis is shown in Figure 4 for a 65 msec segment of the chorus element highlighted in the theoretical study of Omura et al., 2019. E_R, the right hand circularly polarized wave electric field, is the dominant wave component throughout the chorus element [panel (a)].

The chorus element shown in Figure 4 displays five clear subpackets (Santolik et al., 2014). Foster et al., 2021 give a detailed description of the characteristics of the strong subpacket structure observed during the 17 March 2013 event. At the point of observation (L ~ 5.0, magnetic latitude −3.8 deg), f_{pe}/f_{ce} = 3.2. An initial long (>20 ms) coherent subpacket (times <26.233 s) exhibits slowly rising frequency [panel (b)], and wave normal angle (WNA) < 20 deg [panel (c)]. A second stronger subpacket centered near 1/4 f_{ce} at the point of observation (~26.24 s) exhibits rapidly rising frequency (df/dt) and small WNA <10 deg. Figure 5 presents wave magnetic field, Bw, and phase (Δt measured across 5 half wave cycles). Wave frequency and phase vary smoothly both within these first and second subpackets and across the transition between them, providing appropriate conditions for continuous resonant electron phase trapping and leading to good potential for MeV electron acceleration. Pronounced phase discontinuities are seen between higher order subpackets. As described by Zhang et al., 2020, such jumps in phase would cause de-trapping of electrons, and reduce energization caused by phase trapping. The noticeable frequency dip between first and second subpackets has been reported previously in Van Allen Probes observations (Santolik et al., 2014; Foster et al., 2021) and is in keeping with numerical simulations of chorus elements (Hanzelka et al., 2020). Foster et al., 2021 has shown the relative contributions of first and second subpackets to electron energization. In the following we address nonlinear effects associated with a single subpacket and limit our discussion to the strong second subpacket, shown by the black horizontal lines in Figure 4.

4 Pitch angle effects

The simulation studies of Hiraga and Omura (2020) examined electron trapping and acceleration for seed electrons with a wide range of pitch angles. They find that the

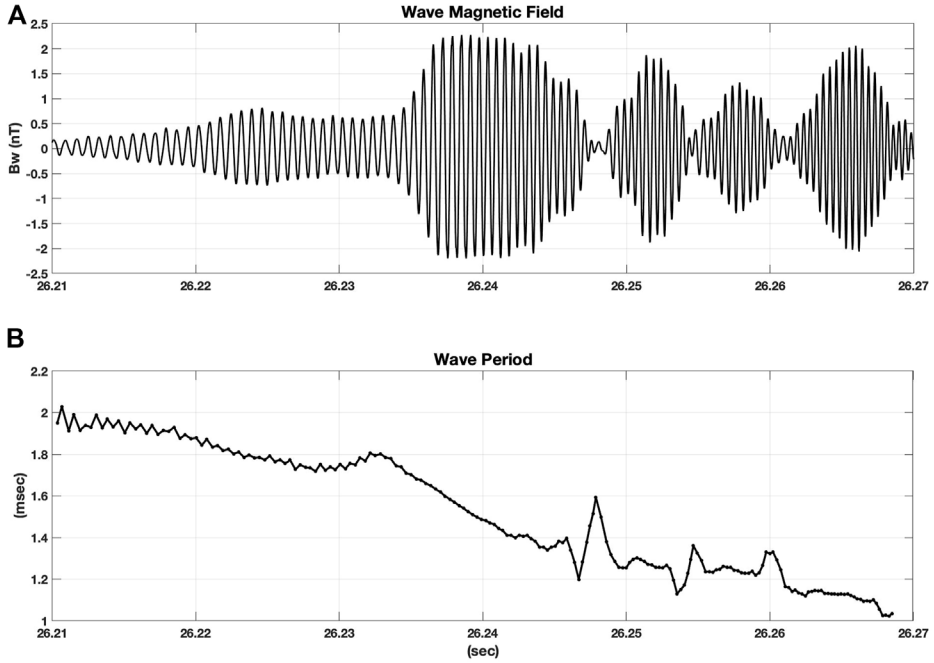

FIGURE 5
(A) Wave magnetic field (Bw)for the chorus element shown in Figure 4 exhibits a smooth transition between the first and second subpackets at ~ 26.233 s |Bw| exceeds 2.2 nT during the strong second subpacket.**(B)** A smooth phase transition occurred between the first and second subpackets with sharp discontinuities across higher order subpacket transitions. Wave period is determined across 2.5 wave cycles at 1/2 wave cycle intervals for Bw shown in panel **(A)**.

interrelationship between the chorus wave propagation velocity and the electron velocity parallel to Earth's magnetic field is an important condition for ultra-relativistic acceleration (URA; Summers and Omura (2007); Omura et al., 2007). When wave propagation and parallel electron velocities are nearly the same, chorus waves cannot interact with electrons traveling in the same direction as the wave propagation. Electrons with higher or lower initial equatorial pitch angles, however, interact with a chorus wave by being either overtaken or catching up with the chorus wave.

The formulae used in our study determine the resonant velocity and pitch angle for electrons of a given energy that are separately in cyclotron or Landau resonance with waves at frequency ω. Eq. 1 gives the relativistic formula for the nth-order electron resonance velocity $V_R^{(n)}$ where Ω_e is the local electron cyclotron frequency, γ is the relativistic Lorentz factor for an electron of given energy, and $k_{||}$ is the magnetic field-aligned component of the wave vector.

$$V_R^{(n)} = \frac{1}{k_\parallel}\left(\omega - \frac{n\Omega_e}{\gamma}\right) \quad (1)$$

For the chorus element indicated in Figure 4, the pitch angles for 500 keV–5 MeV cyclotron resonant electrons were <10 deg from perpendicularity as shown in Figure 6A. At lower energies (<~1 MeV) resonant electron velocities are oppositely directed to the wave propagation and the pitch angles are >90 deg. For Landau resonance, n = 0 and $V_R = \omega/k_{||}$, the field-aligned wave phase velocity is important. As seen in Figure 6B, pitch angles for relativistic Landau resonant electrons lie in the narrow range of 80–83 deg at the off-equatorial point of observation.

Our calculations of energy increase for a given initial electron energy in Section 6 consider only those electrons with a resonant pitch angle (i.e. a fraction of the overall population). We note that for electrons of given energy the pitch angles for Landau and cyclotron resonance differ.

5 Off-equatorial effects on subpacket structure

Van Allen Probes measurements of the chorus waveform are made at a fixed location along the magnetic field line, some distance from the chorus subpacket source region near the equator. Wave frequencies within the rising tone chorus element are fixed in the near-equatorial critical region of wave generation where wave growth is dominated by the df/dt term in S. However, several subsequent processes

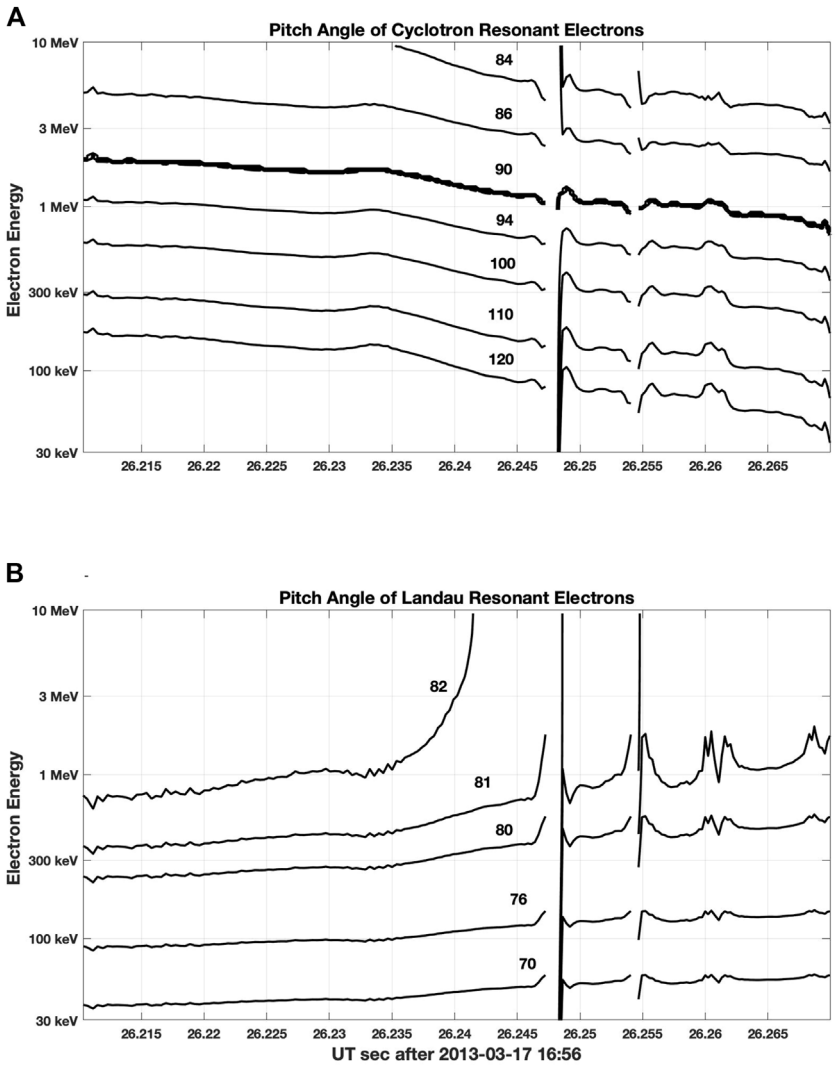

FIGURE 6
Pitch angles for seed electrons resonant with the strong chorus subpacket shown in Figure 4 are shown for **(A)** cyclotron resonant electrons, and **(B)** Landau resonant electrons. For pitch angles >90 deg, the resonance velocity V_R is negative.

alter the strength and appearance of the waveform as the subpacket propagates to the observation point off the equatorial plane.

Van Allen Probes observations (Santolik et al., 2014) indicate that chorus generation within the critical region near the equator is characterized by continuous rising frequency (positive df/dt) arising from optimum nonlinear wave growth conditions. Theory shows that beyond the critical distance away from the equator, convective wave growth saturates when the flux of resonant electrons decreases as the absolute resonance velocity value increases (Omura, 2021). Katoh and Omura (2013; 2016) confirm through simulation that beyond the critical distance, nonlinear wave growth cannot occur as the optimum amplitude of growth becomes less than the threshold amplitude for triggered growth. Our observations in this study are outside the critical distance.

5.1 Frequency dispersion

From magnetoionic propagation considerations, frequency dispersion of VLF waves in the magnetosphere can lead to pronounced distortions of the frequency sweep rate observed at distances away from the source, as observed in whistlers (Storey, 1953). Prominent in our off-equator observations of strong chorus elements is a large-amplitude second subpacket with steep frequency sweep rate, df/dt, near

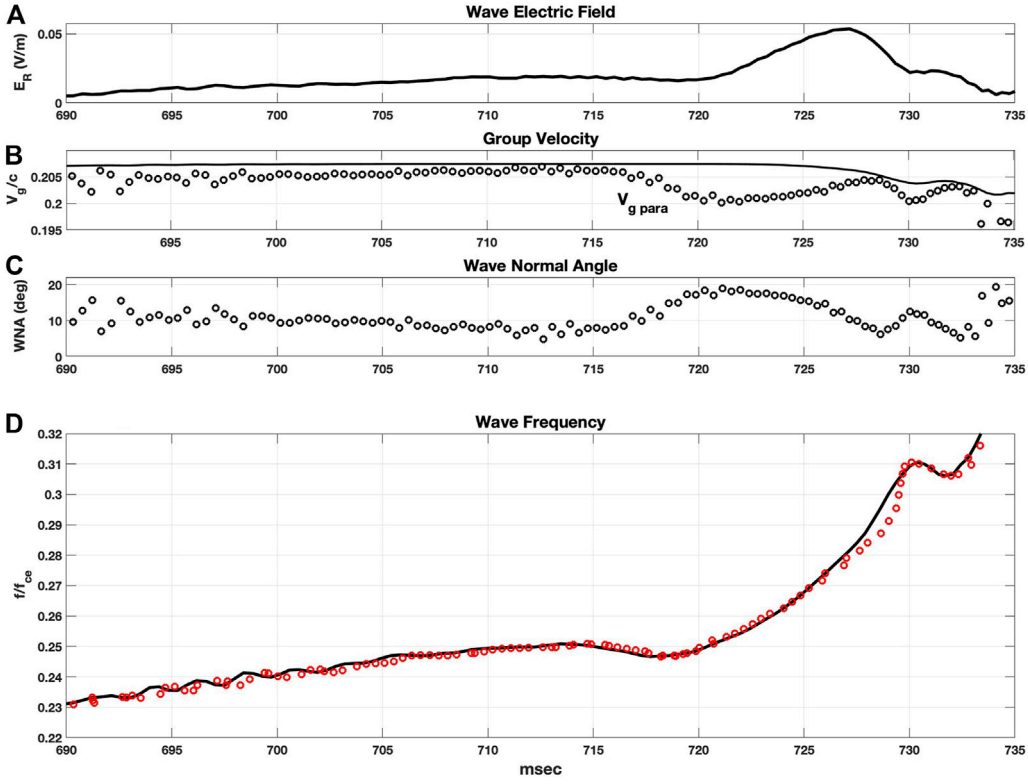

FIGURE 7
Wave parameters evaluated at each 1/2 wave cycle for a chorus wave element observed during the 17 March 2013 event at 16:39:07 UT are shown in black. **(A)** Wave electric field (E_R) shows an initial weak subpacket (690–720 msec) ans a strong (50 mV/m) second subpacket (720–730 msec). **(B)** Wave group velocity is shown by the solid curve while the parallel group velocity, including the effects of varying wave normal angle, is shown as circles. **(C)** Low wave normal angle (<20 deg) is observed through both subpackets with significant variation across the second subpacket. **(D)** The frequency sweep rate observed at the off-equatorial location is shown as the solid black curve. Back projection 3,000 km toward the equator using the observed values of $V_{g\ para}$ estimates the chorus sweep rate profile at the equator (red circles, shifted forward in time 50 msec for comparison with the observed profile).

the local value of 1/4 f_{ce} (cf. Figure 4). When frequency dispersion is active, as constant-frequency wave elements propagate away from the equator, frequencies with greater field-aligned wave velocities catch up with slower wave elements. This leads to a distortion of the observed frequency sweep rate, and such distortion will increase with distance, x, away from the wave generation region. Foster et al. (2021) suggested two potential dispersive processes that could alter the chorus element waveform observed at an off-equatorial location. First, the wave group velocity (V_g) has a maximum at frequencies near the local value of 1/4 f_{ce}. Second, the observed decrease in wave normal angle (WNA) as the wave amplitude increases provides a further increase in parallel propagation velocity. Both such effects could be significant for the strong subpackets observed near 1/4 f_{ce} at the Van Allen Probes location.

For each subpacket, observations, theory, and simulations all indicate a continuous rising frequency generated in the region of chorus development near the equator. To examine the effect of subsequent trajectory-dependent variations of the parallel group velocity ($V_{g\ para}$) on the observed chorus element waveform, we have constructed a simple model using as input the values of df/dt, V_g, and WNA for a chorus wave element observed during the 17 March 2013 event at 16:39:07 UT (L = 5.2; MLT = 2.1; maglat = −4.4). By first combining Vg and WNA to produce an effective $V_{g\ para}$, we then back-project each observed frequency element toward the equator in 1/4 msec steps to estimate the frequency sweep profile at a given distance, −x, upstream from the point of observation. For simplicity and to reflect the qualitative nature of this model, in the calculation, $V_{g\ para}$ is held constant for each frequency and no variation of f_{ce} along the field line has been included. Figure 7 presents the observed variation of wave electric field amplitude, group velocity, wave normal angle, and frequency in panels (a), (b), (c), and (d) respectively. All parameters are calculated at each 1/2 wave cycle following the method of Foster et al., 2017. The resulting back-projected frequency

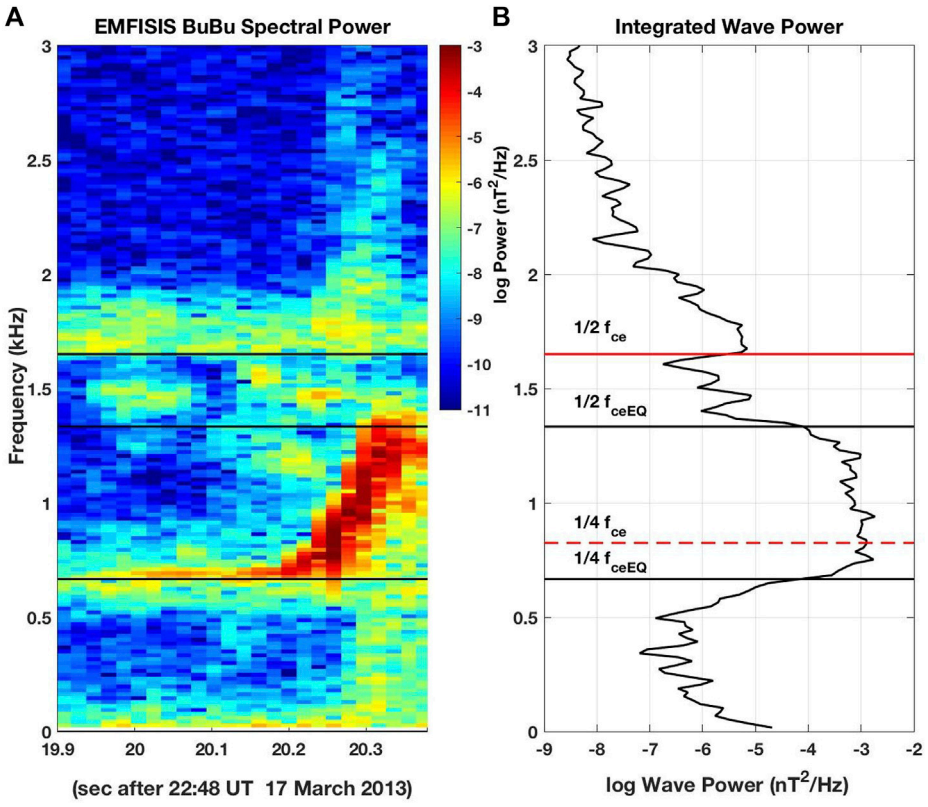

FIGURE 8
(A) The magnetic field spectrogram observed near L = 6.5 by Van Allen Probe B at 22:48:20 UT on 17 March 2013 exhibited clear damping at frequencies below 1/2 the local electron cyclotron frequency (1/2 f_{ce}). **(B)** Integrated signal power at each frequency is shown for the ~400 ms of observations shown in **(A)**. The local value of f_{ce} is observed at the spacecraft and the equatorial value of f_{ceEQ} is determined from the characteristics of the damping of the chorus element (from Foster et al. (2021)).

sweep rate at x = −3,000 km (the approximate distance to the equator) is shown as red circles overplotted on the off-equatorial observation in (d). These model results show that variations in $V_{g\ para}$ can, by themselves, produce a noticeable, but small, sweep rate distortion associated most closely with the decrease and increase of WNA during the strong second subpacket (720–730 msec).

The dominant sweep rate characteristics, such as the steeply rising frequency observed in the strong second subpackets described in Foster et al., 2021, most likely are formed within the critical region of wave generation near the equator as described by e.g. Omura (2021). Beyond this region, however, the propagation effects just described generally depend on the variation of V_g and WNA with frequency. We note that the level of variation of $V_{g\ para}$ for the case shown in Figure 7 is typical of that seen in our off-equatorial chorus observations. However, this match is not universally the case. For example, modeling of observations with nearly constant V_g and WNA across the observed waveform would result in no frequency distortion and no distortion of df/dt. (Ultimately, the actual variation of V_g and WNA along the wave trajectory is not known from measurements at a single location.) In addition, the variations of plasma density and magnetic field along the particle trajectory would change the frequency dependence of V_g and the normalized frequency (f/f_{ce}) for each wave element, producing a different waveform distortion. However, despite its simplicity, the model results shown in Figure 7, and their general agreement with aspects of the observed frequency variation in subpackets, suggest that frequency dispersion effects can make a noticeable contribution to the characteristics of the chorus element waveform observed at an off-equatorial location.

5.2 Damping at ½ f_{ce}

The structure of the chorus wave element also changes as it propagates away from the equator into regions of increasing magnetic field. Both Tsurutani and Smith (1974) and Omura

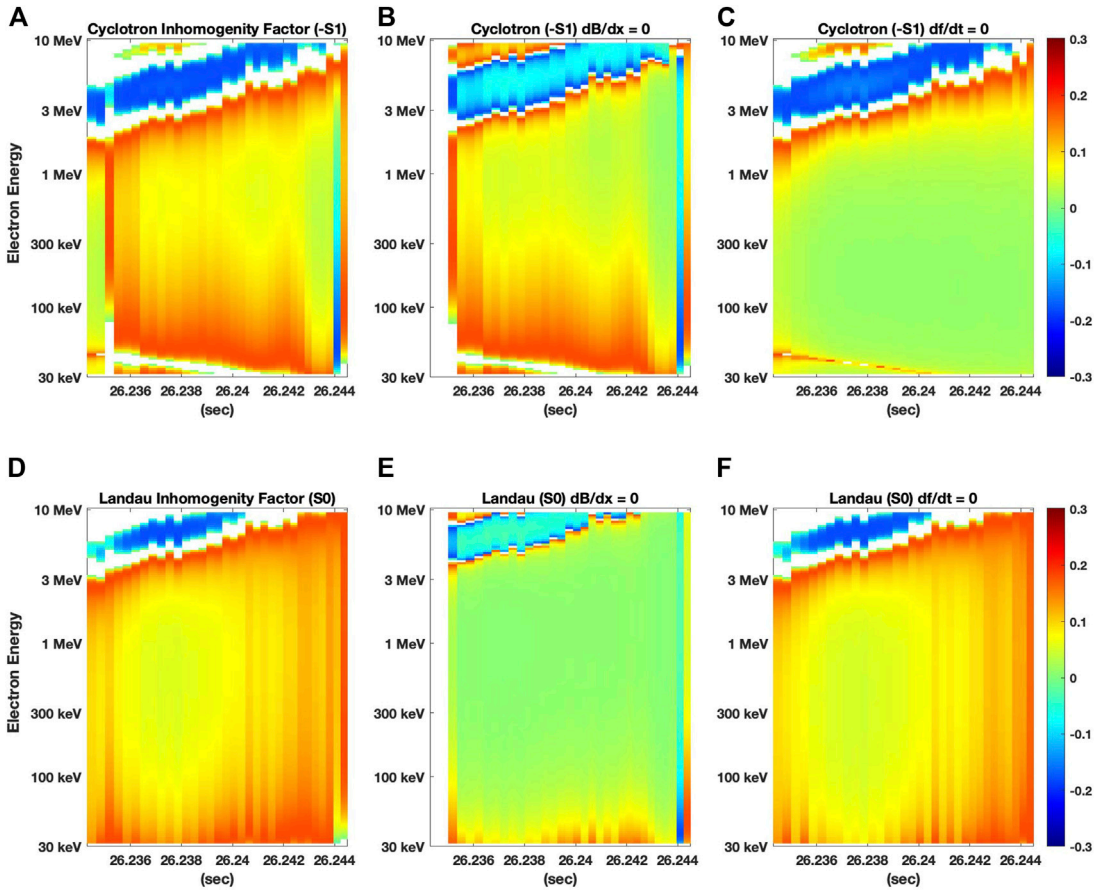

FIGURE 9
The nonlinear inhomogeneity factors for cyclotron (−S1) and Landau (S0) resonance are shown in the upper and lower panels respectively. S factors have been calculated wave cycle by cycle for a range of resonant electron energies for the subpacket indicated in Figure 4. Each value of S1 and S0 has been multiplied by the trapping potential in velocity phase space, F (|S|). White regions on each panel indicate that |S| > 1 where F (|S|) = 0 and trapping does not take place (see text). **(A,D)** present the full calculations for S1 and S0 including both df/dt and dB/dx terms. For panels **(B,E)**, dB/dx has been set to zero. In **(C,F)**, df/dt = 0.

et al. (2019) predict a gap in chorus at 0.5 f_{ce} due to nonlinear damping. Damping at the local value of ½ f_{ce} progressively erodes wave amplitude at frequencies above ½ f_{ceEQ}. As a result, away from the equator, chorus elements are divided into lower and upper band emissions by a pronounced amplitude minimum below the local value ½ f_{ce} [e.g. Tsurutani and Smith (1974)]. Figure 8 presents an example of this effect, plotting magnetic field spectral power as a function of time and focusing on the gap between the lower and upper band emissions. Integrated signal power across the ~400 ms of observations shown in panel (A) is plotted in panel (B), and clearly identifies ½ f_{ceEQ} as the point of onset of the ~1,000x decrease in the lower band chorus element integrated wave power. Thus determined, the value of f_{ceEQ} also indicates that the frequency of initial chorus element wave growth occurred near 0.25 f_{ceEQ}. The wave power damping seen between ½ f_{ce} and ½ f_{ceEQ} is in keeping with the nonlinear damping mechanism described by Hsieh and Omura (2018). We cannot prove that the gap between the lower and upper chorus bands is due to nonlinear damping, but its observation is consistent with that mechanism.

Beside nonlinear damping around 1/2 f_{ce}, several other plausible models exist for the observed lower-upper band gap. Li et al. (2010) states that very isotropic distributions at a few keV produced by Landau resonance are commonly observed in dayside THEMIS data and would contribute to chorus gap formation. Li et al. (2019) use simulations to state that initially excited single-band chorus waves alter the electron distribution immediately via Landau resonance (and suppress it at medium energies), naturally dividing electron anisotropy into low and high energy components exciting upper-band and lower-band chorus waves, respectively. Gao et al. (2016; 2019) posit a natural

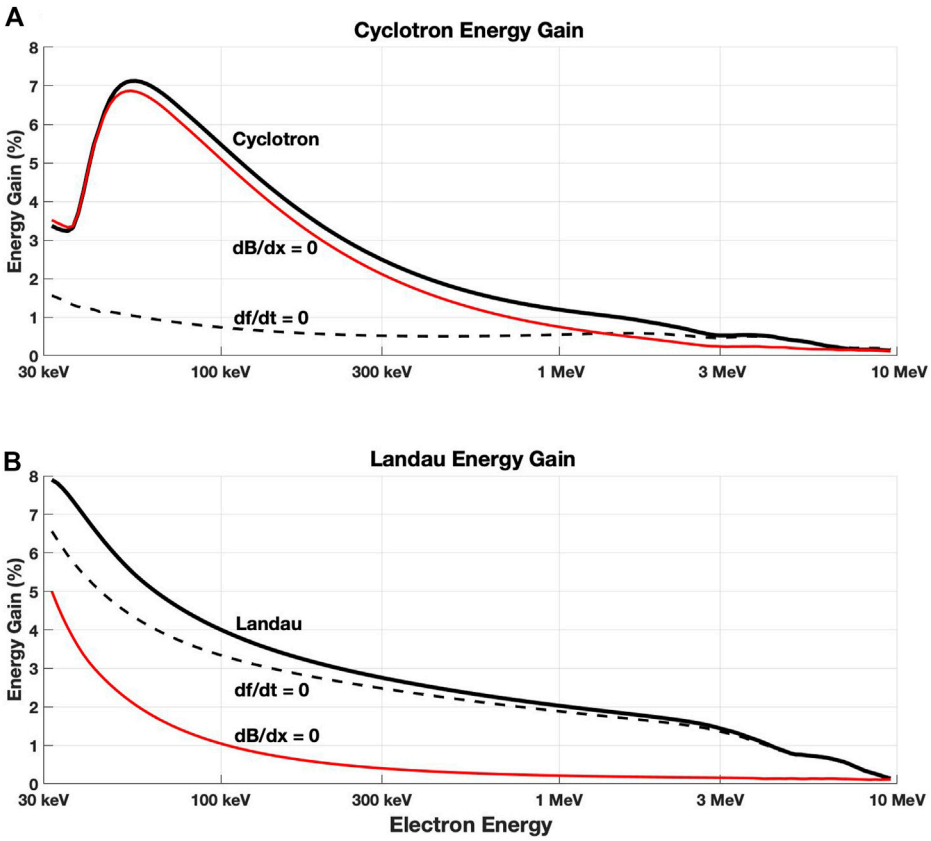

FIGURE 10
Percent energy gain (solid black curves) for electrons with for 30 keV–10 MeV initial energy in cyclotron **(A)** or Landau **(B)** resonance is shown assuming the electrons remain trapped across the 11 ms subpacket indicated in Figure 4. Panels **(A)** and **(B)** respectively show the S-factor dependencies of the cyclotron and Landau energization. For the black dashed curves in both panels the contribution to the electron energization from only the dB/dx gradient term is shown (df/dt has been set to zero). For the red curves the dB/dx terms have been set to zero in the inhomogeneity factors such that the only the contribution to the electron energization is from the frequency variation.

chorus gap emerging from upper band chorus excitation through lower band cascade and second harmonic generation. Simulations by Fu et al. (2014) predict that warm and hot chorus components separately drive quasi-electrostatic upper band and electromagnetic lower band emissions, resulting in a gap. Fu et al. (2015) predict power gaps at several frequencies (including 0.5 fce) due to sub-cyclotron resonances between oblique chorus and thermal electrons.

6 Relativistic electron acceleration—Effect of the inhomogeneity factor

For acceleration of energetic electrons, both a smooth frequency increase and a gradient of the magnetic field are needed at appropriate magnitudes. Zhang et al., 2018 have investigated the properties of intense chorus waves, i.e. those capable of nonlinearly resonating with electrons. They find that 10–15% of chorus wave packets have sufficient effective wave amplitude (B_w > 2–3 nT) for nonlinear interaction to occur and that longer wave packets (>10 wave cycles) are needed to produce a significant energy increase for trapped electrons.

The formula for the nonlinear inhomogeneity factor S has two terms (Eq. 2). The first depends on the frequency sweep rate, df/dt, and the second on the gradient of the magnetic field along the field line, dB/dx. Coefficients A and B are derived in Omura et al., 2019 for each nonlinear resonance. Near the magnetic equator where dB/dx is ~0 or very small, *S* is determined by the frequency sweep rate df/dt, which is nearly constant through propagation of the wave packet away from the equator. The critical distance away from the equator identifies the location marked by a change of the dominant term of the inhomogeneity factor. Within the critical region, triggering of nonlinear wave growth due to frequency variation is possible and this can be

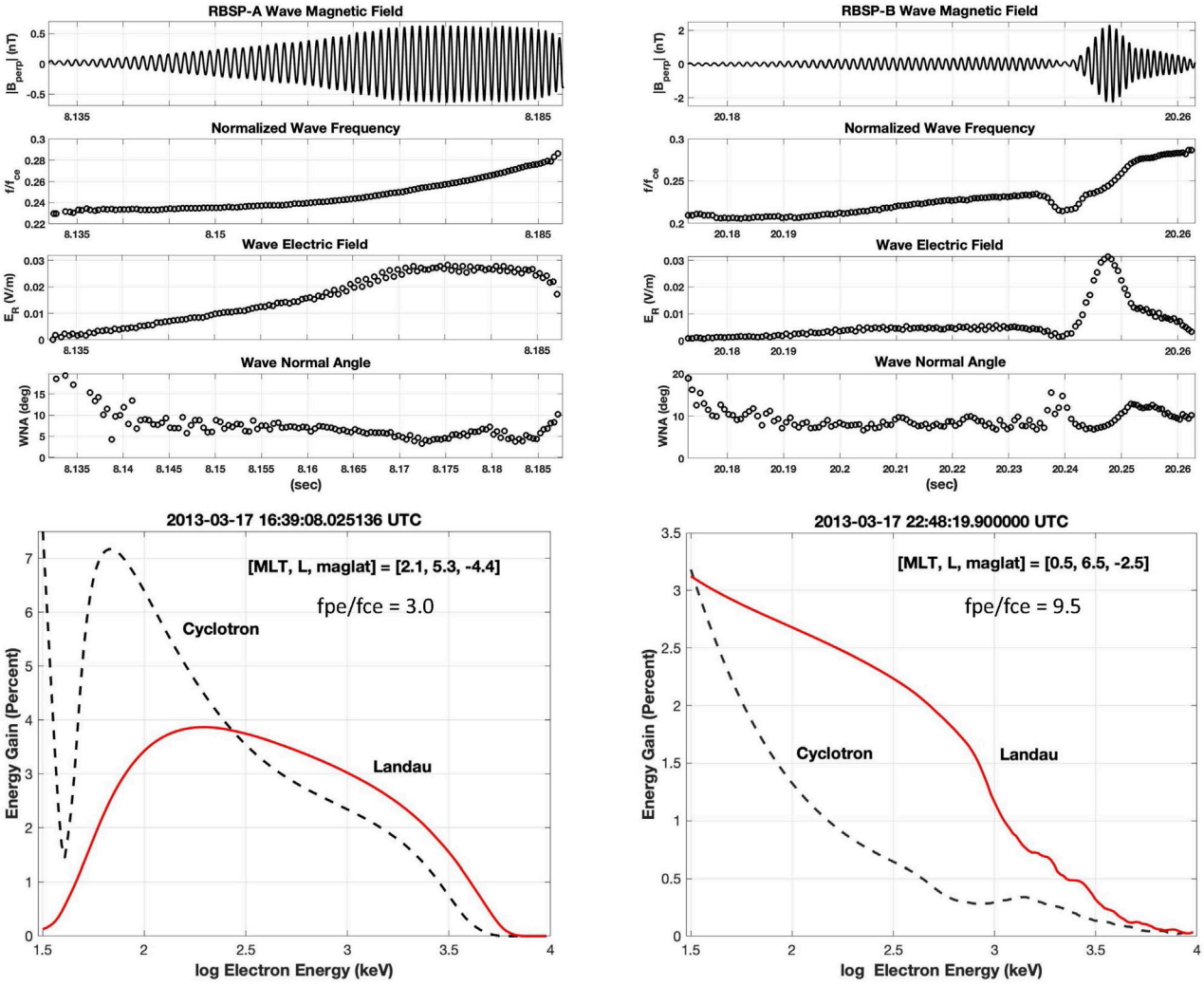

FIGURE 11
Examples of chorus wave elements observed during different injection/acceleration events on 17 March 2013 are shown for RBSP-A at 5.3 R_E (left panels) and RPSP-B at L = 6.5 R_E (right panels). (top panels) Wave magnetic field, normalized wave frequency, wave electric field, and wave normal angle. (bottom panels) Percent energy for seed electrons with for 30 keV–10 MeV initial energy in cyclotron (dashed curve) or Landau (red curve) resonance.

regarded as the generation region of the subpackets forming chorus emissions. Whether inside or outside the critical region, we can make the simplified form of S as

$$S = A\frac{df}{dt} + B\frac{dB}{dx} \quad (2)$$

The Van Allen Probes observations during the 17 March 2013 event were taken at magnetic latitude = −3.8 deg, outside the critical distance. To examine the relative importance of the individual terms in the inhomogeneity factor at this off-equatorial location, we use a maximum effect approach and artificially set either df/dt or dB/dx to 0 for S0 and S1 in the equations for cyclotron (S1) and Landau (S0) electron energization in Omura et al., 2019).

6.1 Off-equatorials S factor

In Figure 9, we present cycle by cycle calculations of cyclotron and Landau inhomogeneity factors as functions of initial electron energy and time across the single strong second subpacket indicated by the horizontal black line in Figure 4. For that 11 ms (19 wave cycles) subpacket, $|E_R|$ = 84 mV/m, $|B_R|$ =

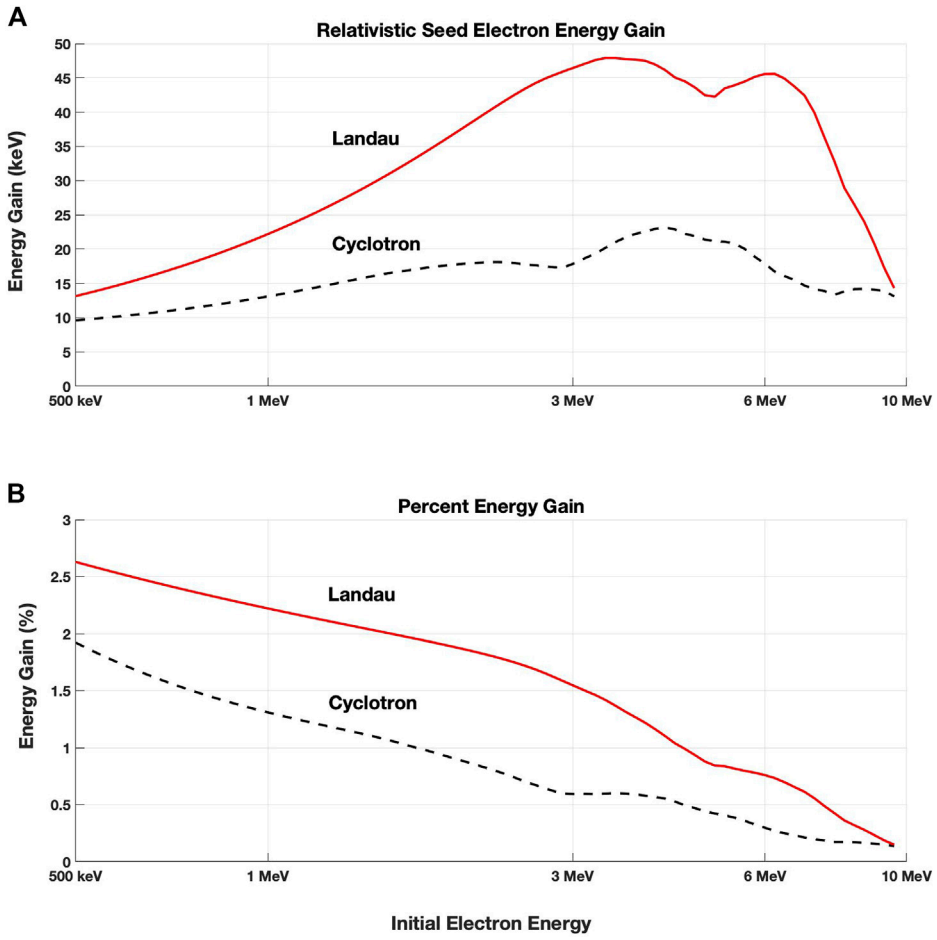

FIGURE 12
Nonlinear energy gain is shown for relativistic and ultra-relativistic seed electrons. **(A)** Energy gains for cyclotron and Landau resonant electrons are shown separately. Landau resonant energization exceeds cyclotron energization at all energies. **(B)** 0.5%–2% energy gain is determined for highly-relativistic and ultra-relativistic seed electrons in their ~11 ms nonlinear interaction with the single strong subpacket denoted in Figure 4.

2 nT. Local conditions for RBSP-A at 16:56 UT were L = 4.9, MLT = 2.3, magnetic latitude = −3.8 deg, local f_{ce} = 6,050 Hz, f_{pe} = 19,440 Hz, f_{pe}/f_{ce} = 3.2. For the gradient terms, dω/dt = 2.5e5 radians/sec and $d\omega_{ce}/dx$ = 9.0e-4 radians s^{-1} m^{-1}. White regions on each panel indicate that |S| > 1, at which point trapping does not take place. The number of trapped particles decreases to 0 as |S| increases from 0 to 1 as the size of the trapping potential in velocity phase space, F(|S|) is given by equation 71 of Omura et al., 2019, shrinks to zero. The values of S0 and S1, plotted in Figure 9 and used in the subsequent sections to determine electron energy gain, have been multiplied by F(|S0|) or F(|S1|) respectively. The fraction of trapped electrons is a decreasing function of |S|, in a manner such that S *F(|S|) for maximal nonlinear acceleration occurs when |S| ~ 0.4.

Panels (A) and (D) of Figure 9 present the full calculations for S1 and S0 including both df/dt and dB/dx terms. For panels (B) and (E), the magnetic field gradient has been set to zero, leaving only the contribution from the df/dt terms to contribute. Conversely, in panels (C) and (F), df/dt = 0. Panel (B) indicates that cyclotron acceleration at MeV energies is significantly reduced when the dB/dx term is cancelled, while cyclotron acceleration is nearly unchanged at sub-relativistic seed energies. Panel (E) indicates that the Landau S0 factor is significantly at all relativistic electron energies when the magnetic field gradient is zero or very small. Cyclotron acceleration at MeV energies is significant, although reduced somewhat, while nearly eliminated completely at non-relativistic energies when frequency sweep rate (df/dt) is near zero [cf. Panel (C)].

For the majority of the Van Allen Probes cases we've examined, the dB/dx term dominates the df/dt term in determining the S factor in keeping with the location of our observing points outside the critical region. It is to be noted,

however, that the critical region relates to nonlinear chorus generation, not to the acceleration of seed electrons.

6.2 S factor dependance of electron energy gain

Having derived full and modified S factors, we can proceed with energy gain calculations for seed electrons for each of the cases shown in Figure 9. As discussed in Section 4, pitch angles differ for electrons in cyclotron or Landau resonance at a given energy so that these different populations are treated separately. In Figure 10, panels 1) and 2) break down the total cyclotron and total Landau contributions to the energization for 30 keV–10 MeV initial electron energies, making the assumption that electrons remain trapped across the entire 11 ms segment of the subpacket indicated in Figure 4. In panels 1) and 2) the solid black curve shows the percent energy gain calculated from equations 69 or 62 in Omura et al., 2019 respectively with both df/dt and dB/dx terms in S1 and S0 unaltered. For the black dashed curves in each panel the contribution to the electron energization from only the dB/dx gradient term is shown (df/dt has been set to zero). Conversely, for the red curves, the dB/dx terms have been set to zero in the inhomogeneity factors and only the contribution from the frequency variation is shown. Again, it is important to remember that our calculations of seed electron energy gain relate to the specific conditions at the point of the observations.

Comparing the solid black curves in Figure 10, it is apparent that cyclotron acceleration is dominant for this individual subpacket at this off-equatorial location for the energization of sub-relativistic seed electrons with energies <250 keV and negative pitch angles of −20 to −30 deg. However, at relativistic energies >500 keV, Landau acceleration is dominant for electrons with ~80 deg pitch angle. Setting the df/dt term to zero reduces the cyclotron energization by up to 60% for non-relativistic seed electrons [panel (a)], while the Landau energization is little changed when df/dt = 0 [panel (b)]. Setting dB/dx to zero results in a minor decrease in cyclotron energization but decreases the Landau energization at all seed energies, reducing the dominant Landau energization by 90^{+} % for relativistic electrons.

The presentation of our analysis of S-function effects and radiation belt electron energization has focused on a single strong chorus wave subpacket observed during the onset of the MeV radiation belt electron recovery event on 17 March 2013. We have performed similar analyses for multiple chorus elements observed at different times and L-space locations during different storms, with similar results and conclusions (Foster et al., 2021 discusses aspects of several further examples). Many of the features presented here are repeatable in nearly every observation (strong second subpacket, steeply rising df/dt near the local value of 1/4 f_{ce}, dominance of cyclotron energization at sub-relativistic seed electron energies). However, there is significant variability among the different cases examined and this is important to remember for future studies aimed at generalizing these results. Figure 11 presents examples of chorus wave elements observed during separate injection/acceleration events on 17 March 2013 by RBSP-A (left panels) and RPSP-B (right panels). These cases differ significantly from the more usual observations shown in Figures 4, 7. RBSP-A (16:39 UT, L = 5.3) observed the smooth growth of an initial 50 msec subpacket to apparent saturation amplitude (E_R 30 mV/m; $|B_{perp}|$ 0.5 nT). For this case, cyclotron energization was dominant at electron energies <300 keV. During the later injection event described by Foster et al., 2014, RBSP-B (22:48 UT; L 6.5) observed weak cyclotron energization such that Landau resonance energization was dominant at all energies.

7 Summary and conclusion

We have examined characteristics and nonlinear effects of strong VLF chorus elements observed at the off-equatorial location of their Van Allen Probes observation. The strong chorus elements we have investigated have maximum wave amplitudes in the range $|E_w|$ ~ 20–100 mV/m. Large wave amplitude depends on a strong source (injection) of resonant electrons combined with proper conditions for the growth of long coherent wave subpackets. For the 16:56 UT subpacket analyzed in this study, frequency varied from 1,400–1900 Hz (0.23–0.31 f_{ce}) and wave growth was associated with the injection of 50–100 s keV resonant electrons as seen in Foster et al., 2021. We have shown the smooth frequency and phase transition between the initial and strong second subpackets, and have found that frequency dispersion can contribute to the chorus frequency sweep rate observed at an off-equatorial location. The frequency gap below 1/2 f_{ce} at the point of observation is consistent with the effects of the progressive erosion of wave amplitude at frequencies above ½ f_{ceEQ} by nonlinear damping near the local value of ½ f_{ce}.

The inhomogeneity factor S that controls the effectiveness of the nonlinear process for electron energization has important dependence on both the time rate of change of the wave frequency and the field-aligned gradient of the magnetic field. Cyclotron acceleration at < MeV energies is significantly reduced when df/dt is very small, and is little changed at all energies when dB/dx is reduced. Landau acceleration is greatly reduced at all relativistic energies when the magnetic field gradient very small and is slightly reduced at sub-relativistic energies when df/dt is very small.

Nonlinear acceleration by strong chorus waves applies both to seed electrons with sub-relativistic and relativistic initial energies. In Figure 12 we emphasize the considerable energy gain experienced by trapped seed electrons with relativistic (>500 keV) and ultra-relativistic (>3 MeV) initial energies. Trapped through with a single coherent subpacket, a 3 MeV electron can experience a 1.5% Landau energy gain in ~11 ms. Nonlinear Landau energy gain for a 6 MeV ultra-relativistic seed electron is 0.75% (45 keV). Significantly, these findings indicate that prompt local acceleration of highly relativistic and ultra-relativistic radiation belt electrons can take place directly through their nonlinear interaction with an individual VLF chorus element.

In general, the multiple *in situ* parameters available in the Van Allen Probes observations permit detailed examination of the features of the nonlinear theory of VLF chorus wave development and the acceleration of radiation belt electrons to MeV energy. In particular, the spacecraft observations provide important information on the chorus wave element at an off-equatorial nearly fixed position. This study analyzed a well sampled and strong subpacket to investigate the characteristics of the nonlinear inhomogeneity factors and their effect on sub-relativistic to relativistic electron acceleration. It is found in this particular case that cyclotron energization provides the dominant contribution at sub-relativistic electron energies while at energies >500 keV Landau acceleration provides the larger contribution. Future similar studies using a large sample of Van Allen Probes observed events can help generalize and advance understanding of this important acceleration pathway for radiation belt dynamics.

Data availability statement

Publicly available datasets were analyzed in this study. This data can be found here: Van Allen Probes observations used in this study can be obtained through instrument websites (EMFISIS wave data: http://emfisis.physics.uiowa.edu; MagEIS and REPT particle data: https://rbsp-ect.lanl.gov/rbsp_ect.php. PSD data presented in Figure 3 can be obtained through the Van Allen Probes Science Gateway (https://rbspgway.jhuapl.edu/psd). The S Functions and electron energy gain shown in Figures 9, 10, and 11 are calculated from the nonlinear formalism presented in Omura et al., 2019.

Author contributions

JF and PE shared in the conception and design of the study. JF performed the analysis of the observations, drafted the discussion and conclusions, and prepared the manuscript. All authors have reviewed the final manuscript and approve it for publication.

Funding

Research at the MIT Haystack Observatory was supported by the NASA Van Allen Probes (RBSP) funding provided under NASA prime contract NAS5-01072, including the EFW investigation (PI: J.R. Wygant, University of Minnesota), and the ECT investigation (PI: H. Spence, University of New Hampshire).

Acknowledgments

The authors thank Y. Omura for guidance and many discussions on nonlinear wave-particle interaction theory, and C. Kletzing and W. Kurth for assistance in obtaining the high-resolution EMFISIS wave observations, and the Reviewers for helpful comments. We acknowledge in particular the architects and contributors to the 'Autoplot' data browser (NASA Grant 05-S3CVO05-11) for its capabilities, which were important for this Van Allen Probes detailed analysis.

Conflict of interest

The authors declare that the research was conducted in the absence of any commercial or financial relationships that could be construed as a potential conflict of interest.

Publisher's note

References

Artemyev, A. V., Krasnoselskikh, V. V., Agapitov, O. V., Mourenas, D., and Rolland, G. (2012). Non-diffusive resonant acceleration of electrons in the radiation belts. *Phys. Plasmas* 19 (12), 122901. doi:10.1063/1.4769726

Baker, D. N., Foster, J. C., Erickson, P. J., Henderson, M. G., Kanekal, S. G., Reeves, G. D., et al. (2014). Gradual diffusion and punctuated phase space density enhancements of highly relativistic electrons: Van allen Probes observations. *Geophys. Res. Lett.* 41, 1351–1358. doi:10.1002/2013GL058942

Baker, D. N., Kanekal, S. G., Hoxie, V. C., Batiste, S., Bolton, M., Li, X., et al. (2012). The Relativistic electron-Proton Telescope (REPT) instrument on board the

Radiation Belt Storm Probes (RBSP) spacecraft: Characterization of Earth's radiation belt high-energy particle populations. *Space Sci. Rev.* 179, 337–381. doi:10.1007/s11214-012-9950-9

Blake, J. B., Carranza, P. A., Claudepierre, S. G., Clemmons, J. H., Crain, W. R., Dotan, Y., et al. (2013). The magnetic electron ion spectrometer (MagEIS) instruments aboard the radiation belt storm Probes (RBSP) spacecraft. *Space Sci. Rev.* 179, 383–421. doi:10.1007/s11214-013-9991-8

Chen, Y., Friedel, R. H. W., and Reeves, G. D. (2006). Phase space density distributions of energetic electrons in the outer radiation belt during two geospace environment modeling inner magnetosphere/Storms selected storms. *J. Geophys. Res.* 111, A11S04. doi:10.1029/2006JA011703

Demekhov, A. G., Trakhtengerts, V. Y., Rycroft, M. J., and Nunn, D. (2006). Electron acceleration in the magnetosphere by whistler-mode waves of varying frequency. *Geomagn. Aeron.* 46 (6), 711–716. doi:10.1134/s0016793206060053

Foster, J. C., Erickson, P. J., Baker, D. N., Claudepierre, S. G., Kletzing, C. A., Kurth, W., et al. (2014). Prompt energization of relativistic and highly relativistic electrons during a substorm interval: Van Allen Probes observations. *Geophys. Res. Lett.* 41, 20–25. doi:10.1002/2013GL058438

Foster, J. C., Erickson, P. J., Omura, Y., Baker, D. N., Kletzing, C. A., and Claudepierre, S. G. (2017). Van Allen Probes observations of prompt MeV radiation belt electron acceleration in nonlinear interactions with VLF chorus. *J. Geophys. Res. Space Phys.* 122, 324–339. doi:10.1002/2016JA023429

Foster, J. C., Rosenberg, T. J., and Lanzerotti, L. J. (1976). Magnetospheric conditions at the time of enhanced wave-particle interactions near the plasmapause. *J. Geophys. Res.* 81 (13), 2175–2182. doi:10.1029/JA081i013p02175

Foster, J. C., Erickson, P. J., and Omura, Y. (2021). Subpacket structure in strong VLF chorus rising tones: Characteristics and consequences for relativistic electron acceleration. *Earth Planets Space* 73, 140. doi:10.1186/s40623-021-01467-4

Fu, X., Cowee, M. M., Friedel, R. H., Funsten, H. O., Gary, S. P., Hospodarsky, G. B., et al. (2014). Whistler anisotropy instabilities as the source of banded chorus: Van Allen Probes observations and particle-in-cell simulations. *J. Geophys. Res. Space Phys.* 119, 8288–8298. doi:10.1002/2014JA020364

Fu, X., Guo, Z., Dong, C., and Gary, S. P. (2015). Nonlinear subcyclotron resonance as a formation mechanism for gaps in banded chorus. *Geophys. Res. Lett.* 42, 3150–3159. doi:10.1002/2015GL064182

Gao, X., Chen, L., Li, W., Lu, Q., and Wang, S. (2019). Statistical results of the power gap between lower-band and upper-band chorus waves. *Geophys. Res. Lett.* 46, 4098–4105. doi:10.1029/2019GL082140

Gao, X., Lu, Q., Bortnik, J., Li, W., Chen, L., and Wang, S. (2016). Generation of multiband chorus by lower band cascade in the Earth's magnetosphere. *Geophys. Res. Lett.* 43, 2343–2350. doi:10.1002/2016GL068313

Hanzelka, M., Santolík, O., Omura, Y., Kolmašová, I., and Kletzing, C. A. (2020). A model of the subpacket structure of rising tone chorus emissions. *J. Geophys. Res. Space Phys.* 125, e2020JA028094. doi:10.1029/2020JA028094

Hiraga, R., and Omura, Y. (2020). Acceleration mechanism of radiation belt electrons through interaction with multi-subpacket chorus waves. *Earth Planets Space* 72, 21. doi:10.1186/s40623-020-1134-3

Hsieh, Y. K., and Omura, Y. (2018). Nonlinear damping of oblique whistler mode waves via Landau resonance. *J. Geophys. Res. Space Phys.* 123, 7462–7472. doi:10.1029/2018JA025848

Jaynes, A. N., Baker, D. N., Singer, H. J., Rodriguez, J. V., Loto'aniu, T. M., Ali, A. F., et al. (2015). Source and seed populations for relativistic electrons: Their roles in radiation belt changes. *JGR. Space Phys.* 120, 7240–7254. doi:10.1002/2015JA021234

Katoh, Y., and Omura, Y. (2013). Effect of the background magnetic field inhomogeneity on generation processes of whistler-mode chorus and broadband hiss-like emissions. *J. Geophys. Res. Space Phys.* 118, 4189–4198. doi:10.1002/jgra.50395

Katoh, Y., and Omura, Y. (2016). Electron hybrid code simulation of whistler-mode chorus generation with real parameters in the Earth's inner magnetosphere. *Earth Planets Space* 68, 192. doi:10.1186/s40623-016-0568-0

Kletzing, C. A., Kurth, W. S., Acuna, M., MacDowell, R. J., Torbert, R. B., Averkamp, T., et al. (2012). The electric and magnetic field instrument and integrated science (EMFISIS) on RBSP. *Space Sci. Rev.* 179, 127. doi:10.1007/s11214-013-9993-6

Kubota, Y., and Omura, Y. (2018). Nonlinear dynamics of radiation belt electrons inter- acting with chorus emissions localized in longitude. *J. Geophys. Res. Space Phys.* 123, 4835–4857. doi:10.1029/2017JA025050

Li, J., Bortnik, J., An, X., Li, W., Angelopoulos, V., Thorne, R. M., et al. (2019). Origin of two-band chorus in the radiation belt of Earth. *Nat. Commun.* 10, 4672. doi:10.1038/s41467-019-12561-3

Li, W., Thorne, R. M., Nishimura, Y., Bortnik, J., Angelopoulos, V., McFadden, J. P., et al. (2010). THEMIS analysis of observed equatorial electron distributions responsible for the chorus excitation. *J. Geophys. Res.* 115, A00F11. doi:10.1029/2009JA014845

Mauk, B. H., Fox, N. J., Kanekal, S. G., Kessel, R. L., Sibeck, D. G., and Ukhorskiy, A. (2012). Science objectives and rationale for the radiation belt storm Probes mission. *Space Sci. Rev.* 179, 3–27. doi:10.1007/s11214-012-9908-y

Omura, Y., Hsieh, Y. K., Foster, J. C., Erickson, P. J., Kletzing, C. A., and Baker, D. N. (2019). Cyclotron acceleration of relativistic electrons through landau resonance with obliquely propagating whistler mode chorus emissions. *J. Geophys. Res. Space Phys.* 124, 2018JA026374–2810. doi:10.1029/2018JA026374

Omura, Y., Katoh, Y., and Summers, D. (2008). Theory and simulation of the generation of whistler-mode chorus. *J. Geophys. Res.* 113, A04223. doi:10.1029/2007JA012622

Omura, Y. (2021). Nonlinear wave growth theory of whistler-mode chorus and hiss emissions in the magnetosphere. *Earth Planets Space* 73, 95. doi:10.1186/s40623-021-01380-w

Omura, Y., Furuya, N., and Summers, D. (2007). Relativistic turning acceleration of resonant electrons by coherent whistler mode waves in a dipole magnetic field. *J. Geophys. Res.* 112, A06236. doi:10.1029/2006JA012243

Reeves, G. D., Spence, H. E., Henderson, M. G., Morley, S. K., Friedel, R. H. W., Funsten, H. O., et al. (2013). Electron acceleration in the heart of the Van Allen radiation belts. *Science* 341 (6149), 991–994. doi:10.1126/science.1237743

Santolik, O., Gurnett, D. A., Picket, J. S., Chum, J., and Cornilleau-Wehrlin, N. (2009). Oblique propagation of whistler mode waves in the chorus source region. *J. Geophys. Res.* 114, A04586. doi:10.1029/2009JA014586

Santolík, O., Kletzing, C. A., Kurth, W. S., Hospodarsky, G. B., and Bounds, S. R. (2014). Fine structure of large-amplitude chorus wave packets. *Geophys. Res. Lett.* 41, 293–299. doi:10.1002/2013GL058889

Storey, L. R. O. (1953). An investigation of whistling atmospherics. *Philosophical Trans. R. Soc. Lond. Ser. A, Math. Phys. Sci.* 246, 113–141. doi:10.1098/rsta.1953.0011

Summers, D., and Omura, Y. (2007). Ultra-relativistic acceleration of electrons in planetary magnetospheres. *Geophys. Res. Lett.* 34, L24205. doi:10.1029/2007GL032226

Tsurutani, B. T., and Smith, E. J. (1974). Postmidnight chorus: A substorm phenomenon. *J. Geophys. Res.* 79, 118–127. doi:10.1029/JA079i001p00118

Zhang, X.-J., Agapitov, O., Artemyev, A. V., Mourenas, D., Angelopoulos, V., Kurth, W. S., et al. (2020). Phase decoherence within intense chorus wave packets constrains the efficiency of nonlinear resonant electron acceleration. *Geophys. Res. Lett.* 47, e2020GL089807. doi:10.1029/2020GL089807

Zhang, X. J., Thorne, R., Artemyev, A., Mourenas, D., Angelopoulos, V., Bortnik, J., et al. (2018). Properties of intense field-aligned lower-band chorus waves: Implications for nonlinear wave-particle interactions. *JGR. Space Phys.* 123 (7), 5379–5393. doi:10.1029/2018JA025390

frontiers | Frontiers in Astronomy and Space Sciences

TYPE Mini Review
PUBLISHED 06 October 2022
DOI 10.3389/fspas.2022.1010133

OPEN ACCESS

EDITED BY
Oliver Allanson,
University of Exeter, United Kingdom

REVIEWED BY
Anton Artemyev,
University of California, Los Angeles, United States

*CORRESPONDENCE
Alain J. Brizard,
abrizard@smcvt.edu

SPECIALTY SECTION
This article was submitted to Space Physics, a section of the journal Frontiers in Astronomy and Space Sciences

RECEIVED 02 August 2022
ACCEPTED 22 August 2022
PUBLISHED 06 October 2022

CITATION
Brizard AJ and Chan AA (2022), Hamiltonian formulations of quasilinear theory for magnetized plasmas. *Front. Astron. Space Sci.* 9:1010133. doi: 10.3389/fspas.2022.1010133

Hamiltonian formulations of quasilinear theory for magnetized plasmas

Alain J. Brizard[1]* and Anthony A. Chan[2]

[1]Department of Physics, Saint Michael's College, Colchester, VT, United States, [2]Department of Physics and Astronomy, Rice University, Houston, TX, United States

Hamiltonian formulations of quasilinear theory are presented for the cases of uniform and nonuniform magnetized plasmas. First, the standard quasilinear theory of Kennel and Engelmann (Kennel, Phys. Fluids, 1966, 9, 2377) is reviewed and reinterpreted in terms of a general Hamiltonian formulation. Within this Hamiltonian representation, we present the transition from two-dimensional quasilinear diffusion in a spatially uniform magnetized background plasma to three-dimensional quasilinear diffusion in a spatially nonuniform magnetized background plasma based on our previous work (Brizard and Chan, Phys. Plasmas, 2001, 8, 4762–4771; Brizard and Chan, Phys. Plasmas, 2004, 11, 4220–4229). The resulting quasilinear theory for nonuniform magnetized plasmas yields a 3 × 3 diffusion tensor that naturally incorporates quasilinear radial diffusion as well as its synergistic connections to diffusion in two-dimensional invariant velocity space (e.g., energy and pitch angle).

KEYWORDS

quasilinear theory, guiding-center approximation, wave-particle resonance, Hamiltonian formulation, action-angle coordinates

1 Introduction

The complex interaction between charged particles and electromagnetic-field wave fluctuations in a magnetized plasma represents a formidable problem with crucial implications toward our understanding of magnetic confinement in laboratory and space plasmas (Kaufman and Cohen, 2019). These wave-particle interactions can be described either linearly, quasi-linearly, or nonlinearly, depending on how the background plasma is affected by the fluctuating wave fields and the level of plasma turbulence associated with them (Davidson, 1972).

In linear plasma wave theory (Stix, 1992), where the field fluctuations are arbitrarily small, the linearized perturbed Vlasov distribution of each charged-particle species describes the charged-particle response to the presence of small-amplitude electromagnetic waves which, when coupled to the linearized Maxwell wave equations, yields a wave spectrum that is supported by the uniform background magnetized plasma (Stix, 1992).

In weak plasma turbulence theory (Sagdeev and Galeev, 1969; Galeev and Sagdeev, 1983), the background plasma is considered weakly unstable so that a (possibly discrete) spectrum of field perturbations grow to finite but small amplitudes. While these small-

amplitude fluctuations interact weakly among themselves, they interact strongly with resonant particles, which satisfy a wave-particle resonance condition in particle phase space (described in terms of unperturbed particle orbits). These resonant wave-particle interactions, in turn, lead to a quasilinear modification of the background Vlasov distribution on a long time scale compared to the fluctuation time scale (Kaufman, 1972a; Dewar, 1973).

Lastly, in strong plasma turbulence theory (Dupree, 1966), nonlinear wave-wave and wave-particle-wave interactions cannot be neglected, and wave-particle resonances include perturbed particle orbits (Galeev and Sagdeev, 1983). The reader is referred to a pedagogical review by Krommes (Krommes, 2002) on the theoretical foundations of plasma turbulence as well as a recent study on the validity of quasilinear theory (Crews and Shumlak, 2022). In addition, the mathematical foundations of quasilinear theory for inhomogeneous plasma can be found in the recent work by Dodin (Dodin, 2022).

1.1 Motivation for this work

The primary purpose of the present paper is to present complementary views of two-dimensional quasilinear diffusion in a uniform magnetized plasma. First, we review the quasilinear theory derived by Kennel and Engelmann (Kennel and Engelmann, 1966), which represents the paradigm formulation upon which many subsequent quasilinear formulations are derived (Stix, 1992). (We mainly focus our attention on non-relativistic quasilinear theory in the text and summarize the extension to relativistic quasilinear theory in Supplementary Appendix A) As an alternative formulation of quasilinear theory, we present a Hamiltonian formulation that relies on the use of guiding-center theory for a uniform magnetic field (Cary and Brizard, 2009). In this Hamiltonian formulation, the quasilinear diffusion equation is described in terms of a diffusion tensor whose structure is naturally generalized to three-dimensional quasilinear diffusion in a nonuniform magnetized plasma, as shown in the works of Brizard and Chan (Brizard and Chan, 2001; Brizard and Chan, 2004).

Next, two formulations of three-dimensional quasilinear theory are be presented. First, we present a generic quasilinear formulation based on the action-angle formalism (Kaufman, 1972b; Mahajan and Chen, 1985), which applies to general magnetic-field geometries. This formulation is useful in highlighting the modular features of the quasilinear diffusion tensor. Our second three-dimensional quasilinear formulation is developed for the case of an axisymmetric magnetic field $\mathbf{B}_0 = \nabla\psi \times \nabla\varphi$, for which the drift action $\mathsf{J}_\mathrm{d} = q\psi/c$ is expressed simply in terms of the magnetic flux ψ. The presentation of this case is based on a summary of the non-relativistic limit of our previous work (Brizard and Chan, 2004).

1.2 Notation for quasilinear theory in a uniform magnetized plasma

In a homogeneous magnetic field $\mathbf{B}_0 = B_0\,\hat{\mathbf{z}}$, the unperturbed Vlasov distribution $f_0(\mathbf{v})$ (for a charged-particle species with charge q and mass M) is a function of velocity $\mathbf{v}$ alone and the perturbed Vlasov-Maxwell fields $(\delta f, \delta\mathbf{E}, \delta\mathbf{B})$ can be decomposed in terms of Fourier components: $\delta f = \delta\tilde{f}(\mathbf{v})\exp(i\vartheta) + \text{c.c.}$ and $(\delta\mathbf{E}, \delta\mathbf{B}) = (\delta\tilde{\mathbf{E}}, \delta\tilde{\mathbf{B}})\exp(i\vartheta) + \text{c.c.}$, where the wave phase is $\vartheta(\mathbf{x}, t) = \mathbf{k}\cdot\mathbf{x} - \omega\, t$ and the dependence of the eikonal (Fourier) amplitudes $(\delta\tilde{f}, \delta\tilde{\mathbf{E}}, \delta\tilde{\mathbf{B}})$ on $(\mathbf{k}, \omega)$, which is denoted by a tilde, is hidden. According to Faraday's law, we find $\delta\tilde{\mathbf{B}} = (\mathbf{k}c/\omega)\times\delta\tilde{\mathbf{E}}$, which implies $\mathbf{k}\cdot\delta\tilde{\mathbf{B}} = 0$. For the time being, however, we will keep the perturbed electric and magnetic fields separate, and assume that the uniform background plasma is perturbed by a monochromatic wave with definite wave vector $\mathbf{k}$ and wave frequency ω.

Following the notation used by Kennel and Engelmann (Kennel and Engelmann, 1966), the velocity $\mathbf{v}$ and wave vector $\mathbf{k}$ are decomposed in terms of cylindrical components

$$\left.\begin{aligned}\mathbf{v} &= v_\parallel\,\hat{\mathbf{z}} + v_\perp\left(\cos\phi\,\hat{\mathbf{x}} + \sin\phi\,\hat{\mathbf{y}}\right)\\ \mathbf{k} &= k_\parallel\,\hat{\mathbf{z}} + k_\perp\left(\cos\psi\,\hat{\mathbf{x}} + \sin\psi\,\hat{\mathbf{y}}\right)\end{aligned}\right\}, \tag{1.1}$$

so that $\mathbf{k}\cdot\mathbf{v} = k_\parallel v_\parallel + k_\perp v_\perp\cos(\phi-\psi)$, where ϕ is the gyroangle phase and ψ is the wave-vector phase. We note that the unperturbed Vlasov equation $\partial f_0/\partial\phi = 0$ implies that $f_0(\mathbf{v})$ is independent of the gyroangle ϕ, i.e., $f_0(v_\parallel, v_\perp)$. In what follows, we will use the definition

$$\begin{aligned}\frac{\mathbf{k}_\perp}{k_\perp} &= \cos\psi\,\hat{\mathbf{x}} + \sin\psi\,\hat{\mathbf{y}} = \frac{1}{2}\,e^{i\psi}\left(\hat{\mathbf{x}} - i\,\hat{\mathbf{y}}\right) + \frac{1}{2}\,e^{-i\psi}\left(\hat{\mathbf{x}} + i\,\hat{\mathbf{y}}\right)\\ &\equiv \frac{1}{\sqrt{2}}\left(\hat{\mathsf{K}} + \hat{\mathsf{K}}^*\right),\end{aligned} \tag{1.2}$$

and the identity

$$\frac{\mathbf{v}_\perp}{v_\perp} \equiv \hat{\perp} = \cos\phi\,\hat{\mathbf{x}} + \sin\phi\,\hat{\mathbf{y}} \equiv e^{i(\phi-\psi)}\hat{\mathsf{K}}\Big/\sqrt{2} + e^{-i(\phi-\psi)}\hat{\mathsf{K}}^*\Big/\sqrt{2}. \tag{1.3}$$

We note that, in the work of Kennel and Engelmann (Kennel and Engelmann, 1966), the right-handed polarized electric field is $\delta\tilde{E}_R \equiv \delta\tilde{\mathbf{E}}\cdot\hat{\mathsf{K}}\,e^{-i\psi}$ and the left-handed polarized electric field is $\delta\tilde{E}_L \equiv \delta\tilde{\mathbf{E}}\cdot\hat{\mathsf{K}}^*\,e^{i\psi}$; we will refrain from using these components in the present work.

2 Kennel-Engelmann quasilinear diffusion equation

In this Section, we review the quasilinear theory presented by Kennel and Engelmann (Kennel and Engelmann, 1966) for the case of a uniform magnetized plasma. Here, we make several changes in notation from Kennel and Engelmann's work in preparation for an alternative formulation presented in Section 3.

2.1 First-order perturbed Vlasov equation

The linearized perturbed Vlasov equation is expressed in terms of the first-order differential equation for the eikonal amplitude $\delta\tilde{f}(\mathbf{v})$:

$$-i(\omega-\mathbf{k}\cdot\mathbf{v})\delta\tilde{f}-\Omega\frac{\partial\delta\tilde{f}}{\partial\phi}\equiv-\Omega\,e^{i\Theta}\frac{\partial}{\partial\phi}\left(e^{-i\Theta}\,\delta\tilde{f}\right)=-\frac{q}{M}\left(\delta\tilde{\mathbf{E}}+\frac{\mathbf{v}}{c}\times\delta\tilde{\mathbf{B}}\right)\cdot\frac{\partial f_0}{\partial\mathbf{v}} \tag{2.1}$$

where $\Omega=qB_0/(Mc)$ denotes the (signed) gyrofrequency and the solution of the integrating factor $\partial\Theta/\partial\phi\equiv\Omega^{-1}d\vartheta/dt=(\mathbf{k}\cdot\mathbf{v}-\omega)/\Omega$ yields

$$\Theta(\phi)=\left(\frac{k_\parallel v_\parallel-\omega}{\Omega}\right)\phi+\frac{k_\perp v_\perp}{\Omega}\,\sin(\phi-\psi)\equiv\varphi(\phi)+\lambda\,\sin(\phi-\psi), \tag{2.2}$$

where $\lambda=k_\perp v_\perp/\Omega$. The perturbed Vlasov Eq. 2.1 is easily solved as

$$\delta\tilde{f}(\mathbf{v})=\frac{q\,e^{i\Theta}}{M\Omega}\int^{\phi}e^{-i\Theta'}\left(\delta\tilde{\mathbf{E}}+\frac{\mathbf{v}'}{c}\times\delta\tilde{\mathbf{B}}\right)\cdot\frac{\partial f_0}{\partial\mathbf{v}'}\,d\phi', \tag{2.3}$$

where a prime denotes a dependence on the integration gyroangle ϕ'. Here, we can write the perturbed evolution operator

$$\frac{q}{M\Omega}\left(\delta\tilde{\mathbf{E}}+\frac{\mathbf{v}}{c}\times\delta\tilde{\mathbf{B}}\right)\cdot\frac{\partial}{\partial\mathbf{v}}\equiv\delta\tilde{V}_\parallel\frac{\partial}{\partial v_\parallel}+\delta\tilde{V}_\perp\frac{\partial}{\partial v_\perp}+\delta\tilde{\phi}\,\frac{\partial}{\partial\phi}, \tag{2.4}$$

which is expressed in terms of the velocity-space eikonal amplitudes.

$$\delta\tilde{V}_\parallel=\frac{q}{M\Omega}\left(\delta\tilde{\mathbf{E}}+\frac{\mathbf{v}_\perp}{c}\times\delta\tilde{\mathbf{B}}\right)\cdot\hat{\mathbf{z}}, \tag{2.5}$$

$$\delta\tilde{V}_\perp=\frac{q}{M\Omega}\left(\delta\tilde{\mathbf{E}}+\frac{v_\parallel\hat{\mathbf{z}}}{c}\times\delta\tilde{\mathbf{B}}\right)\cdot\hat{\perp}, \tag{2.6}$$

$$\delta\tilde{\phi}=\frac{q}{M\Omega}\left(\delta\tilde{\mathbf{E}}+\frac{v_\parallel\hat{\mathbf{z}}}{c}\times\delta\tilde{\mathbf{B}}\right)\cdot\frac{\hat{\phi}}{v_\perp}-\frac{\delta\tilde{B}_\parallel}{B_0}, \tag{2.7}$$

where $\hat{\phi}=\partial\hat{\perp}/\partial\phi=\hat{\mathbf{z}}\times\hat{\perp}$. Whenever direct comparison with the work of Kennel and Engelmann (Kennel and Engelmann, 1966) is needed, we will use Faraday's law to express $\delta\tilde{\mathbf{B}}=(\mathbf{k}c/\omega)\times\delta\tilde{\mathbf{E}}$. With this substitution (see Supplementary Appendix A for details), for example, we note that Eqs. 2.4.7.–.Eqs. 2.2.7 agree exactly with Eq. 2.12 of Kennel and Engelmann (Kennel and Engelmann, 1966).

We now remark that, since $\partial f_0(v_\parallel,v_\perp)/\partial\phi$ vanishes, only the first two terms in Eq. 2.4 are non-vanishing when applied to f_0. Hence, Eq. 2.3 contains the integrals.

$$e^{i\Theta}\int^{\phi}e^{-i\Theta'}d\phi', \tag{2.8}$$

$$e^{i\Theta}\int^{\phi}e^{-i\Theta'}\hat{\perp}'d\phi'. \tag{2.9}$$

In order to evaluate these integrals, we use the Bessel-Fourier decomposition $e^{i\Theta}=e^{i\varphi}\sum_{\ell=-\infty}^{\infty}J_\ell(\lambda)\,e^{i\ell(\phi-\psi)}$, so that the scalar integral Eq. 2.8 becomes

$$e^{i\Theta}\int^{\phi}e^{-i\Theta'}d\phi'=\sum_{m,\ell=-\infty}^{\infty}i\,\Delta_\ell\,J_m(\lambda)\,J_\ell(\lambda)\,e^{i(m-\ell)(\phi-\psi)}, \tag{2.10}$$

where the resonant denominator is

$$\Delta_\ell\equiv\frac{\Omega}{k_\parallel v_\parallel+\ell\,\Omega-\omega}, \tag{2.11}$$

while, using the identity Eq. 1.3, the vector integral Eq. 2.9 becomes

$$e^{i\Theta}\int^{\phi}e^{-i\Theta'}\hat{\perp}'\,d\phi'=\sum_{m,\ell=-\infty}^{\infty}i\,\Delta_\ell\,J_m(\lambda)\,\mathbb{J}_{\perp\ell}(\lambda)\,e^{i(m-\ell)(\phi-\psi)}, \tag{2.12}$$

where we introduced the vector-valued Bessel function

$$\mathbb{J}_{\perp\ell}(\lambda)\equiv\frac{\hat{\mathsf{K}}}{\sqrt{2}}J_{\ell+1}(\lambda)+\frac{\hat{\mathsf{K}}^*}{\sqrt{2}}J_{\ell-1}(\lambda), \tag{2.13}$$

with the identity

$$\mathbf{k}\cdot\mathbb{J}_{\perp\ell}=(J_{\ell+1}+J_{\ell-1})\,k_\perp/2=(\ell\Omega/v_\perp)\,J_\ell, \tag{2.14}$$

which follows from a standard recurrence relation for Bessel functions. The perturbed Vlasov distribution (Eq. 2.3) is thus expressed as

$$\delta\tilde{f}=\sum_{m,\ell}i\,\Delta_\ell\,J_m(\lambda)\,e^{i(m-\ell)(\phi-\psi)}\left(\delta\tilde{V}_{\parallel\ell}\frac{\partial f_0}{\partial v_\parallel}+\delta\tilde{V}_{\perp\ell}\frac{\partial f_0}{\partial v_\perp}\right), \tag{2.15}$$

where the Bessel-Fourier components are

$$\delta\tilde{V}_{\parallel\ell}=\frac{q}{M\Omega}\,\delta\tilde{E}_\parallel\,J_\ell(\lambda)-v_\perp\,\hat{\mathbf{z}}\times\frac{\delta\tilde{\mathbf{B}}}{B_0}\cdot\mathbb{J}_{\perp\ell}(\lambda), \tag{2.16}$$

$$\delta\tilde{V}_{\perp\ell}=\frac{q}{M\Omega}\left(\delta\tilde{\mathbf{E}}+\frac{v_\parallel\hat{\mathbf{z}}}{c}\times\delta\tilde{\mathbf{B}}\right)\cdot\mathbb{J}_{\perp\ell}(\lambda). \tag{2.17}$$

Once again, Eqs. 2.15.17.–.Eqs. 2.2.17 agree exactly with Eq. 2.19 of Kennel and Engelmann (Kennel and Engelmann, 1966) when Faraday's law is inserted in Eqs. 2.16, 2.17; see Supplementary Appendix A for details. The relativistic version of Eqs. 2.15.17.–.Eqs. 2.2.17, which was first derived by Lerche (Lerche, 1968), is also shown in Supplementary Appendix A.

2.2 Quasilinear diffusion in velocity space

We are now ready to calculate the expression for the quasilinear diffusion equation for the slow evolution ($\tau=\epsilon^2t$) of the background Vlasov distribution

$$\frac{1}{\Omega}\frac{\partial f_0}{\partial \tau} = -\mathrm{Re}\left[\left\langle \frac{q}{M\Omega}\left(\delta\tilde{\mathbf{E}}^* + \frac{\mathbf{v}}{c}\times\delta\tilde{\mathbf{B}}^*\right)\cdot\frac{\partial\delta\tilde{f}}{\partial\mathbf{v}}\right\rangle\right] = -\mathrm{Re}\left[\left\langle\left(\delta\tilde{V}_\parallel^*\frac{\partial}{\partial v_\parallel} + \delta\tilde{V}_\perp^*\frac{\partial}{\partial v_\perp} + \delta\tilde{\phi}^*\frac{\partial}{\partial\phi}\right)\delta\tilde{f}\right\rangle\right], \tag{2.18}$$

where ϵ denotes the amplitude of the perturbation fields, $\langle\ \rangle$ denotes a gyroangle average, and $(\delta\tilde{V}_\parallel^*, \delta\tilde{V}_\perp^*, \delta\tilde{\phi}^*)$ are the complex conjugates of Eqs. 2.5–2.7. In addition, the real part appears on the right side of Eq. 2.18 as a result of averaging with respect to the wave phase ϑ. We note that Kennel and Engelmann (Kennel and Engelmann, 1966) ignore the term $\partial f_2/\partial t$ on the left side of Eq. 2.18, which is associated with the second-order perturbed Vlasov distribution f_2 generated by non-resonant particles (Kaufman, 1972a; Dewar, 1973). While this term was shown by Kaufman (Kaufman, 1972a) to be essential in demonstrating the energy-momentum conservation laws of quasilinear theory, it is also omitted here and the right side of Eq. 2.18 only contains resonant-particle contributions.

First, since Eqs. 2.5, 2.6 are independent of $v_\parallel$ and $v_\perp$, respectively, we find

$$\langle\delta\tilde{V}_\parallel^*\frac{\partial\delta\tilde{f}}{\partial v_\parallel} + \delta\tilde{V}_\perp^*\frac{\partial\delta\tilde{f}}{\partial v_\perp}\rangle = \frac{\partial}{\partial v_\parallel}\langle\delta\tilde{V}_\parallel^*\delta\tilde{f}\rangle + \frac{\partial}{\partial v_\perp}\langle\delta\tilde{V}_\perp^*\delta\tilde{f}\rangle = \frac{\partial}{\partial v_\parallel}\langle\delta\tilde{V}_\parallel^*\delta\tilde{f}\rangle + \frac{1}{v_\perp}\frac{\partial}{\partial v_\perp}\times\left(v_\perp\langle\delta\tilde{V}_\perp^*\delta\tilde{f}\rangle\right) - \langle\frac{\delta\tilde{V}_\perp^*}{v_\perp}\delta\tilde{f}\rangle, \tag{2.19}$$

where we took into account the proper Jacobian ($v_\perp$) in cylindrical velocity space ($v_\parallel$, $v_\perp$, ϕ). On the other hand, the third term in Eq. 2.18 can be written as

$$\left\langle\delta\tilde{\phi}^*\frac{\partial\delta\tilde{f}}{\partial\phi}\right\rangle = -\left\langle\left(\frac{\partial\delta\tilde{\phi}^*}{\partial\phi}\right)\delta\tilde{f}\right\rangle = \frac{q}{M\Omega}\left(\delta\tilde{\mathbf{E}}^* + \frac{v_\parallel\hat{\mathbf{z}}}{c}\times\delta\tilde{\mathbf{B}}^*\right)\cdot\left\langle\frac{\hat{\perp}}{v_\perp}\delta\tilde{f}\right\rangle \equiv \left\langle\frac{\delta\tilde{V}_\perp^*}{v_\perp}\delta\tilde{f}\right\rangle,$$

where the last term in Eq. 2.7 is independent of the gyroangle ϕ. Since this term cancels the last term in Eq. 2.19, the quasilinear diffusion Eq. 2.18 becomes

$$\frac{1}{\Omega}\frac{\partial f_0}{\partial\tau} = -\frac{\partial}{\partial v_\parallel}\left(\mathrm{Re}\langle\delta\tilde{V}_\parallel^*\delta\tilde{f}\rangle\right) - \frac{1}{v_\perp}\frac{\partial}{\partial v_\perp}\left(v_\perp\,\mathrm{Re}\langle\delta\tilde{V}_\perp^*\delta\tilde{f}\rangle\right). \tag{2.20}$$

Next, using the identity Eq. 1.3, we find

$$\sum_m J_m(\lambda)\langle(1,\hat{\perp})\,e^{i(m-\ell)(\phi-\psi)}\rangle = (J_\ell(\lambda), \mathbb{J}_{\perp\ell}(\lambda)),$$

so that, from Eq. 2.15, we find

$$\sum_m J_m(\lambda)\langle\delta\tilde{V}_\parallel^* e^{i(m-\ell)(\phi-\psi)}\rangle = \frac{q}{M\Omega}\,\delta\tilde{E}_\parallel^*\,J_\ell(\lambda) - v_\perp\hat{\mathbf{z}}\times\frac{\delta\tilde{\mathbf{B}}^*}{B_0}\cdot\mathbb{J}_{\perp\ell}(\lambda) \equiv \delta\tilde{V}_{\parallel\ell}^*, \tag{2.21}$$

$$\sum_m J_m(\lambda)\langle\delta\tilde{V}_\perp^* e^{i(m-\ell)(\phi-\psi)}\rangle = \frac{q}{M\Omega}\left(\delta\tilde{\mathbf{E}}^* + \frac{v_\parallel\hat{\mathbf{z}}}{c}\times\delta\tilde{\mathbf{B}}^*\right)\cdot\mathbb{J}_{\perp\ell}(\lambda) \equiv \delta\tilde{V}_{\perp\perp\ell}^*. \tag{2.22}$$

Hence, the quasilinear diffusion Eq. 2.20 can be written as

$$\frac{1}{\Omega}\frac{\partial f_0}{\partial\tau} = -\frac{\partial}{\partial v_\parallel}\left\{\mathrm{Re}\left[\sum_{\ell=-\infty}^{\infty} i\,\Delta_\ell\,\delta\tilde{V}_{\parallel\ell}^*\left(\delta\tilde{V}_{\parallel\ell}\frac{\partial f_0}{\partial v_\parallel} + \delta\tilde{V}_{\perp\ell}\frac{\partial f_0}{\partial v_\perp}\right)\right]\right\} - \frac{1}{v_\perp}\frac{\partial}{\partial v_\perp}\left\{v_\perp\,\mathrm{Re}\left[\sum_{\ell=-\infty}^{\infty} i\,\Delta_\ell\,\delta\tilde{V}_{\perp\perp\ell}^*\left(\delta\tilde{V}_{\parallel\ell}\frac{\partial f_0}{\partial v_\parallel} + \delta\tilde{V}_{\perp\ell}\frac{\partial f_0}{\partial v_\perp}\right)\right]\right\} \equiv \frac{\partial}{\partial\mathbf{v}}\cdot\left(\mathbf{D}\cdot\frac{\partial f_0}{\partial\mathbf{v}}\right), \tag{2.23}$$

where the diagonal diffusion coefficients are

$$\mathsf{D}^{\parallel\parallel} \equiv \hat{\mathbf{z}}\cdot\mathbf{D}\cdot\hat{\mathbf{z}} = \sum_{\ell=-\infty}^{\infty}\mathrm{Re}(-i\,\Delta_\ell)\,|\delta\tilde{V}_{\parallel\ell}|^2, \tag{2.24}$$

$$\mathsf{D}^{\perp\perp} \equiv \hat{\perp}\cdot\mathbf{D}\cdot\hat{\perp} = \sum_{\ell=-\infty}^{\infty}\mathrm{Re}(-i\,\Delta_\ell)\,|\delta\tilde{V}_{\perp\ell}|^2, \tag{2.25}$$

while the off-diagonal diffusion coefficients are

$$\mathsf{D}^{\parallel\perp} \equiv \hat{\mathbf{z}}\cdot\mathbf{D}\cdot\hat{\perp} = \sum_{\ell=-\infty}^{\infty}\mathrm{Re}(-i\,\Delta_\ell)\,\mathrm{Re}\left(\delta\tilde{V}_{\parallel\ell}^*\,\delta\tilde{V}_{\perp\ell}\right), \tag{2.26}$$

$$\mathsf{D}^{\perp\parallel} \equiv \hat{\perp}\cdot\mathbf{D}\cdot\hat{\mathbf{z}} = \sum_{\ell=-\infty}^{\infty}\mathrm{Re}(-i\,\Delta_\ell)\,\mathrm{Re}\left(\delta\tilde{V}_{\perp\ell}^*\,\delta\tilde{V}_{\parallel\ell}\right), \tag{2.27}$$

which are defined to be explicitly symmetric (i.e., $\mathsf{D}^{\parallel\perp} = \mathsf{D}^{\perp\parallel}$). Here, using the Plemelj formula (Stix, 1992), we find

$$\mathrm{Re}(-i\,\Delta_\ell) = \mathrm{Re}\left[\frac{i\,\Omega}{(\omega - k_\parallel v_\parallel - \ell\Omega)}\right] = \pi\,\Omega\,\delta(\omega_r - k_\parallel v_\parallel - \ell\Omega), \tag{2.28}$$

where we assumed $\omega = \omega_r + i\,\gamma$ and took the weakly unstable limit $\gamma\to 0^+$. Hence, the quasilinear diffusion coefficients (2.24)–(2.27) are driven by resonant particles, which satisfy the resonance condition $k_\parallel v_{\parallel\mathrm{res}} \equiv \omega - \ell\Omega$. The reader is referred to the early references by Kaufman (Kaufman, 1972a) and Dewar (Dewar, 1973) concerning the role of non-resonant particles in demonstrating the energy-momentum conservation laws of quasilinear theory.

Eq. 2.25 from Kennel and Engelmann (Kennel and Engelmann, 1966) (see Supplementary Appendix A) can be expressed as the dyadic diffusion tensor

$$\mathbf{D} \equiv \sum_\ell \mathrm{Re}\,(-i\,\Delta_\ell)\,\tilde{\mathbf{v}}_\ell^*\,\tilde{\mathbf{v}}_\ell = \sum_\ell \mathrm{Re}\,(-i\,\Delta_\ell)\Big[\Big(\delta\tilde{V}_{\parallel\ell}^*\,\hat{\mathbf{z}} + \delta\tilde{V}_{\perp\ell}^*\,\hat{\perp}\Big)\Big(\delta\tilde{V}_{\parallel\ell}\,\hat{\mathbf{z}} + \delta\tilde{V}_{\perp\ell}\,\hat{\perp}\Big)\Big], \tag{2.29}$$

which is Hermitian since the term $-i\,\Delta_\ell$ is replaced with $\mathrm{Re}(-i\,\Delta_\ell)$. Here, the perturbed velocity

$$\tilde{\mathbf{v}}_\ell = \delta\tilde{V}_{\parallel\ell}\,\hat{\mathbf{z}} + \delta\tilde{V}_{\perp\ell}\,\hat{\perp} = \frac{q\,\delta\tilde{\mathbf{E}}}{M\Omega}\cdot\Big[J_\ell(\lambda)\,\hat{\mathbf{z}}\hat{\mathbf{z}} + \mathbb{J}_{\perp\ell}(\lambda)\,\hat{\perp}\Big] + \hat{\mathbf{z}}\times\frac{\delta\tilde{\mathbf{B}}}{B_0}\cdot\mathbb{J}_{\perp\ell}(\lambda)\,\big(v_\parallel\,\hat{\perp} - v_\perp\,\hat{\mathbf{z}}\big) \tag{2.30}$$

explicitly separates the electric and magnetic contributions to the quasilinear diffusion tensor Eq. 2.29. In particular, the role of the perturbed perpendicular magnetic field is clearly seen in the process of pitch-angle diffusion because of the presence of the terms $(v_\parallel\,\hat{\perp} - v_\perp\,\hat{\mathbf{z}})$ associated with it. We also note that the parallel component of the perturbed magnetic field, $\delta\tilde{B}_\parallel = \hat{\mathbf{z}}\cdot\delta\tilde{\mathbf{B}}$, does not contribute to quasilinear diffusion in a uniform magnetized plasma. The components of the perturbed electric field, on the other hand, involve the parallel component, $\delta\tilde{E}_\parallel = \hat{\mathbf{z}}\cdot\delta\tilde{\mathbf{E}}$, as well as the right and left polarized components, $\delta\tilde{E}_R = \delta\tilde{\mathbf{E}}\cdot(\hat{\mathbf{x}} - i\,\hat{\mathbf{y}})/\sqrt{2}$ and $\delta\tilde{E}_L = \delta\tilde{\mathbf{E}}\cdot(\hat{\mathbf{x}} + i\,\hat{\mathbf{y}})/\sqrt{2}$, respectively, appearing through the definition Eq. 2.13.

Lastly, we note that the dyadic form Eq. 2.29 of the quasilinear diffusion tensor in the quasilinear diffusion Eq. 2.23 can be used to easily verify that the unperturbed entropy $\mathcal{S}_0 \equiv -\int f_0\,\ln f_0\,d^3v$ satisfies the H Theorem:

$$\frac{d\mathcal{S}_0}{dt} = -\epsilon^2\int\frac{\partial f_0}{\partial\tau}\,(\ln f_0 + 1)\,d^3v = \epsilon^2\sum_\ell\int\mathrm{Re}\,(-i\Delta_\ell)\,f_0\left|\tilde{\mathbf{v}}_\ell\cdot\frac{\partial\ln f_0}{\partial\mathbf{v}}\right|^2 d^3v > 0. \tag{2.31}$$

Once again, the energy-momentum conservation laws in quasilinear theory will not be discussed here. Instead the interested reader can consult earlier references (Kaufman, 1972a; Dewar, 1973), as well as Chapters 16–18 in the standard textbook by Stix (Stix, 1992).

2.3 Quasilinear diffusion in invariant velocity space

In preparation for Section 3, we note that a natural choice of velocity-space coordinates, suggested by guiding-center theory, involves replacing the parallel velocity $v_\parallel$ with the parallel momentum $p_\parallel = M\,v_\parallel$ and the perpendicular speed $v_\perp$ with the magnetic moment $\mu = Mv_\perp^2/(2B_0)$. We note that these two coordinates are independent dynamical invariants of the particle motion in a uniform magnetic field.

With this change of coordinates, the quasilinear diffusion Eq. 2.23 becomes

$$\frac{1}{\Omega}\frac{\partial f_0}{\partial\tau} \equiv \frac{\partial}{\partial p_\parallel}\left(D^{pp}\,\frac{\partial f_0}{\partial p_\parallel} + D^{p\mu}\,\frac{\partial f_0}{\partial\mu}\right) + \frac{\partial}{\partial\mu}\left(D^{\mu p}\,\frac{\partial f_0}{\partial p_\parallel} + D^{\mu\mu}\,\frac{\partial f_0}{\partial\mu}\right), \tag{2.32}$$

where the quasilinear diffusion coefficients are

$$\left.\begin{aligned} D^{pp} &= M^2\,\mathsf{D}^{\parallel\parallel} = \sum_\ell \mathrm{Re}\,(-i\,\Delta_\ell)\,|\delta\tilde{P}_{\parallel\ell}|^2 \\ D^{p\mu} &= (M^2 v_\perp/B_0)\,\mathsf{D}^{\parallel\perp} = \sum_\ell \mathrm{Re}\,(-i\,\Delta_\ell)\,\mathrm{Re}\big(\delta\tilde{P}_{\parallel\ell}^*\delta\tilde{\mu}_\ell\big) \\ D^{\mu\mu} &= (Mv_\perp/B_0)^2\,\mathsf{D}^{\perp\perp} = \sum_\ell \mathrm{Re}\,(-i\,\Delta_\ell)\,|\delta\tilde{\mu}_\ell|^2 \end{aligned}\right\}, \tag{2.33}$$

with the eikonal amplitudes

$$\delta\tilde{P}_{\parallel\ell} = \frac{q}{\Omega}\left(\delta\tilde{E}_\parallel\,J_\ell + \frac{v_\perp}{c}\,\mathbb{J}_{\perp\ell}\times\delta\tilde{\mathbf{B}}\cdot\hat{\mathbf{z}}\right), \tag{2.34}$$

$$\delta\tilde{\mu}_\ell = \frac{q}{B_0\Omega}\left(\delta\tilde{\mathbf{E}} + \frac{v_\parallel\,\hat{\mathbf{z}}}{c}\times\delta\tilde{\mathbf{B}}\right)\cdot v_\perp\,\mathbb{J}_{\perp\ell}, \tag{2.35}$$

and the symmetry $D^{\mu p} = D^{p\mu}$ follows from the assumption of a Hermitian diffusion tensor. Lastly, as expected, we note that the eikonal amplitude for the perturbed kinetic energy

$$\delta\tilde{\mathcal{E}}_\ell \equiv M\mathbf{v}\cdot\tilde{\mathbf{v}}_\ell = v_\parallel\,\delta\tilde{P}_{\parallel\ell} + \delta\tilde{\mu}_\ell\,B_0 = \frac{q}{\Omega}\,\delta\tilde{\mathbf{E}}\cdot\big(v_\parallel\,J_\ell\,\hat{\mathbf{z}} + v_\perp\,\mathbb{J}_{\perp\ell}\big), \tag{2.36}$$

only involves the perturbed electric field. Hence, another useful representation of quasilinear diffusion in invariant velocity $(\mathcal{E},\mu)$ space is given by the quasilinear diffusion equation

$$\frac{1}{\Omega}\frac{\partial f_0}{\partial\tau} \equiv v_\parallel\,\frac{\partial}{\partial\mathcal{E}}\left[\frac{1}{v_\parallel}\left(D^{\mathcal{E}\mathcal{E}}\,\frac{\partial f_0}{\partial\mathcal{E}} + D^{\mathcal{E}\mu}\,\frac{\partial f_0}{\partial\mu}\right)\right] + v_\parallel\,\frac{\partial}{\partial\mu}\left[\frac{1}{v_\parallel}\left(D^{\mu\mathcal{E}}\,\frac{\partial f_0}{\partial\mathcal{E}} + D^{\mu\mu}\,\frac{\partial f_0}{\partial\mu}\right)\right], \tag{2.37}$$

where the quasilinear diffusion coefficients are

$$\left.\begin{aligned} D^{\mathcal{E}\mathcal{E}} &= \sum_\ell \mathrm{Re}\,(-i\,\Delta_\ell)\,|\delta\tilde{\mathcal{E}}_\ell|^2 \\ D^{\mathcal{E}\mu} &= \sum_\ell \mathrm{Re}\,(-i\,\Delta_\ell)\,\mathrm{Re}\big(\delta\tilde{\mathcal{E}}_\ell^*\delta\tilde{\mu}_\ell\big) \\ D^{\mu\mu} &= \sum_\ell \mathrm{Re}\,(-i\,\Delta_\ell)\,|\delta\tilde{\mu}_\ell|^2 \end{aligned}\right\}, \tag{2.38}$$

and the Jacobian $1/v_\parallel$ is a function of $(\mathcal{E},\mu)$: $|v_\parallel| = \sqrt{(2/M)(\mathcal{E} - \mu\,B_0)}$, while the sign of $v_\parallel$ is a constant of the motion in a uniform magnetic field.

3 Hamiltonian quasilinear diffusion equation

In Section 2, we reviewed the standard formulation of quasilinear theory in a uniform magnetized plasma (Kennel and Engelmann, 1966). In this Section, we introduce the Hamiltonian formulation of the Vlasov equation from which we will derive the Hamiltonian quasilinear diffusion equation,

which will then be compared with the Kennel-Engelmann quasilinear diffusion Eq. 2.23.

In order to proceed with a Hamiltonian formulation, however, we will be required to express the perturbed electric and magnetic fields in terms of perturbed electric and magnetic potentials. We note that, despite the use of these potentials, the gauge invariance of the Hamiltonian quasilinear diffusion equation will be guaranteed in the formulation adopted here.

3.1 Non-adiabatic decomposition of the perturbed Vlasov distribution

The Hamiltonian formulation of quasilinear diffusion begins with the representation of the perturbed electric and magnetic fields in terms of the perturbed electric scalar potential $\delta\Phi$ and the perturbed magnetic vector potential $\delta\mathbf{A}$, where $\delta\mathbf{E} = -\nabla\delta\Phi - c^{-1}\partial\delta\mathbf{A}/\partial t$ and $\delta\mathbf{B} = \nabla\times\delta\mathbf{A}$. Hence, we find the identity

$$\delta\mathbf{E} + \frac{\mathbf{v}}{c}\times\delta\mathbf{B} = -\nabla\left(\delta\Phi - \frac{\mathbf{v}}{c}\cdot\delta\mathbf{A}\right) - \frac{1}{c}\frac{d\delta\mathbf{A}}{dt} \equiv -\nabla\delta\Psi - \frac{1}{c}\frac{d\delta\mathbf{A}}{dt}, \tag{3.1}$$

where d/dt denotes the unperturbed time derivative. We note that the gauge transformation

$$(\delta\Phi, \delta\mathbf{A}, \delta\Psi) \to \left(\delta\Phi - \frac{1}{c}\frac{\partial\delta\chi}{\partial t},\ \delta\mathbf{A} + \nabla\delta\chi,\ \delta\Psi - \frac{1}{c}\frac{d\delta\chi}{dt}\right) \tag{3.2}$$

guarantees the gauge invariance of the right side of Eq. 3.1.

Next, by removing the perturbed magnetic vector potential $\delta\mathbf{A}$ from the canonical momentum

$$\mathbf{P} = m\mathbf{v} + q\,(\mathbf{A}_0 + \epsilon\,\delta\mathbf{A})/c \to \mathbf{P}_0 = m\mathbf{v} + q\mathbf{A}_0/c,$$

the noncanonical Poisson bracket (which can also be expressed in divergence form)

$$\{f,\ g\} = \frac{1}{M}\left(\nabla f\cdot\frac{\partial g}{\partial\mathbf{v}} - \frac{\partial f}{\partial\mathbf{v}}\cdot\nabla g\right) + \frac{q\mathbf{B}_0}{M^2c}\cdot\frac{\partial f}{\partial\mathbf{v}}\times\frac{\partial g}{\partial\mathbf{v}} \tag{3.3}$$

$$= \frac{\partial}{\partial\mathbf{v}}\cdot\left[\frac{1}{M}\left(\nabla f + \frac{q\mathbf{B}_0}{Mc}\times\frac{\partial f}{\partial\mathbf{v}}\right)g\right] - \nabla\cdot\left(\frac{\partial f}{\partial\mathbf{v}}\frac{g}{M}\right) \tag{3.4}$$

only contains the unperturbed magnetic field $\mathbf{B}_0$., where f and g are arbitrary functions of $(\mathbf{x}, \mathbf{v})$.

The removal of the perturbed magnetic vector potential $\delta\mathbf{A}$ from the noncanonical Poisson bracket Eq. 3.3, however, implies that the perturbed Vlasov distribution can be written as

$$\delta f = \frac{q}{c}\,\delta\mathbf{A}\cdot\frac{\partial f_0}{\partial\mathbf{v}} + \delta g \equiv \frac{q}{c}\,\delta\mathbf{A}\cdot\{\mathbf{x}, f_0\} + \{\delta s,\ f_0\}, \tag{3.5}$$

where the *non-adiabatic* contribution δg is said to be generated by the perturbation scalar field δs (Brizard, 1994; Brizard, 2018; Brizard and Chandre, 2020), which satisfies the first-order eikonal equation

$$i\,(\mathbf{k}\cdot\mathbf{v} - \omega)\delta\tilde{s} - \Omega\,\frac{\partial\delta\tilde{s}}{\partial\phi} = q\left(\delta\tilde{\Phi} - \frac{\mathbf{v}}{c}\cdot\delta\tilde{\mathbf{A}}\right) \equiv q\,\delta\tilde{\Psi}. \tag{3.6}$$

Hence, the eikonal solution for $\delta\tilde{s}$ is expressed with the same integrating factor used in Eq. 2.3:

$$\delta\tilde{s}(\mathbf{v}) = -\frac{q}{\Omega}\,e^{i\Theta}\int^{\phi}\delta\tilde{\Psi}'\,e^{-i\Theta'}\,d\phi' = -\frac{q}{\Omega}\sum_{m,\ell} i\,\Delta_\ell\,J_m(\lambda)\,e^{i(m-\ell)(\phi-\psi)}\,\delta\tilde{\Psi}_\ell, \tag{3.7}$$

where the gyroangle Fourier component of the effective perturbed potential is

$$\delta\tilde{\Psi}_\ell \equiv \left(\delta\tilde{\Phi} - \frac{v_\parallel}{c}\,\delta\tilde{A}_\parallel\right)J_\ell(\lambda) - \frac{v_\perp}{c}\,\delta\tilde{\mathbf{A}}\cdot\mathbb{J}_{\perp\ell}(\lambda), \tag{3.8}$$

and the eikonal amplitude of the non-adiabatic perturbed Vlasov distribution is

$$\delta\tilde{g} = e^{-i\vartheta}\left\{\delta\tilde{s}\,e^{i\vartheta}, f_0\right\} = \frac{1}{M}\left(i\mathbf{k}\,\delta\tilde{s} + \Omega\,\hat{\mathbf{z}}\times\frac{\partial\delta\tilde{s}}{\partial\mathbf{v}}\right)\cdot\frac{\partial f_0}{\partial\mathbf{v}} = \frac{i\mathbf{k}}{M}\cdot\frac{\partial f_0}{\partial\mathbf{v}}\,\delta\tilde{s} - \frac{\Omega}{B_0}\frac{\partial\delta\tilde{s}}{\partial\phi}\frac{\partial f_0}{\partial\mu}, \tag{3.9}$$

where $\mu \equiv M|\mathbf{v}_\perp|^2/(2B_0)$ denotes the magnetic moment. We note that, under the gauge transformations Eq. 3.2, the scalar field δs transforms as $\delta s \to \delta s - (q/c)\,\delta\chi$ (Brizard, 1994; Brizard, 2018; Brizard and Chandre, 2020), and the expression Eq. 3.5 for the perturbed Vlasov distribution is gauge-invariant. Moreover, under the gauge transformation Eq. 3.2, the eikonal Fourier amplitude Eq. 3.8 transforms as

$$\delta\tilde{\Psi}_\ell \to \delta\tilde{\Psi}_\ell + \frac{i}{c}\,(\omega - k_\parallel v_\parallel - \ell\,\Omega)\,J_\ell\,\delta\tilde{\chi}, \tag{3.10}$$

which is consistent with Eq. 3.2.

Next, since the components of the Poisson bracket Eq. 3.3 are constant, the unperturbed time derivative of δf yields the linearized perturbed Vlasov equation

$$\frac{d\delta f}{dt} = \frac{q}{c}\frac{d\delta\mathbf{A}}{dt}\cdot\{\mathbf{x}, f_0\} + \frac{q}{c}\,\delta\mathbf{A}\cdot\{\mathbf{v}, f_0\} + \left\{\frac{d\delta s}{dt},\ f_0\right\} = \frac{q}{c}\frac{d\delta\mathbf{A}}{dt}\cdot\{\mathbf{x}, f_0\} + \frac{q}{c}\,\delta\mathbf{A}\cdot\{\mathbf{v}, f_0\} + \{q\,\delta\Psi,\ f_0\} = \left(\frac{q}{c}\frac{d\delta\mathbf{A}}{dt} + q\,\nabla\delta\Psi\right)\cdot\{\mathbf{x}, f_0\} \equiv -\frac{q}{M}\left(\delta\mathbf{E} + \frac{\mathbf{v}}{c}\times\delta\mathbf{B}\right)\cdot\frac{\partial f_0}{\partial\mathbf{v}}, \tag{3.11}$$

which implies that the non-adiabatic decomposition Eq. 3.5 is a valid representation of the perturbed Vlasov distribution.

3.2 Second-order perturbed Vlasov equation

In order to derive an alternate formulation of quasilinear theory for uniform magnetized plasmas, we begin with second-order evolution of the background Vlasov distribution

$$\frac{\partial f_0}{\partial \tau} = -\frac{q}{M}\left(\delta\mathbf{E} + \frac{\mathbf{v}}{c}\times\delta\mathbf{B}\right)\cdot\frac{\partial \delta f}{\partial \mathbf{v}} = \left(q\nabla\delta\Psi + \frac{q}{c}\frac{d\delta\mathbf{A}}{dt}\right)\cdot\{\mathbf{x},\ \delta f\}, \tag{3.12}$$

where, once again, $\tau = \epsilon^2 t$ denotes the slow quasilinear diffusion time scale, we have ignored the second-order perturbed Vlasov distribution f_2, and we have inserted Eqs. 3.1, 3.3. The first term on the right side of Eq. 3.12 can be written as

$$\begin{aligned} q\nabla\delta\Psi\cdot\{\mathbf{x},\ \delta f\} &= \{q\,\delta\Psi,\ \delta f\} - q\,\frac{\partial\delta\Psi}{\partial\mathbf{v}}\cdot\{\mathbf{v},\ \delta f\} \\ &= \{q\,\delta\Psi,\ \delta f\} + \frac{q}{c}\,\delta\mathbf{A}\cdot\{\mathbf{v},\ \delta f\} \\ &= \left\{q\,\delta\Psi,\ \left(\frac{q}{c}\,\delta\mathbf{A}\cdot\{\mathbf{x}, f_0\} + \delta g\right)\right\} \\ &\quad + \frac{q}{c}\,\delta\mathbf{A}\cdot\{\mathbf{v},\ \delta f\}, \end{aligned} \tag{3.13}$$

where we have inserted the non-adiabatic decomposition Eq. 3.5, so that the first term can be written as

$$\begin{aligned} \left\{q\,\delta\Psi,\ \frac{q}{c}\,\delta\mathbf{A}\cdot\{\mathbf{x}, f_0\}\right\} &= \frac{q^2}{c}\left(\{\delta\Psi,\ \delta\mathbf{A}\}\cdot\{\mathbf{x},\ f_0\}\right. \\ &\quad \left. + \delta\mathbf{A}\cdot\{\delta\Psi, \{\mathbf{x},\ f_0\}\}\right) \\ &= \frac{q^2}{Mc^2}\,\delta\mathbf{A}\cdot\nabla\delta\mathbf{A}\cdot\{\mathbf{x},\ f_0\} \\ &\quad + \frac{q}{c}\,\delta\mathbf{A}\cdot\{q\,\delta\Psi, \{\mathbf{x},\ f_0\}\}, \end{aligned} \tag{3.14}$$

where we used $\{\delta\Psi,\ \delta\mathbf{A}\} = (\delta\mathbf{A}/Mc)\cdot\nabla\delta\mathbf{A}$. The second term on the right side of Eq. 3.12, on the other hand, can be written as

$$\begin{aligned} \frac{q}{c}\frac{d\delta\mathbf{A}}{dt}\cdot\{\mathbf{x},\ \delta f\} &= \frac{q^2}{c^2}\frac{d\delta\mathbf{A}}{dt}\cdot\{\mathbf{x}, \{\mathbf{x}, f_0\}\}\cdot\delta\mathbf{A} \\ &\quad + \frac{d}{dt}\left(\frac{q}{c}\delta\mathbf{A}\cdot\{\mathbf{x},\ \delta g\}\right) - \frac{q}{c}\delta\mathbf{A}\cdot\{\mathbf{v}, \delta g\} \\ &\quad + \frac{q}{c}\delta\mathbf{A}\cdot\{\mathbf{x}, \{f_0,\ q\,\delta\Psi\}\}. \end{aligned} \tag{3.15}$$

Next, by using the Jacobi identity for the Poisson bracket (3.3):

$$\{f, \{g,\ h\}\} + \{g, \{h,\ f\}\} + \{h, \{f,\ g\}\} = 0, \tag{3.16}$$

which holds for arbitrary functions (f, g, h), we obtain

$$\begin{aligned} &\frac{q^2}{c}\,\delta\mathbf{A}\cdot\left(\{\delta\Psi, \{\mathbf{x},\ f_0\}\} + \{\mathbf{x}, \{f_0,\ \delta\Psi\}\}\right) \\ &\quad = \frac{q^2}{c}\,\delta\mathbf{A}\cdot\{f_0, \{\mathbf{x},\ \delta\Psi\}\} \equiv -\{f_0,\ \delta H_2\}, \end{aligned} \tag{3.17}$$

where $\delta H_2 = q^2|\delta\mathbf{A}|^2/(2Mc^2)$ is the second-order perturbed Hamiltonian. We now look at the first term on the right side of Eq. 3.15, which we write as

$$\begin{aligned} \frac{q^2}{c^2}\frac{d\delta\mathbf{A}}{dt}\cdot\{\mathbf{x}, \{\mathbf{x}, f_0\}\}\cdot\delta\mathbf{A} &= \frac{d}{dt}\left(\frac{q^2}{c^2}\,\delta\mathbf{A}\cdot\{\mathbf{x}, \{\mathbf{x}, f_0\}\}\cdot\delta\mathbf{A}\right) \\ &\quad - \frac{q^2}{c^2}\,\delta\mathbf{A}\cdot\left(\{\mathbf{v}, \{\mathbf{x}, f_0\}\} + \{\mathbf{x}, \{\mathbf{v}, f_0\}\}\right) \\ &\quad \cdot\delta\mathbf{A} - \frac{q^2}{c^2}\,\delta\mathbf{A}\cdot\{\mathbf{x}, \{\mathbf{x}, f_0\}\}\cdot\frac{d\delta\mathbf{A}}{dt}. \end{aligned} \tag{3.18}$$

Because of the symmetry of the tensor $\{\mathbf{x}, \{\mathbf{x},\ f_0\}\}$, the last term on the right side (omitting the minus sign) is equal to the left side, so that we obtain

$$\begin{aligned} \frac{q^2}{c^2}\frac{d\delta\mathbf{A}}{dt}\cdot\{\mathbf{x}, \{\mathbf{x}, f_0\}\}\cdot\delta\mathbf{A} &= \frac{d}{dt}\left(\frac{q^2}{2c^2}\,\delta\mathbf{A}\cdot\{\mathbf{x}, \{\mathbf{x}, f_0\}\}\cdot\delta\mathbf{A}\right) \\ &\quad - \frac{q^2}{c^2}\,\delta\mathbf{A}\cdot\{\mathbf{v}, \{\mathbf{x}, f_0\}\}\cdot\delta\mathbf{A}, \end{aligned}$$

where we used the Jacobi identity Eq. 3.16 to find $\{\mathbf{x}, \{\mathbf{v}, f_0\}\} = \{\mathbf{v}, \{\mathbf{x}, f_0\}\}$, since $\{f_0, \{\mathbf{x}, \mathbf{v}\}\} = 0$.

When these equations are combined into Eq. 3.12, we obtain the final Hamiltonian form of the second-order perturbed Vlasov equation

$$\begin{aligned} \frac{\partial f_0}{\partial \tau} &= \{\delta H, \delta g\} + \{\delta H_2, f_0\} + \frac{d}{dt}\left(\frac{q}{c}\,\delta\mathbf{A}\cdot\{\mathbf{x},\ \delta g\}\right. \\ &\quad \left. + \frac{q^2}{2c^2}\,\delta\mathbf{A}\cdot\{\mathbf{x}, \{\mathbf{x},\ f_0\}\}\cdot\delta\mathbf{A}\right), \end{aligned} \tag{3.19}$$

where $\delta H = q\,\delta\Psi = q\,\delta\Phi - q\,\delta\mathbf{A}\cdot\mathbf{v}/c$ and $\delta g = \{\delta s, f_0\}$.

3.3 Hamiltonian quasilinear diffusion equation

We now perform two separate averages of the second-order perturbed Vlasov Eq. 3.19: we first perform an average with respect to the wave phase ϑ, which will be denoted by an overbar, and, second, we perform an average with respect to the gyroangle ϕ. We begin by noting that the averaged second-order perturbed Hamiltonian $\delta\bar{H}_2 = q^2|\delta\tilde{\mathbf{A}}|^2/(2Mc^2)$ is a constant and, therefore, its contribution in Eq. 3.19 vanishes upon eikonal-phase averaging. Likewise, the total time derivative in Eq. 3.19 vanishes upon eikonal-phase averaging.

The Hamiltonian quasilinear diffusion equation is, therefore, defined as

$$\begin{aligned} \frac{\partial f_0}{\partial \tau} &\equiv \frac{1}{2}\left\langle\overline{\{\delta H, \delta g\}}\right\rangle = \frac{1}{2}\overline{\left[\nabla\cdot\left(\frac{q}{Mc}\,\delta\mathbf{A}\,\langle\delta g\rangle\right)\right]} \\ &\quad + \frac{1}{2}\left\langle\frac{\partial}{\partial\mathbf{v}}\cdot\overline{\left[\left(\nabla\delta H + \Omega\,\frac{q}{c}\,\delta\mathbf{A}\times\hat{\mathbf{z}}\right)\frac{\delta g}{M}\right]}\right\rangle \\ &= \frac{1}{2}\left\langle\frac{\partial}{\partial\mathbf{v}}\cdot\overline{\left[\left(\nabla\delta H + \Omega\,\frac{q}{c}\,\delta\mathbf{A}\times\hat{\mathbf{z}}\right)\frac{\delta g}{M}\right]}\right\rangle, \end{aligned} \tag{3.20}$$

where we used the divergence form Eq. 3.4 of the Poisson bracket and the eikonal average of the spatial divergence vanishes. Next, the eikonal average of the first term on the last line of the right side of Eq. 3.20 yields

$$\overline{(\nabla\delta H\delta g)} = i\,\mathbf{k}\left(\delta\tilde{H}\,\delta\tilde{g}^* - \delta\tilde{H}^*\,\delta\tilde{g}\right),$$

so that

$$\langle\frac{\partial}{\partial \mathbf{v}}\cdot\overline{\left(\nabla\delta H\,\frac{\delta g}{M}\right)}\rangle=\frac{\partial}{\partial p_\parallel}\left(ik_\parallel\langle\delta\tilde{H}\,\delta\tilde{g}^*-\delta\tilde{H}^*\,\delta\tilde{g}\rangle\right)+\frac{1}{B_0}\frac{\partial}{\partial\mu}\left[i\mathbf{k}\cdot\langle\mathbf{v}_\perp\left(\delta\tilde{H}\,\delta\tilde{g}^*-\delta\tilde{H}^*\,\delta\tilde{g}\right)\rangle\right], \tag{3.21}$$

where $p_\parallel = M\,v_\parallel$ and $\mu = M|\mathbf{v}_\perp|^2/2B_0$. The eikonal average of the second term on the last line of the right side of Eq. 3.20, on the other hand, yields

$$\frac{\Omega}{2\,v_\perp}\frac{\partial}{\partial v_\perp}\left[\frac{v_\perp}{M}\left(\frac{q}{c}\delta\tilde{\mathbf{A}}\cdot\langle\hat{\phi}\,\delta\tilde{g}^*\rangle+\frac{q}{c}\delta\tilde{\mathbf{A}}^*\cdot\langle\hat{\phi}\,\delta\tilde{g}\rangle\right)\right]\equiv\frac{\Omega}{B_0}\frac{\partial}{\partial\mu}\left[\mathrm{Re}\langle\left(\frac{q}{c}\delta\tilde{\mathbf{A}}\cdot\frac{\partial\mathbf{v}_\perp}{\partial\phi}\right)\delta\tilde{g}^*\rangle\right], \tag{3.22}$$

so that by combining Eqs. 3.21, 3.22 into Eq. 3.20, we find

$$\frac{1}{\Omega}\frac{\partial f_0}{\partial\tau}=\frac{\partial}{\partial p_\parallel}\left(\frac{k_\parallel}{\Omega}\,\mathrm{Re}\langle i\,\delta\tilde{H}\,\delta\tilde{g}^*\rangle\right)+\frac{1}{B_0}\frac{\partial}{\partial\mu}\left[\mathrm{Re}\langle\left(\frac{q}{c}\delta\tilde{\mathbf{A}}\cdot\frac{\partial\mathbf{v}_\perp}{\partial\phi}+i\,\frac{\mathbf{k}\cdot\mathbf{v}_\perp}{\Omega}\,\delta\tilde{H}\right)\delta\tilde{g}^*\rangle\right], \tag{3.23}$$

In order to evaluate the gyroangle averages in Eq. 3.23, we need to proceed with a transformation from particle phase space to guiding-center phase space, which is presented in the next Section.

4 Guiding-center Hamiltonian quasilinear diffusion equation

In this Section, we use the guiding-center transformation (Northrop, 1963) in order to simplify the calculations involved in obtaining an explicit expression for the Hamiltonian quasilinear diffusion Eq. 3.23 that can compared with the standard quasilinear diffusion Eq. 2.32 obtained from Kennel-Engelmann's work (Kennel and Engelmann, 1966).

4.1 Guiding-center transformation

In a uniform background magnetic field, the transformation from particle phase space to guiding-center phase space is simply given as $\mathbf{x} = \mathbf{X} + \boldsymbol{\rho}$, where the particle position $\mathbf{x}$ is expressed as the sum of the guiding-center position $\mathbf{X}$ and the gyroradius vector $\boldsymbol{\rho} \equiv \hat{\mathbf{z}}\times\mathbf{v}_\perp/\Omega$, while the velocity-space coordinates $(p_\parallel,\,\mu,\,\phi)$ remain unchanged (Cary and Brizard, 2009). Hence, the eikonal wave phase $\vartheta = \mathbf{k}\cdot\mathbf{x} - \omega\,t$ becomes

$$\vartheta=\mathbf{k}\cdot\left(\mathbf{X}+\boldsymbol{\rho}\right)-\omega\,t=\theta+\mathbf{k}\cdot\boldsymbol{\rho}\equiv\theta+\Lambda, \tag{4.1}$$

where θ denotes the guiding-center eikonal wave phase and $\Lambda \equiv \lambda\sin(\phi - \psi)$. Next, the particle Poisson bracket (Eq. 3.3) is transformed into the guiding-center Poisson bracket (Cary and Brizard, 2009)

$$\{F,\,G\}_{\rm gc}=\hat{\mathbf{z}}\cdot\left(\nabla F\,\frac{\partial G}{\partial p_\parallel}-\frac{\partial F}{\partial p_\parallel}\,\nabla G\right)-\frac{\Omega}{B_0}\left(\frac{\partial F}{\partial\phi}\,\frac{\partial G}{\partial\mu}-\frac{\partial F}{\partial\mu}\,\frac{\partial G}{\partial\phi}\right)-\frac{c\,\hat{\mathbf{z}}}{qB_0}\cdot\nabla F\times\nabla G, \tag{4.2}$$

where the last term vanishes in the case of a uniform background plasma since the guiding-center functions F and G depend on the guiding-center position only through the guiding-center wave phase θ (with $\nabla\theta = \mathbf{k}$).

4.2 First-order perturbed guiding-center Vlasov equation

The guiding-center transformation induces a transformation on particle phase-space functions f to a guiding-center phase-space function F through the guiding-center push-forward $\mathsf{T}_{\rm gc}^{-1}$: $F \equiv \mathsf{T}_{\rm gc}^{-1} f$. For a perturbed particle phase-space function $\delta g \equiv \delta\tilde{g}\,\exp(i\vartheta) + \text{c.c.}$, we find the perturbed guiding-center phase-space function $\delta G \equiv \delta\tilde{G}\,\exp(i\theta) + \text{c.c.}$, where the eikonal amplitude $\delta\tilde{G}$ is given by the push-forward expression as

$$\delta\tilde{G}=\delta\tilde{g}\,e^{-i\Lambda}=e^{-i\theta}\left\{\delta\tilde{S}\,e^{i\theta},\,f_0\right\}_{\rm gc}=i\,k_\parallel\frac{\partial f_0}{\partial p_\parallel}\,\delta\tilde{S}-\frac{\Omega}{B_0}\frac{\partial f_0}{\partial\mu}\,\frac{\partial\delta\tilde{S}}{\partial\phi}. \tag{4.3}$$

The eikonal amplitude of the guiding-center generating function $\delta\tilde{S} = \delta\tilde{s}\,\exp(-i\Lambda)$ satisfies an equation derived from the first-order eikonal Eq. 3.6:

$$i\,(k_\parallel v_\parallel-\omega)\,\delta\tilde{S}-\Omega\,\frac{\partial\delta\tilde{S}}{\partial\phi}=\delta\tilde{H}\,e^{-i\Lambda}\equiv\delta\tilde{H}_{\rm gc}. \tag{4.4}$$

The solution of the first-order guiding-center eikonal Eq. 4.4 makes use of the gyroangle expansion $\delta\tilde{S} = \sum_{\ell=-\infty}^{\infty}\delta\tilde{S}_\ell\exp[-i\ell\,(\phi-\psi)]$, which yields the Fourier component

$$\delta\tilde{S}_\ell=-\frac{i\,\Delta_\ell}{\Omega}\,\langle\delta\tilde{H}e^{-i\Lambda+i\ell\,(\phi-\psi)}\rangle=-\frac{i\,\Delta_\ell}{\Omega}\,q\,\delta\tilde{\Psi}_\ell. \tag{4.5}$$

Inserting this solution into Eq. 4.3, with the gyroangle expansion $\delta\tilde{G} = \sum_{\ell=-\infty}^{\infty}\delta\tilde{G}_\ell\exp[-i\ell\,(\phi-\psi)]$, yields

$$\delta\tilde{G}_\ell=i\left(k_\parallel\frac{\partial f_0}{\partial p_\parallel}+\frac{\ell\,\Omega}{B_0}\,\frac{\partial f_0}{\partial\mu}\right)\delta\tilde{S}_\ell=\frac{q}{\Omega}\,\delta\tilde{\Psi}_\ell\,\Delta_\ell\left(k_\parallel\frac{\partial f_0}{\partial p_\parallel}+\frac{\ell\,\Omega}{B_0}\,\frac{\partial f_0}{\partial\mu}\right). \tag{4.6}$$

Hence, the solution for the eikonal amplitude $\delta\tilde{g}$ appearing in Eq. 3.23 can be obtained from the guiding-center pull-back expression $\delta\tilde{g} = \delta\tilde{G}\,\exp(i\,\Lambda)$.

4.3 Guiding-center Hamiltonian quasilinear diffusion equation

Using the solution Eq. 4.6 for $\delta\tilde{G}_\ell$, we are now ready to calculate the quasilinear diffusion Eq. 3.23 and obtaina simple dyadic form for the quasilinear diffusion tensor.

4.3.1 Quasilinear diffusion in guiding-center ($p_\parallel$, μ)-space

Now that the solution for the eikonal amplitude δg is obtained in terms of the guiding-center phase-space function $\delta\tilde{g} = \delta\tilde{G}\,\exp(i\,\Lambda)$, we are now able to evaluate the gyroangle-averaged expressions in Eq. 3.23. We begin with the gyroangle-averaged quadratic term

$$\begin{aligned}\langle \delta\tilde{H}\;\delta\tilde{g}^*\rangle &= \langle \delta\tilde{H}\left(\delta\tilde{G}e^{i\Lambda}\right)^*\rangle = \langle\left(\delta\tilde{H}e^{-i\Lambda}\right)\delta\tilde{G}^*\rangle\\ &= \sum_{\ell=-\infty}^{\infty}\delta\tilde{G}_\ell^*\langle\delta\tilde{H}e^{-i\Lambda+i\,\ell\,(\phi-\psi)}\rangle\\ &= \sum_{\ell=-\infty}^{\infty} q\,\delta\tilde{\Psi}_\ell\;\delta\tilde{G}_\ell^*\\ &= \sum_{\ell=-\infty}^{\infty}\frac{q^2}{\Omega}\,|\delta\tilde{\Psi}_\ell|^2\;\Delta_\ell^*\left(k_\parallel\,\frac{\partial f_0}{\partial p_\parallel}+\frac{\ell\,\Omega}{B_0}\,\frac{\partial f_0}{\partial\mu}\right),\end{aligned} \tag{4.7}$$

so that

$$\frac{k_\parallel}{\Omega}\,\mathrm{Re}\langle i\,\delta\tilde{H}\delta\tilde{g}^*\rangle = \sum_{\ell=-\infty}^{\infty} k_\parallel\,\mathcal{D}_\ell\left(k_\parallel\,\frac{\partial f_0}{\partial p_\parallel}+\frac{\ell\,\Omega}{B_0}\,\frac{\partial f_0}{\partial\mu}\right), \tag{4.8}$$

where we introduced the quasilinear perturbation potential

$$\mathcal{D}_\ell = \mathrm{Re}\,(-i\,\Delta_\ell)\,|\,(q/\Omega)\,\delta\tilde{\Psi}_\ell|^2 \equiv \mathrm{Re}\,(-i\,\Delta_\ell)\,|\delta\tilde{\mathcal{J}}_\ell|^2, \tag{4.9}$$

and

$$\frac{\partial}{\partial p_\parallel}\left(\frac{k_\parallel}{\Omega}\,\mathrm{Re}\langle i\,\delta\tilde{H}\delta\tilde{g}^*\rangle\right) \equiv \frac{\partial}{\partial p_\parallel}\left(D_{\rm H}^{pp}\,\frac{\partial f_0}{\partial p_\parallel}+D_{\rm H}^{p\mu}\,\frac{\partial f_0}{\partial\mu}\right), \tag{4.10}$$

where $D_{\rm H}^{pp} = \sum_\ell k_\parallel^2\,\mathcal{D}_\ell$ and $D_{\rm H}^{p\mu} = \sum_\ell k_\parallel\,(\ell\,\Omega/B_0)\,\mathcal{D}_\ell$.

Next, we find

$$\begin{aligned}&\left\langle\left(\frac{q}{c}\delta\tilde{\mathbf{A}}\cdot\frac{\partial\mathbf{v}_\perp}{\partial\phi}+i\,\frac{\mathbf{k}\cdot\mathbf{v}_\perp}{\Omega}\,\delta\tilde{H}\right)\delta\tilde{g}^*\right\rangle\\ &\quad=\left\langle\left(\frac{q}{c}\delta\tilde{\mathbf{A}}\cdot\frac{\partial\mathbf{v}_\perp}{\partial\phi}+i\,\frac{\mathbf{k}\cdot\mathbf{v}_\perp}{\Omega}\,\delta\tilde{H}\right)\left(\delta\tilde{G}e^{i\Lambda}\right)^*\right\rangle\\ &\quad=\left\langle\left[\frac{q}{c}\delta\tilde{\mathbf{A}}\cdot\frac{\partial\mathbf{v}_\perp}{\partial\phi}\,e^{-i\Lambda}-i\,q\frac{\partial\Lambda}{\partial\phi}\left(\delta\tilde{\Phi}-\frac{v_\parallel}{c}\delta\tilde{A}_\parallel-\frac{\mathbf{v}_\perp}{c}\cdot\delta\tilde{\mathbf{A}}\right)\right.\right.\\ &\qquad\left.\left.\times e^{-i\Lambda}\right]\delta\tilde{G}^*\right\rangle\\ &\quad=-\left\langle\frac{\partial}{\partial\phi}\left(\delta\tilde{H}e^{-i\Lambda}\right)\delta\tilde{G}^*\right\rangle=\left\langle\delta\tilde{H}\,e^{-i\Lambda}\,\frac{\partial\delta\tilde{G}^*}{\partial\phi}\right\rangle\\ &\quad=\sum_{\ell=-\infty}^{\infty} i\ell\;\delta\tilde{G}_\ell^*\langle\delta\tilde{H}e^{-i\Lambda+i\,\ell\,(\phi-\psi)}\rangle=\sum_{\ell=-\infty}^{\infty} i\ell\;q\,\delta\tilde{\Psi}_\ell\;\delta\tilde{G}_\ell^*\\ &\quad=\sum_{\ell=-\infty}^{\infty} i\,\Delta_\ell^*\;\ell\Omega\;(q/\Omega)^2\,|\delta\tilde{\Psi}_\ell|^2\left(k_\parallel\,\frac{\partial f_0}{\partial p_\parallel}+\frac{\ell\,\Omega}{B_0}\,\frac{\partial f_0}{\partial\mu}\right),\end{aligned} \tag{4.11}$$

so that

$$\begin{aligned}&\frac{1}{B_0}\,\frac{\partial}{\partial\mu}\left[\mathrm{Re}\left\langle\left(\frac{q}{c}\delta\tilde{\mathbf{A}}\cdot\frac{\partial\mathbf{v}_\perp}{\partial\phi}+i\,\frac{\mathbf{k}\cdot\mathbf{v}_\perp}{\Omega}\,\delta\tilde{H}\right)\delta\tilde{g}^*\right\rangle\right]\\ &\quad=\frac{\partial}{\partial\mu}\left[\sum_{\ell=-\infty}^{\infty}\frac{\ell\,\Omega}{B_0}\,\mathcal{D}_\ell\left(k_\parallel\,\frac{\partial f_0}{\partial p_\parallel}+\frac{\ell\,\Omega}{B_0}\,\frac{\partial f_0}{\partial\mu}\right)\right]\\ &\quad\equiv\frac{\partial}{\partial\mu}\left(D_{\rm H}^{\mu p}\,\frac{\partial f_0}{\partial p_\parallel}+D_{\rm H}^{\mu\mu}\,\frac{\partial f_0}{\partial\mu}\right),\end{aligned} \tag{4.12}$$

where $D_{\rm H}^{\mu p} = \sum_\ell\,(\ell\,\Omega/B_0)\,k_\parallel\,\mathcal{D}_\ell$ and $D_{\rm H}^{\mu\mu} = \sum_\ell\,(\ell\,\Omega/B_0)^2\,\mathcal{D}_\ell$. We can now write the Hamiltonian quasilinear diffusion Eq. 3.23 as

$$\begin{aligned}\frac{1}{\Omega}\,\frac{\partial f_0}{\partial\tau} &= \frac{\partial}{\partial p_\parallel}\left(D_{\rm H}^{pp}\,\frac{\partial f_0}{\partial p_\parallel}+D_{\rm H}^{p\mu}\,\frac{\partial f_0}{\partial\mu}\right)\\ &+\frac{\partial}{\partial\mu}\left(D_{\rm H}^{\mu p}\,\frac{\partial f_0}{\partial p_\parallel}+D_{\rm H}^{\mu\mu}\,\frac{\partial f_0}{\partial\mu}\right).\end{aligned} \tag{4.13}$$

This quasilinear diffusion equation will later be compared with the standard quasilinear diffusion Eq. 2.32 derived by Kennel and Engelmann (Kennel and Engelmann, 1966).

4.3.2 Quasilinear diffusion in guiding-center (J_g, $\mathcal{E}$)-space

Before proceeding with this comparison, however, we consider an alternate representation for the Hamiltonian quasilinear diffusion Eq. 4.13, which will be useful in the derivation of a quasilinear diffusion equation for nonuniform magnetized plasmas. If we replace the guiding-center parallel momentum $p_\parallel$ with the guiding-center kinetic energy $\mathcal{E} = p_\parallel^2/2m + \mu\,B_0$, and the guiding-center magnetic moment μ with the gyroaction $\mathsf{J}_g = \mu B_0/\Omega$, the Fourier eikonal solution Eq. 4.6 becomes

$$\delta\tilde{G}_\ell = q\,\delta\tilde{\Psi}_\ell\,\frac{\partial f_0}{\partial\mathcal{E}}+\frac{q}{\Omega}\,\delta\tilde{\Psi}_\ell\,\Delta_\ell\left(\omega\,\frac{\partial f_0}{\partial\mathcal{E}}+\ell\,\frac{\partial f_0}{\partial\mathsf{J}_g}\right), \tag{4.14}$$

where the first term on the right side is interpreted as a guiding-center adiabatic contribution to the perturbed Vlasov distribution (Brizard, 1994), while the remaining terms (proportional to the resonant denominator Δ_ℓ) are non-adiabatic contributions.

By substituting this new solution in Eq. 4.8, we find

$$\frac{k_\parallel}{\Omega}\,\mathrm{Re}\langle i\,\delta\tilde{H}\delta\tilde{g}^*\rangle = \sum_{\ell=-\infty}^{\infty} k_\parallel\,\mathcal{D}_\ell\left(\omega\,\frac{\partial f_0}{\partial\mathcal{E}}+\ell\,\frac{\partial f_0}{\partial\mathsf{J}_g}\right), \tag{4.15}$$

while

$$\begin{aligned}&\mathrm{Re}\left\langle\left(\frac{q}{c}\delta\tilde{\mathbf{A}}\cdot\frac{\partial\mathbf{v}_\perp}{\partial\phi}+i\,\frac{\mathbf{k}\cdot\mathbf{v}_\perp}{\Omega}\,\delta\tilde{H}\right)\delta\tilde{g}^*\right\rangle\\ &\quad=\sum_{\ell=-\infty}^{\infty}\ell\Omega\,\mathcal{D}_\ell\left(\omega\,\frac{\partial f_0}{\partial\mathcal{E}}+\ell\,\frac{\partial f_0}{\partial\mathsf{J}_g}\right),\end{aligned} \tag{4.16}$$

where the guiding-center adiabatic contribution has cancelled out. The guiding-center quasilinear diffusion Eq. 4.13 becomes

$$\frac{1}{\Omega}\frac{\partial f_0}{\partial \tau} = \nu_\parallel \frac{\partial}{\partial \mathcal{E}}\left[\frac{1}{\nu_\parallel}\left(D_{\rm H}^{\mathcal{E}\mathcal{E}}\,\frac{\partial f_0}{\partial \mathcal{E}} + D_{\rm H}^{\mathcal{E}\mathsf{J}}\,\frac{\partial f_0}{\partial \mathsf{J}_{\rm g}}\right)\right] + \nu_\parallel \frac{\partial}{\partial \mathsf{J}_{\rm g}}\left[\frac{1}{\nu_\parallel}\left(D_{\rm H}^{\mathsf{J}\mathcal{E}}\,\frac{\partial f_0}{\partial \mathcal{E}} + D_{\rm H}^{\mathsf{J}\mathsf{J}}\,\frac{\partial f_0}{\partial \mathsf{J}_{\rm g}}\right)\right], \tag{4.17}$$

where the guiding-center quasilinear diffusion tensor is represented in 2×2 matrix form as

$$\mathbf{D}_{\rm H} \equiv \sum_{\ell=-\infty}^{\infty} \begin{pmatrix} \ell^2 & \ell\omega \\ \omega\,\ell & \omega^2 \end{pmatrix} \mathcal{D}_\ell. \tag{4.18}$$

We note that, because of the simple dyadic form of Eq. 4.18, other representations for the guiding-center quasilinear diffusion tensor $\mathbf{D}_{\rm H}$ can be easily obtained, e.g., by replacing the guiding-center gyroaction $\mathsf{J}_{\rm g}$ with the pitch-angle coordinate $\xi = \sqrt{1 - \mu B_0/\mathcal{E}}$. We also note that the dyadic quasilinear tensor (4.18) has a simple modular form compared to the dyadic form Eq. 2.29.

4.4 Comparison with Kennel-Engelmann quasilinear theory

We can now compare the Kennel-Engelmann quasilinear diffusion Eq. 2.32 with the guiding-center Hamiltonian quasilinear diffusion Eq. 4.13. First, we express the perturbed fields Eqs. 2.34, 2.35 in terms of the perturbed potentials $(\delta\Phi, \delta\mathbf{A})$:

$$\begin{aligned}\delta\tilde{P}_{\parallel\ell} &= M\,\delta\tilde{V}_{\parallel\ell} \\ &= \frac{q}{\Omega}\left[J_\ell\left(-i\,k_\parallel\,\delta\tilde{\Phi} + i\,\frac{\omega}{c}\,\delta\tilde{A}_\parallel\right) - \frac{\nu_\perp}{c}\left(i\mathbf{k}\,\delta\tilde{A}_\parallel - i\,k_\parallel\,\delta\tilde{\mathbf{A}}\right)\cdot\mathbb{J}_{\perp\ell}\right] \\ &= -i\,k_\parallel\,\delta\tilde{\mathcal{J}}_\ell + i(\omega - k_\parallel v_\parallel - \ell\,\Omega)\frac{q\delta\tilde{A}_\parallel}{\Omega\,c}\,J_\ell,\end{aligned} \tag{4.19}$$

and

$$\begin{aligned}\delta\tilde{\mu}_\ell &= \frac{M v_\perp}{B_0}\,\delta\tilde{V}_{\perp\ell} \\ &= \frac{q\,v_\perp\,\mathbb{J}_{\perp\ell}}{B_0\Omega}\cdot\left[-i\mathbf{k}\,\delta\tilde{\Phi} + i\,\frac{\omega}{c}\,\delta\tilde{\mathbf{A}} + \frac{\nu_\parallel}{c}\left(i\mathbf{k}\,\delta\tilde{A}_\parallel - i\,k_\parallel\,\delta\tilde{\mathbf{A}}\right)\right] \\ &= -i\,\frac{\ell\,\Omega}{B_0}\,\delta\tilde{\mathcal{J}}_\ell + i(\omega - k_\parallel v_\parallel - \ell\,\Omega)\frac{q\delta\tilde{\mathbf{A}}}{cB_0\Omega}\cdot\nu_\perp\mathbb{J}_{\perp\ell},\end{aligned} \tag{4.20}$$

which are both gauge invariant according to the transformation (Eq. 3.10). Hence, these perturbed fields are expressed in terms of a contribution from the perturbed action $\delta\tilde{\mathcal{J}}_\ell$ and a contribution that vanishes for resonant particles (i.e., $k_\parallel v_{\parallel\rm res} = \omega - \ell\Omega$). We note that, in the resonant-particle limit ($\Delta_\ell \to \infty$), the difference between the Kennel-Engelmann formulation and the Hamiltonian formulation vanishes. For example, the Kennel-Engelmann quasilinear diffusion coefficient $D^{pp} = \sum_\ell {\rm Re}(-i\Delta_\ell)\,|\delta\tilde{P}_{\parallel\ell}|^2$ is expressed as

$$D^{pp} = \sum_\ell {\rm Re}(-i\Delta_\ell)\left[k_\parallel^2\,|\delta\tilde{\mathcal{J}}_\ell|^2 + 2k_\parallel J_\ell {\rm Re}\left(\frac{\delta\tilde{\mathcal{J}}_\ell^*}{\Delta_\ell}\,\frac{q\delta\tilde{A}_\parallel}{\Omega c}\right) + \left(\frac{q}{\Omega c}\right)^2\frac{|\delta\tilde{A}_\parallel|^2 J_\ell^2}{|\Delta_\ell|^2}\right] \to D_{\rm H}^{pp}, \tag{4.21}$$

which yields $D_{\rm H}^{pp}$ in the resonant-particle limit ($\Delta_\ell \to \infty$).

In summary, we have shown that, in the resonant-particle limit ($\Delta_\ell \to \infty$), the Hamiltonian quasilinear diffusion Eq. 4.13 is identical to the standard quasilinear diffusion Eq. 2.32 derived by Kennel and Engelmann (Kennel and Engelmann, 1966) for the case of a uniform magnetized plasma. In the next Section, we will see how the Hamiltonian quasilinear formalism can be extended to the case of a nonuniform magnetized plasma.

5 Hamiltonian quasilinear formulations for nonuniform magnetized plasma

In this Section, we briefly review the Hamiltonian formulation for quasilinear diffusion in a nonuniform magnetized background plasma. In an axisymmetric magnetic-field geometry, the 2×2 quasilinear diffusion tensor in velocity space is generalized to a 3×3 quasilinear diffusion tensor that includes radial quasilinear diffusion. In a spatially magnetically-confined plasma, the process of radial diffusion is a crucial element in determining whether charged particles leave the plasma. A prime example is provided by the case of radial diffusion in Earth's radiation belt, which was recently reviewed by Lejosne and Kollmann (Lejosne and Kollmann, 2020).

We present two non-relativistic Hamiltonian formulations of quasilinear diffusion in a nonuniform magnetized plasmas. The first one based on the canonical action-angle formalism (Kaufman, 1972b; Mahajan and Chen, 1985; Mynick and Duvall, 1989; Schulz, 1996) and the second one based on a summary of our previous work (Brizard and Chan, 2004).

5.1 Canonical action-angle formalism

When a plasma is confined by a nonuniform magnetic field, the charged-particle orbits can be described in terms of 3 orbital angle coordinates $\boldsymbol{\theta}$ (generically referred to as the gyration, bounce, and precession-drift angles) and their canonically-conjugate 3 action coordinates $\mathbf{J}$ (generically referred to as the gyromotion, bounce-motion, and drift-motion actions). In principle, these action coordinates are adiabatic invariants of the particle motion and they are calculated according to standard methods of guiding-center theory (Tao et al., 2007; Cary and Brizard, 2009), which are expressed in terms of asymptotic expansions in powers of a small dimensionless parameter $\epsilon_B = \rho/L_B \ll 1$ defined as the ratio of a characteristic gyroradius (for a

given particle species) and the gradient length scale L_B associated with the background magnetic field $\mathbf{B}_0$. When an asymptotic expansion for an adiabatic invariant $\mathsf{J} = \mathsf{J}_0 + \epsilon_B \mathsf{J}_1$ is truncated at first order, for example, we find $d\mathsf{J}/dt \sim \epsilon_B^2$ and the orbital angular average $\langle d\mathsf{J}/dt \rangle = 0$ is the necessary condition for the adiabatic invariance of J. The reader is referred to Refs. (Cary and Brizard, 2009) and (Tao et al., 2007) where explicit expansions for all three guiding-center adiabatic invariants are derived in the non-relativistic and relativistic limits, respectively, for arbitrary background magnetic geometry.

The canonical action-angle formulation of quasilinear theory assumes that, in the absence of wave-field perturbations, the action coordinates $\mathbf{J}$ are constants of motion $d\mathbf{J}/dt = -\partial H_0/\partial \boldsymbol{\theta} = 0$, which follows from the invariance of the unperturbed Hamiltonian $H_0(\mathbf{J})$ on the canonical orbital angles $\boldsymbol{\theta}$. In this case, the unperturbed Vlasov distribution $F_0(\mathbf{J})$ is a function of action coordinates only. We note that the action coordinates considered here are either exact invariants or adiabatic invariants (Kaufman, 1972b; Mynick and Duvall, 1989) of the particle motion, and it is implicitly assumed that any adiabatic action invariant used in this canonical action-angle formulation of quasilinear theory can be calculated to sufficiently high order in ϵ_B within a region of particle phase space that excludes non-adiabatic diffusion in action space (Bernstein and Rowlands, 1976). For example, see Ref. (Brizard and Markowski, 2022) for a brief discussion of the breakdown of the adiabatic invariance of the magnetic moment (on the bounce time scale) for charged particles trapped by an axisymmetric dipole magnetic field.

In the presence of wave-field perturbations, the perturbed Hamiltonian can be represented in terms of a Fourier decomposition in terms of a discrete wave spectrum ω_k and orbital angles (with Fourier-index vector $\mathbf{m}$):

$$\delta\mathcal{H}(\mathbf{J},\boldsymbol{\theta},t) = \sum_{\mathbf{m},k} \delta\tilde{\mathcal{H}}(\mathbf{J})\ \exp\left(i\mathbf{m}\cdot\boldsymbol{\theta} - i\,\omega_k t\right) + \text{c.c.}, \tag{5.1}$$

where the parametric dependence of $\delta\tilde{\mathcal{H}}$ on the Fourier indices $(\mathbf{m}, k)$ is hidden. The perturbed Vlasov distribution δF is obtained from the perturbed Vlasov equation

$$\frac{\partial \delta F}{\partial t} + \frac{\partial \delta F}{\partial \boldsymbol{\theta}}\cdot\frac{\partial H_0}{\partial \mathbf{J}} = \frac{\partial \delta\mathcal{H}}{\partial \boldsymbol{\theta}}\cdot\frac{\partial F_0}{\partial \mathbf{J}}, \tag{5.2}$$

from which we obtain the solution for the Fourier component $\delta\tilde{f}$:

$$\delta\tilde{F} = -\left(\frac{\delta\tilde{\mathcal{H}}}{\omega_k - \mathbf{m}\cdot\boldsymbol{\Omega}}\right)\mathbf{m}\cdot\frac{\partial F_0}{\partial \mathbf{J}}, \tag{5.3}$$

where $\boldsymbol{\Omega}(\mathbf{J}) \equiv \partial H_0/\partial \mathbf{J}$ denotes the unperturbed orbital-frequency vector.

The quasilinear wave-particle interactions cause the Vlasov distribution $F_0(\mathbf{J}, \tau)$ to evolve on a slow time scale $\tau = \epsilon^2 t$, represented by the quasilinear diffusion equation

$$\begin{aligned}\frac{\partial F_0(\mathbf{J},\tau)}{\partial \tau} &= \frac{1}{2}\langle\{\delta\mathcal{H},\delta F\}\rangle = \frac{1}{2}\frac{\partial}{\partial \mathbf{J}}\cdot\langle\frac{\partial \delta\mathcal{H}}{\partial \boldsymbol{\theta}}\ \delta F\rangle \\ &= \frac{\partial}{\partial \mathbf{J}}\cdot\left(\sum_{\mathbf{m},k}\mathbf{m}\,\mathrm{Im}\langle\delta\tilde{\mathcal{H}}^*\,\delta\tilde{F}\rangle\right) \\ &= \frac{\partial}{\partial \mathbf{J}}\cdot\left[\mathrm{Im}\left(\sum_{\mathbf{m},k}\frac{-\mathbf{mm}\,|\delta\tilde{\mathcal{H}}|^2}{\omega_k - \mathbf{m}\cdot\boldsymbol{\Omega}}\right)\cdot\frac{\partial F_0}{\partial \mathbf{J}}\right] \\ &\equiv \frac{\partial}{\partial \mathbf{J}}\cdot\left(\mathbf{D}_{\mathrm{QL}}\cdot\frac{\partial F_0}{\partial \mathbf{J}}\right),\end{aligned} \tag{5.4}$$

where $\langle\ \rangle$ includes orbital-angle averaging and wave time-scale averaging, and the canonical quasilinear diffusion tensor

$$\mathbf{D}_{\mathrm{QL}} \equiv \sum_{\mathbf{m},k}\mathbf{mm}\left[\pi\delta(\omega_k - \mathbf{m}\cdot\boldsymbol{\Omega})\right]|\delta\tilde{H}|^2 \tag{5.5}$$

is expressed in terms of a dyadic Fourier tensor $\mathbf{mm}$, a wave-particle resonance condition obtained from the Plemelj formula

$$\mathrm{Im}\left(\frac{-1}{\omega_k - \mathbf{m}\cdot\boldsymbol{\Omega}}\right) = \mathrm{Re}\left(\frac{i}{\omega_k - \mathbf{m}\cdot\boldsymbol{\Omega}}\right) = \pi\,\delta(\omega_k - \mathbf{m}\cdot\boldsymbol{\Omega}),$$

and the magnitude squared of the perturbed Hamiltonian Fourier component $\delta\tilde{H}(\mathbf{J})$, which is an explicit function of the action coordinates $\mathbf{J}$ and the perturbation fields [see of Ref. (Brizard and Chan, 2004), for example]. We note that the perturbed Hamiltonian $\delta\tilde{H}(\mathbf{J})$ will, therefore, include terms that contain a product of an adiabatic action coordinate (such as the gyro action J_g) and a wave perturbation factor (such as $\delta B/B_0 \sim \epsilon_\delta$). This means that an expansion of an adiabatic action coordinate (e.g., $\mathsf{J}_g = \mathsf{J}_g^{(0)} + \epsilon_B\,\mathsf{J}_g^{(1)} + \cdots$) in the factor $|\delta\tilde{H}|^2$ in Eq. 5.5 results in a leading term of order ϵ_δ^2, followed by negligible terms of order $\epsilon_B\,\epsilon_\delta^2 \ll \epsilon_\delta^2$. Hence, only a low-order expansion (in ϵ_B) of the adiabatic action coordinates $\mathbf{J} \simeq \mathbf{J}_0$ is needed in an explicit evaluation of Eq. 5.5. In addition, we note that the form Eq. 5.4, with Eq. 5.5, guarantees that the Vlasov entropy $S_0 = -\int F_0 \ln F_0\, d^3J$

$$\begin{aligned}\frac{dS_0}{dt} &= -\epsilon^2\int\frac{\partial F_0}{\partial \tau}\ (\ln F_0 + 1)\ d^3J \\ &= \epsilon^2\sum_{\mathbf{m},k}\int F_0\left(\mathbf{m}\cdot\frac{\partial \ln F_0}{\partial \mathbf{J}}\right)^2\pi\,\delta(\omega_k - \mathbf{m}\cdot\boldsymbol{\Omega})\,|\delta\tilde{\mathcal{H}}|^2\,d^3J > 0\end{aligned} \tag{5.6}$$

satisfies the H Theorem. Lastly, we note that collisional transport in a magnetized plasma can also be described in terms of drag and diffusion in action space (Bernstein and Molvig, 1983).

5.2 Local and bounce-averaged wave-particle resonances in quasilinear theory

The canonical action-angle formalism presented in Section 5.1 unfortunately makes use of the bounce action $\mathsf{J}_b = \oint p_\parallel(s)\,ds$, which is a nonlocal quantity (Northrop, 1963), while the drift action $\mathsf{J}_d \equiv (q/2\pi c)\oint\psi\,d\varphi = q\psi/c$ is a local coordinate in an axisymmetric magnetic field $\mathbf{B} = \nabla\psi\times\nabla\varphi$,

where the drift action is canonically conjugate to the toroidal angle φ. In our previous work (Brizard and Chan, 2001; Brizard and Chan, 2004), we replaced the bounce action with the guiding-center kinetic energy $\mathcal{E}$ in order to obtain a local quasilinear diffusion equation in three-dimensional $\mathbf{J}^i = (\mathsf{J}_b, \mathcal{E}, \mathsf{J}_d)$ guiding-center invariant space:

$$\frac{\partial F_0}{\partial \tau} = \frac{\partial}{\partial \mathbf{J}} \cdot \left(\mathbf{D}_{\rm QL} \cdot \frac{\partial F_0}{\partial \mathbf{J}} \right) = \frac{1}{\tau_b} \frac{\partial}{\partial \mathsf{J}^i} \left(\tau_b \, D^{ij}_{\rm QL} \, \frac{\partial F_0}{\partial \mathsf{J}^j} \right), \tag{5.7}$$

where the bounce period $\tau_b \equiv \oint ds/v_\parallel$ is the Jacobian. In addition, the 3×3 quasilinear diffusion tensor

$$\mathbf{D}_{\rm QL} = \sum_{\ell,k,m} \begin{pmatrix} \ell^2 & \ell\,\omega_k & \ell\, m \\ \omega_k \ell & \omega_k^2 & \omega_k m \\ m\ell & m\omega_k & m^2 \end{pmatrix} \Gamma_{\ell k m} \tag{5.8}$$

is defined in terms of the Fourier indices ℓ (associated with the gyroangle ζ) and m (associated with the toroidal angle φ) and the wave frequency ω_k, while the scalar $\Gamma_{\ell k m}$ was shown in Ref. (Brizard and Chan, 2004) to include the bounce-averaged wave-particle resonance condition

$$\omega_k = \ell \, \langle \omega_c \rangle_b + n \, \omega_b + m \, \langle \omega_d \rangle_b, \tag{5.9}$$

where $\langle \omega_c \rangle_b = (q/Mc) \, \langle B \rangle_b$ and $\langle \omega_d \rangle_b$ are the bounce-averaged cyclotron and drift frequencies, respectively, and $\omega_b = 2\pi/\tau_b$ is the bounce frequency. Here, the bounce-average operation is defined as

$$\langle \cdots \rangle_b \equiv \frac{1}{\tau_b} \sum_\sigma \int_{s_L}^{s_U} \frac{ds}{|v_\parallel|} \, (\cdots), \tag{5.10}$$

where $\sigma \equiv v_\parallel/|v_\parallel|$ denotes the sign of the parallel guiding-center velocity, and the points $s_{L,U}(\mathbf{J})$ along a magnetic field line are the bounce (turning) points where $v_\parallel$ changes sign (for simplicity, we assume all particles are magnetically trapped). In this Section, we present a brief derivation of the quasilinear diffusion Eq. 5.7, with the 3×3 quasilinear diffusion tensor Eq. 5.8 and the wave-particle resonance condition Eq. 5.9, based on our previous work (Brizard and Chan, 2004), which is presented here in the non-relativistic limit.

We begin with the linear guiding-center Vlasov equation in guiding-center phase space $(s, \varphi, \zeta; \mathbf{J})$:

$$\frac{d_0 \delta F}{dt} = \frac{\partial \delta F}{\partial t} + \{\delta F, \, \mathcal{E}\}_{\rm gc} = -\{F_0, \, \delta H\}_{\rm gc}, \tag{5.11}$$

where the perturbed Hamiltonian is a function of the guiding-center invariants $(\mathsf{J}_b, \mathcal{E}, \mathsf{J}_d)$ as well as the angle-like coordinates (s, φ, ζ). The unperturbed guiding-center Poisson bracket, on the other hand, is

$$\begin{aligned} \{F, G\}_{\rm gc} = & \frac{\partial F}{\partial \zeta} \frac{\partial G}{\partial \mathsf{J}_g} - \frac{\partial F}{\partial \mathsf{J}_g} \frac{\partial G}{\partial \zeta} + \frac{\partial F}{\partial \varphi} \frac{\partial G}{\partial \mathsf{J}_d} - \frac{\partial F}{\partial \mathsf{J}_d} \frac{\partial G}{\partial \varphi} \\ & + \left(\frac{d_0 F}{dt} - \frac{\partial F}{\partial t} \right) \frac{\partial G}{\partial \mathcal{E}} - \frac{\partial F}{\partial \mathcal{E}} \left(\frac{d_0 G}{dt} - \frac{\partial G}{\partial t} \right), \end{aligned} \tag{5.12}$$

and $d_0/dt = \partial/\partial t + v_\parallel \, \partial/\partial s + \omega_d \, \partial/\partial \varphi + \omega_c \, \partial/\partial \zeta$ denotes the unperturbed Vlasov operator (s denotes the local spatial coordinate along an unperturbed magnetic-field line). Since the right side of Eq. 5.11 is

$$-\{F_0, \, \delta H\}_{\rm gc} = \frac{\partial F_0}{\partial \mathsf{J}_g} \frac{\partial \delta H}{\partial \zeta} + \frac{\partial F_0}{\partial \mathsf{J}_d} \frac{\partial \delta H}{\partial \varphi} + \frac{\partial F_0}{\partial \mathcal{E}} \left(\frac{d_0 \delta H}{dt} - \frac{\partial \delta H}{\partial t} \right), \tag{5.13}$$

we can introduce the non-adiabatic decomposition (Chen and Tsai, 1983)

$$\delta F \equiv \delta H \, \frac{\partial F_0}{\partial \mathcal{E}} + \delta G, \tag{5.14}$$

where the non-adiabatic contribution δG satisfies the perturbed non-adiabatic Vlasov equation

$$\frac{d_0 \delta G}{dt} = \left(\frac{\partial F_0}{\partial \mathsf{J}_g} \frac{\partial}{\partial \zeta} + \frac{\partial F_0}{\partial \mathsf{J}_d} \frac{\partial}{\partial \varphi} - \frac{\partial F_0}{\partial \mathcal{E}} \frac{\partial}{\partial t} \right) \delta H \equiv \hat{\mathcal{F}} \, \delta H. \tag{5.15}$$

Next, since the background plasma is time independent and axisymmetric, and the unperturbed guiding-center Vlasov distribution is independent of the gyroangle, we perform Fourier transforms in (φ, ζ, t) so that Eq. 5.15 becomes

$$\begin{aligned} \left[v_\parallel \frac{\partial}{\partial s} - i \, (\omega_k - \ell \, \omega_c - m \, \omega_d) \right] \delta \tilde{G}(s, \sigma) \; & \equiv \hat{\mathcal{L}} \, \delta \tilde{G}(s, \sigma) \\ & = i \, \mathcal{F} \, \delta \tilde{H}(s, \sigma), \end{aligned} \tag{5.16}$$

where the amplitudes $(\delta \tilde{G}, \delta \tilde{H})$ depend on the spatial parallel coordinate s and the sign $\sigma = v_\parallel/|v_\parallel| = \pm 1$, as well as the invariants $\mathbf{J}$, while the operator $\hat{\mathcal{F}}$ becomes $i\,\mathcal{F}$, with

$$\mathcal{F} \equiv \omega_k \, \frac{\partial F_0}{\partial \mathcal{E}} + \ell \, \frac{\partial F_0}{\partial \mathsf{J}_g} + m \, \frac{\partial F_0}{\partial \mathsf{J}_d}. \tag{5.17}$$

In order to remove the dependence of the perturbed Hamiltonian $\delta \tilde{H}$ on σ (which appears through the combination $v_\parallel \delta \tilde{A}_\parallel$), we follow our previous work (Brizard and Chan, 2004) and introduce the gauge $\delta \tilde{A}_\parallel \equiv \partial \delta \tilde{\alpha}/\partial s$ and the transformation $(\delta \tilde{G}, \delta \tilde{H}) \to (\delta \tilde{G}', \delta \tilde{K})$, where $\delta \tilde{G}' = \delta \tilde{G} + i \, (q/c) \mathcal{F} \, \delta \tilde{\alpha}$ and $\delta \tilde{K} = \delta \tilde{H} + (q/c) \, \hat{\mathcal{L}} \, \delta \tilde{\alpha}$, so that Eq. 5.16 becomes $\hat{\mathcal{L}} \, \delta \tilde{G}'(s, \sigma) = i \, \mathcal{F} \, \delta \tilde{K}(s)$.

In order to obtain an integral solution for $\delta \tilde{G}'$, we now introduce the integrating factor

$$\begin{aligned} & \left[v_\parallel \frac{\partial}{\partial s} - i \, (\omega_k - \ell \, \omega_c - m \, \omega_d) \right] \delta \tilde{G}'(s, \sigma) \\ & \quad \equiv e^{i \sigma \theta} v_\parallel \frac{\partial}{\partial s} \left[e^{-i \sigma \theta} \delta \tilde{G}'(s, \sigma) \right] = i \, \mathcal{F} \, \delta \tilde{K}(s), \end{aligned} \tag{5.18}$$

where

$$\theta(s) \equiv \int_{s_L}^{s} \left(\omega_k - \ell \, \omega_c(s') - m \, \omega_d(s') \right) \frac{ds'}{|v_\parallel|} \tag{5.19}$$

is defined in terms of the lower (L) turning point $s_L(\mathbf{J})$. The solution of Eq. 5.18 is, therefore, expressed as

$$\delta\tilde{G}'(s,\sigma) = \delta\bar{G}'\, e^{i\sigma\theta} + i\,\sigma\, e^{i\sigma\theta}\left(\int_{s_L}^{s} \delta\tilde{K}(s')\, e^{-i\sigma\theta(s')}\frac{ds'}{|v_\parallel|}\right)\mathcal{F} \tag{5.20}$$

where the constant amplitude $\delta\bar{G}'$ is determined from the matching conditions $\delta\tilde{G}'(s_L,+1) = \delta\tilde{G}'(s_L,-1)$ and $\delta\tilde{G}'(s_U,+1) = \delta\tilde{G}'(s_U,-1)$ at the two turning points. At the lower turning point, the matching condition implies that $\delta\bar{G}'$ is independent of σ. The matching condition at the upper turning point, on the other hand, is expressed as

$$e^{i\Theta}\,\delta\bar{G}' + \frac{i\tau_b}{2}\,\langle\delta\tilde{K}e^{-i\theta}\rangle_b\, e^{i\Theta}\,\mathcal{F} = e^{-i\Theta}\,\delta\bar{G}' - \frac{i\tau_b}{2}\,\langle\delta\tilde{K}e^{i\theta}\rangle_b \times e^{-i\Theta}\,\mathcal{F},$$

which yields

$$\delta\bar{G}' = -\frac{\tau_b}{2}\Big(\cot\Theta\,\langle\delta\tilde{K}\cos\theta\rangle_b + \langle\delta\tilde{K}\sin\theta\rangle_b\Big)\,\mathcal{F}, \tag{5.21}$$

where

$$\Theta \equiv \theta(s_U) = \frac{\tau_b}{2}\,(\omega_k - \ell\,\langle\omega_c\rangle_b - m\,\langle\omega_d\rangle_b). \tag{5.22}$$

We note that $\cot\Theta$ in Eq. 5.21 has singularities at $n\pi$, which immediately leads to the resonance condition Eq. 5.9.

Now that the solution $\delta\tilde{G}'$ has been determined, we can proceed with the derivation of the quasilinear diffusion equation, which has been shown by Brizard and Chan (Brizard and Chan, 2004) to be expressed as

$$\begin{aligned}\frac{\partial F_0}{\partial\tau} &= \frac{1}{\tau_b}\frac{\partial}{\partial\mathcal{E}}\left[\tau_b\left(\sum_{\ell,k,m}\omega_k\,\Gamma_{\ell km}\,\mathcal{F}\right)\right] + \frac{1}{\tau_b}\frac{\partial}{\partial J_g}\left[\tau_b\left(\sum_{\ell,k,m}\ell\,\Gamma_{\ell km}\,\mathcal{F}\right)\right] \\ &+ \frac{1}{\tau_b}\frac{\partial}{\partial J_d}\left[\tau_b\left(\sum_{\ell,k,m} m\,\Gamma_{\ell km}\,\mathcal{F}\right)\right] \\ &\equiv \frac{1}{\tau_b}\frac{\partial}{\partial J^i}\left(\tau_b\, D^{ij}_{QL}\,\frac{\partial F_0}{\partial J^j}\right),\end{aligned} \tag{5.23}$$

which requires us to evaluate $\Gamma_{\ell km} \equiv \mathcal{F}^{-1}\mathrm{Im}\langle\delta\tilde{H}^*\delta\tilde{G}\rangle_b = \mathcal{F}^{-1}\mathrm{Im}\langle\delta\tilde{K}^*\delta\tilde{G}'\rangle_b$, which is found to be expressed as

$$\Gamma_{\ell km} = \frac{\tau_b}{2}\,\mathrm{Im}\,(-\cot\Theta)\,\left|\langle\delta\tilde{K}\cos\theta\rangle_b\right|^2, \tag{5.24}$$

where, using the Plemelj formula with the identity $\cot z = \sum_{n=-\infty}^{\infty}(z-n\pi)^{-1}$, we finally obtain

$$\Gamma_{\ell km} = \left|\langle\delta\tilde{K}\cos\theta\rangle_b\right|^2 \sum_{n=-\infty}^{\infty}\pi\,\delta(\omega_k - \ell\,\langle\omega_c\rangle_b - n\,\omega_b - m\,\langle\omega_d\rangle_b). \tag{5.25}$$

This expression completes the derivation of the quasilinear diffusion tensor Eq. 5.8 and the perturbed Hamiltonian $\delta\tilde{K}$ is fully defined in Ref. (Brizard and Chan, 2004). We note that, in the limit of low-frequencies electromagnetic fluctuations, we also recover our previous work (Brizard and Chan, 2001) from Eq. 5.8.

We now make a few remarks concerning the bounce-averaged wave-particle resonance condition Eq. 5.9. First, in the case of a uniform magnetized plasma (with the drift frequency $\omega_d \equiv 0$), we substitute the eikonal representations $\delta\tilde{G} = \delta\bar{G}\,\exp(ik_\parallel s)$ and $\delta\tilde{H} = \delta\bar{H}\,\exp(ik_\parallel s)$ in Eq. 5.16 and we recover the uniform quasilinear diffusion Eq. 4.17. Second, the bounce-averaged wave-particle resonance condition Eq. 5.9 assumes that the waves are coherent on the bounce-time scale, which is not realistic for high-frequency (VLF), short-wavelength whistler waves (Stenzel, 1999; Allanson et al., 2021). We recover a local wave-particle resonance condition by introducing the bounce-angle coordinate $\xi(s)$ (Brizard, 2000), which is defined by the equation $d\xi/ds = \omega_b/v_\parallel$, so that $v_\parallel\,\partial/\partial s$ in Eq. 5.16 is replaced with $\omega_b\,\partial/\partial\xi$. Next, by introducing the bounce-angle Fourier series $\delta\tilde{G} = \sum_{n=-\infty}^{\infty}\delta\bar{G}\,\exp(in\xi)$ and $\delta\tilde{H} = \sum_{n=-\infty}^{\infty}\delta\bar{H}\,\exp(in\xi)$ in Eq. 5.16, the integral phase Eq. 5.19 is replaced by the new integral phase

$$\begin{aligned}\sigma\,\chi(s) &= \sigma\,\theta(s) - n\,\xi(s) \\ &= \sigma\int_{s_L}^{s}(\omega_k - \ell\,\omega_c(s') - m\,\omega_d(s') - n\,\omega_b)\frac{ds'}{|v_\parallel|}.\end{aligned} \tag{5.26}$$

If we now evaluate this integral by stationary-phase methods (Stix, 1992), the dominant contribution comes from points s_0 along a magnetic-field line where

$$0 = \chi'(s_0) = |v_\parallel(s_0)|^{-1}\,(\omega_k - \ell\,\omega_c(s_0) - m\,\omega_d(s_0) - n\,\omega_b), \tag{5.27}$$

which yields the local wave-particle resonance condition, provided $v_\parallel(s_0) \neq 0$ (i.e., the local resonance does not occur at a turning point).

6 Summary

In the present paper, we have established a direct connection between the standard reference of quasilinear theory for a uniform magnetized plasma by Kennel and Engelmann (Kennel and Engelmann, 1966) and its Hamiltonian formulation in guiding-center phase space. We have also shown that the transition to a quasilinear theory for a nonuniform magnetized plasma is greatly facilitated within a Hamiltonian formulation. The main features of a Hamiltonian formulation of quasilinear theory is that the quasilinear diffusion tensor has a simple modular dyadic form in which a matrix of Fourier indices is multiplied by a single quasilinear scalar potential, which includes the resonant wave-particle delta function. This simple modular is observed in the case of a uniform magnetized plasma, as seen in Eq. 4.18, as well as in the case of a nonuniform magnetized plasma, as seen in Eq. 5.8. In particular, we note that the quasilinear diffusion tensor Eq. 5.8 naturally incorporates quasilinear radial diffusion as well as its synergistic connections to diffusion in two-dimensional invariant velocity space. These features are easily extended to the quasilinear diffusion of relativistic charged particles that are magnetically confined by nonuniform magnetic fields.

Author contributions

AB has written 90% of the manuscript. AC has added technical references as well as historical context.

Funding

This work was partially funded by grants from (AB) NSF-PHY 2206302 and (AC) NASA NNX17AI15G and 80NSSC21K1323.

Conflict of interest

The authors declare that the research was conducted in the absence of any commercial or financial relationships that could be construed as a potential conflict of interest.

Publisher's note

Supplementary material

The Supplementary Material for this article can be found online at: https://www.frontiersin.org/articles/10.3389/fspas.2022.1010133/full#supplementary-material

References

Allanson, O., Watt, C. E. J., Allison, H. J., and Ratcliffe, H. (2021). Electron diffusion and advection during nonlinear interactions with whistler-mode waves. *JGR. Space Phys.* 126, 028793. doi:10.1029/2020ja028793

Bernstein, I. B., and Molvig, K. (1983). Lagrangian formulation of neoclassical transport theory. *Phys. Fluids* 26, 1488. doi:10.1063/1.864319

Bernstein, I., and Rowlands, G. (1976). Diffusion in velocity space associated with nonadiabatic changes in the magnetic moment of a charged particle. *Phys. Fluids* 19, 1546. doi:10.1063/1.861358

Brizard, A. (1994). Eulerian action principles for linearized reduced dynamical equations. *Phys. Plasmas* 1, 2460–2472. doi:10.1063/1.870574

Brizard, A. J., and Chan, A. A. (2001). Relativistic bounce-averaged quasilinear diffusion equation for low-frequency electromagnetic fluctuations. *Phys. Plasmas* 8, 4762–4771. doi:10.1063/1.1408623

Brizard, A. J., and Chan, A. A. (2004). Relativistic quasilinear diffusion in axisymmetric magnetic geometry for arbitrary-frequency electromagnetic fluctuations. *Phys. Plasmas* 11, 4220–4229. doi:10.1063/1.1773554

Brizard, A. J., and Chandre, C. (2020). Hamiltonian formulations for perturbed dissipationless plasma equations. *Phys. Plasmas* 27, 122111. doi:10.1063/5.0028471

Brizard, A. J. (2000). Nonlinear bounce-gyrocenter Hamiltonian dynamics in general magnetic field geometry. *Phys. Plasmas* 7, 3238–3246. doi:10.1063/1.874189

Brizard, A. J. (2018). Perturbative variational formulation of the Vlasov-Maxwell equations. *Phys. Plasmas* 25, 112112. doi:10.1063/1.5049570

Brizard, A., and Markowski, D. (2022). On the validity of the guiding-center approximation in a magnetic dipole field. *Phys. Plasmas* 29, 022101. doi:10.1063/5.0078786

Cary, J. R., and Brizard, A. J. (2009). Hamiltonian theory of guiding-center motion. *Rev. Mod. Phys.* 81, 693–738. doi:10.1103/revmodphys.81.693

Chen, L., and Tsai, S.-T. (1983). Linear oscillations in general magnetically confined plasmas. *Plasma Phys.* 25, 349–359. doi:10.1088/0032-1028/25/4/001

Crews, D., and Shumlak, U. (2022). On the validity of quasilinear theory applied to the electron bump-on-tail instability. *Phys. Plasmas* 29, 043902. doi:10.1063/5.0086442

Davidson, R. C. (1972). *Methods in nonlinear plasma theory*. Cambridge, Massachusetts, United States: Academic Press.

Dewar, R. (1973). Oscillation center quasilinear theory. *Phys. Fluids* 16, 1102. doi:10.1063/1.1694473

Dodin, I. (2022). Quasilinear theory for inhomogeneous plasma. *J. Plasma Phys.* 88, 905880407. doi:10.1017/s0022377822000502

Dupree, T. (1966). A perturbation theory for strong plasma turbulence. *Phys. Fluids* 9, 1773. doi:10.1063/1.1761932

Galeev, A., and Sagdeev, R. (1983). *Basic plasma physics*, 1. Amsterdam: North Holland.

Kaufman, A. N., and Cohen, B. I. (2019). Theoretical plasma physics. *J. Plasma Phys.* 85, 205850601. doi:10.1017/s0022377819000667

Kaufman, A. (1972). Quasilinear diffusion of an axisymmetric toroidal plasma. *Phys. Fluids* 15, 1063. doi:10.1063/1.1694031

Kaufman, A. (1972). Reformulation of quasi-linear theory. *J. Plasma Phys.* 8, 1–5. doi:10.1017/s0022377800006887

Kennel, C., and Engelmann, F. (1966). Velocity space diffusion from weak plasma turbulence in a magnetic field. *Phys. Fluids* 9, 2377. doi:10.1063/1.1761629

Krommes, J. A. (2002). Fundamental statistical descriptions of plasma turbulence in magnetic fields. *Phys. Rep.* 360, 1–352. doi:10.1016/s0370-1573(01)00066-7

Lejosne, S., and Kollmann, P. (2020). Radiation belt radial diffusion at Earth and beyond. *Space Sci. Rev.* 216, 19. doi:10.1007/s11214-020-0642-6

Lerche, I. (1968). Quasilinear theory of resonant diffusion in a magneto-active, relativistic plasma. *Phys. Fluids* 11, 1720. doi:10.1063/1.1692186

Mahajan, S., and Chen, C. Y. (1985). Plasma kinetic theory in action-angle variables. *Phys. Fluids* 28, 3538. doi:10.1063/1.865308

Mynick, H., and Duvall, R. (1989). Erratum: "A unified theory of tokamak transport via the generalized balescu–lenard collision operator" [phys. Fluids B **1**, 750 (1989)]. *Phys. Fluids B Plasma Phys.* 1, 1758. doi:10.1063/1.859212

Northrop, T. G. (1963). *The adiabatic motion of charged particles*. Geneva: Interscience Publishers.

Sagdeev, R. Z., and Galeev, A. A. (1969). *Nonlinear plasma theory*. California: W. A. Benjamin.

Schulz, M. (1996). Canonical coordinates for radiation-belt modeling. *Geophys. Monogr. - Am. Geophys. Union* 97, 153.

Stenzel, R. L. (1999). Whistler waves in space and laboratory plasmas. *J. Geophys. Res.* 104, 14379–14395. doi:10.1029/1998ja900120

Stix, T. (1992). *Waves in plasmas*. United States: American Institute of Physics.

Tao, X., Chan, A., and Brizard, A. (2007). Hamiltonian theory of adiabatic motion of relativistic charged particles. *Phys. Plasmas* 14, 092107. doi:10.1063/1.2773702

frontiers | Frontiers in Astronomy and Space Sciences

TYPE Original Research
PUBLISHED 13 October 2022
DOI 10.3389/fspas.2022.1040092

OPEN ACCESS

EDITED BY
Xiao-Jia Zhang,
University of California, Los Angeles, United States

REVIEWED BY
Jiang Liu,
University of Southern California, United States
Sheng Tian,
AOS UCLA, United States

*CORRESPONDENCE
Jun Liang,
liangj@ucalgary.ca

SPECIALTY SECTION
This article was submitted to Space Physics, a section of the journal Frontiers in Astronomy and Space Sciences

RECEIVED 08 September 2022
ACCEPTED 30 September 2022
PUBLISHED 13 October 2022

CITATION
Liang J, Gillies D, Donovan E, Parry H, Mann I, Connors M and Spanswick E (2022), On the green isolated proton auroras during Canada thanksgiving geomagnetic storm. *Front. Astron. Space Sci.* 9:1040092. doi: 10.3389/fspas.2022.1040092

On the green isolated proton auroras during Canada thanksgiving geomagnetic storm

Jun Liang[1]*, D. Gillies[1], E. Donovan[1], H. Parry[2], I. Mann[2], M. Connors[3,1] and E. Spanswick[1]

[1]Department of Physics and Astronomy, University of Calgary, Calgary, AB, Canada, [2]Department of Physics, University of Alberta, Edmonton, AB, Canada, [3]Athabasca University Observatories, Athabasca, AB, Canada

The existence of detached/isolated auroral structures in the subauroral ionosphere has been recognized and studied for decades. One major subset of such detached auroras is the so-called "isolated proton aurora" (IPA). IPA is characterized by substantial hydrogen emissions and thus inferred to be proton aurora, but is also accompanied by other emission lines. In particular, IPA is usually dominated by 557.7 nm green-line emissions in optical luminosity. To date, there is still a lack of dedicated spectrographic study and detailed comparison among structures in different emission lines of IPA. The intensity ratios between the 557.7 nm and hydrogen emissions in IPA have not been well established from concurrent observations or theoretical models. In this study, we report an IPA event during ~0245–0345 UT on 12 October 2021, the Canada Thanksgiving storm night. Using multi-station, multi-wavelength optical instruments, including the Transition Region Explorer (TREx) spectrograph, we investigate the evolution and spectrographic properties of the IPA. *In-situ* and ground magnetometer data show evidence of electromagnetic ion cyclotron (EMIC) waves associated with the passage of IPA, supporting a causal link between the EMIC wave and the proton precipitation. The precipitating proton energies are estimated to range between a few keV and a few tens of keV according to the IPA emission heights inferred from triangulation analyses. *Via* careful examination of the spectral intensities and the elevation-angle profiles of the 557.7, 427.8, and 486.1 nm emissions based on the spectrograph data, we conclude that the 557.7 nm emissions contained in the IPA were unlikely to owe their source to energetic electron precipitation from the magnetosphere, but were the byproduct of the proton precipitation. The intensity ratio between the 557.7 nm (427.8 nm) and the 486.1 nm emissions of the IPA are confined within a relatively narrow range around ~26 (~4), which may serve as validation tests for existing and developing proton transport models.

KEYWORDS

isolated proton aurora, EMIC wave, hydrogen emission, green-line emission, TREX

1 Introduction

The existence of detached auroral arcs or isolated blobs/spots in the subauroral region equatorward of the main auroral oval has been known for decades (see e.g., a historical review by Frey, 2007). Such detached arc/blobs/spots may be present in dayside and nightside, and can be caused by either proton or electron precipitation (or both). In the dayside, emissions called afternoon detached proton arcs (Immel et al., 2002; Burch et al., 2002) and subauroral morning proton spots (Frey., 2007) were observed equatorward of the main auroral oval in the afternoon and morning sector, respectively. In the nightside, the so-called "evening corotating patch" (ECP) (Moshupi et al., 1977; Kobuta et al., 2003) was observed in the evening sector and was attributed to high-energy electron precipitation. Zhang et al. (2005; 2008) reported the "nightside detached auroras" caused by energetic proton precipitations during intense magnetic storms. Using data from the multi-wavelength all-sky-imagers (ASI) and induction magnetometers, Sakaguchi et al. (2007; 2008; 2015) investigated the "isolated proton auroras" in the evening sector and found them coincident with Pc1 geomagnetic pulsations. Those detached/isolated proton arcs/blob/spots, despite their differences in shapes and fine structures, are now often deemed to owe their source mechanisms to the electromagnetic ion cyclotron (EMIC) wave and its resulting pitch-angle scattering of ring-current ions in the inner magnetosphere (e.g., Immel et al., 2005; Sakaguchi et al., 2007, 2008, 2015; Yahnin et al., 2007; Yuan et al., 2010; Liang et al., 2014; Kim et al., 2021; Shumko et al., 2022). EMIC waves are generated in the equatorial region of the plasmasphere-magnetosphere by internal wave-particle interaction with ring-current ions (Fraser et al., 2005; Jordanova et al., 2007; Usanova et al., 2016). In ground magnetic observations, they are typically observed as Pc 1–2 (0.one to five Hz) waves (e.g., Mann et al., 2014; Sakaguchi et al., 2015). For a recent comprehensive review of the detached/isolated proton auroras in the subauroral region and their potential connection to EMIC wave activities, see Gallardo-Lacourt et al. (2021). Notwithstanding the diversity of terminologies used by different researchers due to historical reasons, since the study of Sakaguchi et al. (2007; 2008) the term "isolated proton auroras" (IPA) has become prevalent in literature in depicting those detached/isolated proton auroral structures, particularly in the nightside. We shall follow to use the term IPA in this paper, though sometimes we may also call it "detached arc" for a morphological depiction.

The existence of IPA in the subauroral region is also familiar to auroral chasers and citizen scientists. At one time, the name "proton arc" was used by some citizen scientists to depict the STEVE (Strong Thermal Emission Velocity Enhancement) phenomenon — we of course now know they are fundamentally different in many key aspects. That being said, it was indeed noticed that some STEVE events were preceded by IPAs (Nishimura et al., 2020; Liang et al., 2021). Though beyond the interest of the current study, we mention that the event to be studied in this paper was also ensured by the occurrence of a "stable auroral red" (SAR) arc and a STEVE ~1–2 h later. Possible relationship among the IPA, the SAR, and the STEVE, three pronounced subauroral optical phenomena, has been a topic of active research interest recently (e.g., Gallardo-Lacourt et al., 2021; Nishimura et al., 2022).

In this study we shall report an IPA event occurring on 12 October 2021 during a geomagnetic storm interval, commonly known as the Canada Thanksgiving storm. Over that night, a number of subauroral optical structures were seen over Canada, and aroused keen interest and discussions among citizen/professional scientists on social media. The IPAs are among these phenomena. A few spectacular examples of IPAs recorded by citizen scientists are given in Supplementary Material. Knowledgeable and inquisitive citizen scientists have raised the following questions: 1) what is the cause of these IPAs? 2) if these IPAs represent proton auroras, why do they look greenish just as normal electron auroras?

Different auroral emission lines at different wavelengths (colors) are characteristic of different excitation and chemical processes in the ionosphere. Proton precipitation is usually characterized by hydrogen emission lines such as Lyman-α (121.8 nm), Hα (656.3 nm), and Hβ (486.1 nm), among which the Hβ 486.1 nm is the most used in ground-based proton auroral measurements (Eather, 1967). Other pronounced auroral emission lines in the visible wavelength range include 427.8 nm, 557.7 nm, 630 nm, etc. (see e.g., Vallance-Jones, 1974). The 427.8 nm blue-line is among the N_2^+ first-negative-group (1NG), while the 557.7 nm green-line and 630 nm red-line result from excited oxygen atoms. These nitrogen and oxygen auroras can be led by both electron and proton precipitations. It has been known for a long time that proton auroras are accompanied by other emission lines/bands, and that some of these emission lines can be much stronger in optical brightness than the proton auroral lines (e.g., Eather, 1967, 1968). However, Eather (1967) noted that many of the early measurements of proton-induced auroras contained contributions from co-existing electron auroras. For some more recent examples, detached proton arcs seen by the IMAGE satellite show signals on both SI-12 (Lyman-α) and WIC (N_2 LBH band) imagers (Immel et al., 2002, 2005; Frey, 2007). *Via* multi-wavelength ASI observations, Sakaguchi et al. (2007; 2008) noted that IPAs had counterparts in 557.7 and 630 nm wavelengths, and that the 557.7 nm emission dominated in terms of optical luminosity. However, those authors did not perform a detailed comparison among these emission lines. Due to the instrumental design, the 557.7 and 486.1 nm images involved in Sakaguchi et al. (2007)'s study were run at low time resolution (2 min) and were not taken at the same time epoch (separated by 34 s), which is not ideal for a cross-comparison between the two emission lines for dynamically time-varying IPAs. Nishimura et al. (2022) studied the 630 nm red-line emissions accompanying IPAs,

and proposed that the associated red-line emissions may contribute to the initial formation of SAR. However, the relatively low viewing angle and the large difference between the emission altitudes of 630 nm and 486.1 nm hindered efforts to compare their structural shapes in detail. To the authors' knowledge, so far there is still a lack of a dedicated spectrographic study and detailed comparison among emission lines associated with IPAs. It has not been rigorously shown from concurrent observations whether a detached proton arc/blob and its correspondent 557.7 nm arc/blob share the same spatial structures and temporal variations or not. This leads to a remaining uncertainty of whether electron precipitation might co-exist and (partly) contribute to the detached 557.7 nm emissions. Such an uncertainty is compounded by the following complications in both observations and theories. 1) *In-situ* particle instruments usually have an energy limit (e.g., ~30 keV for DMSP), so that electron precipitation beyond the observable range cannot be excluded. 2) It is known that a number of plasma waves, such as plasmaspheric hiss, whistler-mode chorus, and EMIC waves, may lead to electron precipitation in the inner magnetosphere, typically with energies from a few tens of keV up to >1 MeV (e.g., Summers et al., 2007; Miyoshi et al., 2008; Ni et al., 2015, 2017; Zhang et al., 2016, 2022; Fu et al., 2018). At times, hints of such electron precipitation appeared in *in-situ* particle observations in conjunction with IPAs (e.g., Nishimura et al., 2020; Shumko et al., 2022). 3) Detached auroral arcs/patches contributed by electron precipitation are known to exist (Wallis et al., 1979; Kobuta et al., 2003; Yadav and Shiokawa, 2021). For example, a detached arc recently studied by Yadav and Shiokawa. (2021) was found to be related to ~0.1–2 keV electron precipitation. Mendillo et al. (1989) proposed that plasma-sheet-like electron precipitation might co-exist with proton precipitation and co-contribute to the detached arcs. 4) While various nitrogen auroras and OI 630 nm red-line auroras produced by proton precipitation have been quantitively modeled (e.g., Strickland et al., 1993; Lummerzheim et al., 2001; Galand and Lummerzheim, 2004), dedicated models of the OI 557.7 nm green-line emission led by proton auroral precipitation remain scarce in the existing literature. We are aware, both from private communications and from existing publications (e.g., Eather, 1967), that some researchers were not fully convinced that pure proton precipitation alone could lead to visually bright auroral display whose luminosity is dominantly contributed by 557.7 nm emissions.

In this paper, taking advantage of multi-station, multi-wavelength optical instruments, and aided by a variety of other ground and *in-situ* observations, we investigate the properties and dynamics of the IPA. In particular, we shall compare the signatures of IPA in various emission lines based on spectrograph measurements. *Via* such a comparison, we offer compelling arguments that the 557.7 nm green emissions of the detached arc are unlikely to owe their source to energetic electron precipitation from the magnetosphere, but are essentially the byproduct of proton precipitation. We also identify the Helium-band EMIC waves as the likely cause of the proton precipitation. Meanwhile, the intensity ratios among emission lines reported here are intended to set the experimental constraint and serve as validation tests for existing and developing proton auroral transport/emission models.

2 Instruments

The IPA event of interest comes with comprehensive optical observations. Main instruments used in this study include the multi-wavelength all-sky-imagers (ASI) of the Athabasca University Geospace Observatory (AUGSO) at Athabasca (ATHA, Geo. 54.60^{0}N, 113.64^{0}W), the Four-Eight-Six-One (FESO) meridian-scanning photometer at ATHA, and the Transition Region Explorer (TREx) RGB true-color Camera and Meridian Spectrograph at Lucky Lake (LUCK, Geo. 51.15^{0}N, 107.26^{0}W). AUGSO multi-wavelength ASI contains three major auroral/airglow emission lines 557.7, 486.1, and 630.0 nm, and two other wavelengths 480 nm and 620 nm serving as background channels for 486.1 and 630.0 nm, respectively. Among them, the 557.7 nm green-line and 486.1 nm Hβ line will be specifically focused on in this study. AUGSO runs in 60-s cadence for 486.1 nm and 30-s cadence for 557.7 nm. FESO is a meridian-scanning photometer designed for 486.1 nm proton auroras (Unick, et al., 2017), which contains a signal channel (3 nm passband centered at 486.1 nm) and a background channel (average of two 3 nm bands centered at 480 and 495 nm). FESO has a time resolution of 30 s. The TREx Spectrograph (TRSp) is an imaging spectrograph designed to yield the optical spectra between ~400 and 800 nm of night sky emissions at 0.4 nm resolution along a meridian (Gillies et al., 2019). TRSp at LUCK runs at 15-s cadence. The TREx RGB (red-green-blue) ASI is a highly sensitive full-color imager designed to capture "true-color" images of the aurora and airglow (Gillies et al., 2020). The TREx RGB ASI data used in this study has a time resolution of 3 s. We highlight that all the involved instruments are wavelength/color discriminative, serving well for the research purpose of this study.

Besides the optical instruments, we also use the *in-situ* data from the GOES satellite, the DMSP satellite, and the Swarm satellite to aid this study. GOES-17 data (Kress et al., 2020) will be used to infer the drastic change of the inner magnetospheric status in the storm interval. The SSJ instrument (30–30 k eV, Redmon et al., 2017) onboard DMSP F18 will be used to infer the particle precipitation associated with the IPA. The magnetometer measurements onboard Swarm (Friis-Christensen et al., 2006), together with the ground magnetometer data from the Canadian Array for Real-time InveStigations of Magnetic Activity (CARISMA) (Mann et al., 2008), will be used to check the presence of EMIC wave activities associated with the IPA.

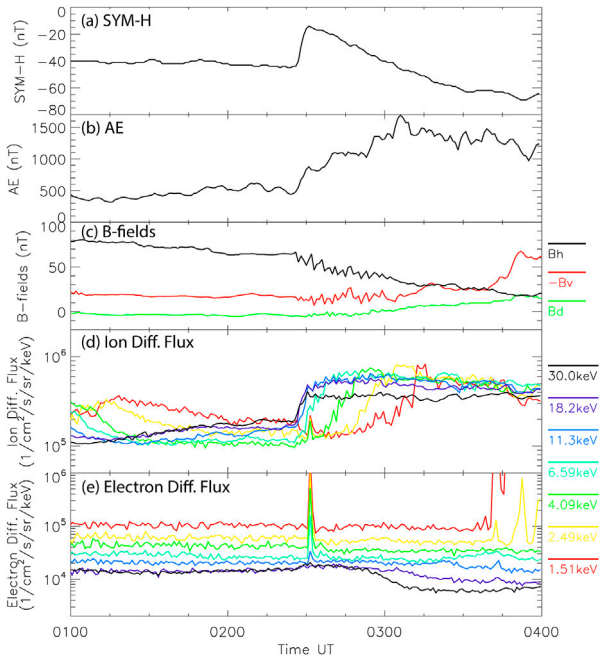

FIGURE 1
(A) SYM-H index. **(B)** AE index. **(C)** GOES-17 magnetic fields in VDH coordinates (-Bv: red; Bd: green; Bh: black). **(D)** GOES-17 omnidirectional proton differential fluxes. **(E)** GOSE-17 omnidirectional electron differential fluxes.

Swarm is the fifth Earth Explorer mission in the Living Planet Programme of European Space Agency. CARISMA is the continuation and expansion of the former Canadian Auroral Network for the OPEN Program Unified Study magnetometer array deployed and operated by the University of Alberta.

3 Observations

3.1 Geophysical/geomagnetic context and geosynchronous observations

The IPA of interest occurred during the Canada Thanksgiving storm. The top two panels of Figure 1 show the SYM-H and AE index during 1–4 UT on 12 October 2021. The SYM-H value had been relatively stable between −40 and −45 nT for a few hours before a sudden rise to −15 nT shortly before ~0230 UT, presumably related to the impact of a coronal mass ejection (CME)-associated interplanetary shock (the CME shock front arrived at the DSCOVR spacecraft at 0147 UT). The SYM-H then gradually decreased to ~ −70 nT. Large-scale geomagnetic disturbances beginning at ~0227 UT were recorded by THEMIS ground magnetometer array over Canada, and the AE index peaked over ~1,500 nT at ~3 UT. Strong auroral intensifications extended from high to mid-latitudes. As seen from the AUGSO ASI movie (see Supplementary Material), the auroras began to strongly intensify at ~0230 UT, both at the poleward portion of the aurora oval (discrete auroras) and in the equatorward diffuse auroras, including the main proton auroral band. The IPA of interest took place in the dusk/evening sector during ~0245–0345 UT, amid the storm interval. The occurrence of detached proton auroras in the dusk/nightside sectors following an interplanetary shock and a storm sudden commencement was previously reported by Zhang et al. (2008).

The remaining three panels of Figure 1 show GOES-17 data at geosynchronous orbit (L~6.6, Geo. 124^{0}W). The ionospheric footprint of GOES-17 estimated *via* empirical magnetic field models (T96/T01/TS02/TS05) ranges between ~62–64^0 MLAT and is ~10^0 west of the AUGSO ASI during the event interval of interest. Notwithstanding the mapping uncertainty GOES-17 is very likely to be located outward of the magnetospheric source region of IPA, but its data shed light on the drastic change of inner magnetospheric status in the dusk sector in our event. Figure 1C shows the magnetic fields in VDH coordinate, in which H-axis is antiparallel to the dipole axis, V-axis is parallel to the magnetic equatorial plane and directed outward, and D-axis completes the right-hand orthogonal system. The B_h component on GOES satellite is typically ~100 nT during quiescent times, but in this event, after ~0226 UT B_h gradually decreases to <20 nT, indicating a significant stretching of the magnetic field in the inner magnetosphere. Figures 1D,E show the omnidirectional ion/electron differential fluxes obtained from the low-energy sensor of the Space Environment *In Situ* Suite (SEISS) onboard GOES-17. We have used the SEISS L1b provisional data and averaged them in 1-min bins and over all view angles of the sensor. Despite the decrease in magnetic fields, the ion fluxes at energies from ~1to 30 keV increase substantially after ~0226 UT. Such intensification is not seen on electrons in the same energy range, except for a suspicious spike, perhaps of geophysical origin, for ≤10 keV energies at ~0231 UT. To summarize, while GOES-17 was not precisely conjugate to our optical observations area, two inferences made from the GOES-17 data are relevant to the duskside inner magnetospheric status and to the dynamics of IPA: 1) the drastic stretching of magnetospheric magnetic fields; 2) the energetic ion injection. We also browsed the Arase/ERG data (https://ergsc.isee.nagoya-u.ac.jp/). The Arase satellite was located at closer radial distances (L ~ 5.5) than GOES-17 but is further west (~17 h MLT). The energetic ion injection after ~0227 UT and the lack of corresponding energetic electron injection are also seen on Arase/ERG data. Clues of intensifications of both energetic ions and electrons are seen on THEMIS A/D/E satellites (http://themis.ssl.berkeley.edu/) at ~0227 UT when the probes were at L~8–9 R_E and ~3 h MLT east of GOES-17, but those energetic electrons might not penetrate deep into the duskside inner magnetosphere due to the Alfvén layer effect (e.g., Korth et al., 1999).

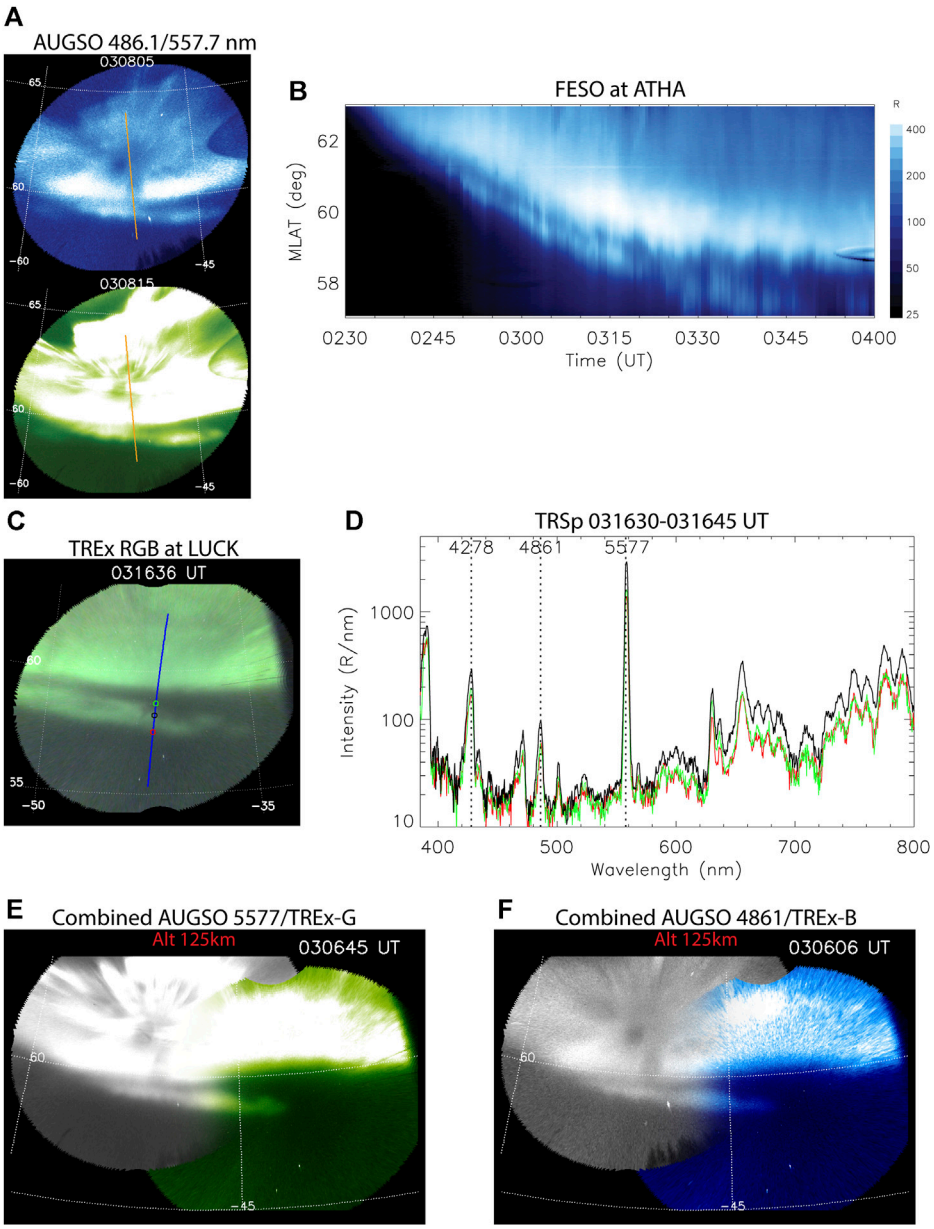

FIGURE 2
(A) Example of ATHA AUGSO 486.1 and 557.7 nm images, with FESO scan line overplotted. **(B)** 486.1 nm proton auroral intensity versus time and MLAT observed by FESO. **(C)** Example of TREX RGB ASI image, with TRSp scan line overplotted. Three colored circles along the TRSp scan line denote where the TRSp data are sampled to be shown in **(D)**. In **(A–C)**, an emission altitude of 125 km is assumed. **(D)** Example of the TRSp-measured optical spectra for three bins labeled in **(C)**. The black curve corresponds to the spectrum of IPA, while the green/red curves denote the spectrum of the northern/southern edge outside the IPA. **(E)** An example of the combined image maps of AUGSO 557.7 nm and TREX RGB ASI green-channel based on the best-fit altitudes of IPA from triangulation analysis. The overlapping FoV of the two ASIs is presented as an alpha-blending overlay of two images. **(F)** Similar to **(E)** but an combined image maps of AUGSO 486.1 nm and TREX RGB ASI blue-channel.

3.2 Summary and demonstration of optical instruments

Figure 2 serves to summarize data from the optical instruments used in this study and demonstrate their geometric combination. Overall, our observation time/area spans over the evening MLT between ~18.5 and ~20.5 h. Figure 2A exemplifies the AUGSO ASI observations at 486.1 557.7 nm. The 486.1 nm is characteristic of proton auroras, while the 557.7 nm usually represents the brightest emissions in

auroras. As seen from both the 486.1 and 557.7 nm images, an azimuthally-extended auroral structure is apparently detached from and equatorward of the main auroral oval, which constitutes the research interest of this study. We have checked the 480 nm image (not shown, see Supplementary Material), which serves as the background channel for the 486.1 nm, and confirmed that such an IPA structure is absent there. Therefore, such an IPA in the 486.1 nm image does not result from a continuum emission like STEVE (Liang et al., 2019) but is truly proton auroras. A movie of AUGSO observations at 486.1/557.7 nm (plotted side-by-side) showing the evolution of the IPA of interest is provided in Supplementary Material. Note that the AUGSO 486.1 and 557.7 nm images are taken at different time epochs and at different time resolutions. In the Supplementary Movie, the observation epochs of the two wavelengths are 10–20 s apart in each movie frame. Nevertheless, one may still infer from the movie the remarkable similarity in the structures and the temporal evolution of the IPA at the two wavelengths. Such a high correlation between the 486.1 nm emissions and the 557.7 nm emissions of the IPA will be specifically examined with TRSp data later in Section 3.5. The IPA also shows imprints in red-line 630 nm AUGSO images (see Supplementary Material), consistent with Nishimura et al. (2022), but the accompanying red-line emissions are not of special interest in this study.

AUGSO is not calibrated into Rayleigh values. An orange line overplotted in Figure 2A marks the scan line of FESO, a photometer specifically designed for 486.1 nm proton auroras (Unick et al., 2017). The FESO data in Figure 2B represents the keogram of the background-channel-subtracted, "pure" proton auroral intensities calibrated into optical Rayleigh. A Van-Rhijn correction is also applied. As seen from Figure 2B, an IPA starts to detach from the main auroral oval after ~0250 UT and moves progressively southward along with the main auroral oval. Such southward motions are, at least partly, related to the drastic stretching of magnetospheric magnetic fields as indicated in Figure 1C. We recall that the equatorward motion of the main proton auroral band is known to be an indication of the magnetic field stretching and the resultant increase of field-line-curvature at the equatorial magnetosphere (Donovan et al., 2012; Yue et al., 2014). The 486.1 nm emission intensity of the IPA reaches a few hundred Rayleigh, which is exceptionally strong for proton auroras (e.g., Eather, 1967; Donovan et al., 2012; Spanswick et al., 2017). We note that the 486.1 nm intensity obtained from FESO is compatible with that inferred from the spectrograph (see Figure 6 later). Such an agreement adds credibility to the two independent instruments and confirms the strength of the proton auroral structure of interest.

Figure 2C exemplifies the data from the TREx RGB ASI at LUCK. The TREx RGB ASI is designed to capture "true color" images of the aurora and airglow (Gillies et al., 2020). Figure 2C displays a true-color image reconstructed from the RGB channel data of the ASI. Of our interest, an auroral arc separated from the main auroral oval exists at ~58^0 MLAT. Such a detached arc appears greenish, similar to the color of the main auroral oval. A movie of the TREx RGB ASI showing the evolution of the IPA of interest is given in Supplementary Material.

A blue line overplotted in Figure 2C indicates the scan line of the TREx spectrograph (TRSp). TRSp is an imaging spectrograph designed to yield the optical spectra between ~400 and 800 nm of night sky emissions along a meridian (Gillies et al., 2019). TRSp is recently carefully calibrated in terms of the absolute optical intensity. To demonstrate, we sample three latitude bins (shown as circles in Figure 2C) from the TRSp: one inside the IPA, and the other two at its northern and southern edges just outside the arc. The optical spectra measured by TRSp from the three bins are shown in Figure 2D. As one can see, the IPA shows elevated spectral intensities at almost all prominent auroral emission lines, including the N_2^+ 1NG series (391.4/427.8/470.9 nm), OI 557.7/630 nm, and the proton Hα (656.3 nm) and Hβ (486.1 nm) lines. The 557.7 nm dominates the absolute optical brightness of the IPA, but the 486.1 nm line is also particularly strong in terms of the relative percentage of the enhancement over that outside the IPA. The Hα emission, albeit brighter than Hβ, is embedded in a broad N_2 1PG band as well as OH airglows, so that it is usually not used in inferring the proton auroral intensity.

In Figures 2A–C, for demonstration purpose a common emission altitude of 125 km is assumed in projecting the images to MLAT/MLON. The AUGSO ASI and the TREx RGB ASI have overlapping field-of-views (FoV). Such a geometry enables us to perform triangulation to evaluate the emission altitude of the IPA, which may not only be useful in determining the geographical location of the auroral structure, but also carry important information about the particle energy of the auroral precipitation. The triangulation methodology and procedures to determine the emission height from two-station observations were described in Gillies et al. (2017) and Liang et al. (2019). In practice, we use the AUGSO 557.7 nm images and the concurrent green-channel data (deemed as proxy of 557.7 nm) of the TREx RGB ASI to evaluate the emission heights of the detached arc of interest. Figure 2E shows an example of the combined image map of AUGSO and TREX RGB ASI based on the best-fit altitude, which is ~125 km for this specific time epoch. The overlapping FoV of the two ASIs is presented as an alpha-blending overlay of two images. We note that a 125 km altitude is approximately the energy deposition height of ~10 keV proton precipitation (see later Figure 8). In the Supplementary Figures S2, S3, we provide more examples of the combined image maps based on the best-fit altitudes of the IPA from triangulation analyses, and demonstrate the gradual change of the best-fit emission altitudes. Throughout the presence of the IPA, the best-fit altitude is initially ~115 km yet gradually elevates with time, reaching ~135 km by ~0320 UT. We also estimated the uncertainties of the best-fit altitude (e.g., Gillies et al., 2017) and found them likely to be at most several km for most of the

interval of interest (except at the late stage of the event, see below for explanation). We have also tried triangulation between AUGSO 486.1 nm images and the blue-channel data of the TREx RGB ASI (see an example in Figure 2F), and achieved very similar outcomes of the best-fit altitudes, within the uncertainty of the triangulation method, throughout the event interval. This hints that the 557.7 nm and major blue-color emissions (Hβ and N_2^+ 1NG series) contained in the IPA all feature similar emission altitudes, an inference to be further corroborated by TRSp measurements later in Section 3.5. After ~0320 UT, the IPA moves to rather low elevation angles of the ATHA ASI, and its view is partially blocked by trees at the south-eastern edge of the camera. We have also tried the triangulation after 0320 UT and found the best-fit altitude of IPA might be ~135–140 km, but with a caveat that the accuracy of the triangulation analysis may become questionable by that time. From now on, the inferences from the triangulation analyses will guide our selection of emission altitudes in the following presentation of ASI images at different time epochs; the emission altitude used will be marked in the respective figure caption or in the relevant text. However, a constant altitude of 125 km is assumed in making all ASI movies in the Supplementary Material.

Our optical observations cover the full temporal and spatial span of the IPA event of interest. As seen from the movies, the IPA starts to discernibly separate from the main auroral oval around ~0248 UT at ~61^0 MLAT, −55^0 MLON (~18.6 h MLT) in the AUGSO ASI FoV. The IPA then undergoes southward motion and extends eastward into the LUCK ASI FoV. Overall, the event lasts for ~1 h; the IPA migrates equatorward from ~61^0 to 56^0 MLAT and features a maximum azimuthal extent of ~25^0 MLON. We also note that the IPA features dynamic spatial-temporal variations. It sometimes appears as an azimuthally-aligned arc, while sometimes exhibits as a few azimuthally-spaced segments containing one or more strongly intensified "blobs." At times, the IPA may actively pulsate in certain azimuthal segments (better seen from the 3s-cadence TREx RGB ASI movie). Furthermore, at ~0309 UT, one other detached arc at further lower latitudes appears to stem from the western edge as seen from AUGSO. In the following we sometimes may still use "arc" in referring to the IPA, but this should not be misunderstood as we actually deem it an azimuthally homogeneous "arc".

3.3 *In-situ* particle observations: DMSP in the conjugate hemisphere

There is unfortunately no *in-situ* particle measurement directly over the IPA. However, DMSP F18 passes over the conjugate area of the arc in the southern hemisphere at ~0318 UT. Figure 3A shows the AUGSO 486.1 and 557.7 nm images overplotted by the trajectory of the northern conjugate footprints of DMSP F18. A T96 model is used in the mapping (Tsyganenko, 1996). Figure 3B shows the electron/ion energy spectrogram measured by the SSJ instrument onboard F18. Notwithstanding the uncertainty of conjugate mapping, the arcs of interest are very likely to be associated with the energetic proton precipitation (>~10 keV) structure equatorward of the electron plasma sheet. There is an absence of plasma sheet electron precipitation corresponding to the proton precipitation structure, except that there are some clues of electron precipitation at ≤ ~100 eV, similar to the observations in Nishimura et al. (2022) in their IPA events.

3.4 Ground and *in-situ* magnetometer data: Evidence of electromagnetic ion cyclotron waves

IPAs have been observed in connection with EMIC wave activities (e.g., Sakaguchi et al., 2007, 2008, 2015; Zhang et al., 2008; Yuan et al., 2010; Kim et al., 2021). In this subsection, we shall examine the potential EMIC wave activities from both ground-based and *in-situ* magnetometer data.

We first look into the CARISMA ground magnetometer data. In this study, we use the data from the Gull Lake (GULL, Geo. 50.06^0N/108.26^0W) fluxgate magnetometer at 8 Hz sampling rate. Figure 4A shows the location of GULL overplotted on the TREx RGB ASI image. The top two panels of Figure 4B show the power spectral density (PSD) of the GULL B_h (magnetic north) and B_d (magnetic east) components obtained *via* FFT analyses. Evident Pc1 wave activities exist in the frequency range ~0.3–0.8 Hz between ~0306–0328 UT. These Pc1 pulsations are commonly recognized as manifestation of EMIC waves in the ionosphere (e.g., Sakaguchi et al., 2008, 2015; Mann et al., 2014; Usanova et al., 2016). To investigate the wave occurrence in the context of IPA, we plot the RGB ASI keogram along GULL in the 3rd of Figure 4B. This is done by sampling the ASI pixels over ±0.25^0 MLON around the GULL magnetic meridian. The bottom panel of Figure 4B shows the 486.1 nm keogram inferred from TRSp observations (see Section 3.6 later for more details), whose scan line is close to the GULL meridian. A constant emission altitude 125 km is assumed in the two keograms since the remnant error in projection is not important compared to the spatial integral range in ground magnetometer observations, with which these auroral keograms are intended to compare. The two horizontal dashed lines in the bottom two panels of Figure 4B indicate ±1^0 MLAT north and south of the GULL station. By such we have taken into account the spatial integral effect of ground magnetometer measurements and the ducting propagation of EMIC waves in the ionospheric waveguide (e.g., Mann et al., 2014). The EMIC wave activities at GULL show clear correspondence with the passage of IPA over the station. Though the IPA pre-exists, EMIC waves are not seen at

GULL before ~0306 UT since the IPA is north/west of, and relatively far away from, the station. The EMIC waves become stronger when the IPA approaches and passes overhead the station. When the IPA fades and moves southward away from the station, the EMIC waves diminish at GULL. We have also checked the magnetometer at other available stations (maintenance of some CARISMA sites was unfortunately affected by the pandemic). Relatively weak and transient EMIC wave activities are also seen at Ministik Lake (Geo. 53.35^{0}N/112.97^{0}W) around ~0255 UT when the early evolution of IPA temporarily passes the station. No clue of EMIC waves is found at Weyburn (Geo. 49.69^{0}N/103.80^{0}W) east of the IPA. The above observations again suggest that the EMIC wave activity is confined to regions not far away from the IPA. To summarize, notwithstanding the complications such as the horizontal propagation of EMIC waves in the ionosphere, the joint magnetic/optical observations in our event strongly indicate an inherent link between the EMIC wave and the IPA.

We then look into *in-situ* observations from Swarm satellites at ~500 km altitude. A T96 model is used in mapping the satellite to the auroral height. Swarm-B crosses the FoV of AUGSO ASI during ~0250–0253 UT, as illustrated in Figure 5A. We note that the satellite trajectory seems to traverse a gap of the visible IPA segments, with a stronger arc segment to its west and a dimmer segment to its east. Nevertheless, a vertical dotted line in Figure 5B marks the approximate time of traversal according to the latitude of the western bright IPA segment. To infer the ULF waves, we resort to the high-resolution (50 Hz) magnetic field data onboard Swarm-B. The identification of Pc1 EMIC waves from *in-situ* satellite measurements involves some complications, e.g., the spatio-temporal ambiguity, the mixture with other wave modes such as shear Alfven waves, and the spectral leakage from lower-frequency broadband ULF waves (e.g., Kim et al., 2021). In our data processing, we first derive the high-passed perturbation fields by subtracting the mean B-fields obtained from a sliding 600-point (12-s) Savitzky-Golay low-pass filter (Savitzky and Golay, 1964). This suppresses B-field variations at frequencies ≤0.1 Hz since it is difficult to distinguish spatial and temporal variations at these low frequencies in satellite data. We then convert the high-passed perturbation fields into a mean-field-aligned (MFA) coordinate system, in which the z-axis is parallel to the mean field direction, the y-axis is perpendicular to both the radial vector (from the Earth's center) of the satellite and the mean–field direction, and the x-axis completes the right-hand orthogonal system. The derived wave fields in the MFA coordinates are shown in the top panel of Figure 5B. We then perform FFT analyses on the transverse wave components B_x & B_y, and present their PSD spectrograms in the mid and bottom panels. As one can see, the waves are strong when the satellite is deep inside the active auroras, yet diminish when the satellite moves into the equatorward portion of the auroral oval. During ~02:51:00–02:51:30 UT when the satellite moves out of the main auroral oval and enters the subauroral region, the waves intensify again. In particular, narrow-band Pc1 waves at ~0.3 Hz are discernible from both the waveforms and the PSD. Though the satellite trajectory seems to pass over a gap of visible IPA segments, we hypothesize that the observed Pc1 waves during ~02:51:00–02:51:30 UT are still evidence of EMIC waves associated with the IPA. It is well known that EMIC waves may undergo ducted propagation in the ionosphere waveguide, and thus propagate away from the footprint of their magnetospheric source region (e.g., Kim et al., 2010). Such ducted waves attenuate during propagation, so that they are expected to be observed within a limited distance from the source region (Mann et al., 2014). Indeed, the wave fades after 02:51:30 UT when the satellite footprint becomes far away from the IPA. It is also possible that Swarm-B is inside the wave source region, but the EMIC wave intensity and its resultant proton scattering at the magnetospheric footprint of Swarm-B are not strong enough to produce visible IPA. We have also performed the polarization analysis (not shown). The polarization of the Pc1 waves of interest is mostly linear and/or weakly right-handed, implying that the EMIC waves may have undergone polarization reversal or change in the course of their propagation from the magnetospheric source region to the ionosphere (e.g., Johnson et al., 1989; Kim et al., 2021).

Later at ~0336 UT, Swarm-A and C traverse the IPA of interest. This occurs at the later stage of the event, when the IPA has moved to ~57.2^0 MLAT. In Figure 5C, we display the Swarm-A/C passage overplotted on the AUGSO image. The trajectories of Swarm-A and Swarm-C overlap, with Swarm-C slightly ahead in time — the difference can be viewed in Figure 5C *via* the separation between Swarm-A footprint (orange circle) and Swarm-C footprint (red circle) at each minute. This configuration helps relieve spatio-temporal ambiguity in satellite data. The derived B-field waveforms on Swarm-C and Swarm-A are shown in the 1st and 3rd panels of Figure 5D, respectively, using the same data processing procedures as above-depicted. The PSD spectrograms of B_y on the two satellites, which represent the major wave components, are given in the 2nd and 4th panels, respectively. As one can see, when the two satellites traverse the IPA around ~0336 UT, the waves intensify evidently. Swarm-C encounters the IPA slightly earlier so that the wave intensification precedes on Swarm-C. This observation unambiguously points to a link between the wave intensification and the IPA crossing. In this event interval, the wave spectra are complicated by the presence of relatively long-lasting/large-scale broadband waves, as can be inferred from the waveforms. Nevertheless, as seen from the B_y PSD on Swarm-A, on top of the long-lasting broadband structure at <~0.3 Hz, a more localized and narrow-banded wave intensification around ~0.6 Hz appears in conjunction with the IPA crossing. Similar localized Pc1 features at ~0.6–0.8 Hz are also seen on Swarm-C B_y PSD, though slightly ahead in time and weaker in wave power. We conceive these to be possible evidence of EMIC waves

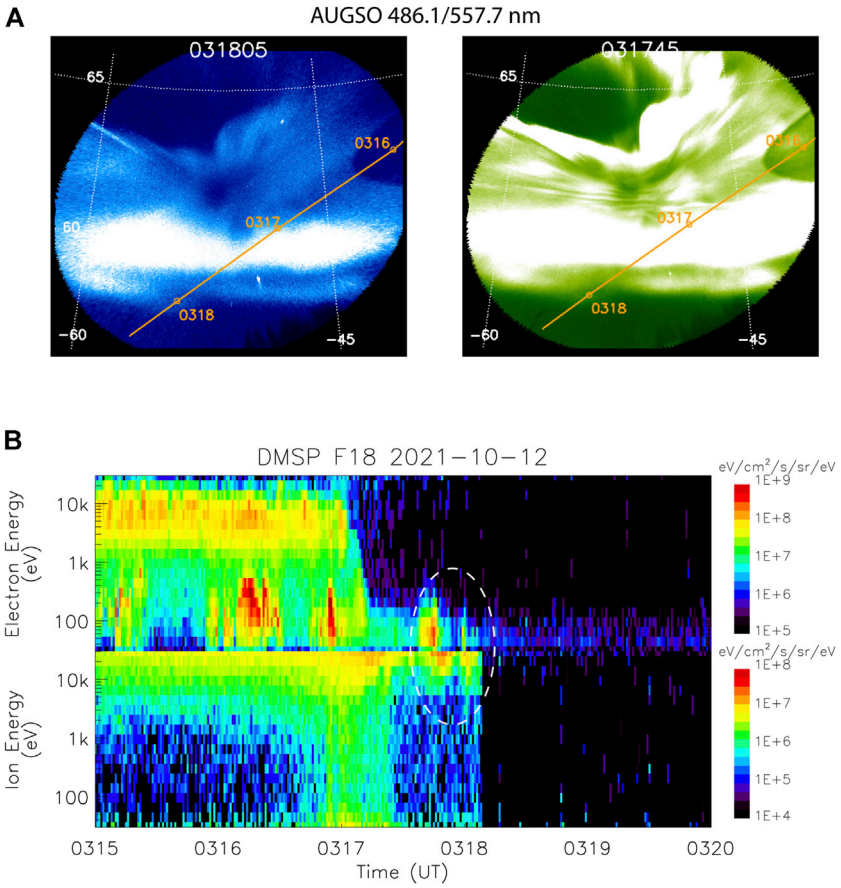

FIGURE 3
(A) AUGSO 486.1 and 557.7 nm images with the trajectory of the norther conjugate footprints of DMSP F18 satellite overplotted. An emission altitude of 135 km is assumed. **(B)** The electron energy flux spectrogram (upper panel) and ion energy flux spectrogram (bottom panel) measured by DMSP F18 SSJ. A dashed oval highlights the potential correspondence with the IPA.

associated with the IPA. The difference between waves seen on the two satellites might allude to the fine-scale modulation of EMIC waves (Ozaki et al., 2018), but such fine temporal variations cannot be resolved by our optical instruments.

3.5 Comparison among emission lines and intensity ratios based on TREx Spectrograph data

As mentioned above, though not observed at precisely the same time epochs, the detached 486.1 nm arc and the detached 557.7 nm arc seen on AUGSO images are fairly similar to each other in terms of shape, location, and time evolution. One merit of this study is that the event comes with high-quality spectrograph data, offering an ideal tool to examine and compare the properties of auroral structures in different emission lines. In this regard, we integrate the spectral intensities at the blue-line (427.8 nm), the Hβ (486.1 nm), and the green-line (557.7 nm), from TRSp measurements to infer the absolute optical intensity of these emissions. The fine spectral profile of individual emission line is contingent on parameters such as the temperature and the energy-dependent doppler shift. In this study, upon an inspection of the overall spectral profile of each emission line seen on TRSp during the event interval, the integral wavelength band is set as 483.6–488.1 nm for Hβ, 556.2–559.7 nm for green-line, and 424.8–429.8 nm for blue-line. For each line, we also subtract a baseline determined from its nearby non-auroral, non-airglow wavelengths. Figures 6A–C shows the keogram of optical intensities of the three emission lines versus time and elevation angle (0^0 indicates the north horizon). For the following analyses, we use the elevation angle without specific assumptions on emission altitudes. Note that the elevation-angle profile of an emission seen by ASI embodies a mixed manifestation of the altitudinal and latitudinal distribution of the emission structure. The

10.3389/fspas.2022.1040092

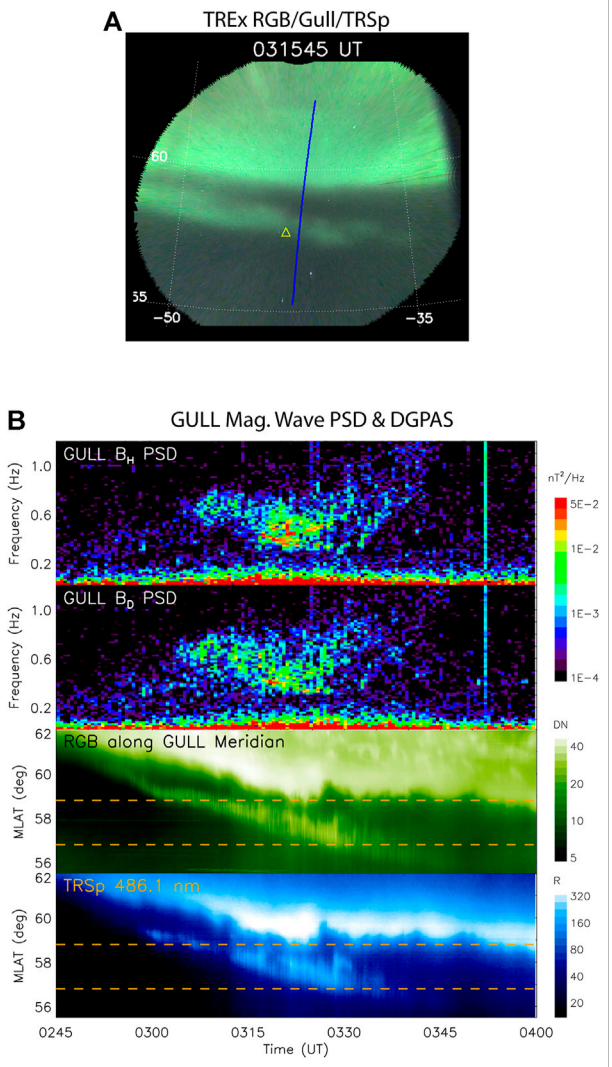

FIGURE 4
(A) TREX RGB ASI image with the GULL station (yellow triangle) and the TRSp scan line (blue line) marked. Emission altitude is 135 km. **(B)** The top two panels show the PSD spectrogram of the Bh and Bd components from the GULL magnetometer data. The third panel shows the RGB ASI keogram sampled along the GULL magnetic meridian. The bottom panel shows the keogram of 486.1 nm emissions calculated from TRSp observations. Two horizontal dashed lines in the bottom two panels indicate $\pm 1^0$ MLAT north and south of the GULL station.

detached arc shows up in all three emission lines, and the structural similarity in the three emissions is straightforward to notice. To achieve a more quantitative evaluation, we first delimit the elevation-angle range of the IPA of interest (marked by dashed curves in Figures 6A–C) during 0258–0345 UT. Figures 6D–F, together with Figure 7, serve to demonstrate the comparison of IPA among three emission lines. The total auroral intensities integrated over the delimited elevation range of IPA are shown in Figure 6D (in arbitrary scales). It is straightforward to see that the IPA temporal variations are almost identical and simultaneous in three emission lines. More quantitatively, *via* a cross-correlation analysis, the total 557.7 (427.8) nm intensity and total 486.1 nm intensity associated with IPA feature a peak correlation coefficient of 0.998 (0.993) at zero time lag.

We then sample the 486.1/427.8/557.7 nm intensities of IPA over the delimited elevation-angle range, and calculate the Pearson correlation among the elevation-angle profiles of these emission lines. To make the comparison meaningful, we are only interested in time epochs when IPA distinguishably stands out of the ambient background, with a threshold of 80 R in terms of the peak 486.1 nm intensity. The threshold also serves to ensure that the counterpart 557.7 nm auroral intensities are presumably an order of magnitude or more above the green-line airglow component. Figure 6E shows the Pearson correlation coefficients between the elevation-angle structures of the 557.7 and 486.1 nm emissions (in green circle) and that between the 427.8 and 486.1 nm emission structures (in blue cross). Figures 7A–F exemplify six frames of such comparison; the 557.7 (427.8) nm intensities are scaled by a factor 1/26 (1/4) in these frames. A full movie showing the comparison and correlation among the three emission lines is given in Supplementary Material. The correlation between the 486.1 nm auroral structure and the 557.7 nm auroral structure is exclusively greater than 0.95 and mostly greater than 0.98. With a proper scaling factor (~1/26), the 557.7 nm emission structures appear to largely overlap with the 486.1 nm emission structures. This can transpire only when both the latitudinal distribution and the emission altitudes of the two emissions are highly alike. As we shall discuss in the next section, such a near-perfect agreement between the 486.1 nm auroral structure and the 557.7 nm structure offers compelling evidence that the latter results almost purely from the proton auroral precipitation.

Figure 6F shows the emission intensity ratios of the IPA. For each TRSp time epoch, we sample the intensity ratio between 557.7 and 486.1 nm, as well as that between 427.8 and 486.1 nm, in each elevation-angle bin of the IPA. We then calculate the weighted (by the 486.1 nm intensity) mean and standard deviation of the sampled ratios over the elevation-angle bins at each time epoch, and present in Figure 6F. The scatter plot of all sampled 557.7 nm versus 486.1 nm emission intensities during the whole IPA interval is shown in Figure 7G, and the scatter plot of sampled 427.8 versus 486.1 nm intensities is given in Figure 7H. Overall, the 5,577–4,861 intensity ratio is confined in a rather narrow range around ~26. The variability of this ratio is within 10% in terms of both the temporal and elevation-angle variations. The above results imply that the 557.7 nm component of the IPA can be approximately viewed as a scaled counterpart of the 486.1 nm emission. In comparison, the distribution of 427.8 versus 486.1 nm emission intensities is a little bit more scattered, with an average ratio of ~4.1 between the two lines.

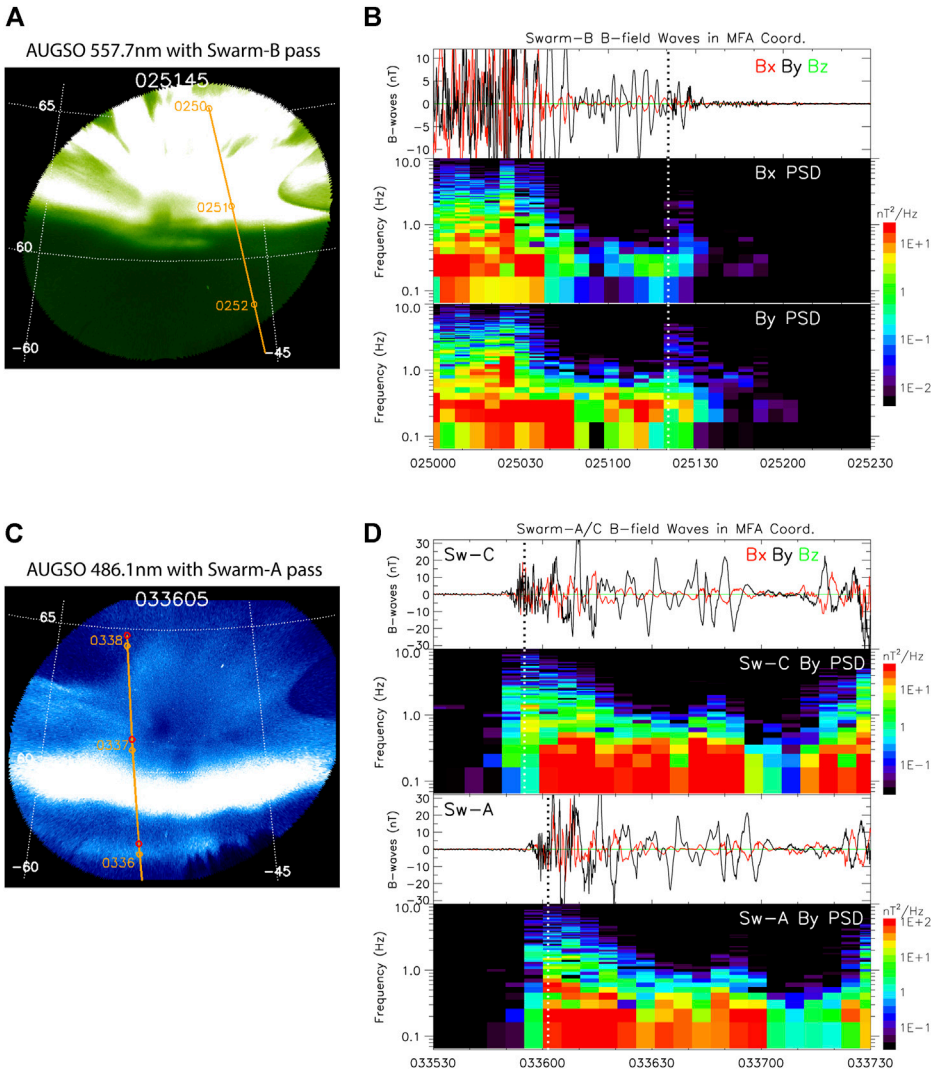

FIGURE 5
(A) AUGSO 557.7 nm images with Swarm-B footprint trajectory overplotted. Emission altitude is 115 km. **(B)** The top panel shows the high-passed magnetic field waves in MFA coordinate. The rest two panels show the PSD spectrogram of the Bx and By wave components. **(C)** AUGSO 486.1 nm images with Swarm-A (orange) and Swarm-C (red) footprint trajectory. Emission altitude is 135 km. **(D)** The top two panels show the B-field waves and By PSD spectrogram on Swarm-C. The bottom two panels show the B-field waves and By PSD spectrogram on Swarm-A. In each panel, a vertical dotted line indicates the estimated center time of IPA traversal.

4 Discussion

In this paper, we report and analyze an IPA event occurring during ~0245–0345 UT on 12 October 2021, following the impact of a CME interplanetary shock. The IPA of interest looms in the dusk sector and subsequently shows a southward and overall eastward (antisunward) propagation. The 486.1 nm emission intensity is very strong for the IPA, indicating intense proton precipitation. Taking advantage of multi-station, multi-wavelength optical instruments, we investigate the evolution and spectrographic properties of the IPA. More specifically, the following discussions are focused on the potential answers to two questions about the IPA: 1) what's the cause of the proton auroral precipitation? and 2) why does the IPA look green and what's the cause of such green emissions?

To preface the following discussions, we present in Figure 8 the altitude profile of the ionization rate led by energetic proton precipitation based on Fang et al. (2013) 's model. This serves to demonstrate the altitude range where most of the energy transfers between precipitating protons/hydrogen atoms and neutrals, *via* impact excitation/ionization, take place in the ionosphere. The model input parameters are conformal to the actual event date and location of the IPA (2021–10-12 03 UT, Geo. 50^0N/110^0W). The neutral atmosphere is from the

NRLMSISE00 model (Picone et al., 2002). Three cases of monoenergetic proton precipitation with energies of 1, 10, and 50 keV, respectively, are computed. A total energy flux of 1 erg/cm^2/s is assumed for all runs. As expected, the energy deposition height decreases with increasing energy. More specifically, the peak ionization height is ~110 km for 50 keV protons yet increases to ~140 km for 1 keV protons. Using the above information, and according to the IPA emission height inferred from the triangulation analysis (~115–135 km, see Figure 2E and Supplementary Figures S2, S3), we estimate that the precipitating energies of protons likely range between a few keV and a few tens of keV, and show a trend of decreasing energy with time when the IPA migrates to lower latitudes. EMIC waves are known to be capable of resonantly scattering magnetospheric protons in this energy range (e.g., Jordanova et al., 2007; Liang et al., 2014; Usanova et al., 2016). To date, the EMIC waves are commonly deemed the underlying mechanism causing the detached proton auroral precipitation in the subauroral region (Immel et al., 2005; Sakaguchi et al., 2007, 2008, 2015; Yahnin et al., 2007; Zhang et al., 2008; Kim et al., 2021; Shumko et al., 2022).

In our event, magnetometer data, in particular the observations from the CARISMA GULL station, show clear correspondence between the EMIC wave activities and the passage of IPA. This result further corroborates the causal link between the EMIC wave and the proton precipitation leading to IPA. GOES-17 data (Figure 1D) unveil the existence of strong energetic ion injection in the inner magnetosphere, which might allude to the energy source of the EMIC wave generation. It is difficult to accurately evaluate the magnetospheric footprint of the IPA and the equatorial magnetic field strength there under the storm condition. We have tried a series of Tsyganenko magnetic field models T89/T96/T01/TS02/TS05 (Tsyganenko, 1996, 2000, 2002; Tsyganenko and Sitnov, 2005) with OMNIWeb solar wind data, and found that none of them could satisfactorily reproduce the degree of stretching as observed by GOES-17 and inferred from the equatorward border of the main proton auroral band (assumed as representing 20 keV proton isotropic boundary, e.g., Yue et al., 2014), particularly at the later stage of the event. Comparatively, the TS05 model is the best-performing one and thus chosen, albeit with caution, in our following evaluation. At ~0251 UT which is close to the start of the event, the IPA is found to be located at ~60.7^0 MLAT as seen by the AUGSO ASI (Figure 5A), and the TS05 model predicts an equatorial B-field strength of ~150 nT (proton gyro-frequency f_{cp}~2.28 Hz) at the magnetospheric root of the arc. The Pc1 waves observed on Swarm-B (Figure 5B) peak at ~0.2–0.3 Hz, consistent with a Helium-Band EMIC. Later after 0315 UT when the IPA moves to ~58^0 MLAT, the TS05 model is found to underestimate the field line stretching and predicts an equatorial B-field of ~380 nT (f_{cp}~5.79 Hz) corresponding to the arc. Notwithstanding the uncertainty — likely an overestimate — of such a model B-field, the observed waves at GULL (peaking at ~0.4–0.5 Hz, Figure 4B) are still very likely the He-band EMIC. Similarly, at ~0336 UT when Swarm-A/C detect ~0.6–0.8 Hz Pc1 waves upon crossing the IPA at ~57.2^0 MLAT, the TS05 model predicts an equatorial B-field strength of ~460 nT (f_{cp}~7.01 Hz) corresponding to the IPA arc, again compatible with the scenario of He-band EMIC. We thus propose that the IPA-associated EMIC waves observed by *in-situ* and ground magnetometers in our event are He-band. This is consistent with the known prevalence of He-band EMIC waves, in terms of the occurrence rate and the wave power, in the duskside inner magnetosphere (e.g., Saikin et al., 2015). We note that He-band EMIC waves were also identified in other IPA events reported in the existing literature (e.g., Sakaguchi et al., 2007, 2008; Kim et al., 2021).

The IPA is visually green as shown in the citizen scientists' photos, and our observations indicate that it is indeed dominated by OI 557.7 nm emissions. The visual dominance of the 557.7 nm line leads some people, including citizen scientists, to wonder about the cause of such green-line emissions. A DMSP passage over the southern conjunction region of the IPA indicates that there is no electron precipitation in the range ~100 eV–30 keV (the ≤~100 eV precipitation structure will be addressed later), but people may still question whether electrons with energies >30 keV might exist and be the main cause of the observed 557.7 emissions. It is known that a number of plasma waves can be operational in pitch-angle scattering energetic/relativistic electrons in the inner magnetosphere and causing their precipitation into the subauroral ionosphere, such as the plasmaspheric hiss, the whistler-mode chorus, the magnetosonic wave, and the EMIC wave (e.g., Summers et al., 2007; Miyoshi et al., 2008; Ni et al., 2015, 2017; Zhang et al., 2022). In this study, using TRSp data we carefully compare the 557.7 nm and 486.1 nm structures corresponding to the IPA. The two emissions are found to be strikingly similar in their elevation-angle profiles, and their intensity ratio is confined within a narrow range. The correlation between the two emission structures is often as high as ~0.99. Such a high degree of similarity would be unthinkable if the 557.7 nm emissions contained in the IPA originate from a magnetospheric electron precipitation source. The rationale is as follows. First, the mechanisms leading to electron precipitation and proton precipitation are different in the magnetosphere, and the source regions of their precipitation are not necessarily co-located, much less do they have the same spatial-temporal variations. Even though certain activities such as EMIC waves are capable of scattering both electrons and ions, the resonant energies of electrons and ions are outright different. EMIC waves in the inner magnetosphere typically scatter relativistic electrons *via* gyro-resonance (e.g., Miyoshi et al., 2008; Ni et al., 2015; Zhang et al., 2016), though under certain conditions they

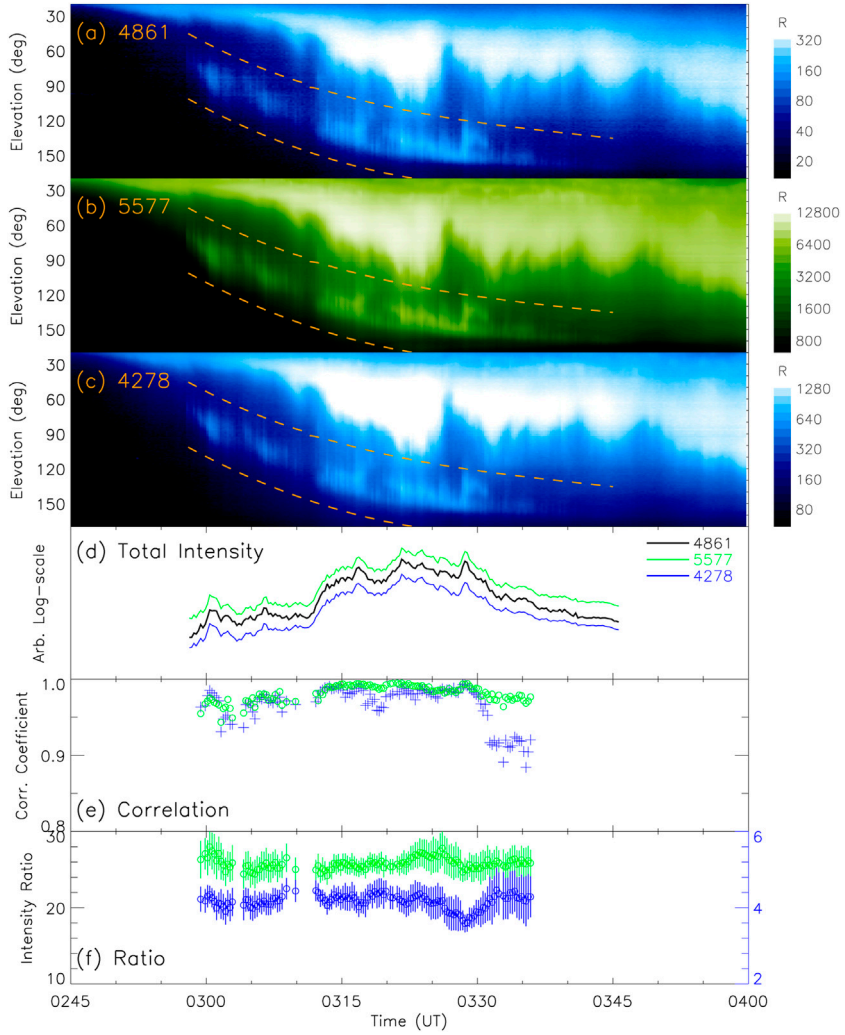

FIGURE 6
The top three panels **(A–C)** show the keogram of 486.1 nm, 557.7 nm, and 427.8 nm emission intensities calculated from TRSp observations, versus time and elevation angle (0 indicates north horizon). The dashed curves shown in these panels indicate the upper and lower bound within which we sample the elevation-angle bins to investigate the IPA structure. **(D)** The total 486.1/557.7/427.8 nm intensity integrated over the delimited elevation-angle range of IPA. Each intensity is plotted in arbitary scale, and only their temporal correlations are of interest in this plot. **(E)** The Pearson correlation coefficient between the elevation-angle structures of 486.1 nm and 557.7 nm (in green circle), and that between the structures of 486.1 nm and 427.8 nm (in blue crosses). **(F)** The mean and standard deviation of the intensity ratios. Green color denotes the 5577-to-4861 ratio, while blue color denotes 4278-to-4861 ratio (y-ticks on the rightside). At each time epoch, a circle denotes the mean over the elevation-angle range of IPA, while a vertical bar denotes the standard deviation.

may also scatter a broad range of electron energies from ~10 MeV down to several tens of keV *via* Landau resonance (Fu et al., 2018). These high-energy electrons are inefficient in producing 557.7 nm emissions. Even if they do, the emission altitudes would be relatively low, presumably ≤~100 km. Note that the IPA is seen at oblique elevation angles on TRSp, particularly after ~0310 UT. There is no reason to conceive that the electron auroras and proton auroras would necessarily have the same emission altitudes, and the discrepancy in their emission altitudes would lead to noticeable dissimilarity in their elevation angle profiles in oblique observations. For example, for an arc 1^0 MLAT south to the station, emission heights of 100 km and 130 km would lead to ~7.5^0 difference in viewing angles. Furthermore, the travel time to the ionosphere is different for high-energy electrons and ~10 keV ions, and such a time difference exceeds the resolution of measurements (15 s for TRSp). For the IPA with dynamic temporal variations, the electron auroras and proton auroras would not be able to keep in perfect pace (see Figure 6D) if they both originated from the equatorial magnetosphere.

Last but not least, it is important to note that electron precipitation and proton precipitation undergo

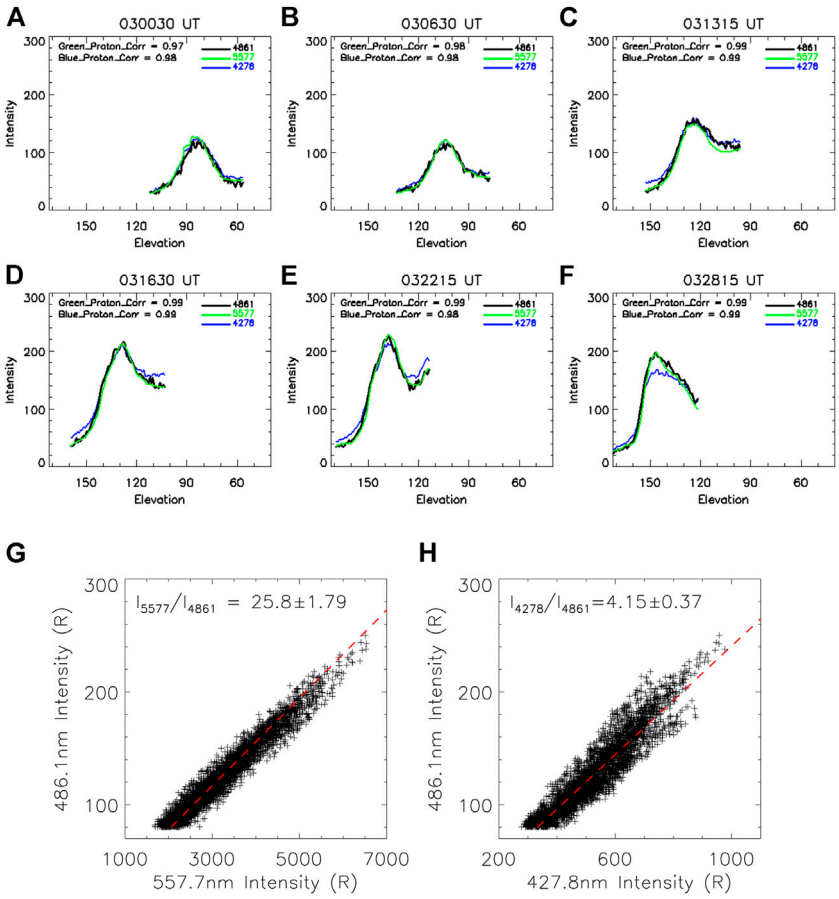

FIGURE 7
(A)–(F) exemplify six time epochs of the comparison and correlation among the elevation-angle structures of 486.1 nm (black), 557.7 nm (green), and 427.8 nm (blue) intensities. The 557.7 nm intensity is scaled by 1/26, while the 427.8 nm intensity is scaled by 1/4, in these plots. **(G)** The scatter plot of all sampled 557.7 and 486.1 nm emission intensities during the entire IPA interval. **(H)** The scatter plot of all sampled 427.8 and 486.1 nm emission intensities. The mean and standard deviation of their ratios are given in **(G)** and **(H)** for reference.

fundamentally different transport processes in the upper ionosphere. When energetic protons from the magnetosphere bombard the Earth's atmosphere, they undergo charge exchange collisions with atmospheric particles and become neutral hydrogen atoms. These neutral hydrogen atoms are also energetic and can become ionized again when they collide with the atmosphere. The above processes repeat until the protons/hydrogen atoms lost all their energies in the atmosphere. Since a neutral hydrogen atom is not magnetized, these ionization/neutralization sequences may cause the drifting of the proton away from the field line that it was incident on, leading to a broadening of spatial scales of the precipitating proton structure (Davidson, 1965; Eather, 1967; Fang et al., 2004). The broadening mostly takes place in the upper ionosphere (>~250 km altitude), while it is suppressed in the lower ionosphere where frequent collisions with neutrals hinder protons and hydrogen atoms from drifting apart. No such spatial spreading effect exists for magnetospheric electron precipitation. This would lead to distinct dissimilarity in the spatial structures of electron auroras and proton auroras (e.g., Donovan et al., 2012; Liang et al., 2017), even under a fortunate circumstance that they come from the same magnetospheric origin and that their precipitation fluxes have the same spatial distribution above the ionosphere.

To conclude, the near-identical structural shape of the 557.7 and 486.1 nm emissions and their narrowly-ranged intensity ratios exclude the possibility that the 557.7 nm emission originates from magnetospheric electron precipitation. Instead, the observation strongly suggests that the 557.7 nm emission contained in the IPA is essentially a byproduct of the proton precipitation. One likely source of such 557.7 nm emissions is the secondary electrons produced by the proton precipitation (e.g.,

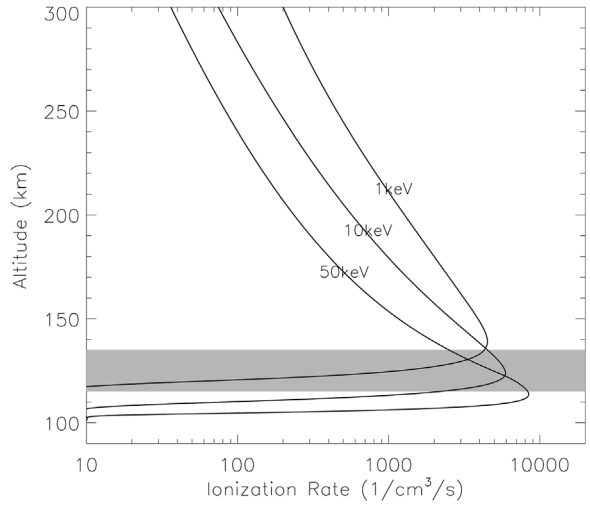

FIGURE 8
Altitude profile of the ionization rate led by 1, 10, and 50 keV monoenergetic proton precipitation, based on Fang et al. (2013). A gray aera marks the estimated range of emission altitudes (115–135 km) in our event inferred from the triangulation analyses.

Strickland et al., 1993). Upon a close look into Figure 3, one may notice the existence of ≤~100 eV electrons corresponding to the IPA (in the conjugate hemisphere) and the energetic proton precipitation. Similar observations were also made in Nishimura et al. (2022). These low-energy electrons at the DMSP altitude (~850 km) are unlikely the direct cause of the 557.7 nm emissions contained in the IPA, but might signify the presence of locally generated or interhemispherically-transported secondary electrons (Khazanov et al., 2015) associated with the proton precipitation. While a full proton-electron transport/emission model is beyond the scope of this study, we notice from Figure 11 of Strickland et al. (1993) that, the secondary electron fluxes at ~100–200 km altitudes led by a Maxwellian incident spectrum of pure proton precipitation with a characteristic energy of 8 keV appear to be fairly close to that caused by a Maxwellian electron precipitation with a characteristic energy of 1 keV (both electron and proton precipitations are normalized to the same total energy flux). Using our TREx-auroral transport model (Liang et al., 2016), we calculate the secondary electron fluxes produced by 1 keV Maxwellian electron precipitation with 1 erg/cm^2/s total flux, and find them capable of inducing 1.05 kR of 557.7 nm emissions (direct impact excitation by primary electrons is artificially excluded in this calculation). In comparison, the 486.1 nm optical yield is estimated by Spanswick et al. (2017) to be ~67 R per unit erg/cm^2/s of proton precipitation flux. We thus semi-quantitatively infer that the secondary electron fluxes induced by proton precipitation can excite 557.7 nm emissions with much higher brightness than the 486.1 nm emissions. One other possible source of the 557.7 nm emissions is the impact excitation by fast hydrogen atoms (Vallance-Jones, 1971; Edgar et al., 1975), which is produced in the aforementioned charge exchange process under the proton precipitation:

$$\mathrm{H}^{+}_{fast} + X \rightarrow \mathrm{H}^{*}_{fast} + X^{+}$$
$$\mathrm{H}^{*}_{fast} \rightarrow \mathrm{H}_{fast} + h\nu_{486.1}$$
$$\mathrm{H}_{fast} + \mathrm{O} \rightarrow \mathrm{H} + \mathrm{O}(^1S)$$
$$\mathrm{O}(^1S) \rightarrow \mathrm{O}(^1D) + h\nu_{557.7}$$

Impact excitation of O(^1S) directly led by energetic protons requires spin exchange and is therefore highly unlikely (Vallance-Jones, 1971; Edgar et al., 1975). For energetic protons, their energy deposition, including the secondary electron production and impact excitation, is supposed to be mostly concentrated in a narrow altitude range in the lower ionosphere (<200 km, see Figure 8), whereas the spatial spreading of precipitating proton/hydrogen fluxes has been already done at higher altitudes (Fang et al., 2004). Under the above-depicted scenario, the 557.7 nm emissions are excited as a byproduct of the proton precipitation as the latter impacts the lower ionosphere, which explains why they feature a similar structural shape to that of the 486.1 nm emissions. We of course recognize that those secondary electrons and fast hydrogen atoms may also exist and have effects at higher altitudes, such as contributing to the 630 nm auroras that also accompany IPAs (Lummerzheim et al., 2001) and to the density enhancement in the upper F-region (Kim et al., 2021).

The 427.8 nm emission structures corresponding to IPA also correlate fairly well (>0.9) with that of 486.1 nm emissions, but the correlation is slightly lower than that between 557.7 and 486.1 nm. The intensity distribution of 427.8 versus 486.1 nm shown in Figure 7H is also a little bit more scattered than that of 557.7 versus 486.1 nm. Based on the above observations, we expect that a majority of the 427.8 nm emissions contained in IPA might also be the byproduct of the proton precipitation, such as led by the secondary electrons produced in the proton precipitation, and the impact excitation by energetic protons and fast hydrogen atoms. However, some of the 427.8 nm emissions might be owing to other sources. As aforementioned, EMIC waves may cause relativistic electron precipitation; observational evidence of such relativistic electron precipitation in conjunction to an IPA patch was recently reported by Shumko et al. (2022). These high-energy electrons are ineffective in producing 557.7 nm emissions, but may partially contribute to the 427.8 nm emissions and thus slightly degrade the correlation between the 427.8 and 486.1 nm emission structures.

Eather, (1967), Eather, (1968) studied the intensity ratios between 486.1 nm and various other emission lines, including

N_2^+ 1NG 391.4/470.9 and OI 557.7 nm, in proton-induced auroras based upon both theoretical calculations and available measurements. The ratios are presumably contingent upon the proton energy flux spectrum and pitch-angle distribution. For 10 keV monoenergetic isotropic proton precipitation, the theoretical calculation outcome of the 3,914–4861 ratio is 13.8, and that of the 4,709–4861 ratio is 0.79 (Eather, 1967). The ratios (to 486.1 nm intensity) inferred from realistic measurements are 10.0–17.5 for 391.4 nm, 0.9–1.3 for 470.9 nm, and 9.0–12.5 for 557.7 nm (Eather, 1968). Though not presented we have also investigated the 470.9 nm emission from TRSp data following the same procedures as above-depicted, and found its intensity ratio to 486.1 nm emissions to be ~0.85 ± 0.07, close to Eather's result. Although the 391.4 nm line is beyond the TRSp calibration range so that its absolute intensity cannot be reliably obtained, using the theoretical branch ratio of N_2^+ 1NG series (0.65/0.2 for 391.4/427.8 nm, see Shamansky and Broadfoot, 1971), we convert the observed 4,278–4,861 ratio into the 3,914–4,861 ratio and find the latter (~13.5 ± 1.2) also consistent with Eather's result. However, the 5,577–4,861 ratio in our study is larger than that in Eather (1968) by a factor of ~2–3.

In the last a few decades, many of the impact cross-sections and rate coefficients involved in proton-induced auroras have been updated, and the N2 2PG, LBH band, and OI 630 nm auroras led by proton precipitation have been specifically modeled according to those renewed cross-sections and rate coefficients (e.g., Strickland et al., 1993; Lummerzheim et al., 2001; Galand and Lummerzheim, 2004). Curiously, to the authors' knowledge there is still a scarcity of efforts in modeling 557.7 nm emissions induced by proton precipitation in recent decades. To be able to do this, all the processes mentioned above, including the charge exchange cycle, fast hydrogen atoms, the spatial spreading, etc., should all be properly taken into account. Such a proton transport model would require a multi-stream or Monte-Carlo approach (e.g., Galand et al., 1997; Fang et al., 2004). Besides, due to the importance of secondary electrons in auroral emissions, the generation of secondary electrons by the proton precipitation and their transport in the ionosphere must also be self-consistently included. The overall model would thus be a combined proton/hydrogen atom/electron transport model (e.g., Strickland et al., 1993). An effort at such a model, as a part of our TREx-auroral transport model for the TREx mission, is currently undergoing and will be the content of a future publication. The quantitative results achieved in this study, such as the intensity ratio between 557.7/427.8 nm emission and the Hβ 486.1 nm emission, will undoubtedly be useful in helping us develop and validate the model. We also welcome research peers to compare our results with the outcome of their existing proton transport/emission models.

5.Summary and conclusion

In this study, we report and analyze an IPA event occurring at ~0245–0345 UT on 12 October 2021, the Canada Thanksgiving storm night. The IPA of interest contained strong Hβ emissions intensities up to a few hundred Rayleigh, indicating intense proton precipitation, yet the 557.7 nm constituted the strongest emission line of the IPA. The IPA was fairly bright and visible to the naked eye over western Canada, and raised extensive interest among citizen scientists. Using a comprehensive set of optical instruments, we investigate the evolution and the spectrographic properties of the IPA. *In-situ* and ground magnetometer data show evidence of He-band EMIC wave activities associated with the passage of IPA, corroborating the commonly conceived link between the EMIC waves and the detached proton precipitation. *Via* careful examination of the spectral intensities and the structural shapes of the 557.7, 427.8, and 486.1 nm emissions based on the TRSp data, we conclude that the 557.7 nm emissions of the detached arc were unlikely to owe their source to energetic electron precipitation from the magnetosphere, but were essentially the byproduct of the proton precipitation, e.g., excited by the secondary electrons produced in the proton precipitation, and/or led by the impact of fast hydrogen atoms. The precipitating proton energies are estimated to range between a few keV and a few tens of keV according to the IPA emission heights inferred from triangulation analyses.

We also obtain the intensity ratios among the 557.7/427.8/486.1 nm emissions of the IPA based on TRSp measurements. The intensity ratios achieved are compatible with Eather, (1967), Eather, (1968) for the proton-induced N_2^+ 1NG series, but are larger than Eather's result by a factor ~2–3 for the 5,577–4,861 ratio. An updated proton auroral emission model, properly taking into account the complicated processes involved in the proton transport and with renewed impact cross sections and rate coefficients, is summoned and currently undertaken by the authors. The results achieved in this study provide a useful guide and can serve as validation tests for existing and developing proton transport/emission models.

Data availability statement

Publicly available datasets were analyzed in this study. This data can be found here: http://data.phys.ucalgary.ca/sort_by_project/other/publication_datasets/fspas.2022.0908.

Author contributions

JL is the corresponding author who conducted most of the data analyses and writing. He also participated in the data calibration. DG is responsible for the calibration of TREx

instruments, including the spectrograph. She also contributed some valuable ideas to the manuscript. Professor Eric Donovan supervised this study. He is the PI of the TREx mission. HP provided the CARISMA magnetometer data and the data processing procedure. Professor IM is the PI of the CARISMA mission, and guided our use of the CARISMA data. MC is the PI of AUGSO imagers and co-PI of FESO. He also contributed to the paper's scientific content and helped edit the manuscript. Professor ES is responsible for the deployment, maintenance and data distribution of TREx instruments.

Funding

The study is supported by the Canadian Space Agency (CSA). TREx is jointly funded by the Canada Foundation for Innovation (CFI), Alberta Economic Development and Trade, and the University of Calgary. FESO is supported by CFI and CSA. AUGSO is supported by the CFI. AUGSO, TREx, and FESO data are publicly available at http://data.phys.ucalgary.ca/sort_by_project/other/publication_datasets/fspas.2022.0908. CARISMA is operated by the University of Alberta and funded by CSA. CARISMA data can be downloaded at https://carisma.ca/. Swarm mission is supported by the European Space Agency; Swarm data can be accessed at http://earth.esa.int/swarm. DMSP SSJ data are downloaded from http://cedar.openmadrigal.org/. GOES data used in this study are from https://ngdc.noaa.gov/stp/satellite/goes-r.html.

Acknowledgments

We acknowledge helpful discussions with Dr. Chao Yue, Dr. Mykhaylo Shumko, and Dr. Binbin Ni.

Conflict of interest

The authors declare that the research was conducted in the absence of any commercial or financial relationships that could be construed as a potential conflict of interest.

Publisher's note

Supplementary material

The Supplementary Material for this article can be found online at: https://www.frontiersin.org/articles/10.3389/fspas.2022.1040092/full#supplementary-material

References

Davidson, G. T. (1965). Expected spatial distribution of low-energy protons precipitated in the auroral zones. *J. Geophys. Res.* 70 (5), 1061–1068. doi:10.1029/JZ070i005p01061

Donovan, E. F., Spanswick, E., Liang, J., Grant, J., Jackel, B. J., and Greffen, M. (2012). Magnetospheric dynamics and the proton aurora. *Auror. Phenomenology Magnetos. Process. Earth Other Planets* 197, 365. doi:10.1029/2012GM001241

Eather, R. H. (1967). Auroral proton precipitation and hydrogen emissions. *Rev. Geophys.* 5, 207. doi:10.1029/rg005i003p00207

Eather, R. H. (1968). Spectral intensity ratios in proton-induced auroras. *J. Geophys. Res.* 73, 119–125. doi:10.1029/ja073i001p00119

Edgar, B. C., Porter, H. S., and Green, A. E. S. (1975). Proton energy deposition in molecular and atomic oxygen and applications to the polar cap. *Planet. Space Sci.* 23 (5), 787–804. doi:10.1016/0032-0633(75)90015-X

Fang, X., Liemohn, M. W., Kozyra, J. U., and Solomon, S. C. (2004). Quantification of the spreading effect of auroral proton precipitation. *J. Geophys. Res.* 109, A04309. doi:10.1029/2003JA010119

Fang, X., Lummerzheim, D., and Jackman, C. H. (2013). Proton impact ionization and a fast calculation method. *JGR. Space Phys.* 118, 5369–5378. doi:10.1002/jgra.50484

Fraser, B. J., Singer, H. J., Adrian, M. L., Gallagher, D. L., and Thomsen, M. F. (2005). "The relationship between plasma density structure and EMIC waves at geosynchronous orbit," in *Inner magnetosphere interactions: New perspectives from imaging, geophys. Monogr. Ser.* Editors J. L. Burch, M. Schulz, and H. Spence (Washington, D. C: AGU),

Frey, H. U. (2007). Localized aurora beyond the auroral oval. *Rev. Geophys.* 45, RG1003. doi:10.1029/2005RG000174

Friis-Christensen, E., Luhr, H., and Hulot, G. (2006). Swarm: A constellation to study the Earth's magnetic field. *Earth Planets Space* 58, 351.

Fu, S., Ni, B., Lou, Y., Bortnik, J., Ge, Y., Tao, X., et al. (2018). Resonant scattering of near-equatorially mirroring electrons by Landau resonance with H^+ band EMIC waves. *Geophys. Res. Lett.* 45, 873. doi:10.1029/2018gl079718

Galand, M., Lilensten, J., Kofman, W., and Sidge, R. B. (1997). Proton transport model in the ionosphere: 1. Multistream approach of the transport equations. *J. Geophys. Res.* 102, 22261–22272. doi:10.1029/97JA01903

Galand, M., and Lummerzheim, D. (2004). Contribution of proton precipitation to space-based auroral FUV observations. *J. Geophys. Res.* 109, A03307. doi:10.1029/2003JA010321

Gallardo-Lacourt, B., Frey, H. U., and Martinis, C. (2021). Proton aurora and optical emissions in the subauroral region. *Space Sci. Rev.* 217, 10. doi:10.1007/s11214-020-00776-6

Gillies, D. M., Donovan, E., Hampton, D., Liang, J., Connors, M., Nishimura, Y., et al. (2019). First observations from the TREx spectrograph: The optical spectrum of STEVE and the picket fence phenomena. *Geophys. Res. Lett.* 46, 7207–7213. doi:10.1029/2019GL083272

Gillies, D. M., Liang, J., Donovan, E., and Spanswick, E. (2020). The apparent motion of STEVE and the Picket Fence phenomena. *Geophys. Res. Lett.* 47, e2020GL088980. doi:10.1029/2020GL088980

Gillies, M., Knudsen, D., Donovan, E., Jackel, B., Gillies, R., and Spanswick, E. (2017). Identifying the 630 nm auroral arc emission height: A comparison of the triangulation, fac profile, and electron density methods. *J. Geophys. Res. Space Phys.* 122, 8181–8197. doi:10.1002/2016JA023758

Immel, T. J., Mende, S. B., Frey, H. U., Patel, J., Bonnell, J. W., Engebretson, M. J., et al. (2005). "ULF waves associated with enhanced subauroral proton precipitation," in *Inner magnetosphere interactions: New perspectives from imaging, geophys. Monogr. Ser.* Editors J. L. Burch, M. Schulz, and H. Spence (Washington, D. C: AGU), 159, 71

Immel, T. J., Mende, S. B., Frey, H. U., Peticolas, L. M., Carlson, C. W., Gerard, J., et al. (2002). Precipitation of auroral protons in detached arcs. *Geophys. Res. Lett.* 29 (11), 1519. doi:10.1029/2001GL013847

Johnson, J. R., Chang, G. B., Crew, B., and Andre, M. (1989). Equatorially generated ULF waves as a source for the turbulence associated with ion conics. *Geophys. Res. Lett.* 16, 1469–1472. doi:10.1029/GL016i012p01469

Jordanova, V. K., Spasojevic, M., and Thomsen, M. F. (2007). Modeling the electromagnetic ion cyclotron wave-induced formation of detached subauroral proton arcs. *J. Geophys. Res.* 112, A08209. doi:10.1029/2006JA012215

Khazanov, G. V., Himwich, E. W., Glocer, A., and Sibeck, D. G. (2015). "Role of multiple atmospheric reflections in formation of electron distribution function in the diffuse aurora region," in *Auroral dynamics and Space weather*. Editors Y. Zhang and L. J. Paxton (Hoboken, NJ: John Wiley & Sons). doi:10.1002/9781118978719.ch9

Kim, H., Lessard, M. R., Engebretson, M. J., and Luhr, H. (2010). Ducting characteristics of Pc 1 waves at high latitudes on the ground and in space. *J. Geophys. Res.* 115. doi:10.1029/2010JA015323

Kim, H., Shiokawa, K., Park, J., Miyoshi, Y., Miyashita, Y., Stolle, C., et al. (2021). Isolated proton aurora driven by EMIC Pc1 wave: PWING, Swarm, and NOAA POES multi-instrument observations. *Geophys. Res. Lett.* 48, e2021GL095090. doi:10.1029/2021GL095090

Korth, H., Thomsen, M. F., Borovsky, J. E., and McComas, D. J. (1999). Plasma sheet access to geosynchronous orbit. *J. Geophys. Res.* 104 (A11), 25047–25061. doi:10.1029/1999JA900292

Kress, B. T., Rodriguez, J. V., and Onsager, T. G. (2020). in *Chapter 20 - the GOES-R Space environment* in situ *suite (SEISS): Measurement of energetic particles in Geospace*. Editors S. J. Goodman, T. J. Schmit, J. Daniels, and R. J. Redmon (The GOES-R Series, Elsevier), 243.

Kubota, M., Nagatsuma, T., and Murayama, Y. (2003). Evening corotating patches: A new type of aurora observed by high sensitivity all-sky cameras in Alaska. *Geophys. Res. Lett.* 30. doi:10.1029/2002GL016652

Liang, J., Donovan, E., Connors, M., Gillies, D., St-Maurice, J. P., Jackel, B., et al. (2019). Optical spectra and emission altitudes of double-layer STEVE: A case study. *Geophys. Res. Lett.* 46, 13630–13639. doi:10.1029/2019GL085639

Liang, J., Donovan, E. F., Ni, B., Yue, C., Jiang, F., and Angelopoulos, V. (2014). On an energy-latitude dispersion pattern of ion precipitation potentially associated with magnetospheric EMIC waves. *J. Geophys. Res. Space Phys.* 119, 8137–8160. doi:10.1002/2014ja020226

Liang, J., Donovan, E., Gillies, D., Spanswick, E., and Connors, M. (2017). Proton auroras during the transitional stage of substorm onset. *Earth Planets Space* 70, 126. doi:10.1186/s40623-018-0899-0

Liang, J., Donovan, E., Jackel, B., Spanswick, E., and Gillies, M. (2016). On the 630 nm red-line pulsating aurora: Red-line Emission Geospace Observatory observations and model simulations. *J. Geophys. Res. Space Phys.* 121, 7988–8012. doi:10.1002/2016ja02290110.1002/2014JA020226

Liang, J., Zou, Y., Nishimura, Y., Donovan, E., Spanswick, E., and Conde, M. (2021). Neutral wind dynamics preceding the STEVE occurrence and their possible preconditioning role in STEVE formation. *JGR. Space Phys.* 126, e2020JA028505. doi:10.1029/2020JA028505

Lummerzheim, D., Galand, M., Semeter, J., Mendillo, M. J., Rees, M. H., and Rich, F. J. (2001). Emission of OI(630 nm) in proton aurora. *J. Geophys. Res.* 106 (A1), 141–148. doi:10.1029/2000ja002005

Mann, I. R., Milling, D. K., Rae, I. J., Ozeke, L. G., Kale, A., Kale, Z. C., et al. (2008). The upgraded CARISMA magnetometer array in the THEMIS era. *Space Sci. Rev.* 141, 413–451. doi:10.1007/s11214-008-9457-6

Mann, I. R., Usanova, M. E., Murphy, K., Robertson, M. T., Milling, D. K., Kale, A., et al. (2014). Spatial localization and ducting of emic waves: Van Allen probes and ground-based observations. *Geophys. Res. Lett.* 41, 785–792. doi:10.1002/2013GL058581

Mendillo, M., Baumgardner, J., and Providakes, J. (1989). Ground-based imaging of detached arcs, ripples in the diffuse aurora, and patches of 6300-Å emission. *J. Geophys. Res.* 94, 5367. doi:10.1029/ja094ia05p05367

Miyoshi, Y., Sakaguchi, K., Shiokawa, K., Evans, D., Albert, J., Connors, M., et al. (2008). Precipitation of radiation belt electrons by EMIC waves, observed from ground and space. *Geophys. Res. Lett.* 35, L23101. doi:10.1029/2008GL035727

Moshupi, M. C., Cogger, L. L., Wallis, D. D., Murphree, J. S., and Anger, C. D. (1977). Auroral patches in the vicinity of the plasmapause. *Geophys. Res. Lett.* 4, 37–40. doi:10.1029/gl004i001p00037

Ni, B., Cao, X., Zou, Z., Zhou, C., Gu, X., Bortnik, J., et al. (2015). Resonant scattering of outer zone relativistic electrons by multiband EMIC waves and resultant electron loss time scales. *JGR. Space Phys.* 120, 7357–7373. doi:10.1002/2015ja021466

Ni, B., Hua, M., Zhou, R., Yi, J., and Fu, S. (2017). Competition between outer zone electron scattering by plasmaspheric hiss and magnetosonic waves. *Geophys. Res. Lett.* 44, 3465–3474. doi:10.1002/2017GL072989

Nishimura, Y., Bruus, E., Karvinen, E., Martinis, C. R., Dyer, A., Kangas, L., et al. (2022). Interaction between proton aurora and stable auroral red arcs unveiled by citizen scientist photographs. *JGR. Space Phys.* 127. e2022JA030570. doi:10.1029/2022JA030570

Nishimura, Y., Donovan, E. F., Angelopoulos, V., and Nishitani, N. (2020). Dynamics of auroral precipitation boundaries associated with STEVE and SAID. *JGR. Space Phys.* 125, e2020JA028067. doi:10.1029/2020JA028067

Ozaki, M., Shiokawa, K., Miyoshi, Y., Kataoka, R., Connors, M., Yagitani, S., et al. (2018). Discovery of 1-Hz range modulation of isolated proton aurora at subauroral latitudes. *Geophys. Res. Lett.* 45, 1209–1217. doi:10.1002/2017GL076486

Picone, J. M., Hedin, A. E., Drob, D. P., and Atkin, A. C. (2002). NRLMSISE-00 empirical model of the atmosphere: Statistical comparisons and scientific issues. *J. Geophys. Res.* 107 (A12), SIA 15–SIA 15-16. doi:10.1029/2002JA009430

Redmon, R. J., Denig, W. F., Kilcommons, L. M., and Knipp, D. J. (2017). New DMSP database of precipitating auroral electrons and ions. *JGR. Space Phys.* 122, 9056–9067. doi:10.1002/2016JA023339

Saikin, A. A., Zhang, J.-C., Allen, R. C., Smith, C. W., Kistler, L. M., Spence, H. E., et al. (2015). The occurrence and wave properties of H+-He+-and O+-band EMIC waves observed by the Van Allen Probes. *JGR. Space Phys.* 120, 7477–7492. doi:10.1002/2015JA021358

Sakaguchi, K., Shiokawa, K., Ieda, A., Miyoshi, Y., Otsuka, Y., Ogawa, T., et al. (2007). Simultaneous ground and satellite observations of an isolated proton arc at subauroral latitudes. *J. Geophys. Res.* 112 (A4), A04202. doi:10.1029/2006ja012135

Sakaguchi, K., Shiokawa, K., Miyoshi, Y., and Connors, M. (2015). "Isolated proton auroras and Pc1/EMIC waves at subauroral latitudes," in *Auroral dynamics and Space weather*. Editors Y. Zhang and L. J. Paxton. doi:10.1002/9781118978719

Sakaguchi, K., Shiokawa, K., Miyoshi, Y., Otsuka, Y., Ogawa, T., Asamura, K., et al. (2008). Simultaneous appearance of isolated auroral arcs and Pc 1 geomagnetic pulsations at subauroral latitudes. *J. Geophys. Res.* 113, A05201. doi:10.1029/2007JA012888

Savitzky, A., and Golay, M. J. E. (1964). Smoothing and differentiation of data by simplified least squares procedures. *Anal. Chem.* 36, 1627–1639. doi:10.1021/ac60214a047

Shemansky, D. E., and Broadfoot, A. L. (1971). Excitation of N2 and N2+ systems by electrons, I: Absolute transition probabilities. *J. Quant. Spectrosc. Radiat. Transf.* 11 (10), 1385–1400. doi:10.1016/0022-4073(71)90105-1

Shumko, M., Gallardo-Lacourt, B., Halford, A. J., Blum, L. W., Liang, J., Miyoshi, Y., et al. (2022). Proton aurora and relativistic electron microbursts scattered by electromagnetic ion cyclotron waves. *Front. Astron. Space Sci.* 9, 975123. doi:10.3389/fspas.2022.975123

Spanswick, E., Donovan, E. F., Kepko, L., and Angelopoulos, V. (2017). The magnetospheric source region of the bright proton aurora. *Geophys. Res. Lett.* 44 (10), 10, 094–110, 099. doi:10.1002/2017GL074956

Strickland, D. J., Daniell, R. E., Jasperse, J. R., and Basu, B. (1993). Transport-theoretic model for the electron-proton-hydrogen atom aurora: 2. Model results. *J. Geophys. Res.* 98 (A12), 21533–21548. doi:10.1029/93JA01645

Summers, D., Ni, B., and Meredith, N. P. (2007). Timescales for radiation belt electron acceleration and loss due to resonant wave-particle interactions: 2. Evaluation for VLF chorus, ELF hiss, and electromagnetic ion cyclotron waves. *J. Geophys. Res.* 112, A04207. doi:10.1029/2006JA011993

Tsyganenko, N. A. (2002). A model of the near magnetosphere with a dawn-dusk asymmetry: 2. Parameterization and fitting to observations. *J. Geophys. Res.* 107 (A8), SMP 10-11–SMP 10-17. doi:10.1029/2001JA000220

Tsyganenko, N. A. (1996). "Effects of the solar wind conditions on the global magnetospheric configuration as deduced from data-based field models," in Proceedings of the Third International Conference on Substorms (ICS-3). Editors E. Rolfe and B. Kaldeich (Versailles, France: Eur. Space Agency Spec. Publ., ESA-SP), 181.

Tsyganenko, N. A. (2000). Modeling the inner magnetosphere: The asymmetric ring current and region 2 Birkeland currents revisited. *J. Geophys. Res.* 105 (27), 27739–27754. doi:10.1029/2000ja000138

Tsyganenko, N. A., and Sitnov, M. I. (2005). Modeling thedynamics of the inner magnetosphere during strong geomagnetic storms. *J. Geophys. Res.* 110 (A3), A03208. doi:10.1029/2004JA010798

Unick, C. W., Donovan, E., Connors, M., and Jackel, B. (2017). A dedicated H-beta meridian scanning photometer for proton aurora measurement. *J. Geophys. Res. Space Phys.* 122, 753–764. doi:10.1002/2016JA022630

Usanova, M. E., Mann, I. R., and Darrouzet, F. (2016). "EMIC waves in the inner magnetosphere," in *Low-frequency waves in Space plasmas*. Editors A. Keiling, D.-H. Lee, and V. Nakariakov. doi:10.1002/9781119055006

Vallance-Jones, A. (1974). *Aurora*. Boston, Mass: D. Reidel.

Vallance-Jones, A. (1971). *Notes from the summer institute on planetary magnetosphere and auroras*. NCAR, 327.

Wallis, D. D., Burrows, J. R., Moshupi, M. C., Anger, C. D., and Murphree, J. S. (1979). Observations of particles precipitating into detached arcs and patches equatorward of the auroral oval. *J. Geophys. Res.* 84 (A4), 1347–1360. doi:10.1029/JA084iA04p01347

Yadav, S., Shiokawa, K., Oyama, S., Inaba, Y., Takahashi, N., Seki, K., et al. (2021). Study of an equatorward detachment of auroral arc from the oval using ground-space observations and the BATS-R-US–CIMI model. *JGR. Space Phys.* 10126, 12. doi:10.1029/2020ja029080

Yahnin, A. G., Yahnina, T. A., and Frey, H. U. (2007). Subauroral proton spots visualize the Pc1 source. *J. Geophys. Res.* 112, A10223. doi:10.1029/2007ja012501

Yuan, Z., Deng, X., Lin, X., Pang, Y., Zhou, M., Décréau, P. M. E., et al. (2010). Link between EMIC waves in a plasmaspheric plume and a detached sub-auroral proton arc with observations of Cluster and IMAGE satellites. *Geophys. Res. Lett.* 37 (7), L07108. doi:10.1029/2010gl042711

Yue, C., Wang, C.-P., Lyons, L., Liang, J., Donovan, E. F., Zaharia, S. G., et al. (2014). Current sheet scattering and ion isotropic boundary under 3-D empirical force-balanced magnetic field. *JGR. Space Phys.* 119, 8202–8211. doi:10.1002/2014JA020172

Zhang, X.-J., Artemyev, A., Angelopoulos, V., Tsai, E., Wilkins, C., Kasahara, S., et al. (2022). Superfast precipitation of energetic electrons in the radiation belts of the Earth. *Nat. Commun.* 13, 1611. doi:10.1038/s41467-022-29291-8

Zhang, X.-J., Li, W., Ma, Q., Thorne, R., Angelopoulos, V., Bortnik, J., et al. (2016). Direct evidence for emic wave scattering of relativistic electrons in space. *JGR. Space Phys.* 121, 6620–6631. doi:10.1002/2016ja022521

Zhang, Y., Paxton, L. J., Morrison, D., Wolven, B., Kil, H., and Wing, S. (2005). Nightside detached auroras due to precipitating protons/ions during intense magnetic storms. *J. Geophys. Res.* 110, A02206. doi:10.1029/2004JA010498

Zhang, Y., Paxton, L. J., and Zheng, Y. (2008). Interplanetary shock induced ring current auroras. *J. Geophys. Res.* 113, A01212. doi:10.1029/2007JA012554

frontiers | Frontiers in Astronomy and Space Sciences

TYPE Original Research
PUBLISHED 13 October 2022
DOI 10.3389/fspas.2022.1004634

OPEN ACCESS

EDITED BY
Katariina Nykyri,
Embry–Riddle Aeronautical University,
United States

REVIEWED BY
Adnane Osmane,
University of Helsinki, Finland
Jun Liang,
University of Calgary, Canada

*CORRESPONDENCE
Clare E. J. Watt,
clare.watt@northumbria.ac.uk

SPECIALTY SECTION
This article was submitted to Space Physics,
a section of the journal
Frontiers in Astronomy and Space Sciences

RECEIVED 27 July 2022
ACCEPTED 22 September 2022
PUBLISHED 13 October 2022

CITATION
Watt CEJ, Allison HJ, Bentley SN, Thompson RL, Rae IJ, Allanson O, Meredith NP, Ross JPJ, Glauert SA, Horne RB, Zhang S, Murphy KR, Rasinskaitė D and Killey S (2022), Temporal variability of quasi-linear pitch-angle diffusion.
Front. Astron. Space Sci. 9:1004634.
doi: 10.3389/fspas.2022.1004634

Temporal variability of quasi-linear pitch-angle diffusion

Clare E. J. Watt[1]*, Hayley J. Allison[2], Sarah N. Bentley[1], Rhys L. Thompson[3], I. Jonathan Rae[1], Oliver Allanson[4], Nigel P. Meredith[5], Johnathan P. J. Ross[5], Sarah A. Glauert[5], Richard B. Horne[5], Shuai Zhang[6], Kyle R. Murphy[1,7], Dovilė Rasinskaitė[1] and Shannon Killey[1]

[1]Department of Mathematics, Physics and Electrical Engineering, Northumbria University, Newcastle upon Tyne, United Kingdom, [2]GFZ German Research Centre for Geosciences, Potsdam, Germany, [3]Department of Mathematics and Statistics, University of Reading, Reading, United Kingdom, [4]Department of Mathematics, University of Exeter, Penryn/Cornwall Campus, Penryn, United Kingdom, [5]British Antarctic Survey, Cambridge, United Kingdom, [6]Department of Earth and Space Sciences, Southern University of Science and Technology, Shenzhen, China, [7]Department of Astronomy, University of Maryland, College Park, MD, United States

Kinetic wave-particle interactions in Earth's outer radiation belt energize and scatter high-energy electrons, playing an important role in the dynamic variation of the extent and intensity of the outer belt. It is possible to model the effects of wave-particle interactions across long length and time scales using quasi-linear theory, leading to a Fokker-Planck equation to describe the effects of the waves on the high energy electrons. This powerful theory renders the efficacy of the wave-particle interaction in a diffusion coefficient that varies with energy or momentum and pitch angle. In this article we determine how the Fokker-Planck equation responds to the temporal variation of the quasi-linear diffusion coefficient in the case of pitch-angle diffusion due to plasmaspheric hiss. Guided by *in-situ* observations of how hiss wave activity and local number density change in time, we use stochastic parameterisation to describe the temporal evolution of hiss diffusion coefficients in ensemble numerical experiments. These experiments are informed by observations from three different example locations in near-Earth space, and a comparison of the results indicates that local differences in the distribution of diffusion coefficients can result in material differences to the ensemble solutions. We demonstrate that ensemble solutions of the Fokker-Planck equation depend both upon the timescale of variability (varied between minutes and hours), and the shape of the distribution of diffusion coefficients. Based upon theoretical construction of the diffusion coefficients and the results presented here, we argue that there is a useful maximum averaging timescale that should be used to construct a diffusion coefficient from observations, and that this timescale is likely less than the orbital period of most inner magnetospheric missions. We discuss time and length scales of wave-particle interactions relative to the drift velocity of high-energy electrons and confirm that arithmetic drift-averaging is can be appropriate in some cases. We show that in some locations, rare but large values of the diffusion coefficient occur during periods of relatively low number density. Ensemble solutions are sensitive to the presence of these rare values, supporting the need for accurate cold plasma density models in radiation belt descriptions.

KEYWORDS
wave-particle interactions, radiation belt, quasilinear, temporal variability, stochastic

1 Introduction

Earth's outer radiation belt is shaped by wave-particle interactions, whereby electromagnetic waves mediate energy and pitch-angle changes of high-energy electrons. There is a large range of electromagnetic waves that are implicated in wave-particle interactions and all play important roles in Earth's radiation belts. Ultra-low frequency (ULF) waves have frequencies ~ 1 mHz and contribute towards radial diffusion (Fei et al., 2006; Su et al., 2015; Mann et al., 2016; Sandhu et al., 2021). Electromagnetic ion cyclotron waves (EMIC) have frequencies ~ 1 Hz and contribute towards loss of enegetic electrons (Anderson et al., 1992; Halford et al., 2010; Usanova et al., 2012; Meredith et al., 2014; Ross et al., 2021). Whistler-mode waves exist as chorus (Tsurutani and Smith, 1977; Santolík and Gurnett, 2003; Li et al., 2009; Meredith et al., 2020), plasmaspheric hiss (Agapitov et al., 2018; Meredith et al., 2018; Kim and Shprits, 2019; Ripoll et al., 2020a), hiss-like emissions outside the plasmasphere (Santolík et al., 2010; Li et al., 2012), lightning-generated whistlers (Green et al., 2020) and even man-made emissions from ground-based high-power transmitters (Ma et al., 2017; Meredith et al., 2019; Ross et al., 2019). Whistler-mode waves contribute to energization (Horne et al., 2005; Thorne et al., 2013; Allison and Shprits, 2020) and loss (Selesnick et al., 2003; Kim et al., 2020) of high-energy electrons, where high-energy is usually understood to correspond to energies $E \gtrsim 0.5$ MeV.

Wave-particle interactions are an important process that govern the variability of the number of high-energy electrons in the outer radiation belt. The strength of resonant wave-particle interactions depends upon the energy of the electrons and the frequency and wavenumber of the electromagnetic waves. The wave frequency ω and wavenumber $\mathbf{k}$ are related by the wave dispersion relation, which in the cold plasma limit depends upon local magnetic field strength, number density and plasma composition. Numerical models of wave-particle interactions can be made using physics-based initial-value simulations. Particle-in-cell methods yield detailed information regarding the linear and nonlinear stages of the wave growth (Hikishima and Omura, 2012; Ratcliffe and Watt, 2017; Li et al., 2019) or the energy and pitch-angle diffusion process itself (Allanson et al., 2019; Allanson et al., 2020). These kinetic plasma numerical experiments provide deep insight into the wave-particle interaction but require short grid lengths dx less than the wavelength of interest, typically of the order of the electron or ion inertial length, or even the Debye length. Explicit schemes require timesteps dt that satisfy the Courant-Friedrichs-Lewy (CFL) condition ($dt < dx/c$, where c is the speed of light), and therefore timesteps that resolve the plasma period are commonplace. These short time and length scale constraints prevent particle-in-cell treatments being used to describe the global evolution of radiation belt dynamics over length scales of tens of thousands of kilometres and timescales of days and weeks. Instead, we use diffusion coefficients D_{ij} (where i, j can indicate energy or momentum and pitch-angle) to describe the results of the wave-particle interaction on much longer timescales, and over much larger spatial scales. The radial diffusion coefficients D_{LL} that are due to ULF wave-particle interactions are constructed in a different way to the localised energy/pitch-angle D_{ij} and are not the focus of this work.

Diffusion coefficients are an extraordinarily powerful way to describe the microphysics of a kinetic wave-particle interaction on timescales of hours and days and across the entire extent of the outer radiation belt. Early methods of calculating diffusion coefficients (Lyons et al., 1972; Lyons, 1974) have been refined (Réveillé et al., 2001; Glauert and Horne, 2005; Ni et al., 2008) and are now routinely used to construct both statistical (Ripoll and Mourenas, 2012; Horne et al., 2013; Cervantes et al., 2020) and event-specific (Thorne et al., 2013; Tu et al., 2014; Ripoll et al., 2016; Zhao et al., 2018; Millan et al., 2021; Pierrard et al., 2021) models of D_{ij}. Radiation belt models that use event-specific D_{ij} often yield different results to those that use averaged models, suggesting that the temporal and spatial variability of the waves and plasma conditions from event to event are not currently captured well by statistical models. Unfortunately, *in-situ* observations of waves and plasma are not routinely available. Even recent state-of-the-art missions that target the radiation belts such as JAXA Arase or NASA Van Allen Probes cannot provide global instantaneous coverage. Both have a finite mission lifetime. When operational, spacecraft may be sampling the dusk sector when there is increased whistler-mode activity in the dawn sector, or at noon when there is key wave activity at midnight. It is still necessary to construct reliable statistical models of wave activity and hence D_{ij} to ensure sufficient global and temporal coverage of past and future events.

Models of D_{ij} are constrained by observation, where the temporally and spatially-varying observations can be combined in different ways. Recent work demonstrates that there is a large and significant difference between the act of processing individual sets of concurrent and simultaneous measurements into an observation-specific diffusion coefficient before averaging, *versus* averaging observations before processing the diffusion coefficients (Watt et al., 2019; Ross et al., 2020). Both the shape and the strength of the diffusion coefficients depends upon the order of the averaging process. When we construct models of wave-particle interactions by averaging observation-specific D_{ij} for particular locations, or geomagnetic conditions (Ross et al., 2020), we imply that it is appropriate to ignore the temporal variability of the diffusion coefficients and consider only the average. We are therefore motivated to explore how the

temporal variability of $D_{ij}(t)$ changes the solution of the Fokker-Planck equation that is often used to describe the evolution of high-energy electron phase space density in Earth's outer radiation belt. Our initial analysis (Watt et al., 2021) indicates that the timescale of variability Δt changes the behaviour of the solutions to the Fokker-Planck equation; there is a significant difference in behaviour for rapid variability (Δt = 2 min) and for much slower variability (Δt = 6 h). In this work, we run a range of ensemble numerical experiments using a range of Δt between these two limits and investigate distributions of diffusion coefficients constructed for different locations in magnetospheric (L^*, MLT)-space, where L^* defines a drift-path for a high-energy electron and MLT is the magnetic local time. The results indicate the importance of being able to estimate Δt for drift-averaged diffusion coefficients, as well as the importance of considering temporal and spatial variation of waves and plasma properties when constructing drift-averaged D_{ij} in the first place. We also highlight the importance of considering the variability in both wave and plasma properties when constructing appropriate models of D_{ij}.

First we describe the methods used to construct the numerical experiments in Section 2 before presenting the results in Section 3. The implications of our results when considering drift-averaging, or how quickly drift-averaged D_{ij} vary, are set out in Section 4.3. The importance of understanding the underlying distribution of D_{ij} and the contribution of rare lower-than-average number density to the D_{ij} is discussed in Section 4.4. Our conclusions are summarized in Section 5.

2 Numerical experiment methods

We make the assumption that for plasmaspheric hiss, pitch-angle diffusion dominates over energy/momentum space diffusion (Lyons et al., 1972). We perform a series of ensemble numerical experiments using a one-dimensional approximation of the Fokker-Planck equation for radiation belt electrons:

$$\frac{\partial f}{\partial t} = \frac{1}{T \sin 2\alpha}\left(\frac{\partial}{\partial \alpha}\left(D_{\alpha\alpha}(t) T \sin 2\alpha \frac{\partial f}{\partial \alpha}\right)\right) - \frac{f}{\tau_L} \quad (1)$$

where f is the phase space density of high-energy electrons, α is the pitch-angle, and T(α) is given by:

$$T(\alpha) = 1.3802 - 0.3198\left(\sin\alpha + \sin^{1/2}\alpha\right). \quad (2)$$

The second term on the right hand side of Eq. 1 accounts for losses due to atmospheric collisions where the loss timescale τ_L is a quarter of the bounce period inside the loss cone α_{LC} and infinite outside (Shprits et al., 2008).

As described in (Watt et al., 2021), Eq. 1 is solved using an explicit time stepping scheme with timesteps of 0.1 s. The resolution of the pitch-angle grid is 1°. The stability of the code with respect to timestep has been established (Watt et al., 2021). We assume that far into the loss cone, collisions result in isotropy of the phase space density distribution, hence $\frac{\partial f}{\partial \alpha} = 0$ at $\alpha = 0°$ (Glauert et al., 2014). We also constrain $\frac{\partial f}{\partial \alpha} = 0$ at 90° to reflect the assumed symmetry of f with pitch-angle. All experiments are initialised with an isotropic pitch-angle distribution $f(\alpha) = 5 \times 10^3\ \mathrm{cm^{-2}s^{-1}sr^{-1}keV^{-1}}$. The distribution is then allowed to evolve over a 30 day period with no additional sources.

The differences in numerical experiments arise from the treatment of $D_{\alpha\alpha}(t)$. To mimic the time variation of $D_{\alpha\alpha}(\alpha)$, we randomly select from empirical distributions of diffusion coefficients $\mathcal{P}[D_{\alpha\alpha}(\alpha)]$ constructed from individual co-located and simultaneous Van Allen Probe measurements of plasmaspheric hiss wave intensity δB^2, electron number density n_e and magnetic field intensity B_0. The distributions $\mathcal{P}[D_{\alpha\alpha}(\alpha)]$ to be used in this investigation are constructed using the British Antarctic Survey PADIE code (Glauert and Horne, 2005). Plasmaspheric hiss is identified by excluding waves with ellipticity less than 0.7 to separate potential magnetosonic wave activity, and using a commonly-used number density threshold (Sheeley et al., 2001) to separate measurements likely made inside the plasmasphere from those likely made outside [full details for construction of the plasmaspheric hiss $D_{\alpha\alpha}(\alpha)$ including information on wave rfequency spectrum, dependence on wavenormal angle, and assume latitudinal dependence of the waves are found in (Watt et al., 2019)]. Electron energy is fixed at E = 0.5 MeV.

The $\mathcal{P}[D_{\alpha\alpha}(\alpha)]$ are obtained for three observation bins in the Van Allen Probe dataset with ($09 < MLT < 10$, $-5° < \lambda < +5°$). We choose three bins in L^* to study the diffusion coefficients due to plasmaspheric hiss; L^* is used rather than another parameter in order to align well with the drift-paths of high-energy radiation belt electrons. Observations with $2.45 < L^* < 2.55$ are referred to as the L^* = 2.5 bin, ($2.95 < L^* < 3.05$) referred to as the L^* = 3.0 bin, and ($3.45 < L^* < 3.55$) referred to as the L^* = 3.5 bin [see (Watt et al., 2019)]. These values of L^* and MLT are chosen because they lie in a region of strong plasmaspheric wave activity (Meredith et al., 2018). The distributions of diffusion coefficients are shown in Figure 1. Although the $\mathcal{P}[D_{\alpha\alpha}(\alpha)]$ are calculated for a fixed energy, the whistler-mode wave resonant condition varies across the 3 L^* bins chosen. The shape of the $D_{\alpha\alpha}(\alpha)$ change between the three bins as a result of the variation in the resonant condition. It is therefore likely that we can generalise some of the results obtained through the numerical experiments shown here to pitch-angle diffusion at other energies.

We assign α_{LC} in the numerical code to its equivalent value for a dipolar field line with $L = L^*$ for each bin. The observation bins are chosen to represent regions of the magnetosphere where plasmaspheric hiss is strong (Meredith et al., 2018), and the size of the bin is chosen to minimise potential radial or MLT variations in the distribution of $D_{\alpha\alpha}(\alpha)$. We therefore interpret the range of $D_{\alpha\alpha}(\alpha)$ in each bin as a result of temporal variation

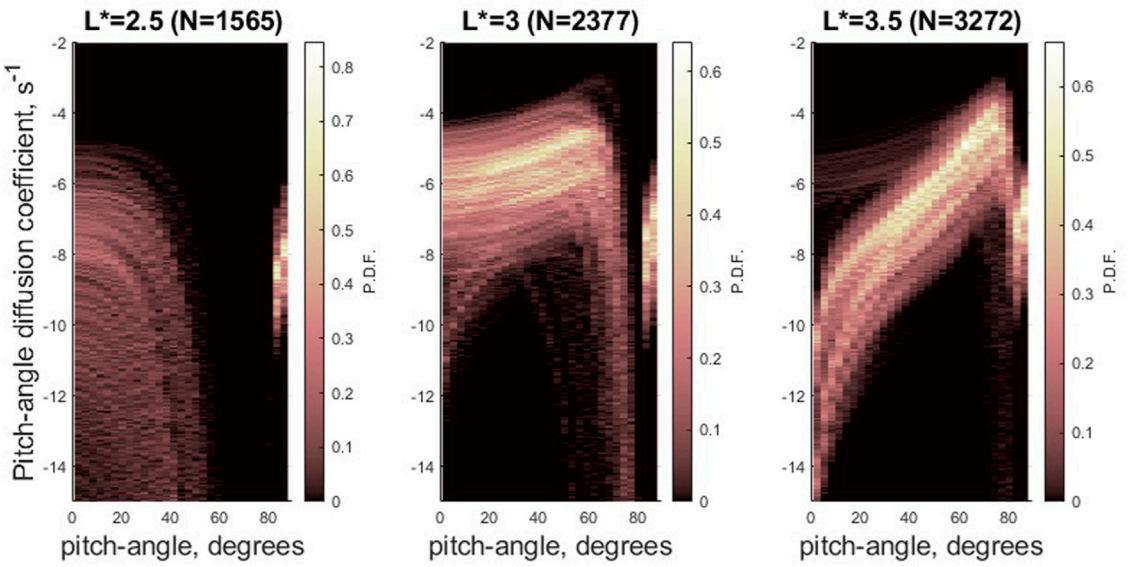

FIGURE 1
Probability distribution functions for $D_{\alpha\alpha}(\alpha)$ in each of the 3 L^* bins used in this numerical study. The number of individual observation-specific $D_{\alpha\alpha}(\alpha)$ in each distribution N is indicated at the top of each panel. See (Watt et al., 2019) for choices made during construction of observation-specific $D_{\alpha\alpha}$.

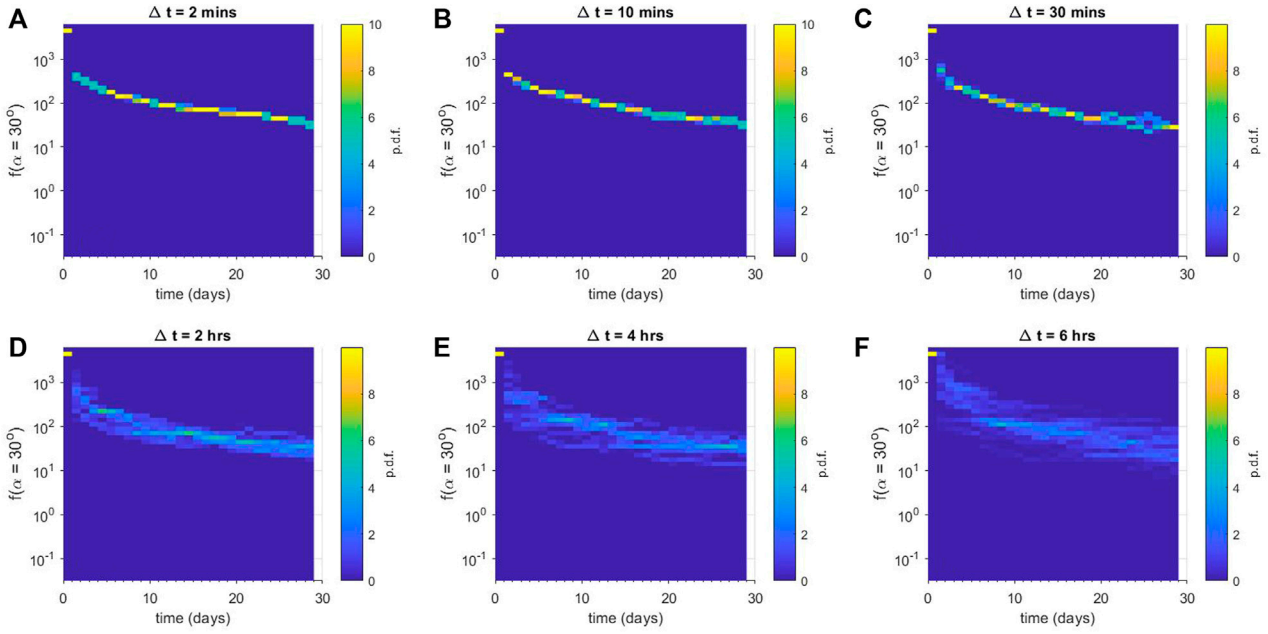

FIGURE 2
Ensemble results for numerical diffusion experiments using $D_{\alpha\alpha}(L^* = 2.5)$. Each panel shows a column-normalised probability distribution function for the phase space density f just outside the loss-cone α_{LC} for **(A)** $\Delta t = 2$ min, **(B)** $\Delta t = 10$ min, **(C)** $\Delta t = 30$ min, **(D)** $\Delta t = 2$ h, **(E)** $\Delta t = 4$ h, and **(F)** $\Delta t = 6$ h. Note that each histogram is displayed using the same vertical binning, giving the histograms a pixelated appearance.

only. There are $N > 1{,}000$ individual $D_{\alpha\alpha}(\alpha)$ in each distribution, where N is indicated at the top of the Figure. It is important to reiterate (Watt et al., 2019; Watt et al., 2021) that both the shape and the strength of $D_{\alpha\alpha}(\alpha)$ varies as a result of the unique combination of δB^2, n_e and B_0 used in its construction.

Each ensemble numerical experiment has 60 scenarios, i.e., 60 individual 30-day experiments are run with the same initial and boundary conditions, the same timescale of variability Δt, but different random selections of $D_{\alpha\alpha}(\alpha)$. Ensemble convergence for more than 60 scenarios in each ensemble is demonstrated in (Watt et al., 2021). The timescale of variability Δt is an important parameter in our numerical experiments. In each scenario in an ensemble of experiments, a time-series of $D_{\alpha\alpha}(\alpha, t)$ is constructed by randomly sampling the appropriate $\mathcal{P}[D_{\alpha\alpha}(\alpha)]$. At time $t_0 = 0$, a random value of $D_{\alpha\alpha}(\alpha)$ is chosen, and kept constant until $t = t_0 + \Delta t$. Then another random value of $D_{\alpha\alpha}(\alpha)$ is chosen from the same $\mathcal{P}[D_{\alpha\alpha}(\alpha)]$, and kept constant until $t = t_0 + 2\Delta t$, and so on. We have run 18 ensemble numerical experiments in this study: 6 values of Δt are used for $\mathcal{P}[D_{\alpha\alpha}(\alpha)]$ from 3 $L^\star$ bins.

In previous work (Watt et al., 2021), the small timescale chosen was $\Delta t = 2$ min, representing the typical length of time the spacecraft take to traverse the observation bin and over which there is often little variation in $D_{\alpha\alpha}(\alpha)$ [see Figure 2 of (Watt et al., 2021)]. The largest timescale chosen was $\Delta t = 6$ h, since it was clear from the orbital sampling of each observation bin that there is significant variation in $D_{\alpha\alpha}(\alpha)$ between each successive orbit. Our initial study indicated that there were significant differences in the ensemble results between $\Delta t = 2$ and $\Delta t = 360$ min. In this study, we investigate $\Delta t = 2$, 10, 30, 120, 240 and 360 min to determine how the results change with temporal scale.

3 Results from numerical experiments

For each numerical experiment, we have 60 scenarios of $f(\alpha, t)$ at 1° resolution in α and 0.1 s resolution in time. To visualize one of the important aspects of the evolution of the ensembles, we choose a value of pitch-angle that is close to but greater than, α_{LC} and plot the probability distribution function of the ensemble as a function of time. For $L^\star = 2.5$, we plot $f(\alpha = 13^\circ)$, for $L^\star = 3.0$, we plot $f(\alpha = 10^\circ)$ and for $L^\star = 3.5$, we plot $f(\alpha = 9^\circ)$.

The results for the $L^\star = 2.5$ bin are shown in Figure 2, where Δt is (a) 2 min, (b), 10 min, (c) 30 min, (d) 120 min, (e) 240 min and (f) 360 min. Panel (a) shows that for the rapidly-varying diffusion coefficients, the ensemble exhibits very little variation from one scenario to another; the probability distribution function has a large peak and very little spread. The evolution of the peak of the distribution indicates a rapid initial drop as the loss-cone is evacuated, followed by a slower decline as pitch-angle scattering acts to smooth out the sharp gradient at the loss-cone. As Δt increases [moving from panels (a) to (f)], the ensemble results show much more spread. The probability distribution function exhibits increasing variation as Δt increases, even though the median ensemble behaviour is similar. Note that in each case, the median behaviour of the ensemble is similar to the behaviour of a numerical diffusion experiment using a diffusion coefficient averaged over the entire distribution of individual diffusion coefficients, $D_{\alpha\alpha,ave}(\alpha) = \langle D_{\alpha\alpha,i}(\alpha)\rangle$. We have chosen not to show this explicitly in individual panels of Figure 2 in order to highlight the narrowness of the distributions in panels (a) and (b), but a comparison can be made with Figure 4A of (Watt et al., 2021).

Figure 3 displays results from the numerical ensemble experiment using diffusion coefficients from the $L^\star = 3$ bin. In this case, the diffusion coefficients for $E = 0.5$ MeV tend to be much larger than those at $L^\star = 2.5$, and so the values of $f(\alpha_{LC})$ reach much lower values than in Figure 2. Similar trends exist as Δt is increased from 2 min to 360 min: for rapidly varying $D_{\alpha\alpha}(\alpha)$, the probability distribution function is strongly peaked with little spread. As Δt increases, the probability distribution function exhibits significant spread.

Finally, we demonstrate the results from the numerical ensemble experiment with $L^\star = 3.5$ in Figure 4. In this observation bin, the values of $D_{\alpha\alpha}(\alpha)$ for $E = 0.5$ MeV are in general much smaller than those seen at $L^\star = 2.5$ or $L^\star = 3$. As expected, for all values of Δt the ensembles indicate that $f(\alpha_{LC})$ remains at much higher levels than for other $L^\star$ experiments. For small values of Δt shown in panels (a), (b) and (c), we again observe that the probability distribution function of $f(\alpha_{LC})$ is strongly peaked and exhibits very little spread. For panels (d), (e) and (f), we see a significant increase in spread of the probability distribution function. Additionally, these numerical experiments exhibit new behaviour that is not seen in Figures 2, 3. For the period $2 < t < 8$ days in panel (d), and $2 < t < 10$ days in panels (e) and (f), there appears to be two different sets of solutions in the ensemble. There is a strong peak at the initial value $f(\alpha_{LC}) = 5 \times 10^3$ cm^{-2}s^{-1}sr^{-1}keV^{-1} that gradually decreases with time, indicating that for many scenarios in the ensemble, very little diffusion has occurred. For a minority of scenarios in each ensemble, a lot more diffusion has occurred, as indicated by a much wider peak in the probability distribution function for $f(\alpha_{LC}) = 1\text{–}4 \times 10^3$ cm^{-2}s^{-1}sr^{-1}keV^{-1}. The strong peak at the initial value of $f(\alpha_{LC})$ fades more slowly as Δt increases.

To compare directly between different Δt, we summarize the numerical experiment results in Figure 5. The top row [panels (a) to (c)] show the median of $log_{10}[f(\alpha_{LC})]$ for each ensemble as a function of time. The $L^\star$ values are indicated at the top of the figure. The bottom row [panels (d) to (f)] show the interquartile range (IQR) of $log_{10}[f(\alpha_{LC})]$, again as a function of Δt and experiment time. To aid with interpretation of information in the bottom row, if IQR = 1 then there is an order of magnitude between the 25th percentile and the 75th percentile of the ensemble. Note that the median and IQR of $log_{10}[f(\alpha_{LC})]$ are used because the ensemble values of $f(\alpha_{LC})$ at each t are not normally-distributed (Watt et al., 2021).

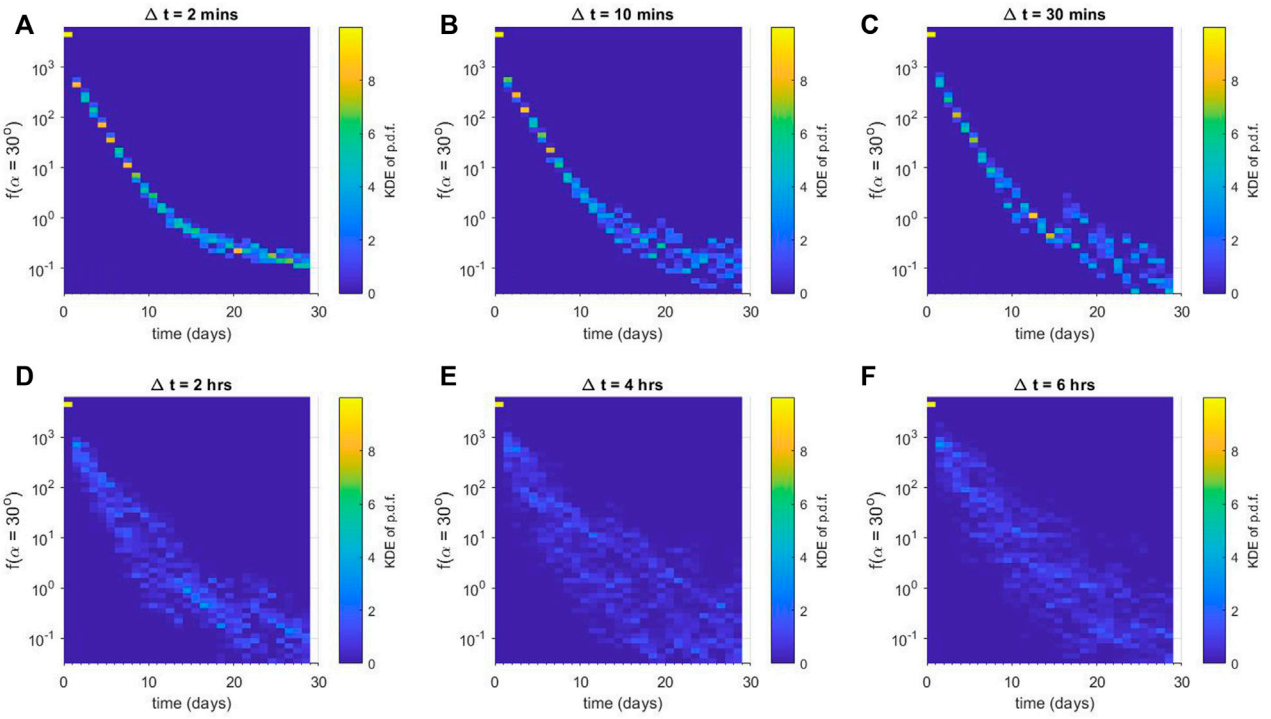

FIGURE 3
Ensemble results for numerical diffusion experiments using $D_{\alpha\alpha}(L^* = 3)$. Each panel shows a column-normalised probability distribution function for the phase space density f just outside the loss-cone α_{LC} for **(A)** Δt = 2 min, **(B)** Δt = 10 min, **(C)** Δt = 30 min, **(D)** Δt = 2 h, **(E)** Δt = 4 h, and **(F)** Δt = 6 h. Note that each histogram is displayed using the same vertical binning, giving the histograms a pixelated appearance.

In general, Figure 5 shows that in each experiment the median value of log_{10} [f (α_{LC})] decreases more slowly as Δt increases, although for L^* = 3.0 the difference in median behaviour is very small. The biggest difference between experiments comes when we consider the IQR; the ensemble results are much more variable as Δt increases. The IQR varies in time in each case, most notably so when Δt is large.

The value of $log_{10}f$ is important in modelling, as models are often interpreted and evaluated on a log scale. However, other physical quantities are important when judging the effects of temporal variability in the ensembles. The ensemble results also indicate large variability in the amount of loss-cone scattering due to plasmaspheric hiss. We calculated the percentage loss in each scenario by comparing the flux integrated over pitch-angle at the beginning of the experiment, and at the end of the experiment. Results are shown in Figure 6 where panels (a-c) show results from numerical experiments with Δt = 2 min, and panels (d-f) show results from experiments with Δt = 6 h. The amount of loss varies at each L^* bin, as does the dependence of loss on Δt. At L^* = 2.5, in the rapidly-varying experiments (i.e., low Δt), there is a total loss of flux of roughly 42% after 30 days in every scenario. However, for slowly-varying experiments (large Δt), the loss varies between 32% and 48%. At L^* = 3.0, all scenarios, no matter the timescale, experience a loss of 85% in f over 30 days. Finally, for L^* = 3.5, in the rapidly-varying experiments, all scenarios show a loss of 38%. However, for slowly-varying experiments, scenarios experience large differences in the amount of loss between 5% and 65%. The loss values are large across all experiments because the initial condition is a full loss cone that is immediately depleted. However, the variation in the amount of loss across the ensemble is due only to the differences in temporal variation in the diffusion coefficients between each scenario.

4 Discussion

4.1 Diffusion coefficients modelled using quasi-linear theory

The quasi-linear theory of wave-particle interactions (Drummond and Pines, 1962; Kennel and Engelmann, 1966; Lyons et al., 1972; Lyons, 1974) yields diffusion coefficients $D_{i,j}$ such that microscopic wave-particle interactions may be included in numerical models with time and length scales that are much longer than those of the waves themselves. To construct models of diffusion coefficients, it is necessary to use observations or models of magnetospheric magnetic field,

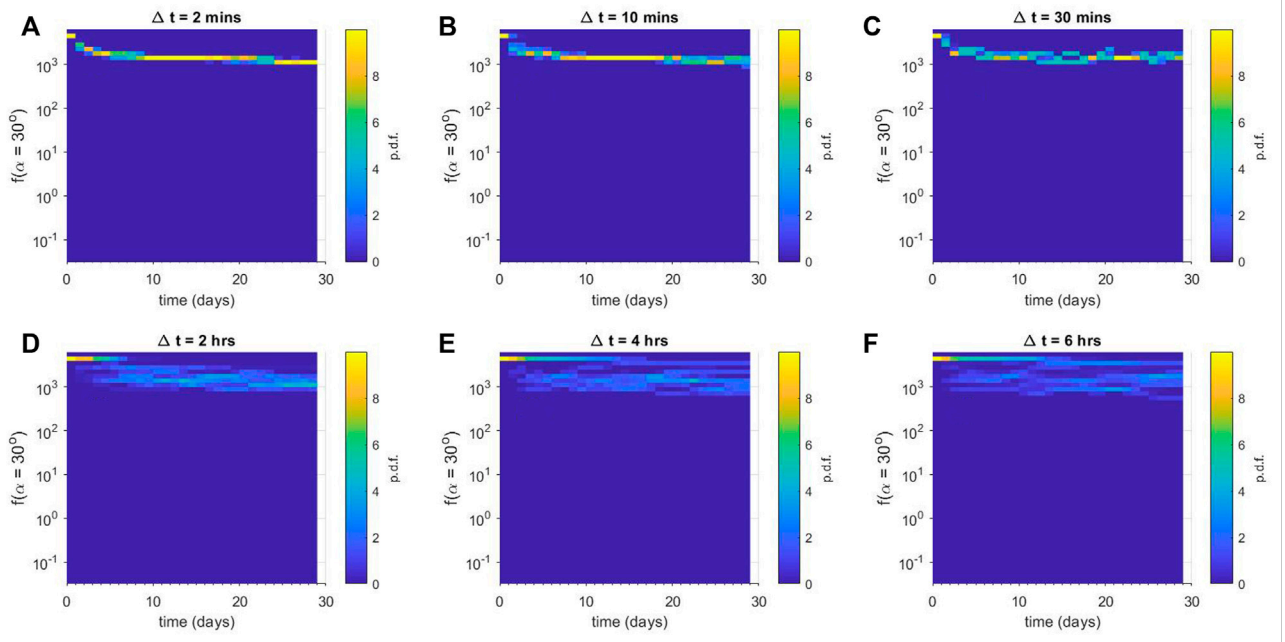

FIGURE 4
Ensemble results for numerical diffusion experiments using $D_{\alpha\alpha}(L^* = 3.5)$. Each panel shows a column-normalised probability distribution function for the phase space density f just outside the loss-cone α_{LC} for **(A)** $\Delta t = 2$ min, **(B)** $\Delta t = 10$ min, **(C)** $\Delta t = 30$ min, **(D)** $\Delta t = 2$ h, **(E)** $\Delta t = 4$ h, and **(F)** $\Delta t = 6$ h. Note that each histogram is displayed using the same vertical binning, giving the histograms a pixelated appearance.

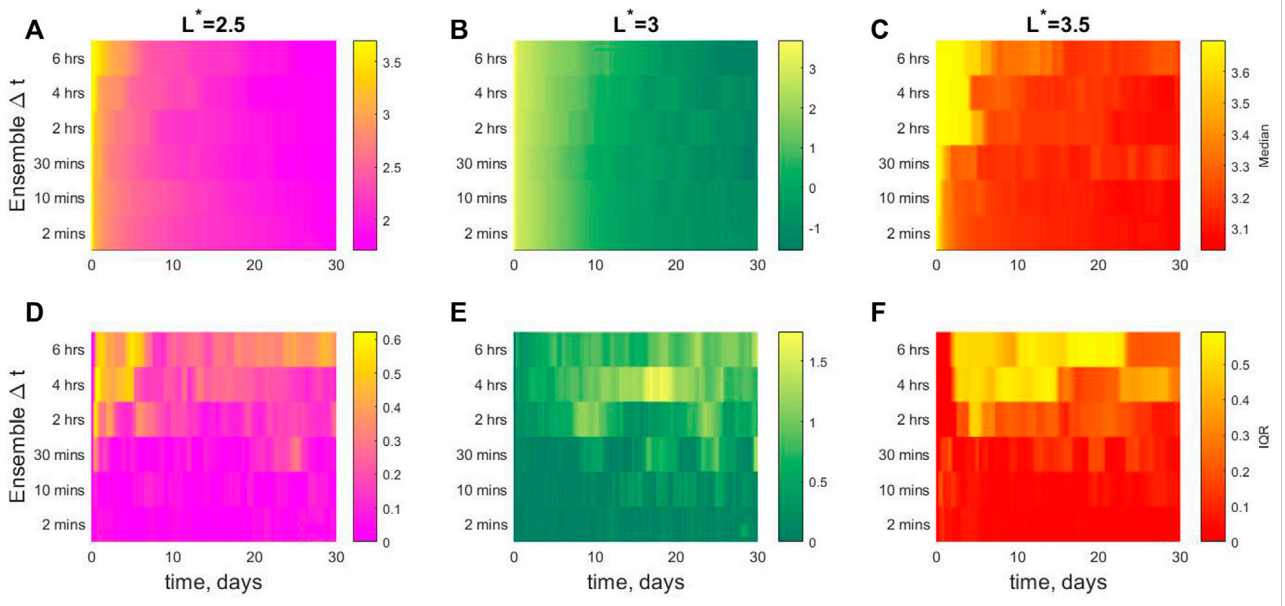

FIGURE 5
Summary figure for each L^* set of experiments **(A–C)** median of log_{10} (f (α_{LC})) and **(D–F)** IQR of log_{10} (f (α_{LC})).

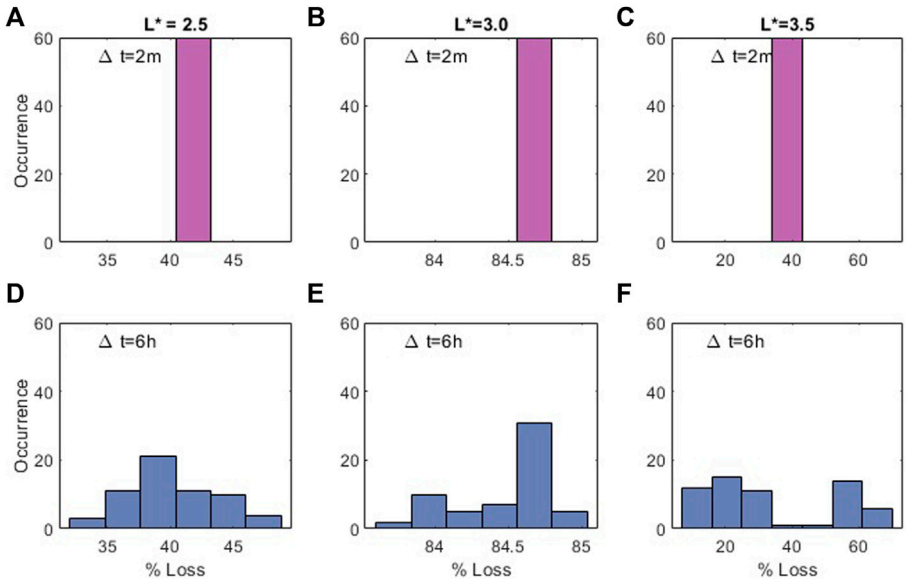

FIGURE 6
Histograms displaying percentage loss in each scenario from 6 different ensemble experiments: **(A,D)** use $\mathcal{P}[D_{\alpha\alpha}(\alpha)]$ from L^* = 2.5, **(B,E)** from L^* = 3 and **(C,F)** from L^* = 3.5. Panels **(A–C)** show ensembles with Δt = 2 min and **(D–F)** show ensembles with Δt = 6 h.

number density, and composition in addition to information about wave intensity and how it varies in space, frequency and wavenormal angle. We discuss here the implications of our numerical results for the accurate modelling of quasi-linear diffusion coefficients using observations from *in-situ* spacecraft.

We have modelled our diffusion coefficients using a statistical distribution of observation-specific (Watt et al., 2019; Ross et al., 2020) values. The free parameter in our numerical study is the temporal scale of variation Δt. Our results indicate that when used in ensembles of Fokker-Planck models, temporal variation of quasi-linear diffusion coefficients with timescales greater than 30 min yields significant uncertainty in the model results. For timescales of variation less than 30 min, an average of the observation-specific diffusion coefficients is a reasonable approximation to the ensemble result (Watt et al., 2021). Recent work (Zhang et al., 2021a) indicates that observed timescales for plasmaspheric hiss patches are typically less than 10 min, and so plasmaspheric hiss activity would appear to vary sufficiently rapidly that averaging observation-specific diffusion coefficients should be appropriate. We discuss timescales relative to drift-averaging in Section 4.3 below.

Quasi-linear diffusion coefficients must be calculated on timescales that are long compared to the wave period $T \sim \Omega_e^{-1}$, and the particle de-correlation time $\tau_C \sim T$, where τ_C increases for decreasing wave amplitude (Lemons, 2012; Liu et al., 2012; Allanson et al., 2020; Allanson et al., 2022). For whistler mode waves in the terrestrial magnetosphere, these timescales are short and usually much less than 1 s. As a result, individual wave-spectra observations from spacecraft such as the NASA Van Allen Probes have already averaged over timescales longer that the appropriate minimum timescale. There are also important upper limits to the time over which diffusion coefficients should be estimated from observations. An important upper limit is a timescale of the order of $D_{\alpha\alpha}^{-1}$ (Lemons, 2012; Liu et al., 2012; Allanson et al., 2022). For many observation-specific diffusion coefficients used in this study, this timescale is at least a few days. However, for the largest diffusion coefficients (see Figure 1), this can be as little as a few hours. It is also implicitly assumed in quasi-linear constructions of diffusion coefficients (Lyons et al., 1972; Lyons, 1974) that ambient conditions such as the magnetic field strength and the number density do not change with time, since these parameters change the resonant condition for the energetic electrons. The dependence of $D_{i,j}$ on energy and pitch-angle is very sensitive to values of number density and ambient magnetic field, and so temporal variation of these quantities is important. It is therefore likely that there is a maximum useful averaging timescale to construct individual diffusion coefficients that describe wave-particle interactions in the inner magnetosphere. For plasmaspheric hiss, the variation in observation-specific diffusion coefficients is much larger between successive Van Allen Probe orbits than it is during an orbital pass through a small region (Watt et al., 2019). This was our original motivation for using a range of Δt that spans a range between 2 min and 6 h. We therefore suggest that a useful maximum averaging period for calculating observation-specific diffusion coefficients should be tied to the grid on which they are constructed.

Many models of $D_{i,j}$ are constructed from long-term statistical studies of wave activity in the magnetosphere. To connect observations to the $D_{i,j}$, a grid is often constructed in real space on which to collect observations that are then statistically averaged. *In-situ* observations relative to that grid are collated and averaged to provide averaged wave amplitudes (Tu et al., 2013; Sicard-Piet et al., 2014; Li et al., 2015; Ma et al., 2017; Meredith et al., 2018; Zhu et al., 2019; Green et al., 2020; Meredith et al., 2020), averaged frequency distributions (Li et al., 2016; Zhu et al., 2019) or averaged wavenormal angle distributions (Ni et al., 2013). The averaged properties are then combined with models of the magnetic field and number density to form diffusion coefficient models (Horne et al., 2013; Wang et al., 2017; Ma et al., 2018). In each case, observations are averaged over many months, sometimes years or decades (Watt et al., 2017; Watt et al., 2019). During these long time periods, all of the inputs are highly variable (Watt et al., 2019). We therefore recommend that where observations are used to constrain models of quasi-linear diffusion coefficients:

- $D_{i,j}$ should be calculated using co-located and simultaneous measurements based upon a grid in e.g. magnetic local time and L^*. Spacecraft such as the NASA Van Allen probes travel through such a grid rapidly enough that observations are quite similar within grid cells [see e.g., (Watt et al., 2019)], and so observations from a single pass through the grid should be used to construct each observation-specific diffusion coefficient.
- Statistical models should then be constructed from those observation-specific values [see e.g., (Ross et al., 2020)]
- The natural timescales of variation for diffusion due to each wave mode should be studied and quantified
- Where timescales of variation are sufficiently short (in the case of plasmaspheric hiss, less than around 30 min), averaged models can then be constructed from averages of the observation-specific values.

Note that although we focus only on the pitch-angle scattering coefficient $D_{\alpha\alpha}$ due to plasmaspheric hiss in this work, the consequences of our results should hold for diffusion coefficients in energy and the cross-terms (Albert et al., 2009), as well as for diffusion coefficients describing wave-particle interactions with other wave modes.

4.2 Temporal scales of variability leads to different levels of uncertainty in model results

It is important to carefully interpret the ensemble results. The median of the ensemble provides an indication of the general trend when a collection of numerical scenarios are grouped together. No single ensemble scenario resembles the median evolution; each individual scenario experiences rare big changes when large values of diffusion coefficients are chosen from the distribution, with very little change at other times when only small values of diffusion coefficients are experienced [see Figure 3 of (Watt et al., 2021) for an example]. The IQR is a measure of the variability of each numerical ensemble. We reiterate from our initial study (Watt et al., 2021) that the time-integrated diffusion in all experiments at the same L^* is the same, the only difference in each case is the value of Δt.

The IQR in each ensemble experiment depends both on Δt and the average strength of the diffusion coefficients in the distribution $\mathcal{P}(D_{\alpha\alpha}(\alpha))$. When Δt is small and average diffusion rates are small, IQR values are also small; ensembles display very little uncertainty. Examples of this can be seen in Figures 5D,F. The long-term behaviour of the ensemble closely mimics that obtained with a time-averaged diffusion coefficient (Watt et al., 2021), and so time-averaging of diffusion coefficients is effective, even when the underlying distribution of diffusion coefficients is highly variable (Watt et al., 2019).

In contrast, large IQR values where Δt is large, or average diffusion rates are large, indicate significant amounts of uncertainty in the outcome of the ensemble numerical experiments. For example, the IQR is more than an order of magnitude in most experiments using $\mathcal{P}(D_{\alpha\alpha}(\alpha))$ for $L^* = 3$, shown in Figure 5E. Where the IQR is large, there are large differences between individual scenarios in the same ensemble. Where average diffusion rates are large, or where temporal scales of variability are large, time-averaging of diffusion coefficients is less effective and masks significant uncertainty in the numerical experiment result.

The numerical experiments reported here only consider resonant quasilinear diffusion coefficients [e.g., (Lyons et al., 1972; Lyons, 1974)]. However, non-resonant wave-particle interactions [e.g., (Zhao et al., 2022)], although usually much weaker, also depend upon wave amplitudes. For the most intense waves, the nonresonant interaction could be as large as the resonant interaction during typical periods. We advocate more research in this important area, towards possible inclusion in large-scale radiation belt models.

Uncertainty in the model results shown in Figures 2–4 provide bounds and other statistical information regarding potential solutions to the diffusion equation under idealized circumstances. In some cases, these bounds are very wide. Over a 30-day period, with no other influences on the evolution of the numerical experiment other than the changing diffusion coefficients (e.g., no sources of phase space density either due to radial or energy diffusion), the uncertainty in the experiments changes in time (see also Figure 5). This is especially marked for large Δt. Large uncertainties in the ensemble solutions can arise due to the changes in the shape of $D_{\alpha\alpha}(\alpha)$ as well as in its strength. The range of α over which $D_{\alpha\alpha}$ is large can change with plasma to gyrofrequency ratio (Horne and Thorne, 2003; Glauert and Horne, 2005; Watt et al., 2019).

For some values of this ratio, the range of large $D_{\alpha\alpha}$ can momentarily extend to large α, and act like a temporary source of plasma to be diffused to low α. These effects are associated with periods of large and varying uncertainty in the ensemble numerical experiments.

When we envisage using stochastic parameterizations of D_{ij} in full 3D radiation belt diffusion models, the consequences of large variability may be compounded. For example, the uncertainties in the amount of loss (Figure 6) can be very large. There is a complicated relationship between the size and shape of the diffusion coefficients, and the resulting uncertainty. In a full 3D diffusion model with diffusion across pitch-angle, energy and L^* space, it is likely that the interplay of uncertainty in diffusion in three dimensions, as well as uncertainty due to variable physical sources included through boundary conditions in L^* and energy space, will result in significantly more uncertainty as models progress. We argue that the results presented here prompt us to seek ways to reduce the uncertainty in the diffusion coefficients used in radiation belt models. Reducing uncertainty is not just about reducing error bars of a model, reducing uncertainty reduces the number of potential paths a model might take through the potential solutions of phase space density in (L^*, E, α) space. Identifying and reducing uncertainty in diffusion coefficient descriptions (Bentley et al., 2019; Watt et al., 2019), boundary conditions, and even the magnetic field models used in coordinate transforms (Loridan et al., 2019; Thompson et al., 2021) will allow us to use models 1) to correctly attribute a change in radiation belt evolution to a particular physical process (Mann et al., 2016; Shprits et al., 2018), 2) to identify a realistic range of radiation belt responses to geomagnetic disturbances or 3) as an effective operational forecast tool.

Where Δt is large, or average diffusion rates are large, uncertainty in model behaviour could be reduced by minimizing the variability in the distribution of diffusion coefficients (Thompson et al., 2020). Reduction of variability can be achieved through parameterization (Bentley et al., 2019), i.e., where diffusion coefficients are binned according to parameters that control their behaviour. Parameterizations are widely used to construct wave amplitude maps (Horne et al., 2013; Glauert et al., 2014; Bentley et al., 2018; Bentley et al., 2020; Meredith et al., 2020; Aryan et al., 2021), and could be used to construct models of diffusion coefficients equally as effectively (Watt et al., 2019; Ross et al., 2020).

4.3 Temporal variability and drift-averaging

Our numerical experiments indicate that there are some circumstances where averaging is appropriate. It is therefore important to determine whether this is true for drift-averaging. It is therefore important to determine whether Recent work (Zhang et al., 2021a) has characterised the temporal and spatial scale sizes of patches of plasmaspheric hiss in the inner magnetosphere. Using both NASA Van Allen Probe spacecraft (Mauk et al., 2013), integrated wave power from the Wave Form Receiver in the Electric and Magnetic Field Instrument Suite and Integrated Science [EMFISIS (Kletzing et al., 2013)] was cross-correlated. The varying separation of the two Van Allen Probes as they travel on similar orbits allows good estimates of both temporal and spatial correlations. Spatial correlations are estimated by correlating the time series of integrated wave power from each satellite with no lag. Zhang et al. (2021a) demonstrated that correlations were higher when the spacecraft were closely separated in space less than $\sim 0.23 R_E$ or ~ 1500 km apart. Temporal correlations are estimated correlating the spatial series of integrated wave power where the temporal lag between the spatial series depends upon the spacecraft separation. In this case, Zhang et al. (2021a) again demonstrated that correlations were higher when the spacecraft were closely separated in time less than 10 min apart.

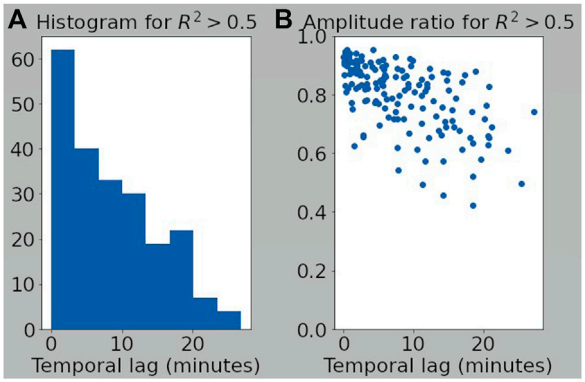

FIGURE 7
(A) Histogram of temporal lags between spacecraft that yield correlations with $R^2 > 0.5$ for whistler-mode wave power. **(B)** Amplitude ratio of whistler-mode waves measured by each spacecraft for temporal lags shown in histogram. Subset of correlation data where Van Allen Probes A and B both have $L^* < 4$ taken from Zhang et al. (2021a).

Although diffusion coefficients depend both on wave amplitude and local parameters such as number density and magnetic field strength, here we will use the results of Zhang et al. (2021a) to consider constraints on the temporal and spatial scales of the plasmaspheric hiss itself. Future investigations should be performed to incorporate the spatial and temporal variability of the number density in the inner magnetosphere, as it is a key parameter in the calculation of diffusion coefficients (see Section 4.4).

In Figure 7, we collect data from the Zhang et al. (2021a) study where both Van Allen Probes have $L^* < 4$ to coincide with our observation bins at $L^* = 2.5$, 3.0 and 3.5. Figure 7A shows a histogram of temporal lags when the correlation coefficient of the

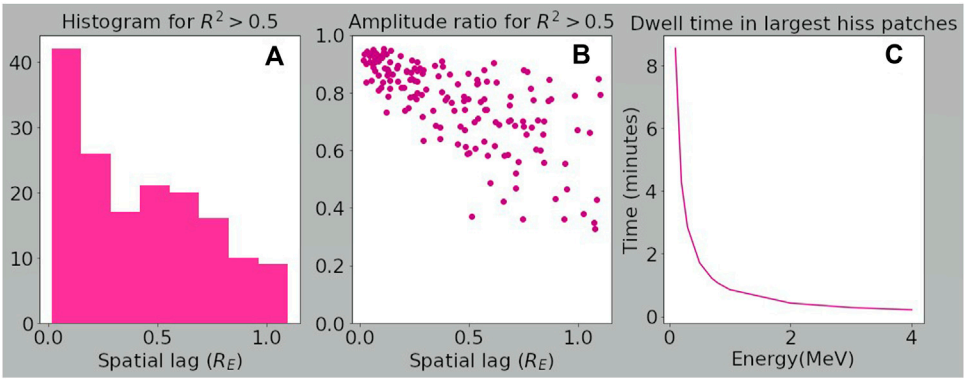

FIGURE 8
(A) Histogram of spatial lags between spacecraft that yield correlations with $R^2 > 0.5$ for whistler-mode wave power. **(B)** Amplitude ratio of whistler-mode waves measured by each spacecraft for spatial lags shown in histogram. **(C)** Estimated dwell time in largest observed whistler-mode wave patches as a function of energy. Subset of correlation data where Van Allen Probes A and B both have $L^* < 4$ taken from Zhang et al. (2021a).

two spacecraft observations $R^2 > 0.5$. The high correlation is used as identification of coherent spatial patches of plasmaspheric hiss activity. The corresponding temporal lags indicate that patches last for a few minutes with an observed maximum of around 25 min. Figure 7B shows the amplitude ratio for the same patches indicating that when the correlation is high, the amplitudes of the patches observed by each spacecraft are similar. If we assume that the patches are not moving in space, then we can interpret the temporal lags as the temporal scale of the patches. When we compare to the results of the numerical experiments, the hiss patch timescale (< 25 min) corresponds to the smaller values of Δt < 30 min, where the experiments often show low values of uncertainty.

It is important to note that when constructing a diffusion coefficient for a high-energy electron (e.g., with $E = 0.5$ MeV), we must also consider its experience as it drifts around the Earth under the influence of gradient and curvature drifts. Some of the "temporal" changes in wave-particle interactions experienced by the drifting electron arise due to its rapid transit of spatially coherent patches of plasmaspheric hiss, and so we must also consider the spatial size of these patches. Figure 8 shows a subset of data with $L^* < 4$ from the Zhang et al. (2021a), study, but this time looking at spatial correlations. Figure 8A shows a histogram of spatial separations when the correlation coefficient of the two spacecraft observations $R^2 > 0.5$. Note that events in this study are chosen such that the spacecraft separation is $< 1R_E$, and so this is an imposed constraint on the extent of spatial scales studied. Most of the highly-correlated events have much smaller separation scales than $1R_E$. Amplitude ratios for these events are shown in Figure 8B, and we see that amplitude ratios of the waves are less similar as spacecraft separation increases.

We consider the largest plasmaspheric hiss patches identified in the Zhang et al. (2021a), study (with the caveat that this largest value is self-imposed), and estimate how long it would take electrons of different energies to gradient-curvature drift through the patches at $L^* = 3$. Assuming the magnetic field is essentially dipolar, and that electrons have 90° pitch-angles, dwell times in hiss patches with scale sizes of $1R_E$ are shown in Figure 8C. For the example energy considered throughout this paper ($E = 0.5$ MeV), dwell times are less than 3 min. So when we consider the apparent timescales of wave patches, as experienced by a drifting high-energy electron at $L^* = 3$, these also correspond to the smallest values of $\Delta t < 10$ min used in the numerical experiments, which again show low values of uncertainty.

Given the numerical experiment results reported here, our analysis of the temporal and spatial scale sizes of patches of plasmaspheric hiss indicate that averaging of diffusion coefficients in the azimuthal direction would provide reasonably accurate determinations of drift-averaged diffusion coefficients as experienced by high-energy electrons in the outer radiation belt. In all of our numerical experiments where we model the variability of wave-particle interactions using small timescales similar to those experienced by an electron as it drifts through a plasmaspheric hiss patch, ensemble scenarios are very similar, and the evolution of the model closely follows that of a model performed with an arithmetic average of the diffusion coefficients. Even when the underlying distribution of diffusion coefficients varies over many orders of magnetidue (see Figure 1), if the timescales of varation are rapid enough, ensembles produce very similar results that tend to the same behaviour as experiments run with averaged values (Watt et al., 2021). Note that averaging is less accurate and leads to more uncertainty as the average value of the diffusion coefficients increases.

We therefore suggest that it is important to perform an analysis of the temporal variation of *drift-averaged* diffusion coefficients in the magnetosphere. For plasmaspheric hiss, this could be achieved with probabilistic models of the evolution and spatial structure of

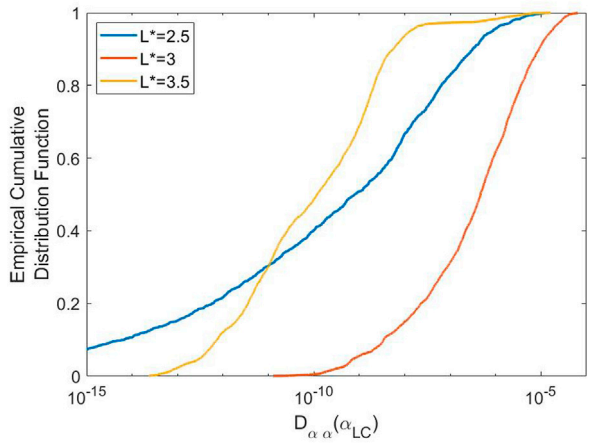

FIGURE 9
Cumulative distribution functions of the $\mathcal{P}[D_{\alpha\alpha}(\alpha_{LC})]$ for L^* = 2.5 (blue),3.0 (orange) and 3.5 (yellow). Note the log_{10} horizontal axis.

wave patches, using distributions of observed wave amplitudes (Watt et al., 2019) and information about their spatial and temporal scales (Zhang et al., 2021a) as well as their distribution in L^* and relative to the plasmapause (Malaspina et al., 2016).

For other magnetospheric waves, such as whistler-mode chorus, it will be necessary to study the effects of averaging the wave-particle interactions over the bursty structure of chorus elements (Li et al., 2012), and over the temporal extent of chorus patches (Zhang et al., 2021b). For chorus, temporal variation is often very fast, again suggesting that arithmetic averages might be reasonable approximations, especially for constructing drift-averages. However, we reiterate the importance of determining how the *drift-averaged* diffusion coefficients vary in time, given what we know about chorus wave behaviour in time and space (Aryan et al., 2016; Agapitov et al., 2018; Shen et al., 2019; Zhang et al., 2021b). The temporal variation of drift-averaged quasilinear diffusion coefficients is currently a key unknown in our modelling efforts.

Note that in the 3 L^* cases we have studied, the average value of the diffusion coefficient at α_{LC} is ~ 10^{-8} s^{-1} at L^* = 2.5, ~ 10^{-6} s^{-1} at L^* = 3.0, and ~ 10^{-8} s^{-1} at L^* = 3.5. Our results suggest that there may be a relationship between average value of diffusion coefficient and the size of the uncertainty in numerical experiments given the Δt used, but we have yet to fully describe that relationship quantitatively. This is left for future work.

4.4 The importance of number density in wave-particle interactions

We turn finally to the ensemble experimental results that display some bifurcation for large Δt, namely those for L^* = 3.5 (see Figure 4). These ensembles are different from others at early times: most of the ensemble members show very little diffuson, whereas a minority display much more. To understand these differences, we analyse the $\mathcal{P}(D_{\alpha\alpha}(\alpha_{LC}))$ for each L^* bin. Empirical cumulative distribution functions (ECDFs) of the $D_{\alpha\alpha}(\alpha_{LC})$ are shown in Figure 9, colour-coded by L^* bin with blue (L^* = 2.5), orange (L^* = 3), and yellow (L^* = 3.5). The ECDFs at L^* = 2.5 and 3 have a smooth profile with gradually changing gradients, indicating that they could probably be accurately estimated by a single, smooth probability distribution function. The ECDF at L^* = 3.5 displays a sharp change in gradient at $D_{\alpha\alpha}(\alpha_{LC}) \simeq 2 \times 10^{-8}$ s^{-1}, indicating that there are perhaps two distributions of diffusion coefficients added together at L^* = 3.5. The first distribution, corresponding to lower ~ 95% of the diffusion coefficients has a median around $D_{\alpha\alpha}(\alpha_{LC}) \simeq 10^{-10}$ s^{-1}, and a similar variance (slope) to the ECDF for L^* = 3. However, the upper ~ 5% of diffusion coefficients is much larger than a smooth continuation of the first distribution would suggest.

The existence of multiple distributions of diffusion coefficients at L^* = 3.5 is a possible explanation for the behaviour of the ensemble of numerical solutions of $f(\alpha_{LC})$ in Figure 4. Let's consider the experiments with large Δt first. For early times in the ensemble (< 10 days), the majority of ensemble members with large Δt experience very little diffusion. This is likely because for the majority of scenarios in the ensemble, the time series of diffusion coefficients picked from $\mathcal{P}(D_{\alpha\alpha}(\alpha_{LC}))$ only includes diffusion coefficients from the lower ~ 95% of the distribution. This part of the distribution is much smaller than in other L^* bins. There are some scenarios, however, where diffusion coefficients from the upper ~ 5% of the distribution have been chosen, and these exhibit significantly more diffusion that the other scenarios in the ensemble. After ~ 10 days, it is likely that more scenarios experience a large diffusion coefficient from the upper ~ 5% of the distribution, and so they also experience increasing diffusion at this energy. For those experiments with small Δt, the entire distribution of $D_{\alpha\alpha}(\alpha_{LC})$ is rapidly sampled, and nearly all scenarios in the ensemble experience roughly the same diffusion.

The unexpectedly large values of $D_{\alpha\alpha}(\alpha)$ in the upper ~ 5% of the distribution can also be seen faintly in the top left of the L^* = 3.5 panel in Figure 1. It would appear that for a minority of cases, $D_{\alpha\alpha}(\alpha)$ is larger and has a much less pronounced gradient at low pitch-angles. To investigate the possible origins of the second distribution of large diffusion coefficients at L^* = 3.5, we investigate two of the parameters used as inputs to the diffusion coefficient calculation. Here we choose number density, which controls the resonance condition between the electrons and the waves, and the wave intensity itself. Note that in the original calculations of diffusion coefficients (Watt et al., 2019), the waves were assumed to have Gaussian dependence on frequency, with a peak at f = 252 Hz, and the wave intensity scales the size of the Gaussian spectra. We isolate a distribution of $D_{\alpha\alpha}(\alpha_{LC}) > 10^{-7}$ s^{-1}, and compare the inputs of those

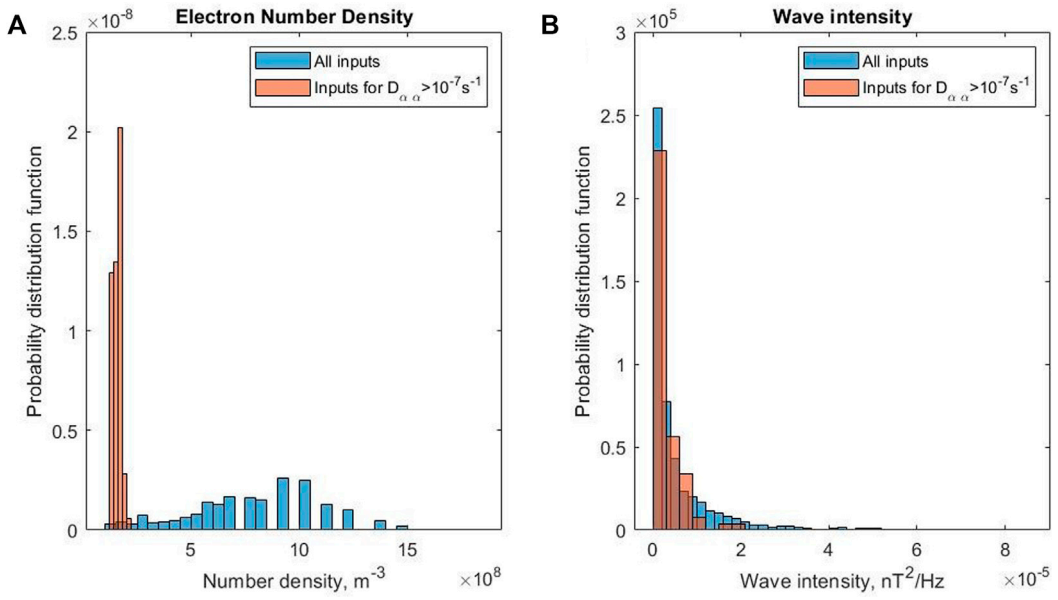

FIGURE 10
Probability distribution functions of **(A)** electron number density and **(B)** wave intensity inputs for calculation of $D_{\alpha\alpha}(\alpha)$ at $L^* = 3.5$. Blue bars show inputs for the entire collection of $D_{\alpha\alpha}(\alpha)$, orange bars indicate inputs for $D_{\alpha\alpha}(\alpha_{LC}) > 10^{-7}$ s^{-1}.

diffusion coefficient calculations to all the inputs used to construct the full distribution of $D_{\alpha\alpha}(\alpha_{LC})$ at $L^* = 3.5$. These results are shown in the form of histograms in Figure 10 with blue indicating all inputs and orange indicating the inputs for $D_{\alpha\alpha}(\alpha_{LC}) > 10^{-7}$ s^{-1}. The histograms are normalized so that the area of the bars adds to 1.

Figure 10A demonstrates that the number density inputs to the diffusion coefficient calculations for particularly high values of $D_{\alpha\alpha}(\alpha_{LC})$ are consistently the lowest values of the overall distribution of number density inputs. In our original diffusion coefficient study (Watt et al., 2019), we applied the Sheeley et al. (2001) number density criterion to identify observations inside and outside the plasmasphere. Although these measurements correspond to values close to that criterion, they are identified as inside the plasmasphere. Figure 10B shows the distribution of wave intensity for $D_{\alpha\alpha}(\alpha_{LC}) > 10^{-7}$ s^{-1} (orange) compared to all inputs at $L^* = 3.5$ (blue) For the wave intensity parameter, there is little difference in the distributions between the particularly large $D_{\alpha\alpha}(\alpha_{LC})$ and all the $D_{\alpha\alpha}(\alpha_{LC})$. We suggest that the origin of the two distributions in $D_{\alpha\alpha}$ is mostly related to the number density. This feature is only seen in the largest L^* bin used in the study, most likely because the other two are too far away from the more dynamic density region closer to the plasmapause.

We interpret these results to indicate the key importance of electron number density in the efficacy of scattering due to plasmaspheric hiss. The plasmapause is not always a sharp boundary and exhibits a lot of spatial and temporal structure (Moldwin et al., 1994; Moldwin et al., 2002), yet rare periods of relatively low density (that are likely near the plasmapause) are very important for wave-particle interactions with hiss as they can result in much higher than usual diffusion coefficients. The temporal and spatial variability for density may be different than that for wave amplitude which would complicate our suggested study of the temporal variability of drift-averaged diffusion coefficients. However, our study adds weight to the increasing evidence for the importance of number density in models of wave diffusion coefficients in Earth's radiation belts (Ripoll et al., 2016; Ripoll et al., 2020a; Ripoll et al., 2020b; Allison et al., 2021).

5 Conclusion

We use ensemble numerical experiments with diffusion coefficient models that are driven by individual Van Allen Probe observations in order to study the pitch-angle diffusion due to plasmaspheric hiss in Earth's magnetosphere. We demonstrate that ensemble solutions of the Fokker-Planck equation depend both upon the timescale of variability (varied between minutes and hours), and the shape of the distribution of diffusion coefficients. The median ensemble solutions vary slightly with timescale, but the inter-quartile range (or variance) of the ensemble solutions depends both upon the timescale and the strength of the diffusion coefficients; longer timescales, and larger average diffusion coefficients result in larger variance.

We use observed time and length scales of plasmaspheric hiss patches to identify suitable methods to construct appropriate

drift-averaged diffusion coefficients for high-energy drifting electrons. Arithmetic averaging of observation-specific diffusion coefficients is appropriate in many cases due to the small temporal and spatial scales of hiss patches, although arithmetic drift-averaging will become less accurate as the size of the diffusion coefficients increases. We argue that arithmetic averaging of observed inputs (e.g., wave amplitude, wave frequency spectrum, number density or background magnetic field strength) prior to constructing diffusion coefficients does not yield appropriate averaged values of the diffusion coefficient because there is a maximum useful averaging timescale that for many missions is shorter than the orbital period.

The distribution of observation-specific diffusion coefficients is found to vary with L^*. In two of the three chosen bins, the distribution of diffusion coefficients is a single probability distribution. In the remaining chosen location, which is at larger L^*, the probability distribution exhibits two different components, where rare but large values of the diffusion coefficient occur during periods of low number density. We argue that it is of vital importance to include accurate cold plasma models to radiation belt diffusion codes to improve the description of wave-particle interactions, especially during times when they are most effective.

Our results, along with others (Thompson et al., 2020; Watt et al., 2021), indicate the importance of understanding timescales of variation of wave-particle interactions throughout the outer radiation belt. Once these timescales are understood, numerical experiments similar to those reported here can be used to indicate where further parameterisation is necessary in order to reduce the uncertainty in our models. Due to the limited temporal and spatial sampling by spacecraft of localised waves and plasma properties in the outer radiation belt, some kind of model will always be required to monitor the evolution of drift-averaged quasilinear diffusion coefficients in Earth's magnetosphere. In this paper we have endeavoured to motivate further important work in this area.

Data availability statement

The datasets presented in this study can be found in online repositories. The names of the repository/repositories and accession number(s) can be found below: https://emfisis.physics.uiowa.edu/data/index; https://doi.org/10.17864/1947.212, Ensemble experiment data can be found at https://doi.org/10.25398/rd.northumbria.2126623.

Author contributions

CW and HA conceived the numerical experiments, in consultation with SB and RT. HA wrote numerical software and performed the numerical experiments. CW analyzed and visualized the results of the numerical experiments, and constructed all Figures. NM curated the Van Allen Probe data necessary to construct the observation-specific diffusion coefficients. SG provided the PADIE software necessary to construct the diffusion coefficients and advised on its use. SZ contributed key analysis of Van Allen Probe data enabling CW to construct Figures 7, 8. DR and SK wrote software necessary for discussion in Section 4.3. IR, OA, SG, JR, RH, NM, and KM provided interpretation of the ensemble numerical experiment results and discussion points. CW wrote the first draft of the manuscript. All authors contributed to editing the manuscript before submission.

Funding

This work was enabled by collaborations supported by the Natural Environment Research Council (NERC) Highlight Topic consortium "Rad-Sat," and the Space Weather Instrumentation, Measurement, Modelling and Risk (SWIMMR) Strategic Priorities Fund consortium "Sat-Risk." Individual grant numbers are noted below. CW is supported by Science and Technology Facilities Council (STFC) grant ST/W000369/1 and Natural Environment Research Council (NERC) grants NE/P017274/1 (Rad-Sat) and NE/V002759/2 (Sat-Risk). HA is supported by an Alexander von Humboldt Postdoctoral Research Fellowship. IR acknowledges support from STFC grant ST/V006320/1 and NERC grants NE/P017185/1 (Rad-Sat) and NE/V002554/2 (Sat-Risk). NM, RH, SG, and JR would like to acknowledge financial support from the NERC Highlight Topic grant NE/P01738X/1 (Rad-Sat) and the NERC grants NE/V00249X/1 (Sat-Risk) and NE/R016038/1. OA acknowledges financial support from the University of Exeter and from the United Kingdom Natural Environment Research Council (NERC) Independent Research Fellowship NE/V013963/1, as well as NE/P017274/1 (Rad-Sat).

Acknowledgments

The authors acknowledge the NASA Van Allen Probes EMFISIS team led by Craig Kletzing at the University of Iowa for the successful build and operation of the high-quality science instruments onboard both probes. The CDAWeb team at GSFC/SPDF are also gratefully acknowledged.

Conflict of interest

The authors declare that the research was conducted in the absence of any commercial or financial relationships that could be construed as a potential conflict of interest.

Publisher's note

References

Agapitov, O., Mourenas, D., Artemyev, A., Mozer, F. S., Bonnell, J. W., Angelopoulos, V., et al. (2018). Spatial extent and temporal correlation of chorus and hiss: Statistical results from multipoint THEMIS observations. *JGR. Space Phys.* 123, 8317–8330. doi:10.1029/2018JA025725

Albert, J. M., Meredith, N. P., and Horne, R. B. (2009). Three-dimensional diffusion simulation of outer radiation belt electrons during the 9 October 1990 magnetic storm. *J. Geophys. Res.* 114. doi:10.1029/2009JA014336

Allanson, O., Elsden, T., Watt, C., and Neukirch, T. (2022). Weak turbulence and quasilinear diffusion for relativistic wave-particle interactions via a markov approach. *Front. Astron. Space Sci.* 8. doi:10.3389/fspas.2021.805699

Allanson, O., Watt, C. E. J., Ratcliffe, H., Allison, H. J., Meredith, N. P., Bentley, S. N., et al. (2020). Particle-in-cell experiments examine electron diffusion by whistler-mode waves: 2. Quasi-linear and nonlinear dynamics. *J. Geophys. Res. Space Phys.* 125, e2020JA027949. doi:10.1029/2020JA027949

Allanson, O., Watt, C. E. J., Ratcliffe, H., Meredith, N. P., Allison, H. J., Bentley, S. N., et al. (2019). Particle-in-cell experiments examine electron diffusion by whistler-mode waves: 1. Benchmarking with a cold plasma. *J. Geophys. Res. Space Phys.* 124, 8893–8912. doi:10.1029/2019JA027088

Allison, H. J., and Shprits, Y. Y. (2020). Local heating of radiation belt electrons to ultra-relativistic energies. *Nat. Commun.* 11, 4533. doi:10.1038/s41467-020-18053-z

Allison, H. J., Shprits, Y. Y., Zhelavskaya, I. S., Wang, D., and Smirnov, A. G. (2021). Gyroresonant wave-particle interactions with chorus waves during extreme depletions of plasma density in the van allen radiation belts. *Sci. Adv.* 7, eabc0380. doi:10.1126/sciadv.abc0380

Anderson, B. J., Erlandson, R. E., and Zanetti, L. J. (1992). A statistical study of pc 1–2 magnetic pulsations in the equatorial magnetosphere: 1. Equatorial occurrence distributions. *J. Geophys. Res.* 97, 3075–3088. doi:10.1029/91JA02706

Aryan, H., Bortnik, J., Meredith, N. P., Horne, R. B., Sibeck, D. G., and Balikhin, M. A. (2021). Multi-parameter chorus and plasmaspheric hiss wave models. *JGR. Space Phys.* 126, e2020JA028403. doi:10.1029/2020JA028403

Aryan, H., Sibeck, D., Balikhin, M., Agapitov, O., and Kletzing, C. (2016). Observation of chorus waves by the van allen probes: Dependence on solar wind parameters and scale size. *J. Geophys. Res. Space Phys.* 121, 7608–7621. doi:10.1002/2016JA022775

Bentley, S. N., Stout, J. R., Bloch, T. E., and Watt, C. E. J. (2020). Random forest model of ultralow-frequency magnetospheric wave power. *Earth Space Sci.* 7, e2020EA001274. doi:10.1029/2020EA001274

Bentley, S. N., Watt, C. E. J., Owens, M. J., and Rae, I. J. (2018). Ulf wave activity in the magnetosphere: Resolving solar wind interdependencies to identify driving mechanisms. *J. Geophys. Res. Space Phys.* 123, 2745–2771. doi:10.1002/2017JA024740

Bentley, S. N., Watt, C. E. J., Rae, I. J., Owens, M. J., Murphy, K., Lockwood, M., et al. (2019). Capturing uncertainty in magnetospheric ultralow frequency wave models. *Space weather.* 17, 599–618. doi:10.1029/2018SW002102

Cervantes, S., Shprits, Y. Y., Aseev, N. A., Drozdov, A. Y., Castillo, A., and Stolle, C. (2020). Identifying radiation belt electron source and loss processes by assimilating spacecraft data in a three-dimensional diffusion model. *JGR. Space Phys.* 125, e2019JA027514. doi:10.1029/2019JA027514

Drummond, W., and Pines, D. (1962). Nonlinear stability of plasma oscillations. *Nucl. Fusion Suppl. Pt* 2, 465.

Fei, Y., Chan, A. A., Elkington, S. R., and Wiltberger, M. J. (2006). Radial diffusion and mhd particle simulations of relativistic electron transport by ulf waves in the september 1998 storm. *J. Geophys. Res.* 111, A12209. doi:10.1029/2005JA011211

Glauert, S. A., and Horne, R. B. (2005). Calculation of pitch angle and energy diffusion coefficients with the padie code. *J. Geophys. Res.* 110. doi:10.1029/2004JA010851

Glauert, S. A., Horne, R. B., and Meredith, N. P. (2014). Three-dimensional electron radiation belt simulations using the BAS Radiation Belt Model with new diffusion models for chorus, plasmaspheric hiss, and lightning-generated whistlers. *J. Geophys. Res. Space Phys.* 119, 268–289. doi:10.1002/2013JA019281

Green, A., Li, W., Ma, Q., Shen, X. C., Bortnik, J., and Hospodarsky, G. B. (2020). Properties of lightning generated whistlers based on van allen probes observations and their global effects on radiation belt electron loss. *Geophys. Res. Lett.* 47, e2020GL089584. doi:10.1029/2020GL089584

Halford, A. J., Fraser, B. J., and Morley, S. K. (2010). Emic wave activity during geomagnetic storm and nonstorm periods: Crres results. *J. Geophys. Res.* 115. doi:10.1029/2010JA015716

Hikishima, M., and Omura, Y. (2012). Particle simulations of whistler-mode rising-tone emissions triggered by waves with different amplitudes. *J. Geophys. Res.* 117. doi:10.1029/2011JA017428

Horne, R. B., Kersten, T., Glauert, S. A., Meredith, N. P., Boscher, D., Sicard-Piet, A., et al. (2013). A new diffusion matrix for whistler mode chorus waves. *J. Geophys. Res. Space Phys.* 118, 6302–6318. doi:10.1002/jgra.50594

Horne, R. B., and Thorne, R. M. (2003). Relativistic electron acceleration and precipitation during resonant interactions with whistler-mode chorus. *Geophys. Res. Lett.* 30. doi:10.1029/2003GL016973

Horne, R. B., Thorne, R. M., Shprits, Y. Y., Meredith, N. M., Glauert, S. A., Smith, A. J., et al. (2005). Wave acceleration of electrons in the Van Allen radiation belts. *Nature* 437, 227–230. doi:10.1038/nature03939

Kennel, C. F., and Engelmann, F. (1966). Velocity space diffusion from weak plasma turbulence in a magnetic field. *Phys. Fluids* 9, 2377–2388. doi:10.1063/1.1761629

Kim, K. C., and Shprits, Y. (2019). Statistical analysis of hiss waves in plasmaspheric plumes using van allen probe observations. *J. Geophys. Res. Space Phys.* 124, 1904–1915. doi:10.1029/2018JA026458

Kim, K. C., Shprits, Y., and Wang, D. (2020). Quantifying the effect of plasmaspheric hiss on the electron loss from the slot region. *J. Geophys. Res. Space Phys.* 125, e2019JA027555. doi:10.1029/2019JA027555

Kletzing, C. A., Kurth, W. S., Acuna, M., MacDowall, R. J., Torbert, R. B., Averkamp, T., et al. (2013). The electric and magnetic field instrument suite and integrated science (emfisis) on rbsp. *Space Sci. Rev.* 179, 127–181. doi:10.1007/s11214-013-9993-6

Lemons, D. S. (2012). Pitch angle scattering of relativistic electrons from stationary magnetic waves: Continuous markov process and quasilinear theory. *Phys. Plasmas* 19, 012306. doi:10.1063/1.3676156

Li, J., Bortnik, J., An, X., Li, W., Angelopoulos, V., Thorne, R. M., et al. (2019). Origin of two-band chorus in the radiation belt of Earth. *Nat. Commun.* 10, 4672. doi:10.1038/s41467-019-12561-3

Li, W., Ma, Q., Thorne, R. M., Bortnik, J., Kletzing, C. A., Kurth, W. S., et al. (2015). Statistical properties of plasmaspheric hiss derived from Van Allen Probes data and their effects on radiation belt electron dynamics. *JGR. Space Phys.* 120, 3393–3405. doi:10.1002/2015JA021048

Li, W., Ma, Q., Thorne, R. M., Bortnik, J., Zhang, X. J., Li, J., et al. (2016). Radiation belt electron acceleration during the 17 march 2015 geomagnetic storm: Observations and simulations. *JGR. Space Phys.* 121, 5520–5536. doi:10.1002/2016JA022400

Li, W., Thorne, R. M., Angelopoulos, V., Bortnik, J., Cully, C. M., Ni, B., et al. (2009). Global distribution of whistler-mode chorus waves observed on the themis spacecraft. *Geophys. Res. Lett.* 36, L09104. doi:10.1029/2009GL037595

Li, W., Thorne, R. M., Bortnik, J., Tao, X., and Angelopoulos, V. (2012). Characteristics of hiss-like and discrete whistler-mode emissions. *Geophys. Res. Lett.* 39. doi:10.1029/2012GL053206

Liu, K., Winske, D., Gary, S. P., and Reeves, G. D. (2012). Relativistic electron scattering by large amplitude electromagnetic ion cyclotron waves: The role of phase bunching and trapping. *J. Geophys. Res.* 117. doi:10.1029/2011JA017476

Loridan, V., Ripoll, J. F., Tu, W., and Scott Cunningham, G. (2019). On the use of different magnetic field models for simulating the dynamics of the outer radiation belt electrons during the october 1990 storm. *J. Geophys. Res. Space Phys.* 124, 6453–6486. doi:10.1029/2018JA026392

Lyons, L. R. (1974). Pitch angle and energy diffusion coefficients from resonant interactions with ion–cyclotron and whistler waves. *J. Plasma Phys.* 12, 417–432. doi:10.1017/S002237780002537X

Lyons, L. R., Thorne, R. M., and Kennel, C. F. (1972). Pitch-angle diffusion of radiation belt electrons within the plasmasphere. *J. Geophys. Res.* 77, 3455–3474. doi:10.1029/JA077i019p03455

Ma, Q., Li, W., Bortnik, J., Thorne, R. M., Chu, X., Ozeke, L. G., et al. (2018). Quantitative evaluation of radial diffusion and local acceleration processes during gem challenge events. *JGR. Space Phys.* 123, 1938–1952. doi:10.1002/2017JA025114

Ma, Q., Mourenas, D., Li, W., Artemyev, A., and Thorne, R. M. (2017). Vlf waves from ground-based transmitters observed by the van allen probes: Statistical model and effects on plasmaspheric electrons. *Geophys. Res. Lett.* 44, 6483–6491. doi:10.1002/2017GL073885

Malaspina, D. M., Jaynes, A. N., Boulé, C., Bortnik, J., Thaller, S. A., Ergun, R. E., et al. (2016). The distribution of plasmaspheric hiss wave power with respect to plasmapause location. *Geophys. Res. Lett.* 43, 7878–7886. doi:10.1002/2016GL069982

Mann, I. R., Ozeke, L. G., Murphy, K. R., Claudepierre, S. G., Turner, D. L., Baker, D. N., et al. (2016). Explaining the dynamics of the ultra-relativistic third Van Allen radiation belt. *Nat. Phys.* 12, 978–983. doi:10.1038/nphys3799

Mauk, B. H., Fox, N. J., Kanekal, S. G., Kessel, R. L., Sibeck, D. G., and Ukhorskiy, A. (2013). Science objectives and rationale for the radiation belt storm probes mission. *Space Sci. Rev.* 179, 3–27. doi:10.1007/s11214-012-9908-y

Meredith, N. P., Horne, R. B., Clilverd, M. A., and Ross, J. P. J. (2019). An investigation of vlf transmitter wave power in the inner radiation belt and slot region. *JGR. Space Phys.* 124, 5246–5259. doi:10.1029/2019JA026715

Meredith, N. P., Horne, R. B., Kersten, T., Fraser, B. J., and Grew, R. S. (2014). Global morphology and spectral properties of emic waves derived from crres observations. *J. Geophys. Res. Space Phys.* 119, 5328–5342. doi:10.1002/2014JA020064

Meredith, N. P., Horne, R. B., Kersten, T., Li, W., Bortnik, J., Sicard, A., et al. (2018). Global model of plasmaspheric hiss from multiple satellite observations. *JGR. Space Phys.* 123, 4526–4541. doi:10.1029/2018JA025226

Meredith, N. P., Horne, R. B., Shen, X. C., Li, W., and Bortnik, J. (2020). Global model of whistler mode chorus in the near-equatorial region ($\|\lambda_m\| < 18^\circ$). *Geophys. Res. Lett.* 47, e2020GL087311. doi:10.1029/2020GL087311

Millan, R. M., Ripoll, J. F., Santolík, O., and Kurth, W. S. (2021). Early-time non-equilibrium pitch angle diffusion of electrons by whistler-mode hiss in a plasmaspheric plume associated with barrel precipitation. *Front. Astron. Space Sci.* 8. doi:10.3389/fspas.2021.776992

Moldwin, M. B., Downward, L., Rassoul, H. K., Amin, R., and Anderson, R. R. (2002). A new model of the location of the plasmapause: Crres results. *J. Geophys. Res.* 107, SMP 2–1–SMP 2–9. doi:10.1029/2001JA009211

Moldwin, M. B., Thomsen, M. F., Bame, S. J., McComas, D. J., and Moore, K. R. (1994). An examination of the structure and dynamics of the outer plasmasphere using multiple geosynchronous satellites. *J. Geophys. Res.* 99, 11475–11481. doi:10.1029/93JA03526

Ni, B., Bortnik, J., Thorne, R. M., Ma, Q., and Chen, L. (2013). Resonant scattering and resultant pitch angle evolution of relativistic electrons by plasmaspheric hiss. *JGR. Space Phys.* 118, 7740–7751. doi:10.1002/2013JA019260

Ni, B., Thorne, R. M., Shprits, Y. Y., and Bortnik, J. (2008). Resonant scattering of plasma sheet electrons by whistler-mode chorus: Contribution to diffuse auroral precipitation. *Geophys. Res. Lett.* 35, L11106. doi:10.1029/2008GL034032

Pierrard, V., Ripoll, J. F., Cunningham, G., Botek, E., Santolik, O., Thaller, S., et al. (2021). Observations and simulations of dropout events and flux decays in October 2013: Comparing MEO equatorial with LEO polar orbit. *JGR. Space Phys.* 126, e2020JA028850. doi:10.1029/2020JA028850

Ratcliffe, H., and Watt, C. E. J. (2017). Self-consistent formation of a 0.5 cyclotron frequency gap in magnetospheric whistler mode waves. *J. Geophys. Res. Space Phys.* 122, 8166–8180. doi:10.1002/2017JA024399

Réveillé, T., Bertrand, P., Ghizzo, A., Simonet, F., and Baussart, N. (2001). Dynamic evolution of relativistic electrons in the radiation belts. *J. Geophys. Res.* 106, 18883–18894. doi:10.1029/2000JA900177

Ripoll, J. F., Claudepierre, S. G., Ukhorskiy, A. Y., Colpitts, C., Li, X., Fennell, J. F., et al. (2020b). Particle dynamics in the Earth's radiation belts: Review of current research and open questions. *J. Geophys. Res. Space Phys.* 125, e2019JA026735. doi:10.1029/2019JA026735

Ripoll, J. F., Denton, M., Loridan, V., Santolik, O., Malaspina, D., Hartley, D. P., et al. (2020a). How whistler mode hiss waves and the plasmasphere drive the quiet decay of radiation belts electrons following a geomagnetic storm. *J. Phys. Conf. Ser.* 1623, 012005. doi:10.1088/1742-6596/1623/1/012005

Ripoll, J. F., and Mourenas, D. (2012). *High-energy electron diffusion by resonant interactions with whistler mode hiss*. Washington, DC: American Geophysical Union, 281–290. doi:10.1029/2012GM001309

Ripoll, J. F., Reeves, G. D., Cunningham, G. S., Loridan, V., Denton, M., Santolík, O., et al. (2016). Reproducing the observed energy-dependent structure of Earth's electron radiation belts during storm recovery with an event-specific diffusion model. *Geophys. Res. Lett.* 43, 5616–5625. doi:10.1002/2016GL068869

Ross, J. P. J., Glauert, S. A., Horne, R. B., Watt, C. E. J., and Meredith, N. P. (2021). On the variability of emic waves and the consequences for the relativistic electron radiation belt population. *JGR. Space Phys.* 126, e2021JA029754. doi:10.1029/2021JA029754

Ross, J. P. J., Glauert, S. A., Horne, R. B., Watt, C. E. J., Meredith, N. P., and Woodfield, E. E. (2020). A new approach to constructing models of electron diffusion by emic waves in the radiation belts. *Geophys. Res. Lett.* 47, e2020GL088976. **n/a**. doi:10.1029/2020GL088976

Ross, J. P. J., Meredith, N. P., Glauert, S. A., Horne, R. B., and Clilverd, M. A. (2019). Effects of vlf transmitter waves on the inner belt and slot region. *JGR. Space Phys.* 124, 5260–5277. doi:10.1029/2019JA026716

Sandhu, J. K., Rae, I. J., Wygant, J. R., Breneman, A. W., Tian, S., Watt, C. E. J., et al. (2021). ULF wave driven radial diffusion during geomagnetic storms: A statistical analysis of van allen probes observations. *JGR. Space Phys.* 126, e2020JA029024. doi:10.1029/2020JA029024

Santolík, O., Gurnett, D. A., Pickett, J. S., Grimald, S., Décreau, P. M. E., Parrot, M., et al. (2010). Wave-particle interactions in the equatorial source region of whistler-mode emissions. *J. Geophys. Res.* 115. doi:10.1029/2009JA015218

Santolík, O., and Gurnett, D. A. (2003). Transverse dimensions of chorus in the source region. *Geophys. Res. Lett.* 30. doi:10.1029/2002GL016178

Selesnick, R. S., Blake, J. B., and Mewaldt, R. A. (2003). Atmospheric losses of radiation belt electrons. *J. Geophys. Res.* 108, 1468. doi:10.1029/2003JA010160

Sheeley, B. W., Moldwin, M. B., Rassoul, H. K., and Anderson, R. R. (2001). An empirical plasmasphere and trough density model: Crres observations. *J. Geophys. Res.* 106, 25631–25641. doi:10.1029/2000JA000286

Shen, X. C., Li, W., Ma, Q., Agapitov, O., and Nishimura, Y. (2019). Statistical analysis of transverse size of lower band chorus waves using simultaneous multisatellite observations. *Geophys. Res. Lett.* 46, 5725–5734. doi:10.1029/2019GL083118

Shprits, Y. Y., Horne, R. B., Kellerman, A. C., and Drozdov, A. Y. (2018). The dynamics of van allen belts revisited. *Nat. Phys.* 14, 102–103. doi:10.1038/nphys4350

Shprits, Y. Y., Subbotin, D. A., Meredith, N. P., and Elkington, S. R. (2008). Review of modeling of losses and sources of relativistic electrons in the outer radiation belt ii: Local acceleration and loss. *J. Atmos. Sol. Terr. Phys.* 70, 1694–1713. Dynamic Variability of Earth's Radiation Belts. doi:10.1016/j.jastp.2008.06.014

Sicard-Piet, A., Boscher, D., Horne, R. B., Meredith, N. P., and Maget, V. (2014). Effect of plasma density on diffusion rates due to wave particle interactions with chorus and plasmaspheric hiss: Extreme event analysis. *Ann. Geophys.* 32, 1059–1071. doi:10.5194/angeo-32-1059-2014

Su, Z., Zhu, H., Xiao, F., Zong, Q. G., Zhou, X. Z., Zheng, H., et al. (2015). Ultra-low-frequency wave-driven diffusion of radiation belt relativistic electrons. *Nat. Commun.* 6, 10096. doi:10.1038/ncomms10096

Thompson, R. L., Morley, S. K., Watt, C. E. J., Bentley, S. N., and Williams, P. D. (2021). Pro-l* - a probabilistic l* mapping tool for ground observations. *Space weather.* 19, e2020SW002602. doi:10.1029/2020SW002602

Thompson, R. L., Watt, C. E. J., and Williams, P. D. (2020). Accounting for variability in ULF wave radial diffusion models. *J. Geophys. Res. Space Phys.* 125, e2019JA027254. doi:10.1029/2019JA027254

Thorne, R. M., Li, W., Ni, B., Ma, Q., Bortnik, J., Chen, L., et al. (2013). Rapid local acceleration of relativistic radiation-belt electrons by magnetospheric chorus. *Nature* 504, 411–414. doi:10.1038/nature12889

Tsurutani, B. T., and Smith, E. J. (1977). Two types of magnetospheric ELF chorus and their substorm dependences. *J. Geophys. Res.* 82, 5112–5128. doi:10.1029/JA082i032p05112

Tu, W., Cunningham, G. S., Chen, Y., Henderson, M. G., Camporeale, E., and Reeves, G. D. (2013). Modeling radiation belt electron dynamics during GEM challenge intervals with the DREAM3D diffusion model. *J. Geophys. Res. Space Phys.* 118, 6197–6211. doi:10.1002/jgra.50560

Tu, W., Cunningham, G. S., Chen, Y., Morley, S. K., Reeves, G. D., Blake, J. B., et al. (2014). Event-specific chorus wave and electron seed population models in DREAM3D using the van allen probes. *Geophys. Res. Lett.* 41, 1359–1366. doi:10.1002/2013GL058819

Usanova, M. E., Mann, I. R., Bortnik, J., Shao, L., and Angelopoulos, V. (2012). Themis observations of electromagnetic ion cyclotron wave occurrence: Dependence on ae, symh, and solar wind dynamic pressure. *J. Geophys. Res.* 117. doi:10.1029/2012JA018049

Wang, C., Ma, Q., Tao, X., Zhang, Y., Teng, S., Albert, J. M., et al. (2017). Modeling radiation belt dynamics using a 3-d layer method code. *J. Geophys. Res. Space Phys.* 122, 8642–8658. doi:10.1002/2017JA024143

Watt, C. E. J., Allison, H. J., Meredith, N. P., Thompson, R. L., Bentley, S. N., Rae, I. J., et al. (2019). Variability of quasilinear diffusion coefficients for plasmaspheric hiss. *J. Geophys. Res. Space Phys.* 124, 8488–8506. doi:10.1029/2018ja026401

Watt, C. E. J., Allison, H. J., Thompson, R. L., Bentley, S. N., Meredith, N. P., Glauert, S. A., et al. (2021). The implications of temporal variability in wave-particle interactions in Earth's radiation belts. *Geophys. Res. Lett.* 48, e2020GL089962. E2020GL089962 2020GL089962. doi:10.1029/2020GL089962

Watt, C. E. J., Rae, I. J., Murphy, K. R., Anekallu, C., Bentley, S. N., and Forsyth, C. (2017). The parameterization of wave-particle interactions in the Outer Radiation Belt. *J. Geophys. Res. Space Phys.* 122, 9545–9551. doi:10.1002/2017JA024339

Zhang, S., Rae, I. J., Watt, C. E. J., Degeling, A. W., Tian, A., Shi, Q., et al. (2021b). Determining the global scale size of chorus waves in the magnetosphere. *JGR. Space Phys.* 126, e2021JA029569. doi:10.1029/2021JA029569

Zhang, S., Rae, I. J., Watt, C. E. J., Degeling, A. W., Tian, A., Shi, Q., et al. (2021a). Determining the temporal and spatial coherence of plasmaspheric hiss waves in the magnetosphere. *J. Geophys. Res. Space Phys.* 126, e2020JA028635. doi:10.1029/2020JA028635

Zhao, H., Friedel, R. H. W., Chen, Y., Reeves, G. D., Baker, D. N., Li, X., et al. (2018). An empirical model of radiation belt electron pitch angle distributions based on van allen probes measurements. *JGR. Space Phys.* 123, 3493–3511. doi:10.1029/2018JA025277

Zhao, J., Lee, L., Xie, H., Yao, Y., Wu, D., Voitenko, Y., et al. (2022). Quantifying wave–particle interactions in collisionless plasmas: Theory and its application to the alfvén-mode wave. *Astrophys. J.* 930, 95. doi:10.3847/1538-4357/ac59b7

Zhu, H., Shprits, Y. Y., Spasojevic, M., and Drozdov, A. Y. (2019). New hiss and chorus waves diffusion coefficient parameterizations from the van allen probes and their effect on long-term relativistic electron radiation-belt verb simulations. *J. Atmos. Solar-Terrestrial Phys.* 193, 105090. doi:10.1016/j.jastp.2019.105090

frontiers | Frontiers in Astronomy and Space Sciences

TYPE Original Research
PUBLISHED 19 October 2022
DOI 10.3389/fspas.2022.987913

OPEN ACCESS

EDITED BY
Yoshiharu Omura,
Kyoto University, Japan

REVIEWED BY
Qiugang Zong,
Peking University, China
Alla V. Suvorova,
National Central University, Taiwan

*CORRESPONDENCE
Sanni Hoilijoki,
sanni.hoilijoki@helsinki.fi

SPECIALTY SECTION
This article was submitted to Space Physics,
a section of the journal
Frontiers in Astronomy and Space Sciences

RECEIVED 06 July 2022
ACCEPTED 16 September 2022
PUBLISHED 19 October 2022

CITATION
Hoilijoki S, Kilpua EKJ, Osmane A, Kalliokoski MMH, George H, Savola M and Asikainen T (2022), Using mutual information to investigate non-linear correlation between AE index, ULF Pc5 wave activity and electron precipitation.
Front. Astron. Space Sci. 9:987913.
doi: 10.3389/fspas.2022.987913

Using mutual information to investigate non-linear correlation between AE index, ULF Pc5 wave activity and electron precipitation

Sanni Hoilijoki[1]*, Emilia K. J. Kilpua[1], Adnane Osmane[1], Milla M. H. Kalliokoski[1], Harriet George[1], Mikko Savola[1] and Timo Asikainen[2]

[1]Department of Physics, University of Helsinki, Helsinki, Finland, [2]Department of Physics, University of Oulu, Oulu, Finland

In this study, we use mutual information from information theory to investigate non-linear correlation between geomagnetic activity indicated by auroral electrojet (AE) index with both the global ultra low frequency (ULF) Pc5 wave power and medium energy (≥30 keV) electron precipitation at the central outer radiation belt. To investigate the energy and magnetic local time (MLT) dependence of the non-linearity, we calculate the mutual information and Pearson correlation coefficient separately for three different energy ranges (30–100 keV, 100–300 keV and ≥300 keV) and four different MLT sectors (0–6, 6–12, 12–18, 18–24). We compare results from 2 years 2004 and 2007 representing geomagnetically more active and less active years, respectively. The correlation analysis between the AE index and electron precipitation shows a clear MLT and energy dependence in both active and quiet conditions. In the two lowest energy ranges of the medium energy electrons (30–100 keV and 100–300 keV) both non-linear correlation and Pearson correlation indicate strong dependence with the AE index in the dawn sector. The linear dependence indicated by the Pearson correlation coefficient decreases from dawn to dusk while the change in the non-linear correlation is smaller indicating an increase in the non-linearity from dawn to dusk. The non-linearity between the AE index and electron precipitation is larger at all MLT sectors except MLTs 6–12 during geomagnetically more active year when larger amount of the activity is driven by interplanetary coronal mass ejections (ICMEs) compared to lower activity year with high speed stream (HSS) and stream interaction region (SIR) driven activity. These results indicate that the processes leading to electron precipitation become more non-linear in the dusk and during geomagnetically more active times when the activity is driven by ICMEs. The non-linearity between the AE index and global ULF Pc5 activity is relatively low and seems not to be affected by the difference in the geomagnetic activity during the 2 years studied.

KEYWORDS

radiation belts, electron precipitation, ULF wave activity, wave-particle interaction, information theory, mutual information

1 Introduction

Earth's radiation belts (e.g., Van Allen, 1981; Li and Hudson, 2019) are occupied by energetic electrons and ions that are trapped in the geomagnetic field. The outer radiation belt above L $\gtrsim$ 3 consists mostly of energetic electrons from a few hundred keVs up to ultra-relativistic energies. The behavior of energetic electrons is affected by multiple different waves modes that are present in the inner magnetosphere (e.g., Baker et al., 2019). The main source of the medium energy electrons (tens to hundreds of keVs) are injections from the Earth's magnetotail during substorms (e.g., Jaynes et al., 2015a). The substorm activity in the magnetotail is captured well by the auroral electrojet (AE) index (e.g., Newell and Gjerloev, 2011). AE index measures the total electrojet activity at the auroral latitudes. It is calculated from magnetometer stations located under the auroral oval as a difference between the AU and AL indices (AE = AU-AL), which are measures of the maximum magnetic field perturbation caused by the strongest eastward and westward currents of the auroral oval, respectively (Davis and Sugiura, 1966). AE index below 300 nT indicates quiet time conditions, during medium activity AE index is 300–1500 nT and AE index increases over 1500 nT during intense AE activity. In a recent statistical study, Nesse Tyssøy et al. (2021) demonstrated that AE index is a good proxy for the precipitation of the medium energy electrons ($\geq$ 30 keV).

Whistler-mode chorus waves have been found to act as both loss and acceleration mechanism of the radiation belt electrons (e.g., Kennel and Petschek, 1966; Reeves et al., 2003; Thorne et al., 2013; Artemyev et al., 2014; Li et al., 2014). Chorus waves are driven by the anisotropic distribution function of the electrons injected from the plasma sheet during a substorm process and they are mainly observed on dawn side from midnight to noon (e.g., Meredith et al., 2020). They are right-hand polarized waves that are observed usually in two frequency bands: lower-band chorus waves with frequencies 0.1–0.5 f_{ce} and upper-band chorus waves with frequencies 0.5–0.8 f_{ce}, where f_{ce} is the equatorial electron cyclotron frequency. The cyclotron resonant interactions between the radiation belt electrons and the chorus waves may progressively accelerate lower energy electrons to high energies up to MeVs (e.g., Jaynes et al., 2015b). The chorus wave generation, growth and subsequent wave-particle interactions can also scatter electrons of keVs to hundreds of keVs into the loss cone causing them to precipitate to the upper atmosphere causing both the diffuse (e.g. Thorne et al., 2010; Ni et al., 2016) and pulsating (Nishimura et al., 2010; Kasahara et al., 2018) aurora. Lam et al. (2010) conducted a correlation analysis between the precipitating > 30 keV electron fluxes and bounce averaged pitch angle diffusion coefficients for lower-band chorus during strong geomagnetic activity (AE > 300 nT). They found high linear Pearson correlation coefficients (> 0.8) at morning hours and at larger L-shells (L > 5.1). The upper-band chorus waves have been found to cause the resonant scattering of < 5 keV electrons whereas for higher energy electrons (30–100 keV) the lower-band chorus waves are the dominant scattering process especially near the edge of the loss cone (e.g., Ni et al., 2008).

The electron population in the outer radiation belt is also affected by ultra low frequency (ULF) waves in the Pc4 (6.7–22 mHz corresponding to period of 45–150 s) and Pc5 (1.7–6.7 mHz corresponding to period of 150–600 s) range (e.g., Elkington et al., 2003; Shprits et al., 2008; Mann et al., 2013, 2016; Zong et al., 2017). These waves can be generated externally by the solar wind-magnetosphere interactions (e.g., Kepko and Spence, 2003; Rae et al., 2005; Claudepierre et al., 2008, 2010; Zhang et al., 2010; Hwang and Sibeck, 2016; Wang et al., 2017) or internally by the drift-bounce resonance, which can be driven by ions injected from the magnetotail during substorms (e.g. Chen and Hasegawa, 1991; Zolotukhina et al., 2008; James et al., 2016; Yamakawa et al., 2019). Pc5 ULF waves can be divided to toroidal and poloidal modes (or combinations of both modes), based on the direction of magnetic field fluctuations. Magnetic field fluctuations of the toroidal mode oscillate in the azimuthal direction and poloidal mode is observed in the radial magnetic field component (Hudson et al., 2004). The toroidal ULF mode can reach the ground magnetometers but the poloidal mode can only be observed from the spacecraft observations (Shi et al., 2018). ULF waves can accelerate radiation belt electrons *via* drift resonance causing radial diffusion (e.g., Elkington et al., 1999; Elkington et al., 2003) and can increase the energetic electron flux up to an order of magnitude (Su et al., 2015).

Previous studies have demonstrated that the statistical dependence between the solar wind and the radiation belts and their electrons in the inner magnetosphere can be non-linear in nature (e.g., Reeves et al., 2011; Kellerman and Shprits, 2012; Wing et al., 2016, 2021; Simms et al., 2021). For example, the combined simultaneous or subsequent interaction of different wave modes with the radiation belt electrons can be non-linear (Simms et al., 2018, 2021). However, commonly used Pearson correlation coefficient only measures the linear dependencies and does not unveil the possible non-linear correlations. Information theory techniques such as mutual information can be used to reveal non-linear dependencies (e.g. Johnson and Wing, 2005; Wing et al., 2016; Cameron et al., 2019; Wing et al., 2021; Osmane et al., 2022). These techniques have been previously used in space plasma physics to study e.g., geoeffectiveness of solar wind shocks with different front orientations (Cameron et al., 2019), solar wind drivers of radiation belt electron fluxes (Wing et al., 2016, 2021) and how geostationary seed and relativistic electron fluxes correlate with the ULF waves (Osmane et al., 2022).

In this paper, we utilize mutual information from information theory to quantify the non-linear correlation coefficient and compare it with the linear Pearson correlation coefficient between substorm activity indicated by the AE index

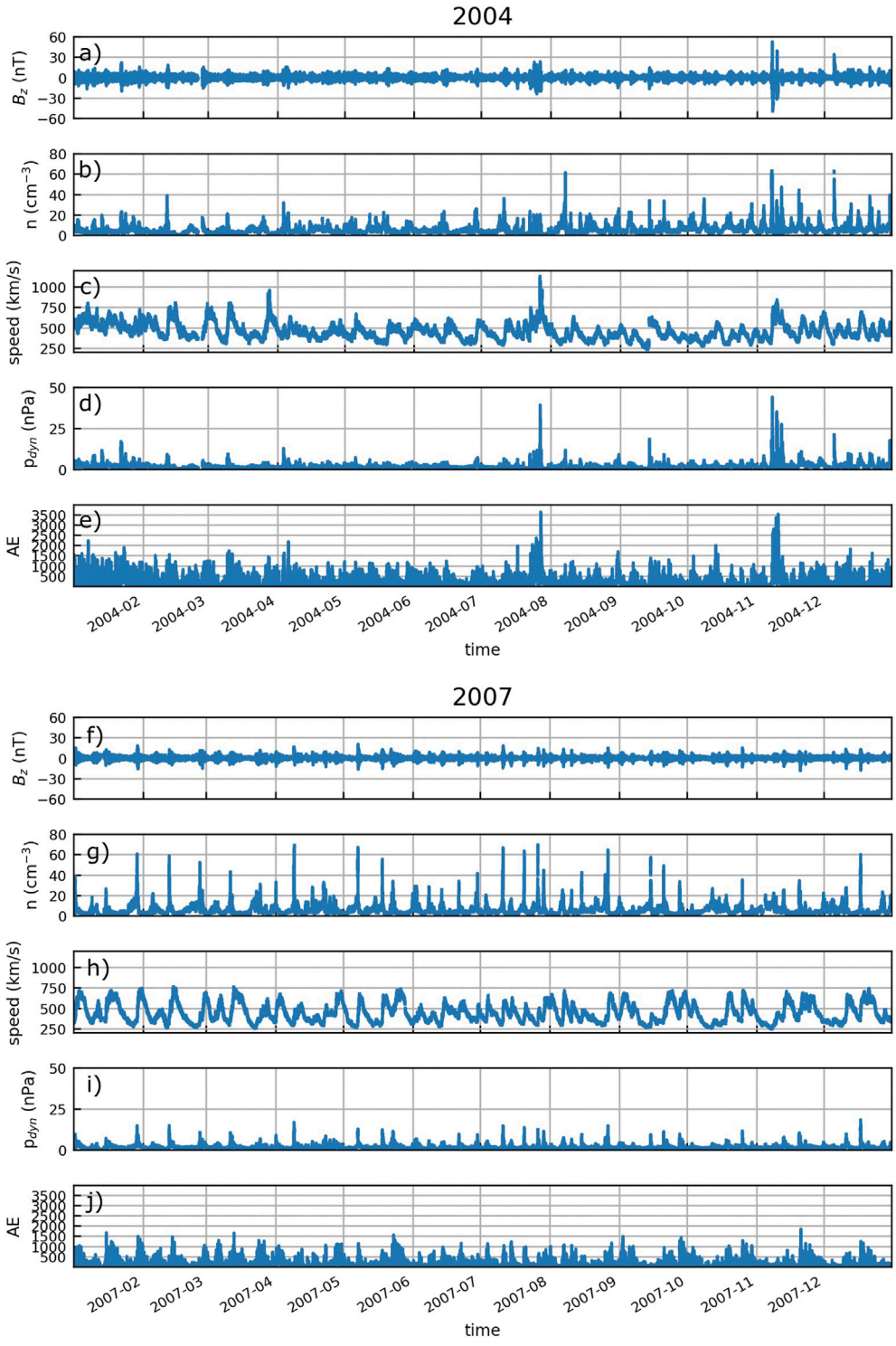

FIGURE 1
Overview of the solar wind parameters, IMF north-south component B_z, number density n, solar wind speed, dynamic pressure p_{dyn} and AE index from 2004 **(A–E)** and 2007 **(F–J)**.

and global Pc5 ULF wave power and AE index and precipitating medium energy electrons at L-shells from 5 to 7. We compare results from years 2004 and 2007, representing geomagnetically more active and less active years, respectively. The correlation analysis between the AE index and geosynchronous and groundbased Pc5 ULF wave indices indicate low non-linearity.

We investigate the correlation between the AE index and electron precipitation separately for three different energy ranges of the medium energy electrons (30–100 keV, 100–300 keV and >300 keV) and from four MLT sectors (0–6, 6–12, 12–18, 18–24). This paper is organized as follows. The data and the methods used in this study are described in Section 2, the results are presented in Section 3, and discussed in Section 4.

2 Data and methods

2.1 Solar wind and geomagnetic activity

The solar wind plasma parameters, the interplanetary magnetic field (IMF), and the auroral electrojet index (AE) are obtained from the NASA OMNIWeb (https://omniweb.gsfc.nasa.gov). Solar wind OMNI data (plotted in Figure 1) is propagated to the Earth's bow shock. We use OMNI data with 1 min resolution and calculate the hourly maximum for the AE index, $AE_{\max}$, which is used in the mutual information and correlation calculations, because we are interested in the impact of the peak geomagnetic activity. The correlation coefficient and mutual information with different time offsets behaves very similarly for both the hourly maximum and hourly mean of the AE index but the latter yields slightly lower values.

2.2 Wave activity

ULF wave indices, T_{geo} and T_{gr}, are 1 h resolution measurements of the total spectral power of the magnetic field fluctuations from geosynchronous and ground based observations, respectively, in the 2–7 mHz frequency band obtained from the data archive: http://ulf.gcras.ru/archive.html (Kozyreva et al., 2007). The ground based ULF wave index T_{gr} is obtained from ground-based magnetometers at 60°–70° latitude from the Northern hemisphere. The geosynchronous T_{geo} is calculated using the data from GOES spacecraft that are located on the geosynchronous orbit at 6.6 R_E on the equatorial plane. The ULF wave indices used in this study are defined as logarithm in base 10 of the total spectral power.

2.3 Precipitating electrons

Electron precipitation data is obtained from polar-orbiting low-altitude Polar Operational Environmental Satellite (POES). The Medium Energy Proton and Electron Detector (MEPED) instrument of the Space Environment Monitor (SEM-2) Suite on board POES spacecraft (NOAA-15, NOAA-16, NOAA-17, NOAA-18 and MetOp-02) measures electrons with 0° and 90° telescopes. At higher latitudes, where the magnetic field lines are almost radial, the 0° telescope measures primarily the electrons in the loss cone while 90° measures the trapped electron population, but it can flip to opposite at the lower latitudes (Asikainen and Mursula, 2013). The angle of view of both telescopes is 30° and they measure electrons in the energy channels >30 keV, >100 keV, >300 keV. The proton contamination and other instrumental problems affecting the POES measurements (see e.g. Rodger et al., 2013) have been corrected from the POES data used in this study (Asikainen and Mursula, 2013; Asikainen, 2017). We want to focus on the region of the outer radiation belt outside the plasmapause, therefore, we use electron precipitation observations at the L shells from 5 to 7 and all MLTs divided into four sectors (0–6, 6–12, 12–18, 18–24 MLT).

At high latitudes local bounce loss cone is usually larger than the field of view of the POES telescopes, and thus the 0° telescope underestimates the precipitating electrons, while at the higher latitudes the 90° telescope observes part of the precipitating flux (e.g., Hargreaves et al., 2010; Rodger et al., 2013). Therefore we estimate the precipitating flux, J_{precip}, as geometric mean between the parallel and perpendicular fluxes, J_0 and J_{90}, respectively, following the approach used by Hargreaves et al. (2010), Rodger et al. (2013), George et al. (2020), and Nesse Tyssøy et al. (2022):

$$J_{precip} = \sqrt{J_0 \cdot J_{90}}. \quad (1)$$

We note that some amount of trapped population seen by 90° telescope of POES spacecraft is always included in the estimated J_{precip}, which could cause underestimation of the total precipitated flux during time periods when the trapped electron flux is low and precipitated flux is high as well as overestimation of the total flux during times of high trapped flux. Nevertheless, this approach will provide much better estimation for the qualitative analysis of the electron precipitation in this study compared to using only the 0° telescope measurements. To calculate the estimated precipitation separately for each energy range 30–100 keV, 100–300 keV, and >300 keV, we first subtract the higher energy range channel from the lower ones (i.e. to get the 30–100 keV electrons the channel >100 keV is subtracted from channel >30 keV) before calculating J_{precip}.

2.4 Mutual information

Pearson correlation coefficient only measures linear correlation between two quantities and does not detect the relationships that are non-linear in nature. A useful measure that also considers non-linear relationships is Mutual Information (MI) from information theory (e.g. Li, 1990; Cover and Thomas, 2006). It quantifies the amount of information that random variables X and Y share. The method is described more in detail by Osmane et al. (2022) but it is presented briefly below. Entropy, H, is commonly used as a measure of the uncertainty, which for each variable can be defined as

$$H(X) = -\sum_{x\in X} p(x)\log p(x); \qquad H(Y) = -\sum_{y\in Y} p(y)\log p(y) \tag{2}$$

where $p(x)$ and $p(y)$ refer to probability mass functions of variables X and Y, respectively. The joint entropy of the two variables is

$$H(X,Y) = -\sum_{x,y} p(x,y)\log\left(p(x,y)\right) \tag{3}$$

The mutual information MI between two variables X and Y is defined as:

$$\begin{aligned} MI(X,Y) &= H(X) + H(Y) - H(X,Y) \\ &= \sum_{y\in Y}\sum_{x\in X} p(x,y)\log_2\left(\frac{p(x,y)}{p(x)p(y)}\right), \end{aligned} \tag{4}$$

where $p(x, y)$ is the joint probability mass function of X and Y. Mutual information is invariant with respect to reparametrization of the variables, i.e., $MI(X, Y) = MI(X', Y')$ for homeomorphisms $X' = F(X)$ and $Y' = G(Y)$ (Kraskov et al., 2004). This means, for example, that the value of mutual information is same for $MI(X, Y)$ and $MI(\log X, \log Y)$.

Mutual information contains both linear and non-linear information from the relation between two variables. In a case where the two variables have normal distributions and the joint distribution is a bivariate normal, MI can be compared to the linear correlation coefficient, ρ, through:

$$\mathrm{MI} = -\frac{1}{2}\log\left(1-\rho^2\right), \tag{5}$$

giving an estimation for the information adjusted correlation for the certain value of MI:

$$\rho_{adj} = \sqrt{1-2^{-2\mathrm{MI}}}, \tag{6}$$

which can be applied for any joint distribution of two variables. Information adjusted correlation coefficient, ρ_{adj}, can be compared with the Pearson correlation coefficient to give an estimation if the Pearson correlation has underestimated the dependence of the two variables due to existing non-linearities. In this study, we quantify the non-linearity as:

$$1 - \frac{|\rho_P|}{\rho_{adj}}. \tag{7}$$

If the information adjusted correlation is larger than the linear Pearson correlation coefficient, the investigated variables have some statistically significant non-linear dependencies and the non-linearity term becomes larger. In the case of the information adjusted correlation being comparable to the Pearson correlation, the non-linear dependencies are not significant or they are not present and the non-linearity is close to zero.

We follow the same procedure to calculate the MI for two variables as Osmane et al. (2022) by binning the data sets used using Freedman-Diaconis rule (Freedman and Diaconis, 1981). This method discretizes the variables, which leads to biases in the in the estimation of the MI that depend on the total number of the measurement points (N) and the statistical dependence between the two variables studied. To estimate an error for the mutual information caused by the discretization of the variables, we calculate so called zero baseline level similarly as described by Osmane et al. (2022). This is done by calculating the mutual information for 200 shuffles of the data sets for each time lag and calculating its standard deviation σ_{MI}. In Figure 2 and 4 the baseline is shown as the orange line and the shaded area is $3\sigma_{MI}$. We estimate the error of the ρ_{adj} by calculating error propagation using Equation 6, where we use $\Delta\mathrm{MI} = 3\sigma_{\mathrm{MI}}$. For the Pearson correlation coefficient we estimate the error by calculating the correlation coefficient for 200 shuffles of the two data sets, and the error is three times the standard deviation of the result ($\Delta\rho_P = 3\sigma_P$).

Mutual information is an integrated measure over how connected two variables are. In order to investigate how the certain values of the two variables are connected, a pointwise mutual information can be used. Definition of pointwise mutual information (PMI) is

$$\mathrm{PMI}(x,y) = \log_2\left(\frac{p(x,y)}{p(x)p(y)}\right). \tag{8}$$

PMI can be used to investigate if a pair of x and y values occur together more often than would be expected from two independent distributions. The parameter would be zero for all x and y if X and Y were independent. PMI for some pair of x and y tells that they occur together 2^{PMI} times more/less often than they would for independent distributions (e.g., Cameron et al., 2019). For example, $\mathrm{PMI} > 1$ tells that the pair of observed x and y occurs more than twice as often ($> 2^1$) as would be expected from independent variables. Similarly $\mathrm{PMI} < -1$ means that the observed pair of x and y occurred less than half as frequently ($< 2^{-1}$) than they would have occurred for independent variables.

3 Results

We compare data from two different years: year 2004 that coincides with early declining phase of Solar Cycle 23 and year 2007 that coincides with the late declining phase of the cycle 23. Figure 1 shows the solar wind conditions and geomagnetic activity from both years from the OMNI data base with 1 min resolution. Year 2004 features a few periods of particularly intense AE activity (AE > 1500 nT) associated to strong Earth-impacting interplanetary coronal mass ejections (ICMEs; e.g., Kilpua et al., 2017), but overall both years have frequent medium and intense level AE activity (AE ~ 500 – 1500 nT). During the year 2004, however, AE

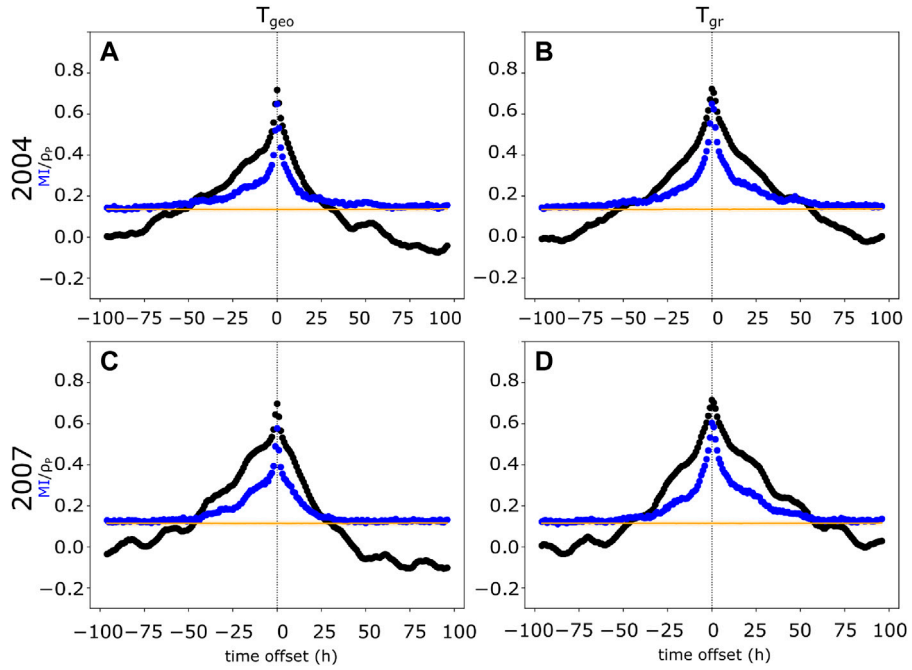

FIGURE 2
Calculation of the MI and Pearson correlation coefficient for [$\log_{10}AE_{max}(t)$, T_{geo} $(t+\tau)$] and [$\log_{10}AE_{max}(t)$, T_{gr} $(t+\tau)$], where τ varies between $\pm$ 96 h. T_{geo} and T_{gr} are the global ULF indices for geosynchronous and ground-based observations, respectively. Panels **(A)** and **(B)** show results from year 2004 and panels **(C)** and **(D)** show results from 2007. The blue dots show the calculated MI and black dots indicate the linear Pearson correlation coefficient. The positive time offset indicates that AE index would precede the ULF wave indices and the negative time offset indicates the opposite. The orange line indicates the zero baseline.

activity seems more continuous while in 2007 it increases and wanes periodically. This likely reflects that in 2007 the clear majority of geomagnetically active periods were related to stream interaction regions (SIRs) and high speed solar wind streams (HSS), while ICMEs had a significant contribution in 2004 (Asikainen and Ruopsa, 2016). The Richardson and Cane ICME list (http://www.srl.caltech.edu/ACE/ASC/DATA/level3/icmetable2.htm) reports 20 ICMEs in the near-Earth solar wind in 2004, while in 2007 only 2 ICMEs were identified. It is also interesting to note that in 2007 there were frequent high dynamics pressure intervals, presumably related to compression at SIRs.

3.1 Geomagnetic activity vs. ULF wave activity

As an indicator of the geomagnetic activity we use the hourly maximum of the AE index (AE_{max}). Because it can vary multiple orders of magnitude, we use logarithm of the AE index ($\log_{10}AE_{max}$) in the mutual information and correlation coefficient calculations. Figure 2 shows the results of the correlation analysis calculated with different time offsets (τ) ranging from −96 to +96 h for both years. We calculate the MI (blue dots) and ρ_P (black dots) between the AE index and ULF wave activity, [$\log_{10}AE_{max}(t)$, $T_{geo/gr}$ $(t+\tau)$]. Positive time offset indicates that the changes in AE index precede the ULF wave power, whereas negative time offset would imply the opposite (i.e., corresponding changes observed in AE index at time t would be observed in ULF wave index at time $t+\tau$ for positive time offset and $t-|\tau|$ for negative τ).

Figure 2 shows that the mutual information and Pearson correlation peak with zero time offset ($\tau_{max}=0$) for [$\log_{10}AE_{max}(t)$, $T_{geo/gr}$ $(t+\tau)$] in case of both the geosynchronous and ground based ULF wave indices. The time offset of the maximum value of the mutual information τ_{max}, maximum mutual information MI, the information adjusted correlation ρ_{adj} (calculated from the mutual information using Equation 6), and the corresponding Pearson correlation coefficient ρ_P are listed in Table 1. The information adjusted correlation is slightly higher than the Pearson correlation for all investigated cases suggesting some non-linear dependencies between AE and ULF wave activity. For 2004 the Pearson correlation and information adjusted correlation are the same for both geosynchronous and ground based ULF wave indices. For 2007 the Pearson correlation is also within the error limits for both ULF indices and the difference in the information adjusted correlation is not

TABLE 1 Maximum value of the Mutual Information at time offset τ_{max}, the corresponding information adjusted correlation, ρ_{adj}, and Pearson correlation coefficient, ρ_P, with the time offset τ_{max} for [$\log_{10}AE_{max}(t)$, T_{geo} $(t + \tau)$] and [$\log_{10}AE_{max}(t)$, T_{gr} $(t + \tau)$].

Year	T	$\tau_{max}(h)$	MI	ρ_{adj}	ρ_P	$1 - \lvert\rho_P\rvert/\rho_{adj}$
2004	T_{geo}	0	0.65 ± 0.01	0.770 ± 0.004	0.72 ± 0.03	0.06
2004	T_{gr}	0	0.65 ± 0.01	0.770 ± 0.005	0.72 ± 0.03	0.06
2007	T_{geo}	0	0.58 ± 0.01	0.742 ± 0.005	0.70 ± 0.04	0.06
2007	T_{gr}	0	0.60 ± 0.01	0.753 ± 0.004	0.72 ± 0.03	0.05

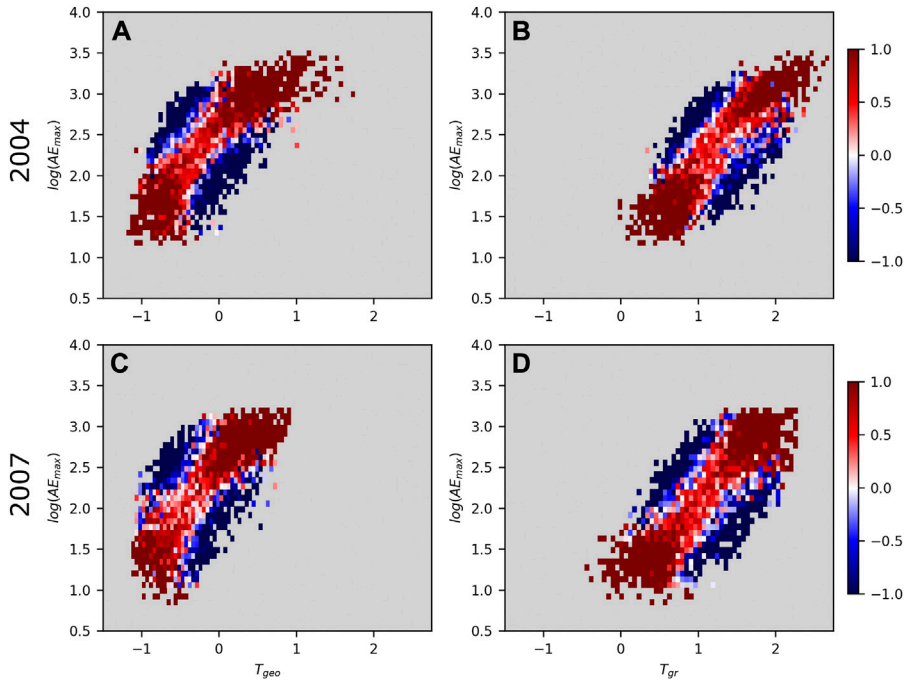

FIGURE 3
PMI map of the $\log_{10}AE_{max}$ and the geosynchronous ULF wave index T_{geo} and ground based T_{gr}, in panels **(A)** and **(B)** from year 2004 and panels **(C)** and **(D)** from year 2007. The color scale is saturated at values >1 and <-1, to highlight the areas where the $\log_{10}AE_{max}$ and $T_{geo/gr}$ occur more than twice or less than half as frequently (2^{PMI}) as would be expected if the variables were independent.

significant. We calculate the non-linearity defined by Equation 7. There are no significant differences in the non-linearity between the geomagnetically more (2004) and less (2007) active years and the geosyncrhonous and ground based ULF wave indices.

Figure 3 shows the map of the pointwise mutual information (PMI) calculated for the zero time offset, i.e., when the mutual information and Pearson correlation peak (Figure 2). The color scale of the PMI map is saturated at values ≤ -1 and ≥ 1, to highlight the areas where the $\log_{10}AE_{max}$ and the ULF indices occur 2 times less/more frequently (2^{PMI}) than would be expected from independent variables. Overall, the maps look similar for both geosynchronous and groundbased ULF indices (left and right column, respectively) and years (top row 2004 and bottom row 2007). A few stronger geomagnetic storms occurred in 2004 and, therefore, AE index and also the ULF wave indices reach higher values in 2004 than in 2007. The lowest ULF wave activity (< -0.5 for T_{geo} and <1.0 for T_{gr}) always occurs with the $\log_{10}AE_{max} < 2$ ($AE_{max} < 100$ nT). The PMI map also shows the general positive correlation between AE index and the ULF wave indices. High ULF wave activity rarely occurs with low AE index, and the ULF wave power is always elevated during intense AE activity. The largest ULF wave index values can occur over broad range of AE activity, also during the times of relatively weak AE activity ($\log_{10}AE_{max} \sim 2.7$ i.e. $AE_{max} \sim 500$ nT). These are likely caused by periods of increased dynamic pressure or high solar wind speed during northward IMF that can generate ULF wave activity as mentioned in the Introduction.

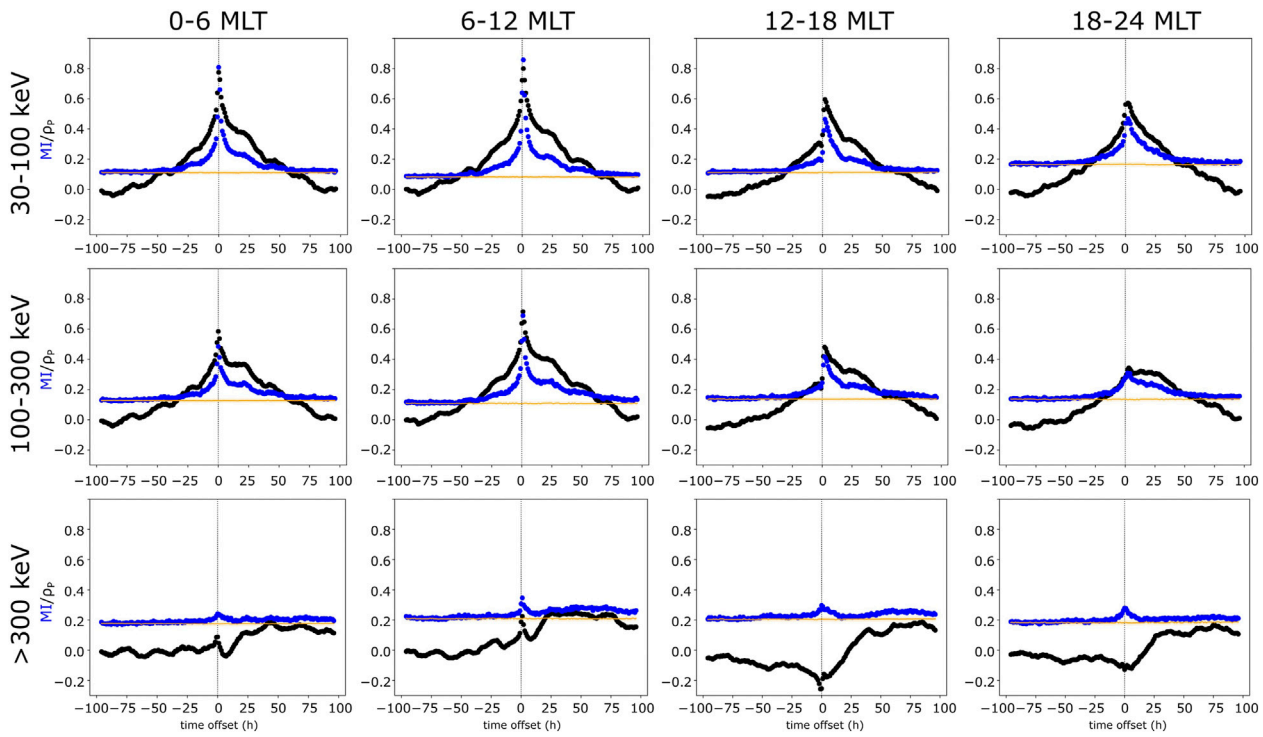

FIGURE 4
Calculation of the MI (blue) and Pearson correlation coefficient (black) between $\log_{10}AE_{max}$ and $\log_{10}$ (J_{30-100}) (top row), $\log_{10}$ ($J_{100-300}$) (middle row), and $\log_{10}$ ($J_{>300}$) (bottom row) from 2004 with different time offsets [$\log_{10}AE_{max}(t)$, $\log_{10}(J)$ $(t + \tau)$]. Columns show the results from different MLT regions. The orange line is the zero baseline.

3.2 Geomagnetic activity vs. electron precipitation

Next, we investigate the relationship between the AE index and electron precipitation. We calculate MI and Pearson correlation coefficient for the logarithm of hourly maximum value of AE ([$\log_{10}$ $AE_{max}(t)$, $\log_{10}$ (J_{precip}) $(t + \tau)$], separately for three different energy ranges (30–100 keV, 100–300 keV and >300 keV) and for four different MLT sections (0–6, 6–12, 12–18, 18–24 MLT). We use the logarithm of the J_{precip} because it can vary over five orders of magnitude during the observed time period. Figure 4 shows the mutual information (blue dots) and Pearson correlation coefficient (black) with different time offsets ranging from ±96 h from year 2004 (as in Figure 2). Columns show the different MLT regions and rows corresponds to the different energy ranges. Positive time offset again indicates that the changes in AE precede the precipitation and negative would imply the opposite. Figure 4 shows that electron precipitation in the 30–100 keV range has a clear peak in both mutual information and Pearson correlations at all MLT sectors. In the dawn sector the peak is quite narrow, but the peak spreads and has lower correlation values in the dusk sector. The tails at positive time lags are more pronounced showing that variations in AE precede variation in electron precipitation, as expected. Results from 2007 overall show similar behaviour (see Supplementary Figure S1).

For both years investigated, τ_{max}, maximum MI, the information adjusted correlation ρ_{adj} (calculated using Eq. 6) and corresponding ρ_P are listed in Table 2 and illustrated in Figure 5 as a function of MLT sector. The y-axis of the panels on the top row show the correlation coefficient and the bottom panel shows the non-linearity (Equation 7). For both 2004 and 2007, ρ_{adj} and ρ_P are considerably higher in the dawn side (0–6 and 6–12 MLT regions) than during the dusk hours (12–18 MLT and 18–24 MLT). The Pearson correlation coefficient decreases more when moving from early morning to evening MLTs than the information corrected correlation and, therefore, the non-linearity (Equation 7) is larger at dusk hours than at dawn hours as can be seen in the bottom panel of Figure 5. This indicates that the relationship between the AE index and precipitation of 30–100 keV electrons is more non-linear in the dusk side of the magnetosphere than at dawn. It is also interesting to note that the time lag of the maximum adjusted correlation increases with MLT. The lag is 0 at 0–6 MLT section, 1 h at 6–12 MLT and finally 2 h in the dusk corresponding to the eastward drift period of ~30 keV equatorial electrons. The

TABLE 2 Maximum value of the Mutual Information at time offset τ_{max}, the information adjusted correlation, ρ_{adj}, and Pearson correlation coefficient ρ_P, for AE index and electron precipitation in three different energy ranges [$\log_{10}AE_{max}(t)$, $\log_{10}(J_{precip})(t+\tau)$]. The value in the parenthesis in τ_{max} column indicate if the maximum of the ρ_P occur at different τ than maximum of the MI at τ_{max}, the corresponding ρ_P is given in the parenthesis in the sixth column.

Year	MLT	τ_{max} (h)	MI	ρ_{adj}	ρ_P	$1-\lvert\rho_P\rvert/\rho_{adj}$
30–100 keV						
2004	0–6	0	0.81 ± 0.01	0.821 ± 0.003	0.78 ± 0.03	0.05
2004	6–12	1	0.86 ± 0.01	0.834 ± 0.003	0.80 ± 0.03	0.04
2004	12–18	2	0.46 ± 0.01	0.689 ± 0.007	0.60 ± 0.03	0.13
2004	18–24	2	0.47 ± 0.01	0.691 ± 0.008	0.57 ± 0.03	0.18
2007	0–6	0	0.91 ± 0.01	0.847 ± 0.003	0.83 ± 0.03	0.02
2007	6–12	1	0.84 ± 0.01	0.830 ± 0.003	0.81 ± 0.03	0.02
2007	12–18	2	0.61 ± 0.01	0.754 ± 0.004	0.72 ± 0.03	0.05
2007	18–24	2	0.45 ± 0.01	0.678 ± 0.006	0.59 ± 0.03	0.13
100–300 keV						
2004	0–6	0	0.49 ± 0.01	0.700 ± 0.006	0.59 ± 0.03	0.16
2004	6–12	1	0.69 ± 0.01	0.785 ± 0.004	0.72 ± 0.03	0.08
2004	12–18	2	0.42 ± 0.01	0.662 ± 0.007	0.48 ± 0.03	0.24
2004	18–24	2 (3)	0.31 ± 0.01	0.591 ± 0.009	0.33 (0.34) ± 0.04	0.44
2007	0–6	0	0.63 ± 0.01	0.761 ± 0.004	0.71 ± 0.03	0.07
2007	6–12	1	0.68 ± 0.01	0.781 ± 0.004	0.73 ± 0.03	0.07
2007	12–18	2	0.51 ± 0.01	0.713 ± 0.005	0.63 ± 0.03	0.12
2007	18–24	2 (15)	0.350 ± 0.01	0.620 ± 0.008	0.46 (0.49) ± 0.03	0.26
> 300 keV						
2004	0–6	0 (45)	0.24 ± 0.01	0.534 ± 0.01	0.09 (0.18) ± 0.04	0.83
2004	6–12	0 (27)	0.35 ± 0.01	0.618 ± 0.006	0.22 (0.25) ± 0.03	0.64
2004	12–18	0	0.30 ± 0.01	0.58 ± 0.01	−0.25 ± 0.03	0.57
2004	18–24	0 (75)	0.28 ± 0.01	0.567 ± 0.01	−0.13 (0.17) ± 0.03	0.77
2007	0–6	69	0.25 ± 0.01	0.54 ± 0.01	0.31 ± 0.03	0.42
2007	6–12	76 (51)	0.28 ± 0.01	0.57 ± 0.01	0.33 (0.35) ± 0.03	0.42
2007	12–18	83	0.29 ± 0.01	0.58 ± 0.01	0.36 ± 0.03	0.38
2007	18–24	-1 (86)	0.29 ± 0.01	0.57 ± 0.01	−0.11 (0.25) ± 0.04	0.81

information adjusted correlation has similar values for both 2004 and 2007, while the Pearson correlation is higher and therefore, non-linearity is smaller for the geomagnetically less active year 2007.

The correlation analysis of the precipitation of 100–300 keV electrons (see Table 2 and Figures 4, 5) shows similar behavior as the results for the 30–100 keV electrons discussed above. Both non-linear and Pearson correlation peak at 6–12 MLT region, and the Pearson correlation is smaller on the dusk side of the magnetosphere than in the dawn. The ρ_{adj} values are overall slightly lower for the 100–300 keV electrons than for the 30–100 keV electrons. The non-linearity behaves also quite similarly for the 100–300 keV electrons as for the 30–100 keV electrons, except in the dusk the drop in the Pearson correlation is more significant and therefore the increase in the non-linearity from dawn to dusk is larger.

Finally, the results clearly show that for the highest energy electrons (> 300 keV), the correlation of the AE index and electron precipitation behave differently from the precipitation of the lower energy electrons. The information adjusted correlation remains between 0.60 and 0.67 for all MLTs. The absolute value of the Pearson correlation is low (< 0.3) and it changes sign with different time offsets as can be seen on the bottom row of Figure 4 and from Table 2. In some cases the Pearson correlation coefficient and MI peak with different time offsets (τ_{max} indicates the maximum MI), however, the Pearson correlation coefficient indicates low correlation at all time offsets between the AE index and the higher energy electrons (Figure 4).

The PMI maps for AE index and electron precipitation at different energy ranges and MLT regions from year 2004 are shown in Figure 6 (from 2007 see Supplementary Figure S2). The maps are constructed using the time offset of maximum MI (τ_{max}

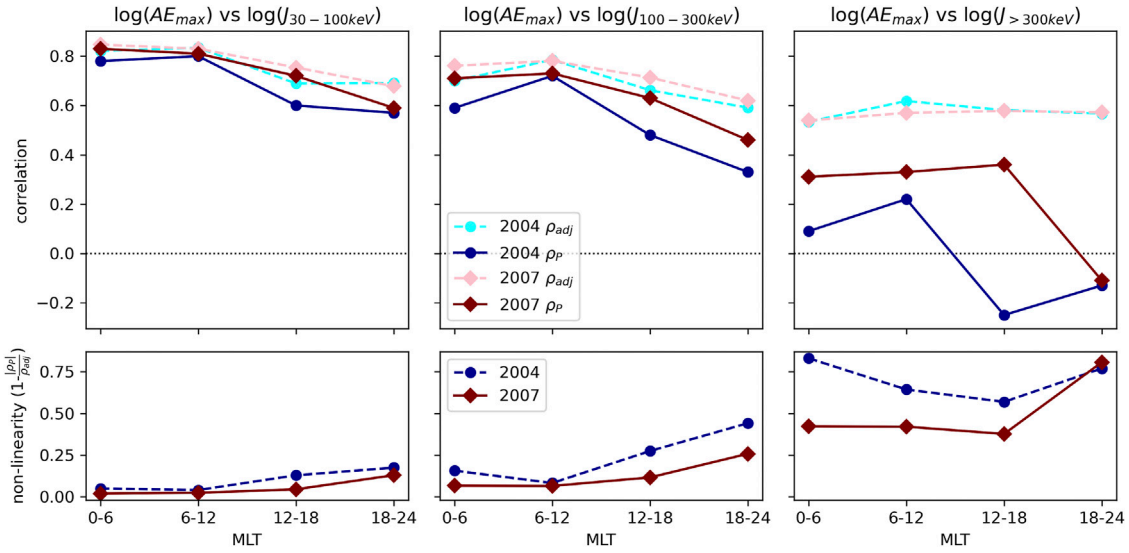

FIGURE 5
Top row shows information adjusted correlation and Pearson correlation coefficient between AE index and 30–100 keV precipitation (left column), 100–300 keV precipitation (middle column), and >300 keV precipitation (right). The bottom row shows the non-linearity ($1 - |\rho_P|/\rho_{adj}$) for each evaluated energy range. The darker colored data points indicate ρ_P and lighter color ρ_{adj}. Circles indicate results from 2004 and diamonds from 2007.

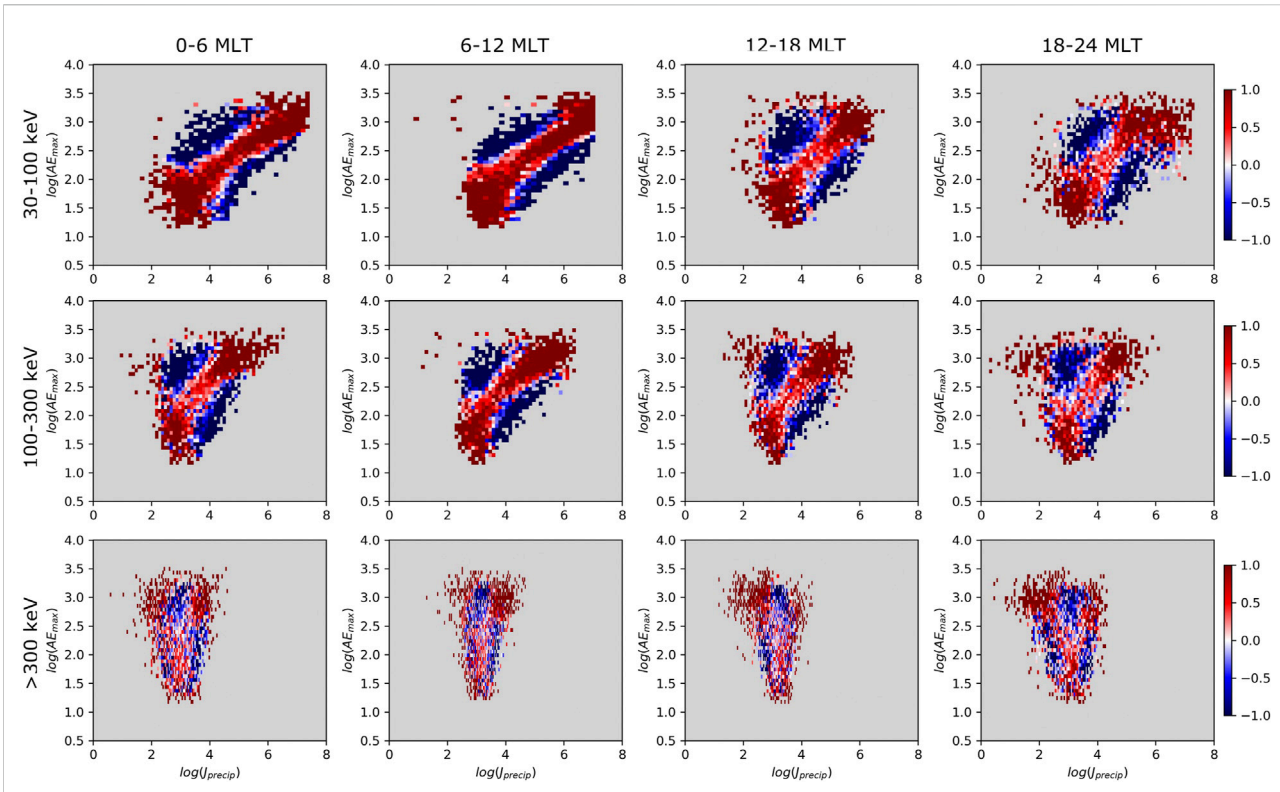

FIGURE 6
PMI map of $\log_{10}AE_{max}$ and $\log_{10}$ (J_{30-100}) (top row), $\log_{10}$ ($J_{100-300}$) (middle row), and $\log_{10}$ ($J_{>300}$) (bottom row) from 2004. The columns show results from different MLT regions. Each panel is plotted with the time offset τ_{max} indicated in Table 2. The color scale is saturated at values >1 and < −1, to highlight the areas where the $\log_{10}AE_{max}$ and $\log_{10}$ (J_{precip}) occur more than twice or less than half as frequently (2^{PMI}) as would be expected if the variables were independent.

in Table 2) for the [$\log_{10}AE_{\max}(t)$, log $J_{30-100keV}$ $(t + \tau_{\max})$]. Again, the dark red (blue) regions show where the PMI ≥ 1 (≤ -1), meaning that the pair of values occurs more than twice (less than half) as often together as would be expected from independent variables. These PMI maps show the change in the correlation between the AE index and the precipitating electron flux from dawn hours (0–12 MLT) to the dusk hours (12–24 MLT) and with increasing energy. For both 30–100 keV and 100–300 keV electrons the logarithm of the precipitating electron flux log (J_{precip}) remains below 4 during the quiet geomagnetic activity (i.e., $AE_{\max} < 300$ nT) showing that there is no strong precipitation at geomagnetically quiet times. Strong precipitation (log (J_{precip}) > 5) can occur with wide range of AE values during medium and high activity ($AE_{\max} >$ 300 nT). The PMI map for > 300 keV electrons show no linear correlation. During quiet times ($AE_{\max} < 300$ nT) the PMI is positive around log (J_{precip}) ≈ 3 but at those flux values the PMI becomes negative with increasing AE index. The lower (log (J_{precip}) < 2.5) and higher (log (J_{precip}) > 3.5) fluxes occur more likely during increased geomagnetic activity instead. This might suggest that during increased geomagnetic activity the flux of higher energy electrons can get either increased or depleted. This could happen also in a few cases for the 100–300 keV electrons in the dusk (12–18 and 18–24 MLT sections), where PMI gets positive values also for low precipitating electron fluxes (log (J_{precip}) ≈ 2) during medium geomagnetic activity.

4 Discussion and conclusions

In this paper, we used mutual information from information theory to study the linear and non-linear dependencies between the AE index as the indicator of the level of geomagnetic activity, Pc5 ULF wave activity given by the global ULF wave index and electron precipitation. We evaluate the correlations for the AE index and electron precipitation separately for three different medium energy ranges (30–100 keV, 100–300 keV, and > 300 keV) and for four MLT regions (0–6, 6–12, 12–18, 18–24). We compared the results from two full years 2004 and 2007 representing geomagnetically more active and more quiet years, respectively. We used the logarithm of the hourly maximum of the AE index for the mutual information and the Pearson correlation coefficient calculation. We note that the calculated electron precipitation is just estimation of the total precipitated flux that could be overestimated during periods of high trapped flux and underestimated during time periods of low trapped flux but high precipitated flux.

Radiation belt electrons at medium energies from tens to a few hundreds of keVs that are injected from the magnetotail during substorms are typically called source electrons as they act as the source of the whistler mode chorus waves. Previous studies have shown that both the precipitating and trapped electrons within this energy range in the outer radiation belts are well correlated with the AE index (e.g. Katsavrias et al., 2021; Nesse Tyssøy et al., 2021). Our results are consistent with the previous studies and show that both the mutual information and Pearson correlation coefficient between AE index and electron precipitation in the energy ranges 30–100 keV and 100–300 keV indicate strong linear correlation ($\rho_P > 0.78$) on the dawn side of the magnetosphere. A recent statistical analysis over a full solar cycle of daily averaged data by Nesse Tyssøy et al. (2021) showed that the AE index is a good proxy for the precipitation of ≥30keV energy electrons. The authors used electron precipitation from NOAA/POES at three energy ranges (> 43 keV, > 114 keV and > 292 keV), and found that the electrons from the lowest of these energy ranges respond to the AE fastest and the correlation is largest, while the correlation decreases and the time lag increases with increasing energy of the precipitating electrons being 2 days for the > 292 keV electrons. This is consistent especially with year 2007 (see Table 2; Supplementary), where the non-linear and linear correlation increases with larger time offsets especially at MLT sectors 6–12 and 12–18.

The drift period of equatorial electrons within the 30–100 keV energy range at L shells 5 to 7 varies between 1 and 5 h. These times correspond well with the increasing time lag of the maximum information adjusted correlation between the AE index and the electron precipitation. At MLTs 0–6 the correlation peaks within the first hour (0 time lag). As the electrons drift eastward the MI peaks with one hour time lag at the MLT 6–12 and in the dusk side of the magnetosphere the time lag is two hours. As the electrons drift they excite chorus waves. This generation process itself causes precipitation of source energy electrons and the chorus waves also start interacting and causing precipitation of seed energy (~ 300 – 700 keV) electrons. The time lags for the peak mutual information between AE and higher energy electrons (> 300 keV) occur at zero time offset for 2004 and multiple days for 2007 (Table 2). The linear correlation coefficients peak with couple of days delay also for 2004, although the Pearson correlation values indicate no significant (≤ 0.3 for 2004) or low correlation (≤ 0.36 for 2007). These results could reflect the dominance of precipitating of seed energy electrons that start immediately as the chorus waves are generated. The effect progresses gradually to higher energies (e.g., Jaynes et al., 2015b).

We find that the linear Pearson correlation between the AE index and electron precipitation in the energy range from 30–300 keV decrease from dawn to dusk, while the decrease in the mutual information (and the information adjusted correlation) is relatively smaller with MLT compared to the Pearson correlation. Our results, therefore, indicate that the linear statistical dependence between the AE index and precipitating electrons is stronger at MLTs < 12, while relationship appears to be more non-linear from noon to

evening sector (MLT > 12). Previous studies have shown that the chorus wave activity driven by the source electrons injected from the magnetotail during the substorm activity have been found to correlate well with the precipitation of the 30–100 keV electrons outside the plasmapause (e.g., Lam et al., 2010; Chen et al., 2014). Chorus waves are mainly exited between 0–12 MLT (e.g., Meredith et al., 2020), therefore, it is likely that they are the main cause of the high linear correlation observed between AE index and 30–300 keV electron precipitation at dawn. The cause of the persisting non-linear relationship between AE index and the precipitating electrons at dusk may be related to excitation of multiple different wave modes and their combined effect of scattering the electrons to the loss cone. In the dusk, the EMIC waves are the dominating cause of the precipitation of the MeV electrons, but they have been found to be responsible also of precipitation of sub-MeV electrons down to ~ 100 keV (e.g., Blum et al., 2019; Hendry et al., 2019). Other possible wave modes that are known to precipitate electrons from a few tens to a few hundred keV range at dusk are magnetosonic mode (e.g., Ma et al., 2016) and hiss (inside the plasmasphere) (e.g., Ma et al., 2021). Another factor causing larger non-linearity in the dusk may be the related to the changes and asymmetries of the electron convection and drift trajectories. Some electrons that drift around the Earth might get lost from the radiation belts before they reach the dusk side or they may end up outside the L shell range investigated in this study.

The Pearson correlation coefficient between the AE index and the electron precipitation at energies 30–100 keV and 100–300 keV is lower for geomagnetically more active year 2004 than for a quieter year 2007 within all other MLT sectors except 6–12, where the high correlation between AE index and electron precipitation is maintained for different solar cycle phases even when typical drivers of geomagnetic activity are different. The difference in the information adjusted correlation between the 2 years is smaller than difference in the linear correlations. In 2004 significant part of the observed geomagnetic activity is driven by ICMEs while in 2007 the activity is mainly caused by SIRs and HSSs (e.g. Asikainen and Ruopsa, 2016; Kilpua et al., 2017). Previous studies have shown that the geomagnetic activity driven by ICMEs is different from HSS driven activity (e.g., Holappa et al., 2014; Asikainen and Ruopsa, 2016). ICMEs are responsible for driving intense geomagnetic storm and the magnetospheric response can vary depending on the properties of the ICMEs (e.g., Borovsky and Denton, 2006), while the substorm process is mainly driven by HHSs (e.g., Tanskanen et al., 2005). Therefore, our results indicate that during geomagnetic activity driven by SIRs and HSSs, the dependency between the AE index and electron precipitation remains more linear while the ICME driven activity cause the response of the inner magnetospheric processes leading to particle precipitation on the dusk side to become more non-linear because ICMEs cause strong and rapid changes in the inner magnetosphere that could vary significantly depending on the properties of the ICMEs.

The non-linearity of the correlation between the AE index and the global ULF wave indices is small for both geosynchronous and groundbased indices. The Pearson correlation coefficient is a little bit smaller than the information adjusted correlation suggesting that some non-linearities could be present but they are not very significant. The correlation coefficients between the AE index and the global ULF wave indices do not show significant difference between the 2 years studied. The information adjusted correlation is slightly smaller for 2007 than 2004, but the difference does not impact the non-linearity significantly. Therefore, the correlation analysis of the AE index and global Pc5 ULF wave indices suggest that the level of the non-linearity does not depend on the level of the geomagnetic activity or its driver (ICMEs in 2004 and SIRs ans HSSs in 2007 as discussed above).

In summary, this study shows that non-linearity of the correlation between the geomagnetic activity indicated by the AE index and the precipitation of the medium energy electrons is dependent on the energy of the electrons and MLT. The non-linear correlation between the AE index and electrons in the energy ranges 30–100 keV and 100–300 keV persist at all MLTs while the significant linear dependence is only present on the pre-noon hours. The linear correlation between the AE index and the electron precipitation is also lower during the geomagnetically more active year when larger portion of the geomagnetic activity is driven by ICMEs. This suggests that during the geomagnetic activity driven by ICMEs the magnetosphere becomes more non-linear or there is a larger variability between each ICME driven storm compared to SIR and HSS driven activity. The correlation analysis between the AE index and ULF Pc5 indices, on the other hand, shows that the non-linearity between the geomagnetic activity and ULF Pc5 wave activity is not very high and it is not affected by the different drivers and intensity of the geomagnetic activity of the 2 years studied.

Author contributions

SH performed the data analysis and wrote the paper. All coauthors assisted with the interpretation of the results and provided comments on the paper. TA provided the POES data that included the corrections from the proton contamination and other instrumental problems. MS wrote the analysis scripts used in this study to analyse the data.

Funding

This research has been supported by the Finnish Centre of Excellence in Research of Sustainable Space, Project 1312390. EKJK acknowledges the European Research Council (ERC) under the European Union's Horizon 2020 Research and Innovation Programme Project SolMAG 724391, and Academy of Finland project 1310445. AO and MS acknowledge funding from the Academy of Finland by the profiling action on Matter and Materials (grant no. 318913). HG acknowledges the Consolidator grant 682068-PRESTISSIMO. TA was supported by the Academy of Finland via PRediction of SPace climate and its Effects in ClimaTe, PROSPECT, (Project 321440) research project.

Acknowledgments

We gratefully acknowledge the Finnish Center of Excellence in Research of Sustainable Space and the Academy of Finland for their funding.

Conflict of interest

The authors declare that the research was conducted in the absence of any commercial or financial relationships that could be construed as a potential conflict of interest.

Publisher's note

All claims expressed in this article are solely those of the authors and do not necessarily represent those of their affiliated organizations, or those of the publisher, the editors and the reviewers. Any product that may be evaluated in this article, or claim that may be made by its manufacturer, is not guaranteed or endorsed by the publisher.

Supplementary material

The Supplementary Material for this article can be found online at: https://www.frontiersin.org/articles/10.3389/fspas.2022.987913/full#supplementary-material

References

Artemyev, A. V., Vasiliev, A. A., Mourenas, D., Agapitov, O. V., Krasnoselskikh, V., Boscher, D., et al. (2014). Fast transport of resonant electrons in phase space due to nonlinear trapping by whistler waves. *Geophys. Res. Lett.* 41, 5727–5733. doi:10.1002/2014GL061380

Asikainen, T. (2017). "Calibrated and corrected POES/MEPED energetic particle observations," in *The ESPAS e-infrastructure: Access to data in near-Earth space*. Editors A. Belehaki, M. Hapgood, and J. Watermann (Les Ulis, France: EDP Science), 57–69. doi:10.1051/978-2-7598-1949-2

Asikainen, T., and Mursula, K. (2013). Correcting the noaa/meped energetic electron fluxes for detector efficiency and proton contamination. *J. Geophys. Res. Space Phys.* 118, 6500–6510. doi:10.1002/jgra.50584

Asikainen, T., and Ruopsa, M. (2016). Solar wind drivers of energetic electron precipitation. *J. Geophys. Res. Space Phys.* 121, 2209–2225. doi:10.1002/2015JA022215

Baker, D. N., Hoxie, V., Zhao, H., Jaynes, A. N., Kanekal, S., Li, X., et al. (2019). Multiyear measurements of radiation belt electrons: Acceleration, transport, and loss. *JGR. Space Phys.* 124, 2588–2602. doi:10.1029/2018JA026259

Blum, L., Artemyev, A., Agapitov, O., Mourenas, D., Boardsen, S., and Schiller, Q. (2019). Emic wave-driven bounce resonance scattering of energetic electrons in the inner magnetosphere. *JGR. Space Phys.* 124, 2484–2496. doi:10.1029/2018JA026427

Borovsky, J. E., and Denton, M. H. (2006). Differences between cme-driven storms and cir-driven storms. *J. Geophys. Res.* 111, A07S08. doi:10.1029/2005JA011447

Cameron, T. G., Jackel, B., and Oliveira, D. M. (2019). Using mutual information to determine geoeffectiveness of solar wind phase fronts with different front orientations. *JGR. Space Phys.* 124, 1582–1592. doi:10.1029/2018JA026080

Chen, L., and Hasegawa, A. (1991). Kinetic theory of geomagnetic pulsations 1. Internal excitations by energetic particles. *J. Geophys. Res.* 96, 1503–1512. doi:10.1029/90JA02346

Chen, Y., Reeves, G. D., Friedel, R. H. W., and Cunningham, G. S. (2014). Global time-dependent chorus maps from low-earth-orbit electron precipitation and van allen probes data. *Geophys. Res. Lett.* 41, 755–761. doi:10.1002/2013GL059181

Claudepierre, S. G., Elkington, S. R., and Wiltberger, M. (2008). Solar wind driving of magnetospheric ULF waves: Pulsations driven by velocity shear at the magnetopause. *J. Geophys. Res.* 113, A05218. doi:10.1029/2007JA012890

Claudepierre, S. G., Hudson, M. K., Lotko, W., Lyon, J. G., and Denton, R. E. (2010). Solar wind driving of magnetospheric ULF waves: Field line resonances driven by dynamic pressure fluctuations. *J. Geophys. Res.* 115, A11202. doi:10.1029/2010JA015399

Cover, T. M., and Thomas, J. A. (2006). *Elements of information theory*. Second Edition. Hoboken, New Jersey: John Wiley & Sons.

Davis, T. N., and Sugiura, M. (1966). Auroral electrojet activity index ae and its universal time variations. *J. Geophys. Res.* 71, 785–801. doi:10.1029/JZ071i003p00785

Elkington, S. R., Hudson, M. K., and Chan, A. A. (1999). Acceleration of relativistic electrons via drift-resonant interaction with toroidal-mode pc-5 ulf oscillations. *Geophys. Res. Lett.* 26, 3273–3276. doi:10.1029/1999GL003659

Elkington, S. R., Hudson, M. K., and Chan, A. A. (2003). Resonant acceleration and diffusion of outer zone electrons in an asymmetric geomagnetic field. *J. Geophys. Res.* 108, 1116. doi:10.1029/2001JA009202

Freedman, D., and Diaconis, P. (1981). On the histogram as a density estimator: l2 theory. *Z. Wahrscheinlichkeitstheorie Verw. Geb.* 57, 453–476. doi:10.1007/bf01025868

George, H., Kilpua, E., Osmane, A., Asikainen, T., Kalliokoski, M. M. H., Rodger, C. J., et al. (2020). Outer Van Allen belt trapped and precipitating electron flux responses to two interplanetary magnetic clouds of opposite polarity. *Ann. Geophys.* 38, 931–951. doi:10.5194/angeo-38-931-2020

Hargreaves, J. K., Birch, M. J., and Evans, D. S. (2010). On the fine structure of medium energy electron fluxes in the auroral zone and related effects in the ionospheric D-region. *Ann. Geophys.* 28, 1107–1120. doi:10.5194/angeo-28-1107-2010

Hendry, A. T., Santolik, O., Kletzing, C. A., Rodger, C. J., Shiokawa, K., and Baishev, D. (2019). Multi-instrument observation of nonlinear emic-driven electron precipitation at sub–mev energies. *Geophys. Res. Lett.* 46, 7248–7257. doi:10.1029/2019GL082401

Holappa, L., Mursula, K., and Asikainen, T. (2014). A new method to estimate annual solar wind parameters and contributions of different solar wind structures to geomagnetic activity. *J. Geophys. Res. Space Phys.* 119, 9407–9418. doi:10.1002/2014JA020599

Hudson, M. K., Denton, R. E., Lessard, M. R., Miftakhova, E. G., and Anderson, R. R. (2004). A study of pc-5 ulf oscillations. *Ann. Geophys.* 22, 289–302. doi:10.5194/angeo-22-289-2004

Hwang, K. J., and Sibeck, D. G. (2016). Role of low-frequency boundary waves in the dynamics of the dayside magnetopause and the inner magnetosphere. *Wash.*

D.C. Am. Geophys. Union Geophys. Monogr. Ser. 216, 213–239. doi:10.1002/9781119055006.ch13

James, M. K., Yeoman, T. K., Mager, P. N., and Klimushkin, D. Y. (2016). Multiradar observations of substorm-driven ulf waves. *J. Geophys. Res. Space Phys.* 121, 5213–5232. doi:10.1002/2015JA022102

Jaynes, A. N., Baker, D. N., Singer, H. J., Rodriguez, J. V., Loto'aniu, T. M., Ali, A. F., et al. (2015a). Source and seed populations for relativistic electrons: Their roles in radiation belt changes. *JGR. Space Phys.* 120, 7240–7254. doi:10.1002/2015JA021234

Jaynes, A. N., Lessard, M. R., Takahashi, K., Ali, A. F., Malaspina, D. M., Michell, R. G., et al. (2015b). Correlated pc4–5 ulf waves, whistler-mode chorus, and pulsating aurora observed by the van allen probes and ground-based systems. *JGR. Space Phys.* 120, 8749–8761. doi:10.1002/2015JA021380

Johnson, J. R., and Wing, S. (2005). A solar cycle dependence of nonlinearity in magnetospheric activity. *J. Geophys. Res.* 110. doi:10.1029/2004JA010638

Kasahara, S., Miyoshi, Y., Yokota, S., Mitani, T., Kasahara, Y., Matsuda, S., et al. (2018). Pulsating aurora from electron scattering by chorus waves. *Nature* 554, 337–340. doi:10.1038/nature25505

Katsavrias, C., Aminalragia–Giamini, S., Papadimitriou, C., Sandberg, I., Jiggens, P., Daglis, I., et al. (2021). On the interplanetary parameter schemes which drive the variability of the source/seed electron population at geo. *JGR. Space Phys.* 126, e2020JA028939. doi:10.1029/2020JA028939

Kellerman, A. C., and Shprits, Y. Y. (2012). On the influence of solar wind conditions on the outer-electron radiation belt. *J. Geophys. Res.* 117. doi:10.1029/2011JA017253

Kennel, C. F., and Petschek, H. E. (1966). Limit on stably trapped particle fluxes. *J. Geophys. Res.* 71, 1–28. doi:10.1029/JZ071i001p00001

Kepko, L., and Spence, H. E. (2003). Observations of discrete, global magnetospheric oscillations directly driven by solar wind density variations. *J. Geophys. Res.* 108, 1257. doi:10.1029/2002JA009676

Kilpua, E., Koskinen, H. E. J., and Pulkkinen, T. I. (2017). Coronal mass ejections and their sheath regions in interplanetary space. *Living Rev. Sol. Phys.* 14, 5. doi:10.1007/s41116-017-0009-6

Kozyreva, O., Pilipenko, V., Engebretson, M., Yumoto, K., Watermann, J., and Romanova, N. (2007). In search of a new ulf wave index: Comparison of pc5 power with dynamics of geostationary relativistic electrons. *Planet. Space Sci.Ultra-Low Freq. Waves Magnetos.* 55, 755–769. doi:10.1016/j.pss.2006.03.013

Kraskov, A., Stögbauer, H., and Grassberger, P. (2004). Estimating mutual information. *Phys. Rev. E* 69, 066138. doi:10.1103/PhysRevE.69.066138

Lam, M. M., Horne, R. B., Meredith, N. P., Glauert, S. A., Moffat-Griffin, T., and Green, J. C. (2010). Origin of energetic electron precipitation >30 kev into the atmosphere. *J. Geophys. Res.* 115. doi:10.1029/2009JA014619

Li, W., and Hudson, M. K. (2019). Earth's van allen radiation belts: From discovery to the van allen probes era. *JGR. Space Phys.* 124, 8319–8351. doi:10.1029/2018JA025940

Li, W. (1990). Mutual information functions versus correlation functions. *J. Stat. Phys.* 60, 823–837. doi:10.1007/BF01025996

Li, W., Thorne, R. M., Ma, Q., Ni, B., Bortnik, J., Baker, D. N., et al. (2014). Radiation belt electron acceleration by chorus waves during the 17 March 2013 storm. *JGR. Space Phys.* 119, 4681–4693. doi:10.1002/2014JA019945

Ma, Q., Li, W., Thorne, R. M., Bortnik, J., Kletzing, C. A., Kurth, W. S., et al. (2016). Electron scattering by magnetosonic waves in the inner magnetosphere. *JGR. Space Phys.* 121, 274–285. doi:10.1002/2015JA021992

Ma, Q., Li, W., Zhang, X. J., Bortnik, J., Shen, X. C., Connor, H. K., et al. (2021). Global survey of electron precipitation due to hiss waves in the earth's plasmasphere and plumes. *JGR. Space Phys.* 126, e2021JA029644. doi:10.1029/2021JA029644

Mann, I. R., Lee, E. A., Claudepierre, S. G., Fennell, J. F., Degeling, A., Rae, I. J., et al. (2013). Discovery of the action of a geophysical synchrotron in the Earth's Van Allen radiation belts. *Nat. Commun.* 4, 2795. doi:10.1038/ncomms3795

Mann, I. R., Ozeke, L. G., Murphy, K. R., Claudepierre, S. G., Turner, D. L., Baker, D. N., et al. (2016). Explaining the dynamics of the ultra-relativistic third Van Allen radiation belt. *Nat. Phys.* 12, 978–983. doi:10.1038/nphys3799

Meredith, N. P., Horne, R. B., Shen, X.-C., Li, W., and Bortnik, J. (2020). Global model of whistler mode chorus in the near-equatorial region (—λ_m— 18). *Geophys. Res. Lett.* 47, e87311. doi:10.1029/2020GL087311

Nesse Tyssøy, H., Partamies, N., Babu, E. M., Smith-Johnsen, C., and Salice, J. A. (2021). The predictive capabilities of the auroral electrojet index for medium energy electron precipitation. *Front. Astron. Space Sci.* 8, 167. doi:10.3389/fspas.2021.714146

Nesse Tyssøy, H., Sinnhuber, M., Asikainen, T., Bender, S., Clilverd, M. A., Funke, B., et al. (2022). Heppa iii intercomparison experiment on electron precipitation impacts: 1. Estimated ionization rates during a geomagnetic active period in april 2010. *JGR. Space Phys.* 127, e2021JA029128. doi:10.1029/2021JA029128

Newell, P. T., and Gjerloev, J. W. (2011). Evaluation of supermag auroral electrojet indices as indicators of substorms and auroral power. *J. Geophys. Res.* 116. doi:10.1029/2011JA016779

Ni, B., Thorne, R. M., Shprits, Y. Y., and Bortnik, J. (2008). Resonant scattering of plasma sheet electrons by whistler-mode chorus: Contribution to diffuse auroral precipitation. *Geophys. Res. Lett.* 35, L11106. doi:10.1029/2008GL034032

Ni, B., Thorne, R. M., Zhang, X., Bortnik, J., Pu, Z., Xie, L., et al. (2016). Origins of the earth's diffuse auroral precipitation. *Space Sci. Rev.* 200, 205–259. doi:10.1007/s11214-016-0234-7

Nishimura, Y., Bortnik, J., Li, W., Thorne, R. M., Lyons, L. R., Angelopoulos, V., et al. (2010). Identifying the driver of pulsating aurora. *Science* 330, 81–84. doi:10.1126/science.1193186

Osmane, A., Savola, M., Kilpua, E., Koskinen, H., Borovsky, J. E., and Kalliokoski, M. (2022). Quantifying the non-linear dependence of energetic electron fluxes in the earth's radiation belts with radial diffusion drivers. *Ann. Geophys.* 40, 37–53. doi:10.5194/angeo-40-37-2022

Rae, I. J., Donovan, E. F., Mann, I. R., Fenrich, F. R., Watt, C. E. J., Milling, D. K., et al. (2005). Evolution and characteristics of global Pc5 ULF waves during a high solar wind speed interval. *J. Geophys. Res.* 110, A12211. doi:10.1029/2005JA011007

Reeves, G. D., McAdams, K. L., Friedel, R. H. W., and O'Brien, T. P. (2003). Acceleration and loss of relativistic electrons during geomagnetic storms. *Geophys. Res. Lett.* 30, 1529. doi:10.1029/2002GL016513

Reeves, G. D., Morley, S. K., Friedel, R. H. W., Henderson, M. G., Cayton, T. E., Cunningham, G., et al. (2011). On the relationship between relativistic electron flux and solar wind velocity: Paulikas and blake revisited. *J. Geophys. Res.* 116. doi:10.1029/2010JA015735

Rodger, C. J., Kavanagh, A. J., Clilverd, M. A., and Marple, S. R. (2013). Comparison between poes energetic electron precipitation observations and riometer absorptions: Implications for determining true precipitation fluxes. *J. Geophys. Res. Space Phys.* 118, 7810–7821. doi:10.1002/2013JA019439

Shi, X., Baker, J. B. H., Ruohoniemi, J. M., Hartinger, M. D., Murphy, K. R., Rodriguez, J. V., et al. (2018). Long-lasting poloidal ULF waves observed by multiple satellites and high-latitude SuperDARN radars. *JGR. Space Phys.* 123, 8422–8438. doi:10.1029/2018JA026003

Shprits, Y. Y., Elkington, S. R., Meredith, N. P., and Subbotin, D. A. (2008). Review of modeling of losses and sources of relativistic electrons in the outer radiation belt I: Radial transport. *J. Atmos. Solar-Terrestrial Phys.* 70, 1679–1693. doi:10.1016/j.jastp.2008.06.008

Simms, L. E., Engebretson, M. J., Clilverd, M. A., Rodger, C. J., and Reeves, G. D. (2018). Nonlinear and synergistic effects of ulf pc5, vlf chorus, and emic waves on relativistic electron flux at geosynchronous orbit. *J. Geophys. Res. Space Phys.* 123, 4755–4766. doi:10.1029/2017JA025003

Simms, L. E., Engebretson, M. J., Rodger, C. J., Dimitrakoudis, S., Mann, I. R., and Chi, P. J. (2021). The combined influence of lower band chorus and ulf waves on radiation belt electron fluxes at individual l-shells. *JGR. Space Phys.* 126, e2020JA028755. doi:10.1029/2020JA028755

Su, Z., Zhu, H., Xiao, F., Zong, Q. G., Zhou, X. Z., Zheng, H., et al. (2015). Ultra-low-frequency wave-driven diffusion of radiation belt relativistic electrons. *Nat. Commun.* 6, 10096. doi:10.1038/ncomms10096

Tanskanen, E. I., Slavin, J. A., Tanskanen, A. J., Viljanen, A., Pulkkinen, T. I., Koskinen, H. E. J., et al. (2005). Magnetospheric substorms are strongly modulated by interplanetary high-speed streams. *Geophys. Res. Lett.* 32, L16104. doi:10.1029/2005GL023318

Thorne, R. M., Li, W., Ni, B., Ma, Q., Bortnik, J., Chen, L., et al. (2013). Rapid local acceleration of relativistic radiation-belt electrons by magnetospheric chorus. *Nature* 504, 411–414. doi:10.1038/nature12889

Thorne, R. M., Ni, B., Tao, X., Horne, R. B., and Meredith, N. P. (2010). Scattering by chorus waves as the dominant cause of diffuse auroral precipitation. *Nature* 467, 943–946. doi:10.1038/nature09467

Van Allen, J. A. (1981). "Observations of high intensity radiation by satellites 1958 Alpha and 1958 Gamma," in *Space science comes of age: Perspectives in the history of the space Sciences*. Editors P. A. Hanle, V. D. Chamberlain, and S. G. Brush, 58–73.

Wang, C.-P., Thorne, R., Liu, T. Z., Hartinger, M. D., Nagai, T., Angelopoulos, V., et al. (2017). A multispacecraft event study of Pc5 ultralow-frequency waves in the magnetosphere and their external drivers. *JGR. Space Phys.* 122, 5132–5147. doi:10.1002/2016JA023610

Wing, S., Johnson, J. R., Camporeale, E., and Reeves, G. D. (2016). Information theoretical approach to discovering solar wind drivers of the outer radiation belt. *JGR. Space Phys.* 121, 9378–9399. doi:10.1002/2016JA022711

Wing, S., Johnson, J. R., Turner, D. L., Ukhorskiy, A., and Boyd, A. J. (2021). Untangling the solar wind and magnetospheric drivers of the radiation belt electrons. *Earth Space Sci. Open Archive* 66. doi:10.1002/essoar.10508584.1

Yamakawa, T., Seki, K., Amano, T., Takahashi, N., and Miyoshi, Y. (2019). Excitation of storm time pc5 ulf waves by ring current ions based on the drift-kinetic simulation. *Geophys. Res. Lett.* 46, 1911–1918. doi:10.1029/2018GL081573

Zhang, X. Y., Zong, Q.-G., Wang, Y. F., Zhang, H., Xie, L., Fu, S. Y., et al. (2010). Ulf waves excited by negative/positive solar wind dynamic pressure impulses at geosynchronous orbit. *J. Geophys. Res.* 115. doi:10.1029/2009JA015016

Zolotukhina, N. A., Mager, P. N., and Klimushkin, D. Y. (2008). Pc5 waves generated by substorm injection: A case study. *Ann. Geophys.* 26, 2053–2059. doi:10.5194/angeo-26-2053-2008

Zong, Q., Rankin, R., and Zhou, X. (2017). The interaction of ultra-low-frequency pc3-5 waves with charged particles in Earth's magnetosphere. *Rev. Mod. Plasma Phys.* 1, 10. doi:10.1007/s41614-017-0011-4

frontiers | Frontiers in Astronomy and Space Sciences

TYPE Original Research
PUBLISHED 03 November 2022
DOI 10.3389/fspas.2022.1007240

OPEN ACCESS

EDITED BY
Oliver Allanson,
University of Exeter, United Kingdom

REVIEWED BY
Seong-yeop Jeong,
Northumbria University,
United Kingdom
Xinliang Gao,
University of Science and Technology of China, China

*CORRESPONDENCE
Scott Karbashewski,
scott.karbashewski@ualberta.ca

SPECIALTY SECTION
This article was submitted to Space Physics,
a section of the journal
Frontiers in Astronomy and Space Sciences

RECEIVED 30 July 2022
ACCEPTED 21 September 2022
PUBLISHED 03 November 2022

CITATION
Karbashewski S, Sydora RD and Agapitov OV (2022), Cascading parametric decay coupling between whistler and ion acoustic waves: Darwin particle-in-cell simulations.
Front. Astron. Space Sci. 9:1007240.
doi: 10.3389/fspas.2022.1007240

Cascading parametric decay coupling between whistler and ion acoustic waves: Darwin particle-in-cell simulations

Scott Karbashewski[1,2]*, Richard D. Sydora[2] and Oleksiy V. Agapitov[1]

[1]Space Sciences Laboratory, University of California, Berkeley, Berkeley, CA, United States, [2]Department of Physics, University of Alberta, Edmonton, AB, Canada

We present the results of numerical studies of the whistler wave parametric decay instability in the system with the suppressed Landau damping of ion acoustic waves (IAWs) based on the self-consistent Darwin particle-in-cell (PIC) model. It has been demonstrated that a monochromatic whistler wave launched along the background magnetic field couples to a counter-propagating whistler mode and co-propagating ion acoustic mode. The coupling of the electromagnetic mode to the electrostatic mode is guided by a ponderomotive force that forms spatio-temporal beat patterns in the longitudinal electric field generated by the counter-propagating whistler and the pump whistler wave. The threshold amplitude for the instability is determined to be $\delta B_w/B_0 = 0.028$ and agrees with a prediction for the ion decay instability: $\delta B_w/B_0 = 0.042$ based on the linear kinetic damping rates, and $\delta B_w/B_0 = 0.030$ based on the simulation derived damping rates. Increasing the amplitude of the pump whistler wave, the secondary and tertiary decay thresholds are reached, and cascading parametric decay from the daughter whistler modes is observed. At the largest amplitude ($\delta B_w/B_0 \sim 0.1$) the primary IAW evolves into a short-lived and highly nonlinear structure. The observed dependence of the IAW growth rate on the pump wave amplitude agrees with the expected trend; however, quantitatively, the growth rate of the IAW is larger than expected from theoretical predictions. We discuss the relevant space regimes where the instability could be observed and extensions to the parametric coupling of whistler waves with the electron acoustic wave (EAW).

KEYWORDS

plasma waves parametric decay, nonlinear whistler decay, wave-wave interactions, whistler waves, ion acoustic waves, self-consistent PIC model

1 Introduction

Finite-amplitude electromagnetic fluctuations known as whistler waves are frequently observed in the Earth's magnetosphere (Burtis and Helliwell, 1969; Maksimovic et al., 2001; Cattell et al., 2008) and solar wind (Lacombe et al., 2014; Tong et al., 2019; Agapitov et al., 2020; Cattell et al., 2021). They are known to play a significant role in regulating the electron populations in the radiation belt region (Thorne, 2010), especially during active periods of geomagnetic activity (Meredith et al., 2001; Reeves et al., 2013; Mourenas et al., 2014). In addition to the nonlinear interactions between the whistler waves and resonant electrons in this space plasma environment (Agapitov et al., 2015a), these waves contribute to heating and acceleration processes in the solar wind (Vocks et al., 2005) and magnetosheath regions (Huang et al., 2018). The nonlinear resonant wave-particle interaction manifests itself as the frequency chirping phenomena in the whistler mode chorus waves (Omura et al., 2008; Gao et al., 2014). Multiband chorus waves have been detected by the THEMIS satellites and nonlinear wave-wave coupling mechanisms have been proposed as a potential generation mechanism for this observation (Gao et al., 2016), and more recently, the origin of the chorus emission period has been linked to the drift velocity of energetic electrons (Gao et al., 2022). Furthermore, an analysis of waveforms from the Van Allen Probes has revealed possible parametric coupling between whistler waves and electron acoustic modes (Agapitov et al., 2015b).

Under certain conditions, large amplitude monochromatic plasma waves are nonlinearly unstable and can decay into other types of fluctuations. One such nonlinear process is the parametric decay instability in which a forward propagating parent wave decays into two daughter waves (Forslund et al., 1972). The decay instability has been investigated in whistler mode waves Umeda et al. (2014), circularly polarized Alfvén waves (Terasawa et al., 1986), Langmuir waves (Umeda and Ito, 2008), and light waves (Usui et al., 2002). In the parametric decay instability of parallel propagating whistler waves, a backward propagating daughter whistler wave and forward or backward ion acoustic or electron acoustic wave mode are involved. The instability threshold is determined by the product of the damping rates of the daughter waves, which can be large due to the increased Landau damping rate of the ion acoustic waves, particularly when the electron and ion temperatures are comparable in the plasma. When the ion and electron temperatures are comparable there is a possibility of parametric decay *via* an ion quasimode, however, this involves non-parallel propagation (Shukla, 1977).

Previous studies of the whistler wave parametric decay instability have been made using one and two-dimensional fully electromagnetic particle-in-cell (PIC) simulation models (Umeda et al., 2014, 2018; Ke et al., 2018). For a large amplitude pump whistler wave ($\delta B_w/B_o \sim 0.3$) and frequency near the electron cyclotron frequency, the energy of the electron bulk velocity supporting the parent wave is converted into thermal energy perpendicular to the background magnetic field. This increase of perpendicular thermal energy relative to parallel thermal energy triggered an electron temperature anisotropy instability which in turn, caused heating and acceleration of the electrons. For smaller amplitudes ($\delta B_w/B_o \sim 0.03$–0.07) and only parallel propagation, it was found that proton heating and field-aligned acceleration occurred through the Landau resonance due to the enhanced ion acoustic wave. Above $\delta B_w/B_o \sim 0.05$ it has been reported that a secondary parametric decay of the daughter whistler wave can occur (Karbashewski, 2017; Ke et al., 2017). Two-dimensional simulations indicate that the 2D decay instability is quite different compared to purely parallel propagation, with different time scales and wave-particle interaction dynamics (Umeda et al., 2017; Ke et al., 2018).

The purpose of this paper is to investigate the growth and subsequent nonlinear evolution of the parametrically unstable, parallel propagating electron whistler modes. Since the ion dynamics are essential, we use a magneto-inductive PIC simulation (Darwin model) (Busnardo-Neto et al., 1977) which allows for larger time steps due to the exclusion of the light wave branch. The threshold, growth rate, and saturation dynamics of the parametric decay instability are investigated and one of the main results is the establishment of the threshold condition for initiation of multiple decays of the daughter modes generated from the initial single wave decay process.

The organization of this paper is as follows: in Section 2 we detail the relevant theory for the coupling and parametric decay instability between whistler waves and ion acoustic waves and outline the setup of the UPIC simulation software; in Section 3 we present the simulation results and analysis of the parametric decay pathways; and in Section 4 we make a comparison of the simulation results with models, discuss relevant regimes for the observation of the instability, and summarize the main results.

2 Theory and modeling

2.1 Whistler-ion acoustic parametric decay

In this section, we present a model for the ponderomotive coupling and parametric decay of a whistler wave into daughter whistler and ion acoustic waves. We consider a uniform plasma with a background magnetic field oriented along the x-component of a Cartesian coordinate system, $\mathbf{B} = B_0\hat{\mathbf{x}}$. Electromagnetic and electrostatic waves are considered to propagate with wave vectors parallel to the background magnetic field and thus the transverse electromagnetic wave fields will be strictly in the yz-components, and the longitudinal electrostatic field is strictly in the x-component. The whistler wave dispersion relation for parallel propagation

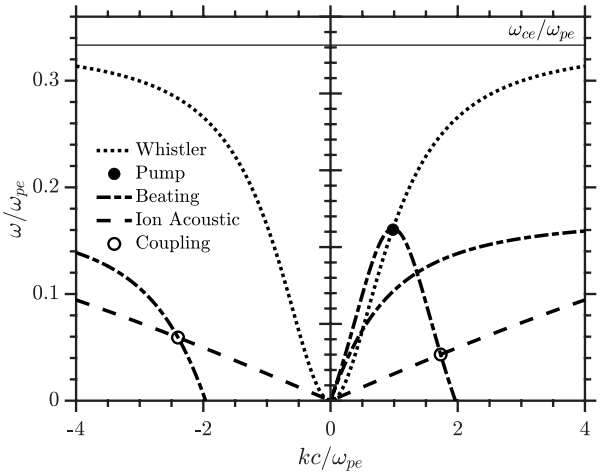

FIGURE 1
Ponderomotive coupling between whistler waves and ion acoustic waves. A pump whistler wave (black filled circle) creates ponderomotive beat patterns (black dash-dotted curve) with the whistler wave branch (black dotted curve). The ion acoustic branch (black dashed curve) is coupled to the pump whistler wave and whistler branch where it intersects with the pondermotive beating (black hollow circles). The solid black line indicates ω_{ce}/ω_{pe} =1/3.

with respect to the background magnetic field is derived from the cold plasma dispersion relation for magnetized plasmas, or Lassen-Appleton-Hartree equation, as, (Lassen, 1926; Appleton, 1927; Hartree, 1931; Gurnett and Bhattacharjee, 2005),

$$\frac{k^2c^2}{\omega_{pe}^2} \simeq 1 - \frac{\omega_{pe}}{\omega(\omega - \omega_{ce})} \tag{1}$$

where ω_{pe} is the electron plasma frequency and ω_{ce} is the electron cyclotron frequency; in formulating the dispersion ion motion has been neglected. Figure 1 is a plot of ω/ω_{pe} as a function of kc/ω_{pe} with Eq. 1 shown by the black dotted curve; ω_{ce}/ω_{pe} = 1/3 is used to construct the curve and is the same as the ratio used in the simulations presented herein. The parallel propagating whistler wave is a right-hand, circularly polarized, transverse electromagnetic wave that approaches a resonance at ω_{ce} as k increases. Near the resonance, the wavelength is on the order of the electron cyclotron radius and the phase velocity and group velocity of the whistler wave both approach zero. The wave-particle interactions are strong near resonance and the wave will experience cyclotron damping as energy is transferred to the electrons; as a result, the whistler branch is more strongly damped as k increases.

Ion acoustic waves (IAWs) are low-frequency electrostatic, longitudinal waves manifesting as oscillations of the plasma ions and electrons that are analogous to collisional sound waves in a gas. The dispersion relation for ion acoustic waves of singly ionized ions is dependent on both the temperature of the electrons, T_e, and ions, T_i, as well as the mass of the ions, M, and defines the ion acoustic velocity c_s,

$$c_s = \left(\frac{\gamma_e k_B T_e}{M}\frac{1}{1 + k^2\lambda_{De}^2} + \frac{\gamma_i k_B T_i}{M}\right)^{1/2} \tag{2}$$

where k_B is the Boltzmann constant, λ_{De} is the electron Debye length, and γ_s is the heat capacity ratio with $\gamma_i = 3$ for ions in one-dimension and $\gamma_e = 1$ for isothermal electrons (Chen, 1984). Ion acoustic waves experience heavy Landau damping by ions moving at velocities near the ion acoustic phase velocity, thus the waves become significant only when $T_e \gg T_i$ and the contribution of the ion temperature term becomes negligible. Under this assumption, an inspection of Eq. 2 reveals that the ion acoustic wave has a nearly linear relationship between ω and k until $k^2\lambda_{De}^2 \gg 1$, at which point the ion acoustic wave approaches a resonance at the ion plasma frequency ω_{pi}; this condition is only for large k and for the relevant parameter space of the present study the ion acoustic wave is dispersionless ($c_s^2 \approx k_B T_e/M$). The dashed black curve in Figure 1 shows Eq. 2 for the parameters used in the simulation, which will be detailed in Section 2.2.

The coupling of whistler waves, which are transverse electromagnetic waves, and ion acoustic waves, which are longitudinal electrostatic waves, is achieved through the ponderomotive force, or Miller force (Miller, 1958). The ponderomotive force is a nonlinear effect that has been used to describe many plasma phenomena, such as the self-focusing of lasers in a plasma (Max, 1976), electromagnetic-electrostatic mode conversion in non-uniform plasmas (Morales and Lee, 1974), and density structures in the auroral ionosphere (Bellan and Stasiewicz, 1998). The force arises due to spatial variations in the amplitude of an oscillating electric field $\delta\mathbf{E} = \mathbf{E}_s(\mathbf{r})\cos(\omega t)$; the force per m^3 on the electrons in a plasma is (Chen, 1984),

$$\mathbf{F_p} = -\frac{\epsilon_0}{2}\frac{\omega_{pe}^2}{\omega^2}\nabla\langle E_s^2\rangle \tag{3}$$

where $\langle \ldots \rangle$ indicates a time average over the period of the wave, $2\pi/\omega$. The force is the same for both electrostatic and electromagnetic perturbations though the mechanism behind the force is different. In the electrostatic case, particles are forced into regions of lower field amplitude by the larger electric force in high field regions. In the case of an electromagnetic wave, the force arises from a second order Lorentz $\mathbf{v} \times \mathbf{B}$ force along the wave vector that varies with the spatial variation of the electric field. In both cases, the Miller force due to the spatial variations of the electric field results in a build-up of particle density in lower field regions. Equation 3 is for electrons, but one can see that the ponderomotive force is proportional to the spatial gradient of the electric field as well as the density of the region and will therefore be felt by all charged particles. However, because of the mass dependence, the effect is smaller for ions relative to the force on electrons by a

factor of m_e/M. Thus, the ponderomotive force on the ions can often be neglected; however, at low frequencies, the ions will respond to the charged regions created by the ponderomotive force on electrons.

A subset of nonlinear wave-wave interactions are known as parametric decay instabilities and involve a three-wave coupling between a pump wave and two daughter modes. The three coupled waves involved must satisfy a set of matching conditions Neubert (1982).

$$\omega_w = \omega_T \pm \omega_L \tag{4}$$

$$\mathbf{k}_w = \mathbf{k}_T \pm \mathbf{k}_L \tag{5}$$

Where the subscript w refers to the pump wave, the subscript T refers to the transverse daughter wave, and the subscript L is the longitudinal daughter wave. In Section 3 we present 1-D PIC simulations designed to observe parametric coupling of an imposed, monochromatic, pump whistler wave with daughter whistler and IAW waves that exist in the plasma as thermal modes. The pump whistler forms spatial beats in the transverse electric fields with each of the thermal whistler modes and this sets up a ponderomotive force in the parallel direction equal to,

$$\mathbf{F_P} = -\frac{\epsilon_0}{2}\frac{\omega_{pe}^2}{\omega^2}\nabla\langle(\mathbf{E}_w + \mathbf{E}_T)^2\rangle \simeq -\epsilon_0\frac{\omega_{pe}^2}{\omega_B^2}\nabla\langle\mathbf{E}_w \cdot \mathbf{E}_T\rangle \tag{6}$$

where we assume a uniform pump wave with $\langle E_w^2\rangle = 0$, the gradient of the $\langle E_T^2\rangle$ term is small and may be discarded, and only the cross term $\langle \mathbf{E}_w \cdot \mathbf{E}_T\rangle$ will contribute to the ponderomotive force. Here, we denote all of the whistler modes apart from the pump as $\mathbf{E}_T$. The ponderomotive beating will force low amplitude electrostatic perturbations parallel to B_0 with frequency $\omega_B = \omega_w - \omega_T$ and wavenumber $k_B = k_w - k_T$ when $\omega_w > \omega_T$, and frequency $\omega_B = \omega_T - \omega_w$ and wavenumber $k_B = k_T - k_w$ when $\omega_T > \omega_w$. In Figure 1 the pump whistler is indicated by a filled black circle and the ponderomotive beating patterns are indicated by the dash-dotted curves. In Section 3 we will demonstrate that this ponderomotive beating of the whistler branch with a monochromatic pump does form low amplitude electrostatic wave perturbations with the pattern predicted in Figure 1.

The ponderomotive beating branch facilitates coupling to an ion acoustic mode at (k_L, ω_L), so long as $k_B \approx k_L$ and $\omega_B \approx \omega_L$, and forms a set of three coupled waves between the pump, daughter whistler, and daughter IAW. The ponderomotive force will drive the growth of the resonant IAW which will in return drive the growth of the resonant daughter whistler. The location of the electrostatic coupling in ωk-space between the electromagnetic whistler modes and electrostatic IAW occurs at the intersections of the pondermotive beating and IAW branch; this is indicated in Figure 1 by the hollow circles. For the present electrostatic mode, only beating with counter-propagating whistler waves will lead to a parametric decay channel.

In the regime where $\omega_{ce} < \omega_{pe}$ the whistler wave pump generates parametric instabilities above a certain threshold amplitude. The parametric instability that is dominant over a wide range of parameters is the ion decay instability. Near the threshold amplitude, with the matching conditions satisfied, the threshold is given by (Nishikawa, 1968; Forslund et al., 1972),

$$\left(\frac{B_w}{B_o}\right)^2 > 8\left(1 + \left(\frac{ck_w}{\omega_{pe}}\right)^2\right)\beta_e\left(\frac{\gamma_T}{\omega_T}\right)\left(\frac{\gamma_L}{\omega_L}\right) \tag{7}$$

where k_w is the pump wavenumber, electron plasma beta is defined as $\beta_e = 8\pi nT_e/B_o^2$, and γ_T and γ_L are the damping rates of the transverse and longitudinal daughter modes, respectively. The frequency and wavenumber matching conditions require $\omega_L \simeq 2k_w c_s$ and $\omega_T \simeq \omega_w$ at $-k_w$. Therefore, the product of the linear damping rates of the transverse and longitudinal daughter modes essentially determines the threshold amplitude needed to excite the parametric decay instability. These damping rates can be computed from linear kinetic theory to give an estimate of threshold pump wave amplitude.

Above threshold, the real frequency and maximum growth rate of the parametrically unstable ion wave are given by $\omega \approx \omega_L + i\Gamma$, where $\omega_L \simeq 2k_w c_s$ and,

$$\frac{\Gamma}{\omega_T} \simeq \sqrt{\frac{\omega_{ci}}{\omega_L}}\frac{B_w}{B_o} \tag{8}$$

This result implies that the growth rate scales linearly with pump wave amplitude and is inversely proportional to the square root of the ion mass. These analytical results will be used to compare with the simulations. We mention here that the equation for the ion wave growth rate is obtained from the dispersion relation for the three-wave mode coupling presented in (Forslund et al., 1972).

2.2 Simulation setup

To investigate the nonlinear growth and saturation of the parametric decay instability for parallel propagating monochromatic whistler waves the Darwin particle-in-cell (PIC) simulation model is used and based on the spectral code developed as part of the UCLA particle-in-cell (UPIC) framework (Decyk, 2007). The simulation has previously been used to model the whistler wave instabilities driven by the temperature anisotropy in the solar wind and Earth's magnetosphere (Hughes et al., 2016).

The Darwin PIC model removes the transverse component of the displacement current in Ampere's law, therefore, the high-frequency light waves are excluded while leaving the other waves, such as the whistler wave, unaffected (Busnardo-Neto et al., 1977). In comparison to the conventional explicit electromagnetic PIC model, the Darwin PIC method is more computationally efficient since the Courant condition for the

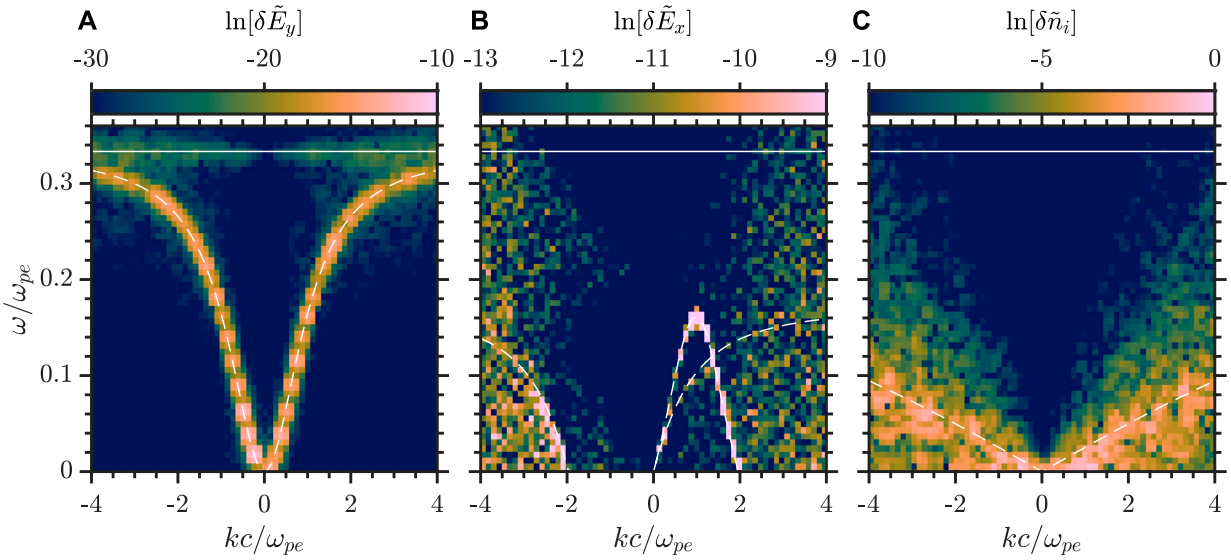

FIGURE 2
(A) Whistler branch visible in $\delta\tilde{E}_y$ in a cold electron, fixed ion simulation. **(B)** Ponderomotive coupling pattern in $\delta\tilde{E}_x$ for a low amplitude pump whistler ($\delta B_w/B_0$=0.1) in a cold electron, fixed ion simulation. **(C)** Ion acoustic branch seen in $\delta\tilde{n}_i$ in a hot electron, cold ion simulation (T_e/T_i =100). The solid line in each is ω_{ce}/ω_{pe} and the dashed curves represent the respective branch shown in each panel.

time step is not restricted to following the light waves. The grid spacing, Δ_x, is required to resolve the Debye length to avoid numerical heating of the plasma. Since we focus on the parametric decay of the parallel propagating whistler wave, a 1-D PIC simulation model with periodic boundary conditions is utilized. Fully 3-D electromagnetic fields and velocities are included but only spatial variation in the x-direction is present. A uniform background magnetic field is imposed along the x-axis.

The UPIC code uses dimensionless parameters where time is normalized to the plasma frequency, $t \rightarrow \omega_{pe}t$, space is normalized to the grid spacing, $x \rightarrow x/\Delta_x$, where the grid spacing is determined by the dimensionless thermal velocity of the electrons $v_{te} \rightarrow v_{te}/\Delta_x\omega_{pe}$ and is an input to the code, the charge of each species s is normalized to the elementary charge, $q_s \rightarrow q_s/e$, the mass of each species is normalized to the mass of an electron, $m_s \rightarrow m_s/m_e$, and these provide the necessary normalizations for all other quantities (Decyk, 2007). The simulation input parameters used, unless otherwise stated, are the time step $\Delta_t = 0.2\omega_{pe}t$, electron thermal velocity $v_{te} = 1.00$, number of time steps $N_t = 5001$, number of grid cells $N_x = 512$, number of particles per species $N_p = 184320$, and cyclotron frequency $\omega_{ce}/\omega_{pe} = 1/3$, $c/\omega_{pe}\Delta_x = 10$, electron-ion temperature ratio $T_e/T_i = 100$, and electron-ion mass ratio $M/m_e = 16$.

The choice of the low mass ratio is justified and made for several reasons: (i) computational efficiency, higher mass ratios require significantly more time steps to resolve the long time scales associated with ion dynamics and require a larger spatial grid to achieve sufficient k-space resolution; (ii) increasing the IAW frequency to the order of the whistler waves, this makes the illustration of the dynamics in both simulations and theoretical descriptions more clear; and (iii) part of the motivation for this work is a similar process that could occur for the EAW, the low mass ratio IAW decay is a precursor for studies of the EAW with a similar dispersion.

The UPIC code was modified to enable the external driving of transverse electric fields. The whistler wave driving is accomplished by adding sinusoidal wave fields each iteration to the self-consistent electric fields; the amplitude is slowly increased as the system responds to the external fields and when done correctly the wave continues to propagate once the driver is turned off. To launch a whistler wave the external driver needs to be right-hand circularly polarized and the external electric fields added to the self-consistent fields are.

$$E_{wz} = E_w(t)\cos(k_w x - \omega_w t) \quad (9)$$

$$E_{wy} = E_w(t)\sin(k_w x - \omega_w t) \quad (10)$$

In all simulations, the amplitude $E_w(t)$ increases linearly to some maximum at $\omega_{pe}t = 100$ and the driver fields are eliminated. The driven wave mode is chosen to have $\omega_w \approx 0.161\omega_{pe}$ and $k_w c/\omega_{pe} \approx 0.98$ corresponding to mode number $m_w = 8$ where $k = 2\pi m/N_x$. The amplitude of the self-consistently propagating electromagnetic wave is determined from the magnetic field at $\omega_{pe}t = 150$. It is not necessary to perturb the transverse magnetic fields and velocities as the system will respond each iteration to the pumped electric fields and set up the necessary conditions for the wave to continue propagating if the pump is matched to a real

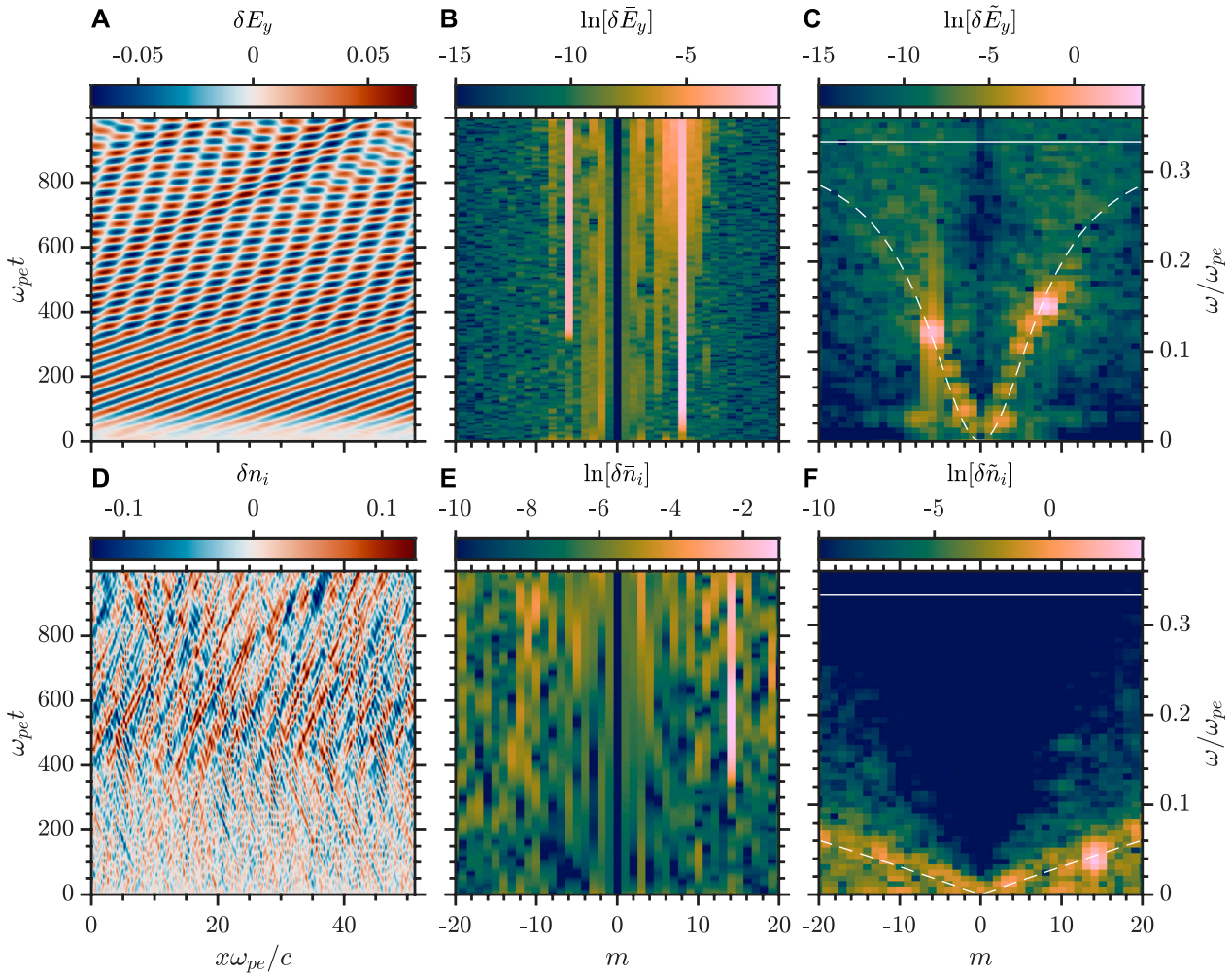

FIGURE 3
Single parametric decay of whistler wave with $\delta B_w/B_0$=0.032 **(A)**,**(B)**, and **(C)** *xt*-space, *mt*-space, and *mω*-space of δE_y, respectively **(D)**,**(E)**, and **(F)** *xt*-space, *mt*-space, and *mω*-space of δn_i, respectively. Dashed curves indicate the whistler and IAW branches in **(C)** and **(F)**, respectively, and the solid line is ω_{ce}/ω_{pe}. The mode number m is related to the wave number by the relation $k = 2\pi m/N_x$.

mode of the plasma. Additionally, since a parallel whistler mode has no longitudinal component the particles are loaded uniformly at time $\omega_{pe}t = 0$.

3 Results

We begin this section by demonstrating with the PIC simulation the ponderomotive beating model outlined in Section 2.1. Throughout this section a quantity A in *xt*-space may be shown in *kt*-space and *mω*-space (i.e. *kω*-space); the spatially Fourier transformed quantity will be denoted as $\bar{A}$ and the spatio-temporally Fourier transformed quantity will be denoted as $\tilde{A}$. Figure 2A shows the transverse electric field fluctuations $\delta\tilde{E}_y$ and illustrates the thermal whistler branch in a simulation where the ions remain fixed, the wave driver is kept off, and the electrons are relatively cold at $v_{te} = 0.10$ to reduce the cyclotron damping at frequencies close to ω_{ce}. The theoretical curve for the whistler branch from Figure 1 is shown by the white dashed line and is in excellent agreement with the simulation. It is these low amplitude whistler waves that will form spatial beats in the transverse electric fields with the pump wave to produce the ponderomotive force along x.

Figure 2B shows the longitudinal field fluctuations $\delta\tilde{E}_x$ for the same simulation parameters but with the driven wave launched with an amplitude of $\delta B_w/B_0 \sim 0.1$. With no electrostatic wave to couple to due to the fixed ions, the low amplitude ponderomotive beating patterns are observed and

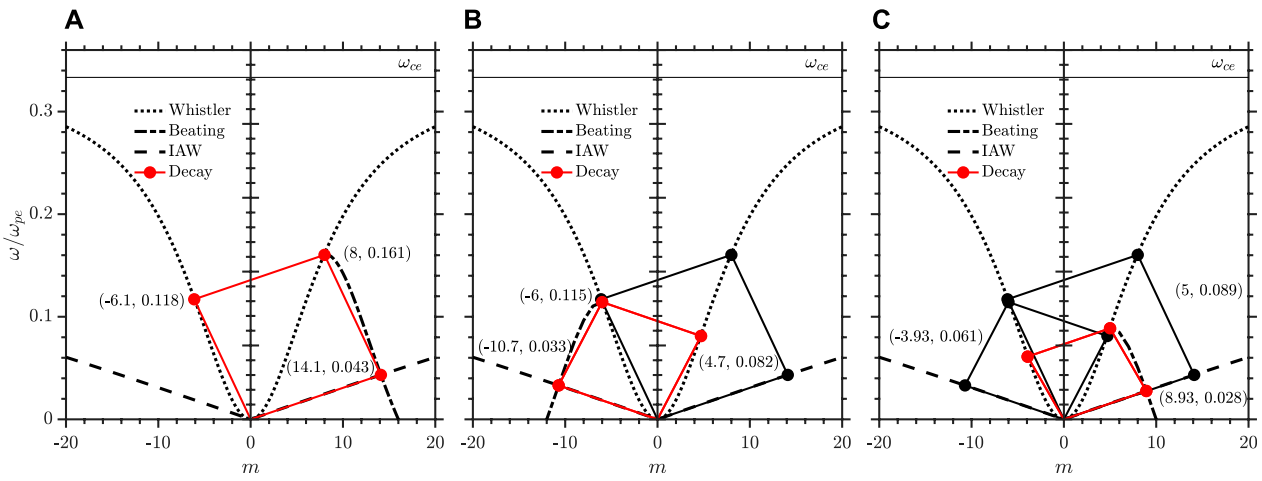

FIGURE 4
Cascading parametric decay paths. The dotted curve is the whistler branch, the dash-dotted black curve is the ponderomotive beating with the counter-propagating low-frequency whistlers, and the dashed black line is the ion acoustic wave. The parametric 3-wave coupling is indicated by the solid red curve where the (*x*, *y*) pairs in each panel are the locations of the red circles **(A)** Primary decay of pump whistler wave. **(B)** Secondary decay of the daughter whistler wave. **(C)** Tertiary decay of the secondary daughter whistler wave.

show remarkable agreement with the theoretical curves. The beating with whistler waves higher than the pump is suppressed relative to the low-frequency waves, as is the beating with co-propagating waves when compared to the counter-propagating waves; thus it may be expected that the dominant decay path will involve the lower frequency counter-propagating whistler and co-propagating IAW highlighted in Figure 1. Next, the electron thermal velocity is returned to the nominal value of $v_{te} = 1.00$, the moving ions are introduced and the driven wave is removed; the resulting thermal ion acoustic fluctuations in $\delta\tilde{n}_i$ are shown in Figure 2C and again are in good agreement with the predicted dispersion.

The ingredients for observing the parametric decay of the whistler wave are all contained in Figure 2 and demonstrate the ponderomotive model. The inclusion of the pump wave with the nominal simulation parameters creates the situation where the parametric decay may be observed for a large enough amplitude pump. The first observed decay activity occurs at $\delta B_w/B_0 = 0.028$. Figure 3 shows the simulation result for a pump wave with amplitude $\delta B_w/B_0 = 0.032$. In Figure 3A the xt-space evolution of δE_y shows the linear growth of the pump whistler and its subsequent self-consistent propagation after $\omega_{pe}t = 100$. In Figure 3B the same is seen at mode number $m = 8$ in kt-space. At $\omega_{pe}t \approx 350$ we observe the rapid growth of a monochromatic electromagnetic wave counter-propagating to the pump wave. This is confirmed as a whistler wave in Figure 3C where the pump mode and a daughter whistler mode are observed at $m_w = 8$ and $m_{T1} = -6$ along the whistler branch.

In Figure 3D, E we observe the growth of an electrostatic structure in δn_i and $\delta\bar{n}_i$, respectively, coinciding with the growth of the whistler wave at $\omega_{pe}t \approx 350$. The $k\omega$-space of $\delta\tilde{n}_i$ in Figure 3F shows this is an ion acoustic daughter wave at $m_{L1} = 14$. The parametric decay conditions in Eqs 4, 5 for the wave frequency and mode number yield: $\omega_{T1} + \omega_{L1} = (0.119 + 0.038)\omega_{pe} = 0.157\omega_{pe}$ and $m_{T1} + m_{L1} = -6 + 14 = 8$; this is approximately equal to ω_w and matches m_w. Figure 4A shows the expected parametric decay path for a counter-propagating daughter whistler wave with $\omega_T < \omega_w$; a comparison of the theoretical and observed decay shows a small difference due to the non-integer mode numbers that are unavailable to the spectral code.

In Figure 1 we highlighted that there were two possible locations for coupling to the ion acoustic wave in $k\omega$-space by a given pump wave; for both couplings, the daughter whistler wave is counter-propagating with the pump wave, however, one corresponds to $\omega_T < \omega_w$ and the other to $\omega_T > \omega_w$. While the latter is certainly a possible decay channel, the former dominates and this is likely due to the increased cyclotron damping of the higher whistler modes. This is supported by the amplitude of the pondermotive beat modes in Figure 2B that show beats with $\omega_T < \omega_w$ whistler modes are the strongest and the beating becomes nearly non-existent as ω_T approaches ω_{ce}. Though not investigated here, the coupling to the counter-propagating IAW and counter-propagating whistler with $\omega_T > \omega_w$ could conceivably occur under the right conditions.

Figure 5 presents the simulation result for a pump wave with amplitude $\delta B_w/B_0 = 0.052$ in the same format as Figure 3. The

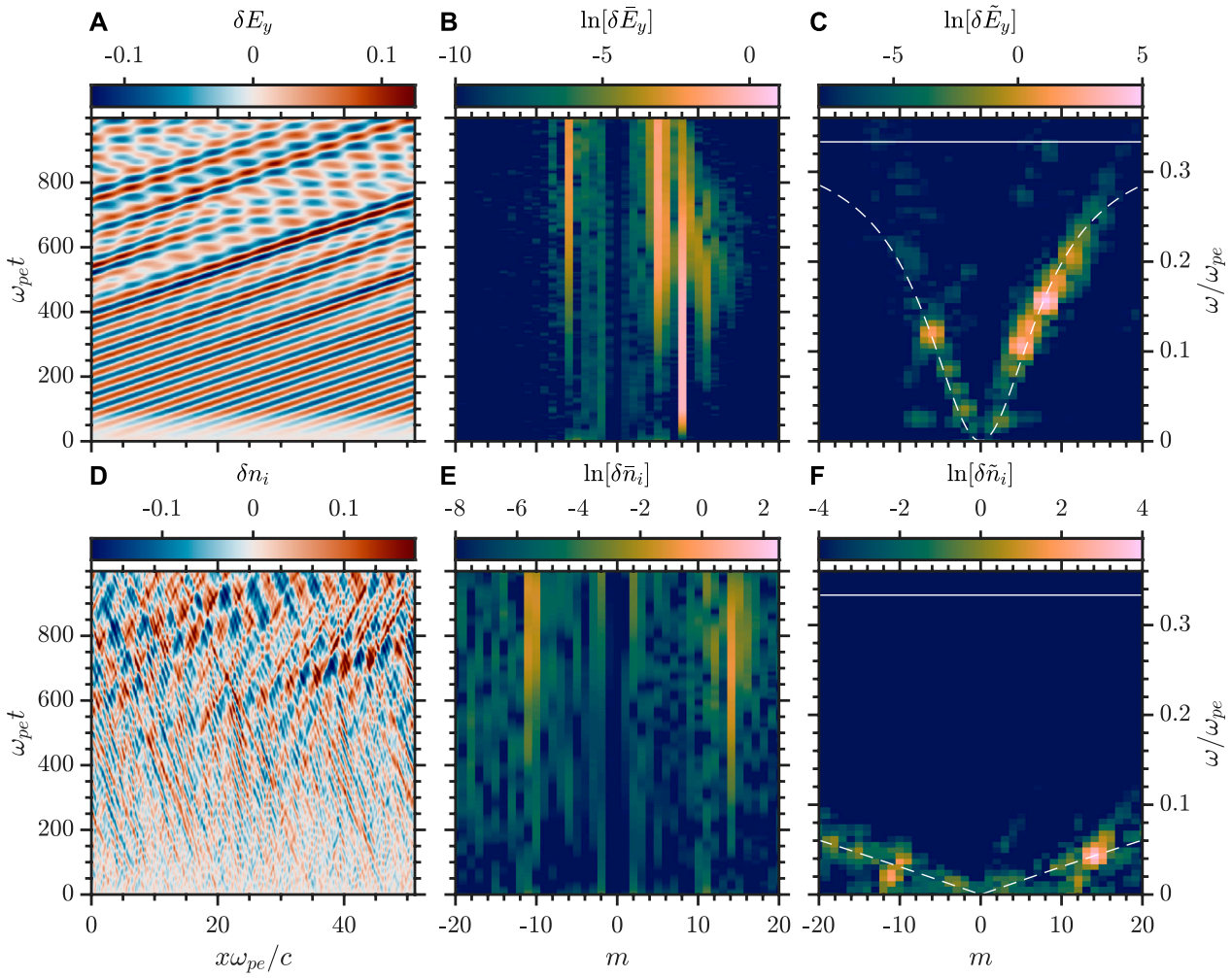

FIGURE 5
Double parametric decay of whistler wave with $\delta B_w/B_0$=0.052 **(A)**,**(B)**, and **(C)** xt-space, mt-space, and $m\omega$-space of δE_y, respectively **(D)**,**(E)**, and **(F)** xt-space, mt-space, and $m\omega$-space of δn_i, respectively. Dashed lines indicate the whistler and IAW branches in **(C)** and **(F)**, respectively, and the solid line is ω_{ce}/ω_{pe}.

growth of the $T1$ wave begins earlier at $\omega_{pe}t \approx 200$ but the rate of the growth is considerably reduced as seen in the panel of $\delta \bar{E}_y$. The $T1$ mode is accompanied by the simultaneous and more rapid growth of another electromagnetic mode; this is confirmed to be a counter-propagating (with respect to $T1$) whistler wave, $T2$, at $m_{T2} = 5$ and $\omega_{T2} = 0.107\omega_{pe}$. In the ion fluctuations, there is first the growth of the $L1$ mode and this is followed by the growth of a co-propagating (with respect to $T1$) ion acoustic structure, $L2$, at $m_{L2} = -11$ and $\omega_{L2} = 0.019\omega_{pe}$.

The observed decay path is still the primary decay seen at lower pump amplitudes, however, this is accompanied by a secondary decay. The growth of the primary decay is significantly reduced due to the cascade of energy to the secondary decay as the pump wave drives the growth of all four daughter waves. The expected matching conditions of the secondary decay channel are shown in Figure 4B, where $m_{T1} = -6$ is explicitly used as the intermediate pump wave, and agree favourably with the simulation results. Notably, the mode numbers again are non-integers and this explains the small discrepancies between the simulation and prediction. The threshold for the secondary decay occurs at $\delta B_w/B_0 \approx 0.036$ and can be identified by a rapid reduction in the growth rate of the primary daughter modes as will be discussed in Section 4.

Increasing the pump wave further to $\delta B_w/B_0 \gtrsim 0.063$ results in a tertiary decay channel of another counter-propagating whistler wave and IAW to $L1$. This is shown in Figure 6 for $\delta B_w/B_0 = 0.103$ in the same format as Figures 3, 5. In the δE_y and $\delta \bar{E}_y$ plots we observe a larger growth rate for

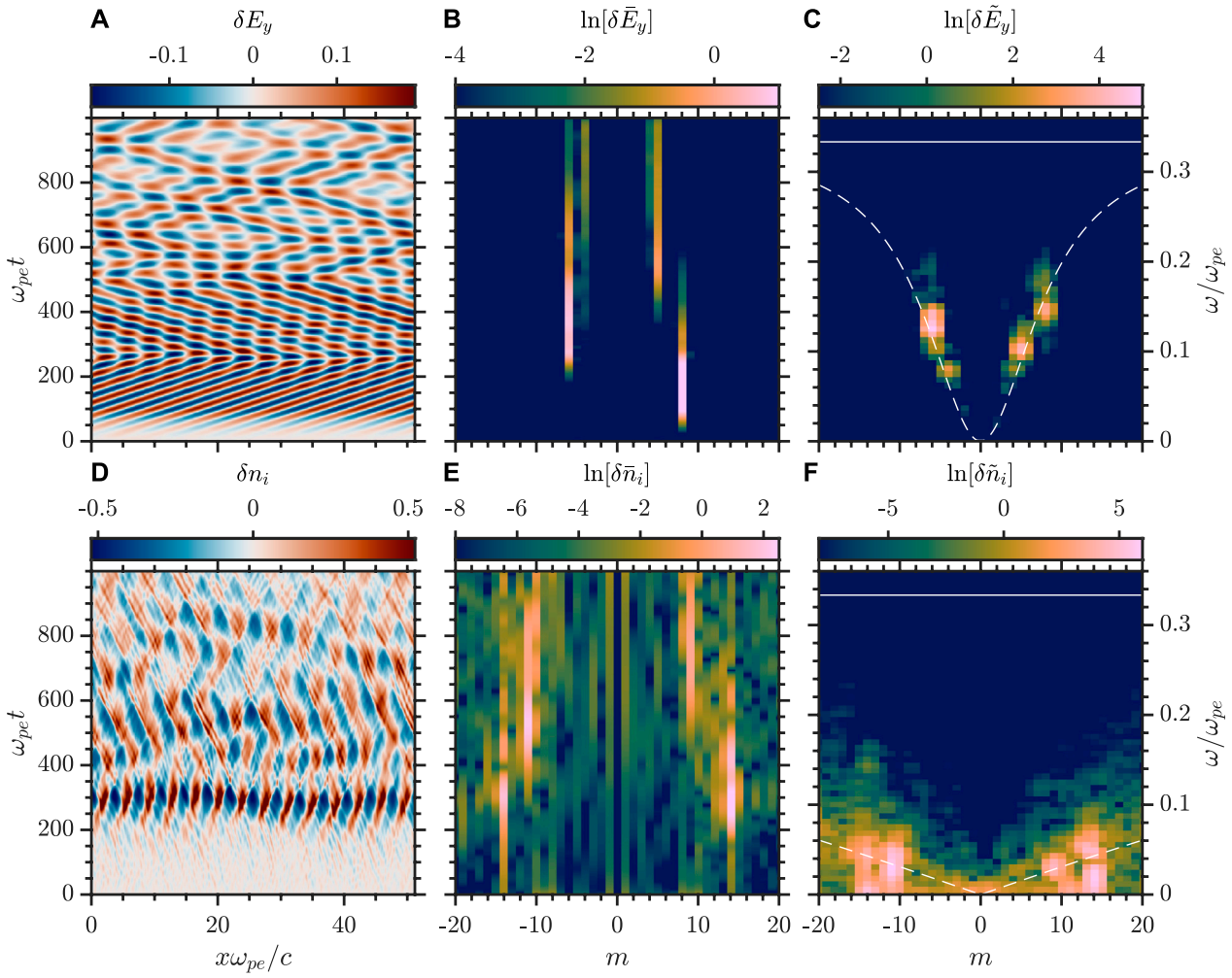

FIGURE 6
Triple parametric decay of whistler wave with $\delta B_w/B_0$=0.103 **(A)**,**(B)**, and **(C)** xt-space, mt-space, and $m\omega$-space of δE_y, respectively **(D)**,**(E)**, and **(F)** xt-space, mt-space, and $m\omega$-space of δn_i, respectively. Dashed lines indicate the whistler and IAW branches in **(C)** and **(F)**, respectively, and the solid line is ω_{ce}/ω_{pe}.

the primary decay, followed by the secondary, and finally the tertiary, $T3$ mode. However, in the δn_i and $\delta \bar{n}_i$ panels the $L1$ structure is observed to grow to a very large amplitude at $\omega_{pe}t \approx 300$ and become highly nonlinear; this is evidenced by the development of a mirror mode at $m^{\star}L1 = -14$ and the zero frequency content at m_{L1} and $m^{\star}_{L1}$ in the $\delta \bar{n}_i$ plot. The structure initially propagates with the ion acoustic velocity but slows and becomes nearly stationary as the wave steepens; the structure is short-lived and decays rapidly as energy cascades to the other daughter modes. Given the continuous cascade of parametric decays, it is interesting this over-driven primary IAW regime does not lead to a quaternary decay or even higher decay channels that provide a sink for the excess pump energy.

The electromagnetic modes remain linear and follow a clearly defined decay path with all four whistler modes highlighted in the $\delta \tilde{E}_y$ plot; similarly, apart from the zero frequency modes, the three daughter IAWs are observed in $\delta \tilde{n}_i$. The tertiary whistler mode $T3$ has $m_{T3} = -4$ and $\omega_{T3} = 0.075\omega_{pe}$, and the tertiary IAW $L3$ has $m_{L3} = 9$ and $\omega_{L3} = 0.031\omega_{pe}$. These modes meet the matching conditions with $T2$ and are close to the expected decay channel in Figure 4C.

Lastly, we investigate a case with cascading parametric decays for a higher mass ratio of $M/m_e = 400$ to demonstrate the universality of the effect. The grid size has been expanded to $N_x = 2048$, while the number of particles per cell has been kept constant by increasing the total number of particles per species to

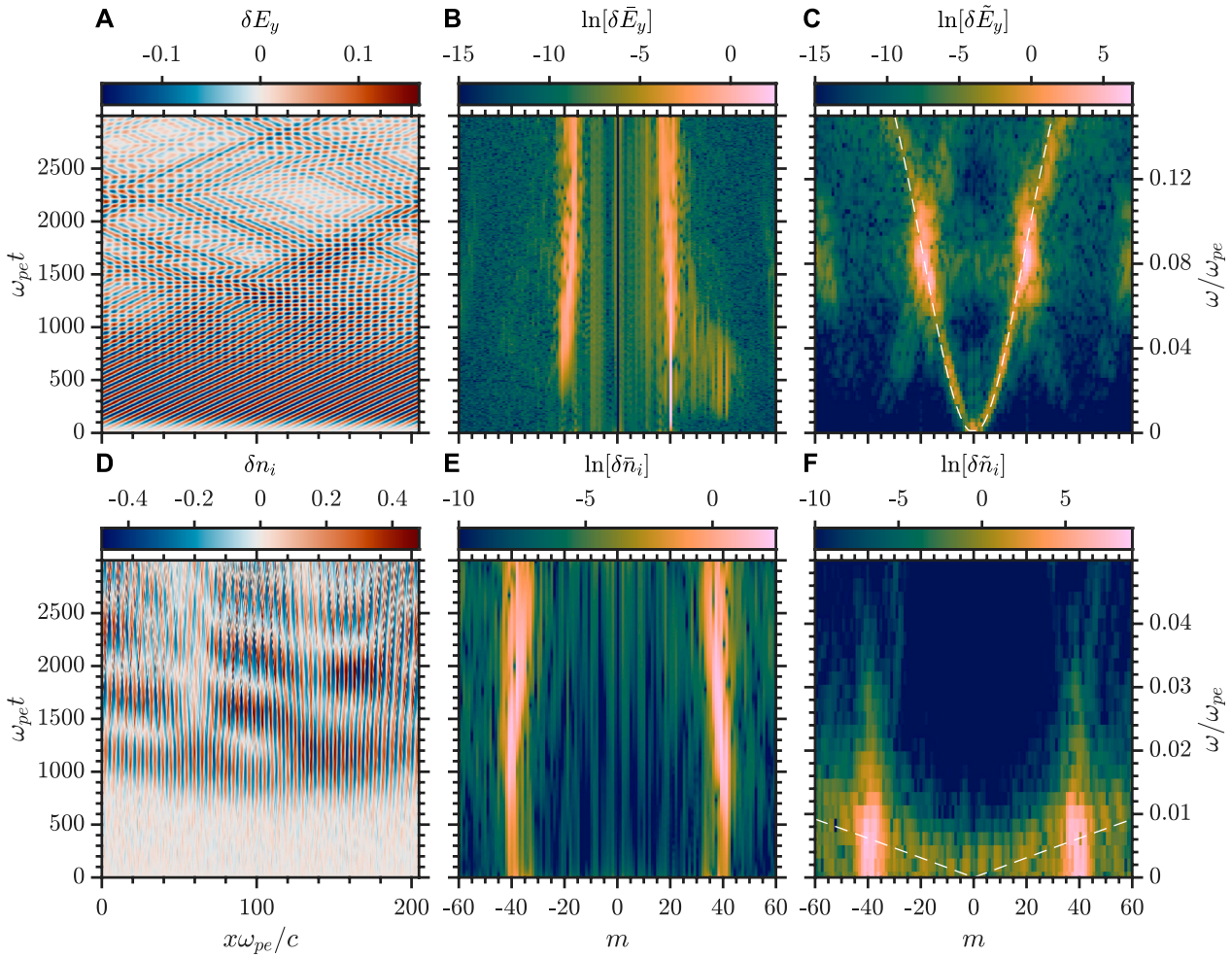

FIGURE 7
Triple parametric decay of whistler wave with $\delta B_w/B_0$=0.095 with a mass ratio of M/m_e =400 **(A)**,**(B)**, and **(C)** xt-space, mt-space, and $m\omega$-space of δE_y, respectively **(D)**,**(E)**, and **(F)** xt-space, mt-space, and $m\omega$-space of δn_i, respectively. Dashed lines indicate the whistler and IAW branches in **(C)** and **(F)**, respectively, and the solid line is ω_{ce}/ω_{pe}.

N_p = 737280. We choose here to pump mode number m_w = 20 ($\omega_w \approx 0.09$) — and not m_w = 32 for a direct comparison to the smaller grid—to keep the dynamics in xt-space more easily visible; this is expected to somewhat reduce the threshold for instability, and indeed the primary decay threshold is observed to be $\delta B_w/B_0 \approx 0.02$, however, to observe a cascade still requires the amplitude to be well above the threshold. The small IAW frequency at the relevant mode numbers for decay to occur means that the whistler modes involved have very little spread in frequency and mode number compared with the previous cases; the primary decay has $m_{T1} = -19$ and $\omega_{T1} \approx 0.08$ for the daughter whistler, and M_{L1} = 39 and $\omega_{T1} \approx 0.01$ for the daughter IAW. Thus, any cascade will be observed as a sequential decrease in mode number for the subsequent daughter modes. Figure 7 presents the cascade at the higher mass ratio in the same format as the previous cases. It is clear from the evolution of the dominant mode numbers in the mt-space diagrams that a parametric decay cascade is occurring. We again observe nonlinear and nearly stationary structures in the ion density as there is considerable power in the zero-frequency modes.

4 Discussion

In this section, we discuss the dynamics of the daughter wave growth, parametric instability thresholds, relevance to the radiation belts and solar wind, and finish with a summary of the main results. Figure 8 displays the evolution of the field and particle energies and the mode growth for the triple parametric decay case in Figure 6. Figure 8A displays the fractional transverse and longitudinal electric field energy, relative to the total electric field energy; Figure 8B displays the fractional energy

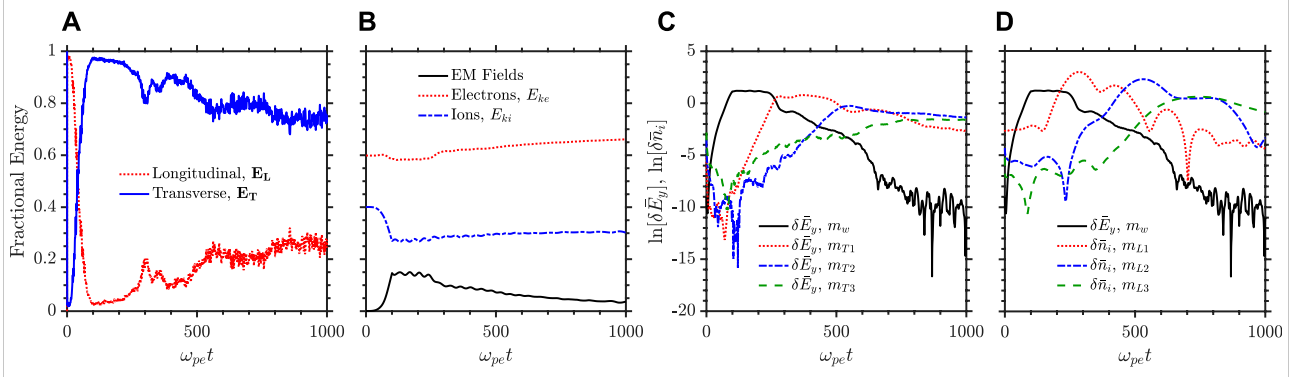

FIGURE 8
Analysis of energy transfer and wave growth during the triple decay for $\delta B_w/B_0$=0.103 **(A)** Fractional electric field energy that is contained in the longitudinal electric field (red dotted curve) and transverse electric field (blue solid curve) **(B)** Fractional energy of the electromagnetic fields (black solid curve), electron kinetic energy (red dotted curve), and ion kinetic energy (blue dash-dotted curve) **(C)** and **(D)** growth of the parametric decay modes for the daughter whistler and ion acoustic waves, respectively. The solid black curve is the pump whistler, the red dotted curve is the primary decay, the blue dash-dotted curve is the secondary decay, and the green dashed curve is the tertiary decay.

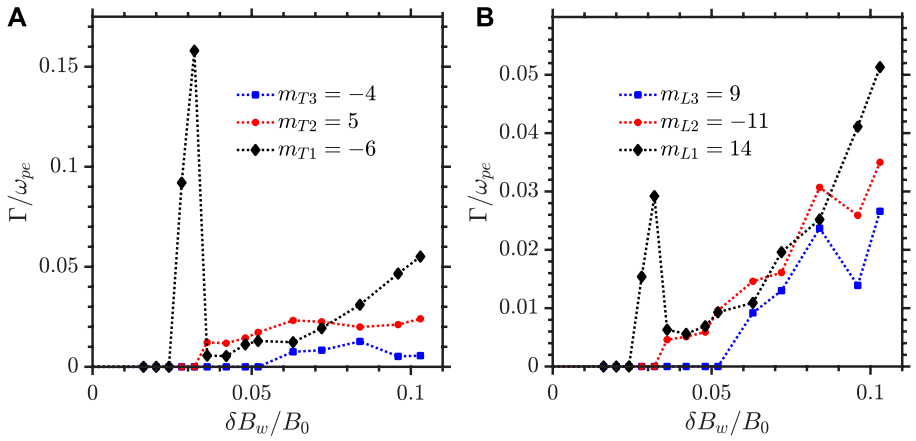

FIGURE 9
Growth rates of whistler and IAW modes as the pump amplitude, $\delta B_P/B_0$, increases show clear transitions between single, double and triple decay **(A)** Whistler modes. **(B)** IAW modes.

of the electromagnetic fields and kinetic energies of the electrons and ions; and Figures 8C, D show the m vs t growth of the whistler and IAW daughter modes, respectively. The initial ramp of the driven whistler wave puts the majority of the field energy into the transverse component. The first decay of the pump and subsequent growth of the nonlinear ion acoustic structure occurs at $\omega_{pe}t$ = 300 and rapid transfer of energy from the transverse to the longitudinal electrostatic field occurs simultaneously. This is accompanied by a small growth in the electron and ion kinetic energies (**B**), though only minimal heating is observed throughout the decay process. The growth of the primary decay is rapid and the whistler wave $T1$ experiences only slight damping (**C**) in comparison to the IAW damping (**D**); this results in the growth of the transverse fraction compared to the longitudinal. Each subsequent decay is observed in the fractional electric field energy (**D**) as an increase in the longitudinal fraction and subsequent decay.

The growth rates, γ/ω_{pe}, of the daughter modes can be extracted from the mt-space for each pump wave amplitude. Figure 9 shows these growth rates from $\delta B_w/B_0 \sim 0.016$–$0.103$. The scaling of the growth rate for the ion acoustic mode with pump mode amplitude is shown in Figure 9B and this agrees with the trend obtained in Eq. 8. Quantitatively, the theoretical growth rates are lower than the simulation values indicating that modifications to the theory are needed in this parameter regime.

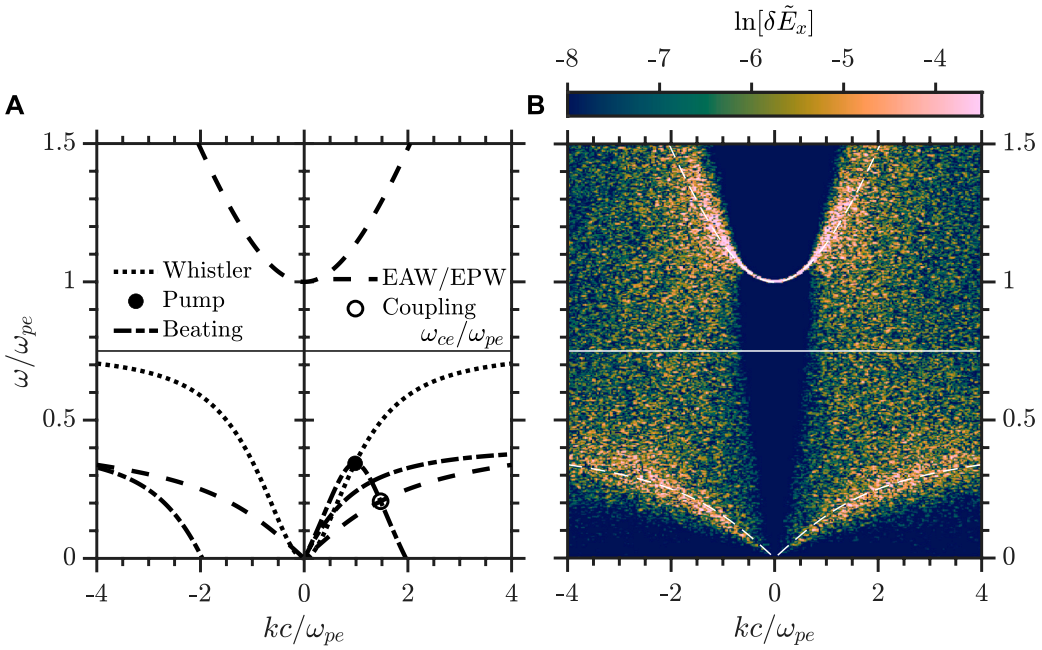

FIGURE 10
Ponderomotive coupling between whistler waves and electron acoustic waves (EAW). **(A)** In the same format as Figure 1, the pondermotive beating of the pump whistler wave and whistler branch can couple to the electron acoustic wave of a two-electron-species plasma **(B)** Demonstration of the electron acoustic mode in the UPIC simulation using T_h/T_c =100, *vth* =3.16 (v_{tc} =0.316), n_h =0.9n_e (n_c =0.1n_e), and ω_{ce}/ω_{pe} =3/4.

The threshold value of the single parametric decay instability from the simulations is $\delta B_w/B_0 \sim 0.028$ and the theoretical value obtained from Eq. 7 is found to be $\delta B_w/B_0 \sim 0.042$, using the linear kinetic theory results for the daughter mode damping rates. This discrepancy is possibly due to the linear orbit approximations used to compute the damping rates. Damping rates used from the simulation, Figure 8D, gives a threshold value of $\delta B_w/B_0 \sim 0.030$ which is in closer agreement with the measured simulation value.

At $\delta B_w/B_0 \sim 0.036$ the secondary decay threshold is reached and the growth rates of the primary whistler and IAW modes rapidly drop. At the threshold, the growth rate of the secondary whistler mode exceeds that of the primary whistler, while the ion acoustic wave growth rates are comparable to each other. The tertiary threshold is reached at $\delta B_w/B_0 \sim 0.063$, as the pump amplitude is increased the secondary and tertiary whistler growth rates appear to saturate while the primary whistler growth rate increases linearly with the pump amplitude. The IAW rates all continue to increase with the primary IAW exceeding the growth rate prior to any of the cascades.

While this study is focused on the parametric interaction of whistlers with ion acoustic waves, there is the possibility of a similar parametric interaction with the electron acoustic wave (EAW) that has been proposed by Agapitov et al. (2015b) as a generation mechanism of nonlinear electrostatic structures observed in the Earth's radiation belts. The electron acoustic wave is heavily damped and can largely be ignored in a plasma with a single electron component, i.e. an electron population associated with a single temperature. However, under certain conditions, in plasmas with both hot (subscript *h*) and cold (subscript *c*) electron populations the electron acoustic wave becomes only weakly damped; the conditions for this were first mapped by Gary and Tokar (1985) and are approximately $T_h/T_c > 10$ and $0 < n_c < 0.8n_e$ where $n_c + n_h = n_e$. In Figure 10A we show a possible setup for observation of the whistler-EAW parametric instability, and in Figure 10B we demonstrate the existence of the lightly damped EAW in the UPIC simulation. The parameters for the EAW are $T_h/T_c = 100$, $n_c/n_e = 0.1$, $vth = 3.16$, and $\omega_{ce} = 3\omega_{pe}/4$. As outlined in Figure 10A the pump wave should decay to a co-propagating EAW and counter-propagating whistler, in a similar fashion to the IAW coupling. However, from preliminary studies we observe that the dominant coupling of the whistler wave is to the electron plasma (Langmuir) wave branch (upper branch in Figure 10) that is more unstable than the EAW. It is possible to drive the EAW instability with a relative drift between the hot and cold populations (Gary, 1987) and this condition was present in the observations by Agapitov et al. (2015b); this relative drift configuration may be required to observe the whistler-EAW parametric instability.

Recently, Parker Solar Probe has revealed that wave-wave interactions may be as common in the solar wind as they are in the Earth's magnetosphere (Ma et al., 2021). Whistler waves are assumed to control the generation of the superthermal electrons in the solar corona and their dynamics during propagation in the solar wind (Vocks and Mann, 2003; Vocks et al., 2005). The recent observations by Solar Orbiter showed only anti-sunward propagation of whistler waves at around 100 $R_\odot$ (solar radii) (Kretzschmar et al., 2021). However, observations of the Parker Solar Probe at heliocentric distances from 20 to 50 $R_\odot$ revealed whistler waves propagating sunward (Agapitov et al., 2020; Dudok de Wit et al., 2022), anti-sunward (Dudok de Wit et al., 2022), and counter-streaming whistlers (Karbashews et al., 2022). The sunward propagating whistler waves can significantly contribute to scattering the strahl electrons into the halo population (Vocks et al., 2005; Roberg-Clark et al., 2019). The higher amplitude of these waves (5–10 times greater compared to whistlers observed by Solar Orbiter) can suggest the local generation of these waves (supported by the localized region of whistlers observation: above 22–25 $R_\odot$ (Cattell et al., 2022)) by electron instabilities (probably together with anti-sunward waves) or from a turbulent cascade of anti-sunward whistler waves generated locally by beam instabilities. Observations of ion acoustic waves in this region (reported in (Mozer et al., 2020) and earlier from Helios observations (Gurnett and Frank, 1978)) make the parametric cascading through the ion acoustic mode to be a potentially feasible generation mechanism of the observed sunward propagating whistler population.

The main results of this paper can be summarized as follows. A Darwin particle-in-cell (PIC) simulation model has been used to study the parametric decay instability of parallel propagating whistler waves in the presence of an undamped ion acoustic wave (IAW). A field-aligned monochromatic whistler wave is launched and couples to a counter-propagating whistler mode and co-propagating ion acoustic mode. The coupling of the electromagnetic fields to the electrostatic field *via* the ponderomotive force forms spatio-temporal beat patterns in the longitudinal electric field generated by the counter-propagating whistlers and pump whistler wave. The threshold amplitude for the instability is determined and agrees with a prediction using the ion decay instability. As the amplitude of the pump whistler wave is increased, secondary and tertiary decay thresholds are reached and are observed to cascade from the daughter whistler modes. At the largest amplitude ($\delta B_w/B_0 \sim 0.1$) the primary IAW evolves into a short-lived and highly nonlinear structure. The growth rate scaling with amplitude for the primary decay channel compares favourably with analytical expressions. We presented preliminary results on the parametric coupling of whistler waves with the electron acoustic wave (EAW).

Concerning future studies, the present simulation model will be used to explore the conditions under which parametric instability involving the EAW can be present as has been observed in space plasmas. Plasma conditions that support an undamped electron acoustic wave are likely to also have a weakly damped ion acoustic wave; future simulations could be performed with both modes present to determine the dominant electrostatic coupling and under what conditions this holds. Last, the present study focused on 1-D processes, similar 2-D and/or 3-D studies could provide insight into parametric interactions of oblique whistler waves that are commonly found in both the magnetosphere and solar wind.

Data availability statement

The raw data supporting the conclusions of this article will be made available by the authors, without undue reservation.

Author contributions

SK ran the simulations, formulated the whistler-ion acoustic ponderomotive coupling and parametric decay model, produced the figures, and wrote parts of the theory and discussion sections and the majority of the results section. RS advised on the simulations, compared the simulation results with the for instability thresholds and growth rates, and wrote parts of the theory and discussion sections and the majority of the introduction. OA reviewed the results, advised on manuscript content, and contributed to the introduction and discussion sections.

Funding

SK acknowledges support from NSERC, NASA grants 80NNSC19K0264, 80NNSC19K0848, and NSF grant 1914670, RS acknowledges support from NSERC, and OA. acknowledges support from 80NNSC19K0848, 80NSSC22K0522, 80NSSC20K0218, 80NSSC22K0433, 80NSSC21K1770, and NSF grant number 191467.

Acknowledgments

We would like to acknowledge the assistance of Viktor Decyk with using the UPIC simulation software, and acknowledge the use of the perceptually uniform and colour-vision-deficiency friendly colour maps developed by Crameri et al. (2020) for public use.

Conflict of interest

The authors declare that the research was conducted in the absence of any commercial or financial relationships that could be construed as a potential conflict of interest.

Publisher's note

References

Agapitov, O. V., Artemyev, A. V., Mourenas, D., Mozer, F. S., and Krasnoselskikh, V. (2015a). Nonlinear local parallel acceleration of electrons through landau trapping by oblique whistler mode waves in the outer radiation belt. *Geophys. Res. Lett.* 42, 2015GL066887. doi:10.1002/2015GL066887

Agapitov, O. V., Krasnoselskikh, V., Mozer, F. S., Artemyev, A. V., and Volokitin, A. S. (2015b). Generation of nonlinear electric field bursts in the outer radiation belt through the parametric decay of whistler waves. *Geophys. Res. Lett.* 42, 3715–3722. doi:10.1002/2015GL064145

Agapitov, O. V., Wit, T. Dd, Mozer, F. S., Bonnell, J. W., Drake, J. F., Malaspina, D., et al. (2020). Sunward-propagating whistler waves collocated with localized magnetic field holes in the solar wind: *Parker solar probe* observations at 35.7 $R_\odot$ radii. *Astrophys. J.* 891, L20. doi:10.3847/2041-8213/ab799c

Appleton, E. V. (1927). *URSI proceedings*. Brussels: Washington General Assembly.

Bellan, P. M., and Stasiewicz, K. (1998). Fine-scale cavitation of ionospheric plasma caused by inertial alfvén wave ponderomotive force. *Phys. Rev. Lett.* 80, 3523–3526. doi:10.1103/physrevlett.80.3523

Burtis, W. J., and Helliwell, R. A. (1969). Banded chorus—A new type of vlf radiation observed in the magnetosphere by ogo 1 and ogo 3. *J. Geophys. Res.* 74, 3002–3010. doi:10.1029/JA074i011p03002

Busnardo-Neto, J., Pritchett, P., Lin, A., and Dawson, J. (1977). A self-consistent magnetostatic particle code for numerical simulation of plasmas. *J. Comput. Phys.* 23, 300–312. doi:10.1016/0021-9991(77)90096-1

Cattell, C., Breneman, A., Dombeck, J., Hanson, E., Johnson, M., Halekas, J., et al. (2022). Parker solar probe evidence for the absence of whistlers close to the sun to scatter strahl and to regulate heat flux. *Astrophys. J. Lett.* 924, L33. doi:10.3847/2041-8213/ac4015

Cattell, C., Breneman, A., Dombeck, J., Short, B., Wygant, J., Halekas, J., et al. (2021). Parker solar probe evidence for scattering of electrons in the young solar wind by narrowband whistler-mode waves. *Astrophys. J. Lett.* 911, L29. doi:10.3847/2041-8213/abefdd

Cattell, C., Wygant, J. R., Goetz, K., Kersten, K., Kellogg, P. J., von Rosenvinge, T., et al. (2008). Discovery of very large amplitude whistler-mode waves in earth's radiation belts. *Geophys. Res. Lett.* 35, L01105. doi:10.1029/2007GL032009

Chen, F. F. (1984). *Introduction to plasma physics and controlled fusion*. 2nd edn. New York: Plenum Press.

Crameri, F., Shephard, G. E., and Heron, P. J. (2020). The misuse of colour in science communication. *Nat. Commun.* 11, 5444. doi:10.1038/s41467-020-19160-7

Decyk, V. K. (2007). Upic: A framework for massively parallel particle-in-cell codes. *Comput. Phys. Commun.* 177, 95–97. doi:10.1016/j.cpc.2007.02.092

Dudok de Wit, T., Krasnoselskikh, V. V., Agapitov, O., Froment, C., Larosa, A., Bale, S. D., et al. (2022). First results from the SCM search-coil magnetometer on parker solar probe. *JGR. Space Phys.* 127, e2021JA030018. doi:10.1029/2021JA030018

Forslund, D. W., Kindel, J. M., and Lindman, E. L. (1972). Parametric excitation of electromagnetic waves. *Phys. Rev. Lett.* 29, 249–252. doi:10.1103/PhysRevLett.29.249

Gao, X., Chen, R., Lu, Q., Chen, L., Chen, H., and Wang, X. (2022). Observational evidence for the origin of repetitive chorus emissions. *Geophys. Res. Lett.* 49, e2022GL099000. doi:10.1029/2022GL099000

Gao, X., Li, W., Thorne, R. M., Bortnik, J., Angelopoulos, V., Lu, Q., et al. (2014). New evidence for generation mechanisms of discrete and hiss-like whistler mode waves. *Geophys. Res. Lett.* 41, 4805–4811. doi:10.1002/2014GL060707

Gao, X., Lu, Q., Bortnik, J., Li, W., Chen, L., and Wang, S. (2016). Generation of multiband chorus by lower band cascade in the earth's magnetosphere. *Geophys. Res. Lett.* 43, 2343–2350. doi:10.1002/2016GL068313

Gary, S. P. (1987). The electron/electron acoustic instability. *Phys. Fluids (1994).* 30, 2745–2749. doi:10.1063/1.866040

Gary, S. P., and Tokar, R. L. (1985). The electron-acoustic mode. *Phys. Fluids (1994).* 28, 2439–2441. doi:10.1063/1.865250

Gurnett, D. A., and Bhattacharjee, A. (2005). *Introduction to plasma physics: With space and laboratory applications*. Cambridge University Press, 84–90.

Gurnett, D. A., and Frank, L. A. (1978). Ion acoustic waves in the solar wind. *J. Geophys. Res.* 83, 58–74. doi:10.1029/JA083iA01p00058

Hartree, D. R. (1931). The propagation of electromagnetic waves in a refracting medium in a magnetic field. *Math. Proc. Camb. Phil. Soc.* 27, 143–162. doi:10.1017/S0305004100009440

Huang, S. Y., Sahraoui, F., Yuan, Z. G., Contel, O. L., Breuillard, H., He, J. S., et al. (2018). Observations of whistler waves correlated with electron-scale coherent structures in the magnetosheath turbulent plasma. *Astrophys. J.* 861, 29. doi:10.3847/1538-4357/aac831

Hughes, R. S., Wang, J., Decyk, V. K., and Gary, S. P. (2016). Effects of variations in electron thermal velocity on the whistler anisotropy instability: Particle-in-cell simulations. *Phys. Plasmas* 23, 042106. doi:10.1063/1.4945748

Karbashews, S., Agapitov, O. V., and Kim, H. Y. (2022). *Counter-streaming whistlers collocated with magnetic field inhomogeneities in the solar wind: Parker solar probe observations during encounter 1 at 42.6r⊙. The Astrophysical Journal in Preparation.*

Karbashewski, S. (2017). *Large amplitude whistler waves: Nonlinear dynamics and interactions*. Master's thesis. Edmonton, AB: University of Alberta. doi:10.7939/R33776B4R

Ke, Y., Gao, X., Lu, Q., Hao, Y., and Wang, S. (2018). Parametric decay of oblique whistler waves in the earth's magnetosphere: 2-d pic simulations. *Phys. Plasmas* 25, 072901. doi:10.1063/1.5037763

Ke, Y., Gao, X., Lu, Q., and Wang, S. (2017). Parametric decay of a parallel propagating monochromatic whistler wave: Particle-in-cell simulations. *Phys. Plasmas* 24, 012108. doi:10.1063/1.4974160

Kretzschmar, M., Chust, T., Krasnoselskikh, V., Graham, D., Colomban, L., Maksimovic, M., et al. (2021). Whistler waves observed by solar orbiter/RPW between 0.5 AU and 1 AU. *Astron. Astrophys.* 656, A24. doi:10.1051/0004-6361/202140945

Lacombe, C., Alexandrova, O., Matteini, L., SantolÃk, O., Cornilleau-Wehrlin, N., Mangeney, A., et al. (2014). Whistler mode waves and the electron heat flux in the solar wind:clusterobservations. *Astrophys. J.* 796, 5. doi:10.1088/0004-637X/796/1/5

Lassen, H. I. (1926). Über die ionisation der atmosphäre und ihren einfluß auf die ausbreitung der kurzen elektrischen wellen der drahtlosen telegraphie. *Z. für Hochfrequenztech.* 28, 109.

Ma, J., Gao, X., Yang, Z., Tsurutani, B. T., Liu, M., Lu, Q., et al. (2021). Nonlinear wave–wave coupling related to whistler-mode and electron bernstein waves observed by the parker solar probe. *Astrophys. J.* 918, 26. doi:10.3847/1538-4357/ac0ef4

Maksimovic, M., Harvey, C. C., Santolík, O., Lacombe, C., de Conchy, Y., Hubert, D., et al. (2001). Polarisation and propagation of lion roars in the dusk side magnetosheath. *Ann. Geophys.* 19, 1429–1438. doi:10.5194/angeo-19-1429-2001

Max, C. E. (1976). Strong self-focusing due to the ponderomotive force in plasmas. *Phys. Fluids (1994).* 19, 74–77. doi:10.1063/1.861305

Meredith, N. P., Horne, R. B., and Anderson, R. R. (2001). Substorm dependence of chorus amplitudes: Implications for the acceleration of electrons to relativistic energies. *J. Geophys. Res.* 106, 13165–13178. doi:10.1029/2000JA900156

Miller, M. A. (1958). Motion of charged particles in the high-frequency electromagnetic fields. *Radiophysics* 1, 110–123.

Morales, G. J., and Lee, Y. C. (1974). Ponderomotive-force effects in a nonuniform plasma. *Phys. Rev. Lett.* 33, 1016–1019. doi:10.1103/physrevlett.33.1016

Mourenas, D., Artemyev, A. V., Agapitov, O. V., Krasnoselskikh, V., and Li, W. (2014). Approximate analytical solutions for the trapped electron distribution due to quasi-linear diffusion by whistler mode waves. *JGR. Space Phys.* 119, 9962–9977. doi:10.1002/2014JA020443

Mozer, F. S., Bonnell, J. W., Bowen, T. A., Schumm, G., and Vasko, I. Y. (2020). Large-amplitude, wideband, Doppler-shifted, ion acoustic waves observed on the parker solar probe. *Astrophys. J.* 901, 107. doi:10.3847/1538-4357/abafb4

Neubert, T. (1982). Stimulated scattering of whistler waves by ion acoustic waves in the magnetosphere. *Phys. Scr.* 26, 239–247. doi:10.1088/0031-8949/26/3/016

Nishikawa, K. (1968). Parametric excitation of coupled waves i. general formulation. *J. Phys. Soc. Jpn.* 24, 916–922. doi:10.1143/JPSJ.24.916

Omura, Y., Katoh, Y., and Summers, D. (2008). Theory and simulation of the generation of whistler-mode chorus. *J. Geophys. Res.* 113. doi:10.1029/2007JA012622

Reeves, G. D., Spence, H. E., Henderson, M. G., Morley, S. K., Friedel, R. H. W., Funsten, H. O., et al. (2013). Electron acceleration in the heart of the van allen radiation belts. *Science* 341, 991–994. doi:10.1126/science.1237743

Roberg-Clark, G. T., Agapitov, O., Drake, J. F., and Swisdak, M. (2019). Scattering of energetic electrons by heat-flux-driven whistlers in flares. *Astrophys. J.* 887, 190. doi:10.3847/1538-4357/ab5114

Shukla, P. K. (1977). Parametric coupling of a large-amplitude whistler wave with ion quasimodes in plasmas. *Phys. Rev. A* 16, 1294–1296. doi:10.1103/PhysRevA.16.1294

Terasawa, T., Hoshino, M., Sakai, J. I., and Hada, T. (1986). Decay instability of finite-amplitude circularly polarized alfven waves: A numerical simulation of stimulated brillouin scattering. *J. Geophys. Res.* 91, 4171–4187. doi:10.1029/JA091iA04p04171

Thorne, R. M. (2010). Radiation belt dynamics: The importance of wave-particle interactions. *Geophys. Res. Lett.* 37. doi:10.1029/2010GL044990

Tong, Y., Vasko, I. Y., Artemyev, A. V., Bale, S. D., and Mozer, F. S. (2019). Statistical study of whistler waves in the solar wind at 1 au. *Astrophys. J.* 878, 41. doi:10.3847/1538-4357/ab1f05

Umeda, T., and Ito, T. (2008). Vlasov simulation of Langmuir decay instability. *Phys. Plasmas* 15, 084503. doi:10.1063/1.2965494

Umeda, T., Saito, S., and Nariyuki, Y. (2018). Decay of nonlinear whistler mode waves: 1D versus 2D. *Phys. Plasmas* 25, 072118. doi:10.1063/1.5031483

Umeda, T., Saito, S., and Nariyuki, Y. (2014). Electron acceleration during the decay of nonlinear whistler waves in low-beta electron-ion plasma. *Astrophys. J.* 794, 63. doi:10.1088/0004-637X/794/1/63

Umeda, T., Saito, S., and Nariyuki, Y. (2017). Rapid decay of nonlinear whistler waves in two dimensions: Full particle simulation. *Phys. Plasmas* 24, 054503. doi:10.1063/1.4982609

Usui, H., Matsumoto, H., and Gendrin, R. (2002). Numerical simulations of a three-wave coupling occurring in the ionospheric plasma. *Nonlinear process. geophys.* 9, 1–10. doi:10.5194/npg-9-1-2002

Vocks, C., and Mann, G. (2003). Generation of suprathermal electrons by resonant wave-particle interaction in the solar corona and wind. *Astrophys. J.* 593, 1134–1145. doi:10.1086/376682

Vocks, C., Salem, C., Lin, R. P., and Mann, G. (2005). Electron halo and strahl formation in the solar wind by resonant interaction with whistler waves. *Astrophys. J.* 627, 540–549. doi:10.1086/430119

Frontiers in
Astronomy and Space Sciences

Explores planetary science and extragalactic astronomy in all wavelengths

Advances the understanding of our universe - from planetary science to extragalactic astronomy, to high-energy and astroparticle physics.

Discover the latest Research Topics

See more →

Frontiers

Avenue du Tribunal-Fédéral 34
1005 Lausanne, Switzerland
frontiersin.org

Contact us

+41 (0)21 510 17 00
frontiersin.org/about/contact